Combining kinematic and photometric constraints on the galaxy-halo connection

Tariq Yasin

Balliol College

University of Oxford

A thesis submitted for the degree of

Doctor of Philosophy

Trinity 2023

Abstract

In this thesis I develop methods to maximise the information extracted on the galaxy-halo connection from forthcoming large-scale surveys. In particular I focus on combining photometric and kinematic constraints on the galaxy-halo connection.

I present constraints on the dark matter halo mass and concentration of ~22,000 individual galaxies visible both in HI (from the ALFALFA survey) and optical light (from the SDSS). This is achieved by combining two Bayesian models, one for the HI line width as a function of the stellar and neutral hydrogen mass distributions in a galaxy using kinematic modelling, and the other for the galaxy's total baryonic mass using the technique of inverse subhalo abundance matching. I hence quantify the constraining power on halo properties of spectroscopic and photometric observations, and assess their consistency. I find good agreement between the two sets of posteriors, although there is a sizeable population of low-line width galaxies that favour significantly smaller dynamical masses than expected from abundance matching (especially for cuspy halo profiles). Abundance matching provides significantly more stringent bounds on halo properties than the HI line width, even with a mass–concentration prior included, although combining the two provides a mean gain of 40% for the sample when fitting an NFW profile. I also use the kinematic posteriors to construct a baryonic mass–halo mass relation, which I find to be near power-law, and with a somewhat shallower slope than expected from abundance matching. My method demonstrates the potential of combining photometric and spectroscopic observations to precisely map out the dark matter distribution at the galaxy scale using upcoming HI surveys such as the SKA.

The precision of constraints on halo parameters is a complex function of properties of the measurements as well as properties of the galaxy itself. Forthcoming surveys will resolve rotation curves to varying degrees of precision, or measure their integrated effect in the HI linewidth. To ascertain the relative significance of the relevant quantities for constraining halo properties, I study the information on halo mass and concentration as

quantified by the Kullback–Leibler divergence of the kinematics-informed posterior from the uninformative prior. I calculate this divergence as a function of the different types of spectroscopic observation, properties of the measurement, galaxy properties and auxiliary observational data on the baryonic components. Using the SPARC sample, I find that fits to the full rotation curve exhibit a large variation in information gain between galaxies, ranging from ∼1 to ∼11 bits. The variation is predominantly caused by the vast differences in the number of data points and the size of velocity uncertainties between the SPARC galaxies. I also study the relative importance of the minimum HI surface density probed and the size of velocity uncertainties on the constraining power on the inner halo density slope, finding the latter to be significantly more important. I spell out the implications of these results for the optimisation of galaxy surveys aiming to constrain galaxies' dark matter distributions, highlighting the need for precise velocity measurements.

I then combine my Bayesian forward model for the HI line profile with IFU stellar kinematic data from the MaNGA survey in order to constraint the halo properties of high mass late-type galaxies. I find combining IFU and HI data is able to greatly strengthen constraints on halo properties, as the two pieces of data probe different parts of the rotation curve and hence are able to break degeneracies. I find evidence that high-mass late-type galaxies have on average very high star-formation efficiencies, converting nearly all of their cosmologically available baryons to stars, in agreement with my ALFALFA study. I also find evidence the inner slope parameter of our sample is slightly shallower (~ 0.75) than an NFW halo, in disagreement with expectations from simulations.

I conduct a preliminary investigation on using weak lensing to achieve precision constraints on the galaxy-halo connection using a Bayesian hierarchical lensing formalism. I find strong evidence that a standard modelling assumption in Bayesian lensing methods: that the sampling distribution of the shear is a Gaussian with width given by the `lensfit` uncertainties, leads to a biased inference of model parameters. I conclude that it is necessary to treat the intrinsic galaxy ellipticity distribution and/or photometric uncertainties

in galaxy shape measurements with a more sophisticated approach that accounts for any non-Gaussianity, and possibly to jointly infer the intrinsic ellipticity distribution as part of the inference.

I conclude by discussing open challenges in the field, and highlighting how the methods I have developed above, when applied to the trove of data from forthcoming galaxy surveys, will help revolutionise our knowledge of the galaxy-halo connection and ultimately the processes that underlie galaxy formation.

Acknowlegements

With many thanks to my wonderful supervisors Harry Desmond, Julien Devriendt and Adrianne Slyz, with a special mention to Harry for turning an ambiguous lockdown zoom call into years of great supervision. A special thanks also to Jonathan Patterson for battling to keep the cluster running smoothly in the face of all sorts of deviancies.

I thank Michele Cappellari, Alessandro Sonnenfeld, Anastasia Ponomareva, Richard Stiskalek, Harley Katz, Martin Rey, Federico Lelli, Johannes Buchner, Jamie Bamber and Stacy McGaugh for useful inputs and discussions and Federico Lelli, Richard Stiskalek, Martha Haynes and Jing Wang for sharing their data with us.

I am supported by STFC. Projects in this thesis have received funding from the European Research Council (ERC) under the European Union's Horizon 2020 research and innovation programme (grant agreement No 693024).

Statement of Originality

I hereby declare that no part of this thesis has been accepted, or is currently being submitted, for any degree or diploma or certificate or any other qualification at the University of Oxford or elsewhere. The work in this thesis is entirely my own, and has been carried out under the supervision of Dr. Harry Desmond, Professor Julien Devriendt and Professor Adrianne Slyz.

Chapter 3 presents work published in Monthly Notices of the Royal Astronomical Society: T. Yasin, H. Desmond, J. Devriendt, A. Slyz **"Inferring dark matter halo properties for HI-selected galaxies"** (Yasin et al., 2023a).

Chapter 4 presents work published in Monthly Notices of the Royal Astronomical Society: T. Yasin, H. Desmond, J. Devriendt, A. Slyz **"The information on dark matter halo profiles contained in spectroscopic observations of late-type galaxies"** (Yasin et al., 2023b).

Contents

Chapter 1

Introduction

1.1 The cosmological model

1.1.1 General relativity

The starting point for modern cosmology was the development of the theory of General Relativity by Einstein in the early 20th century (Einstein, 1916). The theory developed from Einstein's insight that the apparent equivalence between inertial mass and gravitational mass necessitates an equivalence between accelerating frames and gravitational fields. In particular, the weak equivalence principle states it is always possible to pick an accelerating reference frame for an observer falling in a gravitational field such that there appears locally to be no gravitational field. Although the historical development of the theory is debated, from this principle alone it is possible to derive the geodesic equation describing how an object moves in a gravitational field (Weinberg, 1972)

$$\frac{d^2x^\beta}{d\tau^2} + \Gamma^\beta{}_{\alpha\nu}\frac{dx^\alpha}{d\tau}\frac{dx^\nu}{d\tau} = 0, \tag{1.1}$$

where $x^\beta \equiv (ct, x, y, z)$ is the spacetime position of an object, τ is the proper time and $\Gamma^\beta{}_{\alpha\nu}$ is the Christoffel symbol

$$\Gamma^\beta{}_{\alpha\nu} = \frac{1}{2}g^{\mu\beta}\left(\partial_\alpha g_{\mu\nu} + \partial_\nu g_{\mu\alpha} - \partial_\mu g_{\alpha\nu}\right), \tag{1.2}$$

where the metric $g^{\mu\beta}$ encodes the geometry of spacetime through the invariant square of the infinitesimal line element

$$ds^2 = g_{\mu\nu}dx^\mu dx^\nu. \tag{1.3}$$

In a flat spacetime the Christoffel symbols are equal to zero, so test particles follow straight lines through spacetime. However in non-flat spacetime the particles accelerate along curved paths, which we identify as acceleration due to gravitational forces. In this formulation gravity is not a force acting within spacetime, but is instead in fact a consequence of spacetime curvature itself.

The second fundamental component of General Relativity is the Einstein field equations, which describe the curvature of the four-dimensional spacetime by the matter and energy contents within it

$$G_{\mu\nu} = 8\pi G T_{\mu\nu} + \Lambda g_{\mu\nu}, \tag{1.4}$$

where $G_{\mu\nu}$ is the Einstein tensor

$$G_{\mu\nu} = R_{\mu\nu} - \frac{1}{2}R g_{\mu\nu} \tag{1.5}$$

with $R_{\mu\nu}$ the Ricci tensor and $R \equiv g_{\mu\nu}R^{\mu\nu}$ the Ricci scalar, both of which are related to the curvature of spacetime, quantified by the Riemann curvature tensor $R^\nu_{\mu\alpha\nu}$. $T_{\mu\nu}$, the stress-energy tensor, describes the matter and energy content of the universe. Λ, now known as the cosmological constant, was initially set to zero by Einstein, but as we shall discuss later has become an essential part of our cosmological model. The Einstein field equations relate the curvature of spacetime in a given region (left side) to the distribution of matter and energy within that region (right side). Their derivation is beyond the scope of this thesis, but their form is dictated by requirements of general covariance and their reduction to Poisson's equation in the weak-field limit. Combined with the geodesic equation they fully describe the movement of matter/energy through spacetime, and in turn how spacetime distorts in response to the position of the matter/energy. The theory of General Relativity

is validated to high precision by numerous experimental tests at a range of scales including the procession of the perihelion of mercury, gravitational lensing (Dyson et al., 1920) and gravitational redshift (Pound & Rebka, 1960). However, despite its success, it has yet be reconciled with quantum mechanics, another pillar of modern physics. As a result it fails to provide a complete description of gravitational effects in the universe.

1.1.2 An expanding universe

The Friedmann equations (Friedmann, 1922) describe the dynamics of the universe in the context of general relativity. They assume that the universe is homogeneous and isotropic, thereby adhering to the Copernican principle: that humans, as observers, do not inhabit a special place in the universe.

Under this assumption the most general metric tensor is the Friedmann-Lemaître-Robertson-Walker (FLRW) metric

$$c^2 \mathrm{d}\tau^2 = -c^2 \mathrm{d}t^2 + a(t)^2 \mathrm{d}\boldsymbol{\Sigma}^2 \tag{1.6}$$

where $\boldsymbol{\Sigma}$ is a three-dimensional metric of constant curvature (which can be either negative, zero or positive). $\boldsymbol{\Sigma}$ is independent of t, with all time-dependence encoded in $a(t)$. This metric is used in the Einstein field equations and the energy-momentum tensor $T_{\mu\nu}$ for a perfect fluid is assumed, which has the form

$$T^{\mu\nu} = \left(\rho_m + \frac{p}{c^2}\right) U^\mu U^\nu + p\, g^{\mu\nu} \tag{1.7}$$

where ρ_m is the rest-frame energy density of the fluid, p is the rest-frame pressure U_μ is the four-velocity and c is the speed of light. The results in the Friedmann equations, which describe the time-evolution of the universe

$$H^2 = \left(\frac{\dot{a}}{a}\right)^2 = \frac{8\pi G}{3}\rho - \frac{kc^2}{a^2} \tag{1.8}$$

$$\frac{\ddot{a}}{a} = -\frac{4\pi G}{3}\left(\rho + \frac{3p}{c^2}\right) + \frac{\Lambda c^2}{3}, \tag{1.9}$$

where H is the Hubble parameter, $\dot{a}$ and $\ddot{a}$ are its first and second time derivatives and k is the spatial curvature parameter (with units m^{-2}), with $k < 0$ corresponding to a universe with open geometry, $k = 0$ to a flat universe, and $k > 0$ to a closed universe.

By adopting equations of state, $p = w\rho c^2$, corresponding to the different species present in the universe, the Friedmann equations can be solved for the evolution of the universe as a function of its content. Non-relativistic matter is treated as a pressureless dust, with $w = 0$. Photons and neutrinos, which are ultrarelativistic, have $w = 1/3$ from statistical thermodynamics. Λ, or *dark energy*, can be treated as contributing an effective pressure and density to $T_{\mu\nu}$, with $w = -1$ the simplest assumption, in which case it acts as a constant additional energy density and pressure over time.

By decomposing ρ into the density contribution from matter, radiation and dark energy, equation 1.8 can be written as

$$\left(\frac{H}{H_0}\right)^2 = \Omega_{\mathrm{m}} a^{-3} + \Omega_{\mathrm{rad}} a^{-4} + \Omega_{\Lambda} + \Omega_{\mathrm{k}} a^{-2} \tag{1.10}$$

where H_0 (the Hubble constant) is the value of the Hubble parameter H today, and we define

$$\Omega_x = \frac{8\pi G}{3H_0^2}\rho_x, \quad \Omega_k = \frac{-kc^2}{H_0^2}, \quad \Omega_{\Lambda} = \frac{\Lambda}{3H_0^2} \tag{1.11}$$

for the x different species (here matter and radiation), with ρ_x their present day density. This equation shows clearly that the evolution of the universe is strongly dependent on its content. Most strikingly $\ddot{a}$ can either be positive, negative or zero depending on the relative abundance of matter, radiation, dark energy and the curvature.

In 1929 Hubble found evidence that the universe is expanding from studying the redshift of galaxies, finding that the velocity of galaxies is proportional to their distance from us (Hubble, 1929). This is led to the development of theories of a very hot and dense early universe which has been expanding ever since. Alpher et al. (1948) developed a theory for the synthesis of heavy elements in the hot early universe, which Hoyle described this as hypothesising a "Big Bang", a term that has stuck to refer to this class of theory. Until

the 1960s there was much debate between these theories and steady state theories with a non-evolving universe. However the discovery of the cosmic microwave background (CMB) at Bell Labs in 1964 (Penzias & Wilson, 1965) provided stunning confirming of the Big Bang. The CMB is relic radiation from the early universe when baryons, in the form of ionised plasma, and photons were coupled through Compton scattering. The plasma neutralised at the end of recombination, and the photons emitted at that time have travelled uninterrupted until reaching us today. Therefore the power and polarisation as a function of angular position of the CMB encodes much information about the content and conditions of the early universe.

1.1.3 ΛCDM

Over the past few decades evidence has accumulated in favour of the standard model of cosmology ΛCDM, in which the present day density of the universe primarily consists of dark energy ($\Omega_\Lambda = 0.7$) and matter ($\Omega_m = 0.3$). The present day radiation density ($\Omega_{\rm rad} \sim 10^{-4}$) and the curvature ($|\Omega_k| < 0.01$) are strongly constrained by observations, with the latter set to zero in the simplest flat ΛCDM model. 85% of the matter is in the form of cold dark matter, a collisionless and at most weakly interacting particle, with the remaining 15% consisting of the observed baryons.

The model has two parameters to describe the primordial fluctuations in the early universe that later gave rise to the anisotropies in the CMB. They are characterised by a power spectrum describing how the amplitude of the fluctuations varies with scale

$$\mathcal{P}_{\rm s}(k) \propto A_s \left(\frac{k}{k_*}\right)^{n_{\rm s}-1}, \tag{1.12}$$

with k the wavenumber of the fluctuations, the amplitude A_s setting the overall amplitude or strength of the fluctuations, the spectral index n_s, describing how the amplitude of the fluctuations changes with scale and k_* a characteristic wavenumber. With $n_s = 1$, the spectrum is scale-invariant, meaning the amplitude is the same on all scales.

The final free parameter is τ_*, the optical depth to reionization, which is a measure of the opacity of the universe to CMB photons due to Thomson scattering. For a given set of primordial perturbations, the Boltzmann equations describing the evolution of different particle species in an expanding space-time can be solved and photon paths propagated to generate statistical properties of the CMB as a function of the ΛCDM parameters, which can then be constrained by the data.

With only six independent parameters and few ingredients in the base model, ΛCDM provides a compelling explanation for a large variety of observations including the cosmic microwave background, the large scale structure of galaxies, big bang nucleosynthesis and the accelerating expansion of the universe. It has proved difficult for other models to usurp - they can often provide better evidence for individual observations but not the ensemble. Modern CMB experiments beginning with WMAP (Komatsu et al., 2009) and most recently Planck (Collaboration et al., 2016) have mapped out the CMB to incredible precision, allowing the ΛCDM cosmological parameters to be tightly constrained. We show the parameters obtained from Planck in Table 1.1. Whilst the CMB anisotropy is the only probe able to simultaneous constrain all six parameters, and also gives the most precise constrains, the strongest validation of the ΛCDM theory comes from the consistency between cosmological parameters measured by a variety of different probes.

In particular the large-scale distribution of galaxies (the *large-scale structure*) can be used to constrain cosmology in a number of different ways. The Baryon Acoustic Oscillations (e.g. Bassett & Hlozek, 2009) are a preferred length scale in the galaxy distribution imprinted by waves in the baryon-photon fluid which became frozen into the matter distribution during recombination. Redshift Space Distortions (RSD) are distortions in the observed spatial distribution of galaxies due to the peculiar velocities of galaxies, which cause additional redshifts besides those caused by the expansion of the universe. They are sensitive to the density-weighted growth rate $f\sigma_8$ (an alternative ΛCDM parameterisation that quantifies the growth of structure in the universe), and were recently measured to

Parameter	Symbol	Value
Hubble constant	H_0	67.4 ± 0.5 km/s/Mpc
Dark matter density	$\Omega_{\rm DM}$	0.2607 ± 0.0045
Baryon density	Ω_b	0.02233 ± 0.00015
Scalar spectral amplitude	$\ln(10^{10} A_s)$	3.045 ± 0.016
Scalar spectral index	n_s	0.9649 ± 0.0044
Optical depth to reionisation	τ_*	0.0544 ± 0.0081

Table 1.1: The cosmological parameters from the Planck TT+TE+EE+lowE data. The uncertainties correspond to 68% confidence intervals.

high-precision by the BOSS survey (Alam et al., 2017).

Another useful probe is weak gravitational lensing, the distortions in the shapes of background galaxies caused by the deflection of light due to foreground matter. Measuring cosmic shear, the autocorrelation of observed galaxy shapes, is particularly useful for cosmology as it is sensitive to the overall matter distribution of the universe, and therefore is independent of the *bias* model that is required when using galaxies to trace the overall matter density field using the distribution of galaxies as in the above tests. Recently cosmic shear has been measured by a variety of surveys, constraining Ω_m and the $\sigma_8(\Omega_m/0.3)^{1/2}$ (Asgari et al., 2021; Collaboration et al., 2022; Lu et al., 2023b), where σ_8 quantifies the amplitude of mass fluctuations on a scale of 8 Mpc/h.

A notable exception to the concordance between probes is the disagreement between H_0 measured through supernovae (Riess et al., 2022), which is now in 5-sigma tension with the CMB constraint. There is much ongoing debate about whether this result necessitates new physics or may be due to systematics, as well as concerted efforts to seek out new independent probes of H_0 such as strong lensing tomography (Shajib & Strides, 2020). In spite of some tensions the general agreement of the cosmological parameters from different probes has served to bolster confidence that ΛCDM, or a theory not all too different from it, is a true description of the universe.

1.1.3.1 Alternative gravity models

Modified Newtonian Dynamics (MOND) is an alternative gravity model which seeks to account for the discrepancy between observed and measured gravitational effects using modifications to gravity instead of new, invisible particles. However, it is non-trivial to reproduce CMB data and the matter power spectrum in MOND theories (e.g. Dodelson, 2011; Pardo & Spergel, 2020). Perhaps the biggest challenge is the presence of large baryon acoustic oscillations in the matter power spectrum due to the lack of dark matter to damp them in such theories. However recently Skordis & Złośnik (2021) proposed a theory that reduces to MOND in the weak field limit and is able to reproduce both the CMB and the linear power spectrum (whilst matching constraints on gravitational wave tensor mode propagation from LIGO-Virgo). The phenomenology of the theory on non-linear scales is still to be fully explored.

1.1.4 The nature of dark matter

1.1.4.1 Non-cosmological evidence

As discussed above, in the past half century cosmological probes have been found to imply that $\sim 85\%$ of the matter in the universe is in the form of weakly interacting matter. However there has long been other evidence for significant amounts of non-luminous matter being present in the universe. An early study of note is Oort (1932), who studied the vertical dynamics of the Milky Way disc, and found about double the visible mass is necessary to generate the observed velocities. Shortly after Zwicky (1933) inferred the presence of dark matter came from the dynamics of galaxies in the Coma cluster.

In the 1970s, aided by the development of computing, it was noticed that large quantities of dark matter were required in order to keep the discs stable (Ostriker & Peebles, 1973). Simultaneously the rotation curves of galaxies of galaxies were measured using stars and HI for the first time, which were found to be flat extending out to large radius (Rubin et al.,

1980). Theory and observation combined to suggest that galaxies were embedded in much more extended *dark matter halos*. More recently weak lensing measurements have shown that the mass around galaxies and clusters is higher than can be explained the baryons alone (Geiger & Schneider, 1998), with the additional mass required consistent with rotation curves.

The Bullet Cluster (Clowe et al., 2006), shown in Fig. 1.1, is one of the most direct pieces of evidence for collisionless dark matter. The image is interpreted as being a head on collision between two large clusters. The hot gas component appears to be shocking at the centre of the collision, whereas the centres of the mass distributions of the two clusters (measured by weak lensing and believed to be dominated by the dark matter) have passed straight through each other. Furthermore there are two peaks in the distribution of galaxies that coincide with the mass centres, which is expected if the dark matter is similarly collisionless to the galaxies. The Bullet Cluster seems to contradicts theories where the extra mass is in some way tied to the baryons and provides limits on possible interactions of dark matter (e.g. Robertson et al., 2017).

1.1.4.2 Dark matter candidates

Dark matter candidates can be divided into three main types: hot, warm and cold. These refer to the mass of the particle, which governs their thermal velocities and the time in the expansion history of the universe at which they stopped behaving relativistically. Hot dark matter refers to candidate particles that are still relativistic today, such as neutrinos. As they are relativistic, their *free-streaming* eliminates low mass structure. Cold dark matter refers to massive particles ($\gtrapprox 1 GeV$) that were already non-relativistic early in the universe. It can form fluctuations on arbitrarily small scales. Warm dark matter (Blumenthal et al., 1982; Bode et al., 2001) has masses in between cold and hot dark matter.

Simulations of structure formation with different dark matter masses is shown in Fig. 1.2. The difference in structure in the cosmic web is pronounced between models, and hot and

most warm models are ruled out strongly by high redshift data (e.g. Seljak et al., 2006). Some argue the high redshift data still permits lower mass warm dark matter with mass around 1keV (e.g. Dayal & Giri, 2023). However astrophysical evidence from the distribution of satellite galaxies (e.g. Nadler et al., 2021), strong lensing (e.g. Gilman et al., 2020), the Lyman-α forest (e.g. Villasenor et al., 2023) and subhalo interactions with stellar streams (e.g. Banik et al., 2021) give stronger constraints, with each of these studies suggesting a dark matter mass greater than $\sim$ 3keV.

Cold dark matter candidates can be divided into WIMPs (Weakly Interacting Massive Particles) and MACHOS (Massive Compact Halo Object). MACHOS are massive baryonic candidates for the unseen matter such as black holes, faint stars and planets. The combination of the lower than necessary frequency of microlensing events in the Milky Way (e.g. Wambsganss & Schmidt, 1998), and the large discrepancy between Ω_b and Ω_m implying the existence of large amounts of non-baryonic dark matter, mean the consensus view is that MACHOS are unlikely to make up a significant fraction of dark matter.

WIMP candidates are numerous, often inspired by beyond the standard model theories. One popular theory is that dark matter is the lightest superpartner in supersymmetric theories (Jungman et al., 1996). However the LHC has now ruled out the simplest supersymmetric models, diminishing the theoretical motivation for such a particle (Arcadi et al., 2018). However, new theories abound. A massive direct detection effort is underway to directly detect the dark matter particle (e.g. XENON Collaboration 7 et al., 2018), or at least constrain their possible interaction cross-sections.

One interesting proposed warm dark candidate is sterile neutrinos (reviewed in Boyarsky et al., 2019). Whilst currently known neutrinos cannot be dark matter candidates due to their low masses and too strong couplings to other particles, it is possible that heavier "sterile neutrinos" with higher masses and weaker interactions with other particles exist. They are predicted by some particle physics models designed to explain the phenomenon of neutrino oscillations. Another warm dark matter candidate is the gravitino, the supersymmetric

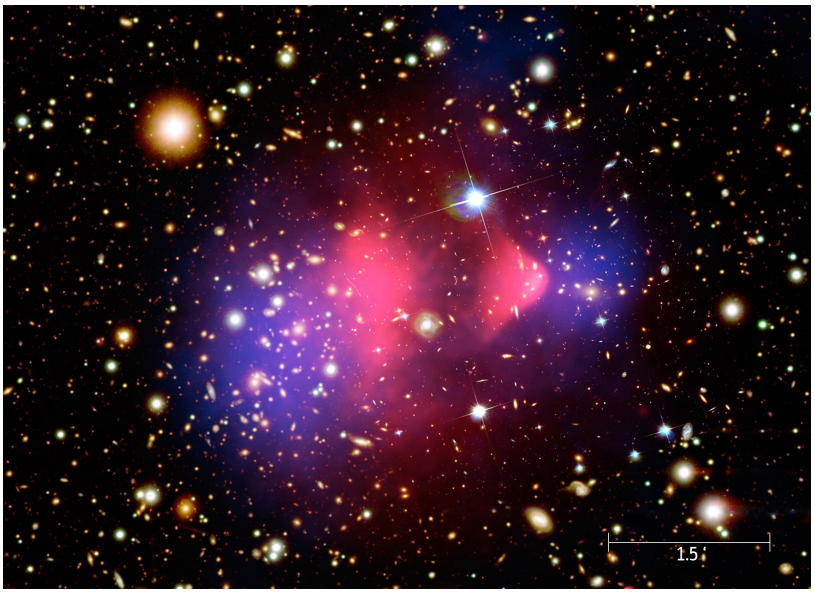

Figure 1.1: The bullet cluster, with the X-ray image (pink) superimposed on the matter distribution calculated from weak lensing (blue) as well as background galaxies. In ΛCDM this is interpreted as two clusters colliding, with the hot gas shocking and the two dark matter halos passing through each other. *NASA/CXC/M. Weiss - Chandra X-Ray Observatory*

partner of the hypothetical graviton (Arbey et al., 2015).

1.1.5 Structure formation

We now give a qualitative account of structure formation in the ΛCDM paradigm from recombination. As previously discussed, at the time of the emission of the CMB the universe was almost homogenous. Assuming cold dark matter, the evolution of density perturbations can be modelled using the equations of an ideal, non-relativistic, self-gravitating fluid. Under gravity regions with higher than normal density grow, and eventually separate from the cosmic expansion and form structure. First sheets form, then filaments, then clumps (Zel'dovich, 1970). The smallest structures form first, and then grow and merge over time in a process called hierarchical merging.

The size of perturbations can be characterised using the overdensity δ,

$$\delta(\vec{r}) = \frac{\rho(\vec{r}) - \bar{\rho}}{\bar{\rho}}, \tag{1.13}$$

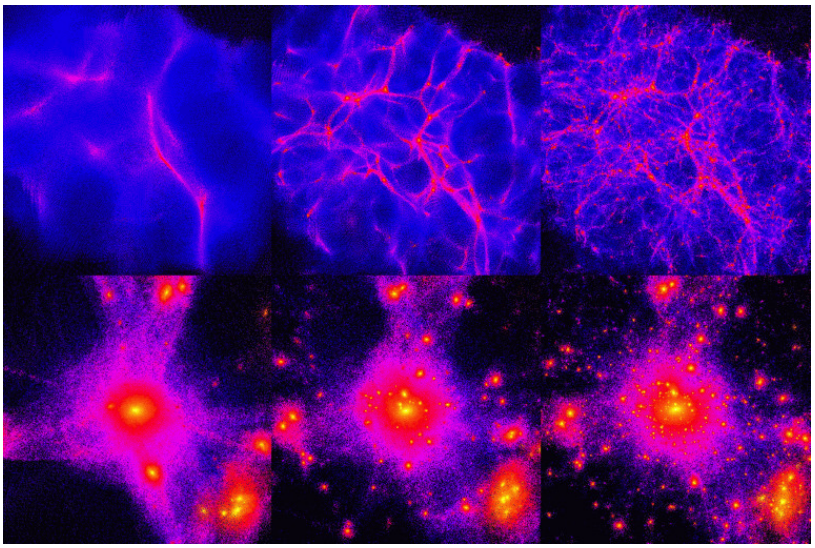

Figure 1.2: Simulations of structure formation with (*from left to right*) hot, warm and cold dark matter. The top panel shows the cosmic web and the bottom panel the zoom-in of a galaxy.
Credit: ITP, University of Zurich

where $\bar{\rho}$ is the mean cosmic density and ρ is the density at position $\vec{r}$. Whilst the perturbations are still small ($\delta \ll 1$) linear perturbation theory can be used. The linear approximation breaks down when $\delta \sim 1$ and structures begin to collapse and virialize, leading to a highly non-linear situation where more complex theoretical approaches are needed to accurately describe the dynamics. The collapse under self-gravity of these dense clumps stops when the dark matter virialises, forming regions of gravitationally bound overdensities called dark matter halos.

The process of halo collapse can be described using analytical models that employ simplifying assumptions. One such model is the spherical collapse model (Tomita, 1969; Gunn & Gott, 1972; Mo et al., 2010), which considers a spherical region characterized by a constant overdensity sufficient to trigger collapse. The evolution of this "proto-halo" under its own self-gravity is tracked in an expanding spacetime. The influence of the accelerated expansion of the universe can be included, but its effects are subdominant. Up to the point where the trajectories of dark matter particles intersect for the first time (*shell-crossing*),

the radius r in physical coordinates of a proto-halo of total mass M evolves over time t as

$$\frac{d^2r}{dt^2} = -\frac{GM}{r^2}. \tag{1.14}$$

For an overdensity that collapses, the equation admits the parametric solution

$$r(\theta) = A(1 - \cos\theta)\ , \qquad t(\theta) = B(\theta - \sin\theta)\ , \tag{1.15}$$

where θ is a reparameterisation of time: $\theta = 0$ corresponds to $t = 0$, $\theta = \pi$ corresponds to the time where the expansion reverses and the halo begins to collapse (*turnaround*), and the halo is fully collapsed at $\theta = 2\pi$. The coefficients $A = GM/2|E|$ and $B = GM/(2|E|)^{2/3}$ are related to the sphere's total energy E. Rewriting in terms of overdensity (using $M = 4\pi/3r^3\bar{\rho}(1+\delta)$) gives

$$1 + \delta = \frac{\rho}{\bar{\rho}} = \frac{9}{2}\frac{(\theta - \sin\theta)^2}{(1 - \cos\theta)^3}. \tag{1.16}$$

Expanding for small t or θ gives the prediction of linear theory for the overdensity as the sphere expands with the Hubble flow

$$\delta_{\rm lin} = \frac{3}{20}(6\pi)^{2/3}\left(\frac{t}{t_{\rm ra}}\right)^{2/3}, \tag{1.17}$$

where $t_{\rm ta}$ is the time at turnaround. The collapse finishes at $\theta = 2\pi = 2t_{\rm ta}$, at which time extrapolating linear theory gives

$$\delta_{\rm c} \approx \frac{3}{20}(12\pi)^{2/3} = 1.69. \tag{1.18}$$

Therefore under this model overdensities in the linearly extrapolated density field with $\delta_{\rm lin} > 1.69$ would have collapsed. This value is useful for estimating the distribution of halos in the universe analytically as we will return to shortly.

In the spherical collapse model the density actually collapses to infinity at $\theta = 2\pi$. However in reality overdensities are neither spherical nor homogeneous, and instead virialise to form a roughly spherical halo. The properties of the virialised halo can be estimated by applying conservation of energy and the virial theorem. Evaluating equation 1.16 at

turnaround time $t_{\rm ta}$ ($\theta = \pi$) gives $\delta_{\rm ta} = 9\pi^2/16 \approx 5.55$. The total energy of the sphere is equal to the potential energy at turnaround time $E_{\rm ta} = -3GM^2/5r_{\rm ta}$. If the virialised halo was uniform, its potential energy would be $W \sim -3GM^2/5r_{\rm vir}$, where $r_{\rm vir}$ is the final *virial radius* of the collapsed halo. From the virial theorem $W = 2E$, so $r_{\rm vir} = r_{\rm ta}/2$. Therefore from turnaround to virialisation the mean density of the halo has increased by a factor of 8. In an Einstein-de Sitter (flat, matter-only) cosmology the density of the background has decreased by a factor of 4. Evaluating at collapse time $t_{\rm coll}$ ($\theta = 2\pi$), the virialised overdensity $\Delta_{\rm vir}$ is

$$1 + \Delta_{\rm vir} \equiv 1 + \delta\left(t_{\rm coll}\right) = \frac{\rho\left(t_{\rm coll}\right)}{\bar{\rho}\left(t_{\rm coll}\right)} = \frac{8\rho_{\rm ta}}{\bar{\rho}\left(t_{\rm ta}\right)/4}. \tag{1.19}$$

For non-Einstein de Sitter cosmologies $\Delta_{\rm vir}$ is a more complex function of cosmology. A useful approximation is given by (Bryan & Norman, 1998)

$$\Delta_{\rm vir} \approx \left(18\pi^2 + 82x - 39x^2\right)/\Omega_m\left(z\right) \tag{1.20}$$

where $x = \Omega_m(z-1)$, which gives $\Delta_{\rm vir} \approx 178$ for our universe at $z = 0$.

A useful analytical prescription for distribution of halos is the Press-Schechter formalism (Press & Schechter, 1974), which gives the *halo mass function*, the comoving number density of halos as a function of mass. Here the matter density of the universe is described as a Gaussian random field based on the evolution of the initial perturbations under linear theory. Regions with overdensity greater than δ_c are identified as collapsed (equation 1.18). A "fudge factor" of two is necessary to account for the fact that the model only considers the formation of overdensities, ignoring underdensities. Although historically important, the simplifying assumptions embedded in the Press-Schechter formalism are insufficient for generating halo statistics with the precision required for many modern applications.

Nowadays the main method to investigate structure formation in the non-linear regime is through large scale numerical simulations of model universes. For a given set of cosmological parameters, the dark matter fluid is discretised into particles, and evolved under

Newtonian gravity. Algorithms called halo finders are used to create catalogues of the dark matter halos in the simulation and their physical properties. As there is no well defined boundary between virialised and non-virialised material in a halo, it is instead standard practice to define dark matter halos as spherical regions of radius $R_{\rm vir}$ with overdensity greater than $\Delta_{\rm vir}$. As discussed above, this definition is based on the crude spherical collapse model, so is somewhat arbitrary. It also has the undesirable property of artificially evolving halo properties with redshift (Diemer et al., 2013). There has been recent work to instead define halo boundaries using the *splashback radius*, the radius where newly accreted particles reach the apocenter of their first orbit (More et al., 2015).

1.1.5.1 Halo internal properties

The halos in simulations are found be mildly triaxial (Bullock, 2002), with the majority being oblate spheroids (although the inclusion of baryons increases the sphericity somewhat e.g. Kelso et al. 2016). Observational constraints on halo shape have been obtained from from weak lensing and kinematic tracers of Local Universe galaxies (e.g. Schrabback et al., 2021; Posti & Helmi, 2019). In spite of this, it is standard practice to characterise halos by their spherically averaged density profiles. Navarro et al. (1997) (NFW) found that the halos in dark matter-only (DMO) simulations are well fit by a universal profile

$$\rho(r) = \frac{\rho_0}{\frac{r}{r_s}\left(1 + \frac{r}{r_s}\right)^2}, \tag{1.21}$$

parameterised by a scale density ρ_0 and a scale length r_s for each halo. This profile is *cuspy*: its density rapidly increases at small radius. As simulation resolution increases, halos were found contain a lot of substructure, called subhalos. These are peaks in the density field that are gravitationally bound to the main halo. Modern *zoom* simulations have found self-similar structures from galaxy clusters down to earth-mass halos at their resolution limit (Wang et al., 2020b).

The NFW profile can be alternatively parameterised by halo mass $M_{\rm vir}$ and concentration

$c_{\rm vir} = R_{\rm vir}/r_s$. NFW found that the concentration tends to increase with decreasing halo mass. This is attributed to the low-mass halos collapsing earlier, when the universe was at higher density. There is a scatter in the relationship, due to halos at a given mass collapsing at different times as a result of varied histories and environments. In logarithmic space this *mass-concentration relationship* is approximately linear, with a constant scatter in $c_{\rm vir}$ at all values $M_{\rm vir}$ (e.g. Dutton & Macciò, 2014). Differences in halo properties based on their assembly history is called *halo assembly bias*.

1.2 Galaxies

1.2.1 Background

In the ΛCDM paradigm, galaxies form from the condensation of baryons in the centre of dark matter haloes. Initially the baryons and dark matter are assumed to be well mixed, and the baryons simply follow the potential of the dark matter into halos. As the baryon density rises, pressure becomes important and shocks form, heating the gas. The gas then loses energy via radiation and falls to the centre of the dark matter halo's potential well. In heavy enough halos, the baryon density at the centre of the halo becomes high enough to form stars and eventually the luminous galaxies we observe today (White & Rees, 1978). Galaxies can either grow through the continuous formation of stars (*in situ*) or through the mergers of their dark matter halos (*ex situ*). The above suggests that the internal properties of galaxies and their spatial distribution should be closely related to the properties and distributions of the underlying dark matter halos.

In this basic picture efficient cooling at the high densities found at high redshift is expected to transform most gas into stars, in disagreement with observations that only $\sim$ 20% of baryons on the universe have formed stars (Fukugita et al., 1998). To resolve this, it is necessary to introduce *feedback* mechanisms which inject energy back into the gas to make star formation inefficient. Prime candidates are energy injected by supernovae

explosion, active galactic nuclei, magnetic fields and cosmic rays (see Naab & Ostriker 2017 for a review).

1.2.2 Galaxy properties

Due to the complex interplay of physical processes that enter into galaxy formation: gravity, gas dynamics, star formation, mergers and feedback from black holes and supernovae, galaxies have a massive diversity in properties. In terms of scale, the largest galaxies are the Brightest Central Galaxies (BCGs) found at the centre of clusters, with stellar mass of $\sim 10^{12}\,\mathrm{M}_{\odot}$. At the other extreme are ultrafeint dwarf galaxies, such as Segue 1 which has only 1000 $\mathrm{M}_{\odot}$ (Martinez et al., 2011). It is speculated that in ΛCDM there may even exist dark galaxies that contain almost no stars, consisting of only dark matter and gas (e.g. Leisman et al., 2017).

Galaxies are observed to display a wide range of visual appearances on the sky, reflecting different underlying morphologies. Hubble (1926) developed the original classification scheme for galaxies. It classifies galaxies into two main types, elliptical (E) and spiral (S). Spiral galaxies have prominent stellar discs with spiral arms. Elliptical galaxies on the other hand are more rounded in appearance and are smooth and featureless, with elliptical isophotes of constant brightness. Lenticular galaxies are intermediate, possessing smooth disc but no spiral arms.

Galaxies display pronounced, strongly correlated, bimodalities when classified by various properties, most notably colour, star-formation rate and morphology. *Late-type* galaxies are characterised by high star-formation rates, and hence blue colours, cold gas and either spiral or irregular morphologies. *Early-type* galaxies have low star-formation rates, and hence red colours, are mostly devoid of cold gas and have either elliptical or lenticular morphologies.

Galaxies also differ vastly in the kinematics of their stars and gas. Late-type galaxies have gas and stars that follow approximately circular orbits around the centre of the galaxy.

Elliptical galaxies on the other hand tend to have depleted their gas, and their stellar kinematics are more pressure-supported (*slow rotators*). Over the past decade integral-field unit (IFU) surveys such as ATLAS^{3D} (Cappellari et al., 2011), CALIFA (Sánchez et al., 2016) and MANGA (Bundy et al., 2014; Fraser-McKelvie & Cortese, 2022) have found that many early-type galaxies do in fact have significant amounts of rotation (*fast rotators*). Finally the picture is also more nuanced by the fact that galaxies can have multiple components, for example a pressure-supported red bulge as well as a blue star-forming disk, even if one of them dominates the visual appearance. These different types of kinematics necessitate different analysis techniques, which we will return to in future sections. The kinematics of galaxies may also hold clues to the assembly of structure in the universe, and hence its underlying dynamics (e.g. Peebles, 2020).

A key challenge in galaxy formation theory is explaining how galaxies quickly transition from being red to blue, without spending long in the sparsely populated intermediate "green valley" (e.g. Schawinski et al., 2014), and elucidating the relationship between the quenching of star formation and other correlated features such as mass, morphology, kinematics, gas content and environment. Feedback from active galactic nuclei plays a prominent role in many current theoretical models (Baldry et al., 2006).

1.2.2.1 Dynamical scaling relationships

Galaxies display surprising dynamical regularities (McGaugh et al., 2019), most notably flat rotation curves (Rubin et al., 1980), the Tully-Fisher relationship (Tully & Fisher, 1977) for late-type galaxies, the Fundamental Plane for ellipticals (Djorgovski & Davis, 1987) and the Radial Acceleration Relationship (e.g. McGaugh et al., 2016; Brouwer et al., 2021). It has been argued that the observed correlations between the dark matter and baryons implied by the rotation curves cannot be explained in the cold dark matter paradigm. This has lead to an abundance of proposed extensions to the standard model, either in the form of new dark matter physics (e.g. Khelashvili et al., 2022; Adhikari et al., 2022) or modifications to

the theory of gravity (e.g. Milgrom, 1983; Burrage et al., 2017; Naik et al., 2019). Improved precision on the constraints on the galaxy-halo connection is therefore also vital to assess the viability of dark matter models. One approach is to compare the halo properties inferred from kinematics to cosmological expectations (e.g Katz et al., 2017; Li et al., 2020; Posti & Fall, 2021; Mancera Piña et al., 2022).

The most notable of these alternative models is MOND, which modifies Newton's law in low acceleration environments to generate the observed flat rotation curves (Milgrom, 1983). Whilst the theory predicted several aspects of the radial dynamics of galaxies in advance of their observation (e.g. Lelli et al., 2017; Brouwer et al., 2021; Desmond, 2023; Stiskalek & Desmond, 2023), it cannot readily explain observations of the kinematics of galaxy clusters (Aguirre et al., 2001; Li et al., 2023) and some dwarf galaxies (Safarzadeh & Loeb, 2021; Freundlich et al., 2022; Read et al., 2019). There are also exotic dark matter theories with a baryon-dark matter coupling that reproduce aspects of MOND phenomenology in galaxies (e.g. Blanchet & Tiec, 2009).

It has been argued that galaxy-scale MOND phenomenology arises naturally in ΛCDM, first by Kaplinghat & Turner (2002), who argued it comes about due to details of structure formation (such as the self-similarity of dark matter halos) in tandem with numerical coincidences. However their derivation assumed a fix fraction of baryons collapsing into stars, which we know now not to be the case. Subsequently however, it has been shown that semi-analytical models and hydrodynamical simulations are able to qualitatively reproduce scaling relationships such as the Tully-Fisher and radial acceleration relationships (e.g. Santos-Santos et al., 2016), which is again attributed to the self-similarity of dark matter halos and the physical scales introduced by the process of galaxy formation (Navarro et al., 2017). However quantitative details (including the scatter and secondary correlations) are still debated in literature (e.g. Desmond, 2017a; Paranjape et al., 2021). It also still needs to be proven that feedback actually does operate in the manner required by ΛCDM models to reproduce said phenomenology (Katz et al., 2017).

1.2.3 The galaxy-halo connection

The physical and statistical relationship between the properties of galaxies and those of their host halos has been termed *the galaxy-halo connection* (see Wechsler & Tinker 2018 for a review). Mapping out the galaxy-halo connection quantitatively and understanding its physical origin is of vital importance for several areas of modern astrophysics.

Firstly it is an important intermediate step to constructing a full theory of galaxy formation. The theoretical distribution of dark matter in ΛCDM is well understood: competing theories disagree on the baryonic physics, which is well embodied by which galaxies form in which halos. Therefore a well mapped galaxy-halo connection will be an important guide to understanding the different baryonic mechanisms at play and to discriminate between theories. In recent times increasing emphasis has been put on forward modelling theory to more directly observable quantities. However comparing theory to the measured galaxy-halo connection is valuable, as physical interpretation is clearer at this higher level, and the theory space of possible formation models is vast.

Improving knowledge of the galaxy-halo connection is also important for constraining cosmological parameters in the era of "precision cosmology". Cosmological parameters are constrained using galaxy surveys, which must be connected to the underlying dark matter distribution on small scales using the galaxy-halo connection. Future wide-field surveys are focused on better constraining the ΛCDM cosmological parameters, the dark energy equation of state, the inflationary potential, the mass of the neutrino, primordial non-gaussianity and extensions to general relativity. It has recently been argued that at least one apparent cosmological tension may be a result of using insufficient galaxy-halo connections in analyses (Contreras et al., 2023).

The sensitivity of the galaxy-halo connection to both galaxy formation physics and the nature of dark matter establishes it as a vital tool for discriminating between dark matter models. By comparing the observed galaxy-halo connection with theoretical predictions, one can test the robustness of the ΛCDM paradigm and constrain different dark matter

models by examining the distinct galaxy-halo connections they imply. For example, the statistics of halos and subhalos in different theories will lead to different predictions about which galaxies inhabit which halos.

1.2.3.1 Empirical models of the galaxy-halo connection

The properties of dark matter haloes can be inferred from photometric data using empirical models that connect the properties of haloes in dark matter-only (DMO) cosmological simulations to large-scale galaxy surveys. These models assign galaxy properties to simulated haloes by making simple parameterised assumptions, which are then tested and the parameters constrained using observations such as galaxy clustering. This avoids invoking a full galaxy formation model as in hydrodynamical simulations or semi-analytical models, the complex baryonic physics of which are not yet well understood. Empirical method have been made possible by the advent of large galaxy surveys such as SDSS which measure galaxy mass/luminosity functions and clustering, as well as the development of numerical simulations capable of obtaining subhalo and halo statistics for volumes large enough for clustering to be measured.

Subhalo abundance matching (SHAM) posits that the most massive (or brightest) galaxy forms in the most massive halo or subhalo, the second most massive galaxy in the second most massive halo and so on (Kravtsov et al., 2004). When applied to a galaxy survey and an equivalently sized simulation box this yields a monotonic relationship between halo mass and galaxy mass. Conroy et al. (2006) showed that this simple non-parametric model could produce an excellent fit to galaxy clustering from the present day up to $z = 5$. The model has been extended to allow stochasticity through the SHAM scatter parameter σ_{AM}, which models both intrinsic scatter in the galaxy–halo connection and scatter from observational uncertainties in the galaxy mass or luminosity (Behroozi et al., 2010, henceforth BCW10). Halo assembly bias can be included in the SHAM framework by allowing secondary halo parameters such as concentration to affect the order in which galaxies are assigned to haloes

(Reddick et al., 2013; Lehmann et al., 2016; Chaves-Montero et al., 2016; Stiskalek et al., 2021).

An alternative to SHAM is halo occupation distribution modelling (HOD). Here the relationship between galaxies and halos is specified by the probability distribution that a halo contains a number of galaxies N with a property (e.g. luminosity) above a certain threshold. Usually this probably distribution is conditioned on mass P(N|M). HOD is generally described by 3-5 parameter models (e.g. Zheng et al., 2005), although recently more complex models with assembly bias have been developed (e.g. Hadzhiyska et al., 2020). HOD and abundance matching are commonly used to forward model galaxy surveys in order to constrain cosmological parameters.

More complex empirical models assume a relationship between the mass accretion of a halo and its star formation rate (e.g. Conroy & Wechsler, 2009; Behroozi et al., 2019), which enables the halo mass and stellar mass of each simulated halo to be evaluated at different epochs. These methods are powerful, as they predict the star-formation history and hence the multiband photometry of the galaxy in each halos. However in general non-physically motivated functional forms with large numbers of free parameters are used to relate the halo mass accretion and star formation, removing the simplicity which gives confidence in the veracity of models such as abundance matching.

An important output of many empirical models is the stellar-to-halo-mass relationship (SHMR), shown in Fig. 1.3. The models agree that galaxy formation peaks in efficiency ($M_*/M_{\rm vir}$) for Milky Way mass galaxies. Supernova and AGN feedback are the leading candidates to explain the drop in formation at lower and higher masses respectively. A weakness of empirical models is that they only constrain the galaxy-halo connection at high masses where clustering is available. Future large-scale surveys such as DESI and the SKA will improve the mass range and redshift for which clustering data is available, and enable the application of higher order statistics to better constrain model parameters.

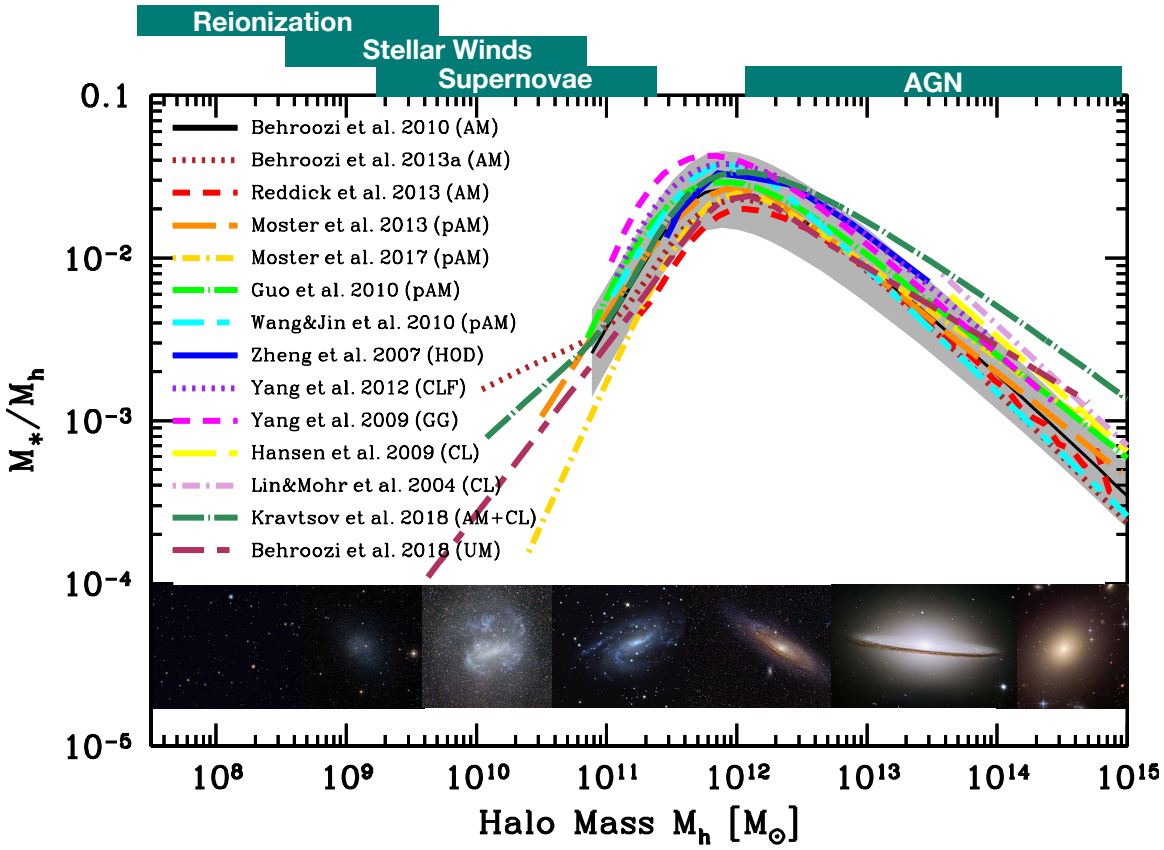

Figure 1.3: The stellar-to-halo mass relationship (SHMR) from different empirical models of the galaxy-halo connection. The models are in reasonable agreement at high mass where they are constrained by clustering. The grey band shows the canonical ~0.2 dex scatter in the galaxy-halo connection. The primary mechanism believed to be responsible for reducing the galaxy formation efficiency in each mass range is shown in green. *Figure reproduced from Wechsler & Tinker 2018.*

1.2.3.2 Mapping the dark matter distribution directly

We now review direct methods to infer the galaxy-halo connection, where some observable of the gravitational potential is used to constrain the mass distribution around specific galaxies without assuming a cosmological model (as is necessary for the empirical methods above). Perhaps the most direct method to infer dark matter properties is through spectroscopic observations of the kinematics of astrophysical objects, such as the gas and stars of galaxies. The mass distribution is inferred by comparing the observed motions of the tracer to that expected from the observed luminous matter through Newtonian gravity. Late-type galaxies are ideal systems to study, as their stars and gas follow approximately circular orbits that directly trace the underlying potential. Spatially resolved observations are able to measure rotation curves (RCs), the rotational velocity of the stars and gas as a function of radius (e.g. Walter et al. 2008; Ponomareva et al. 2016; Lelli et al. 2016a). For systems where the stars have significant pressure support, more sophisticated techniques are required to model the orbits, such as action-angle modelling (e.g. Binney, 2010), Schwarzchild orbit superposition modelling (Schwarzschild, 1979) and Jeans Anisotropic Modelling (Cappellari, 2008).

Dynamical modelling can also use other collisionless tracers such as globular clusters, planetary nebulae and satellite galaxies orbiting in groups or clusters.

The X-ray temperature of gas is used to probe the mass distribution in massive ellipticals and clusters by assuming hydrostatic equilibrium. A related method is the use of thermal Sunyaev–Zeldovich effect, the scattering of CMB photons by energetic electrons in clusters, to probe the gas temperature and hence infer the halo mass (although it has been argued that this requires calibration with hydrodynamical simulations e.g. Yang et al. 2022).

The distortion of background light by foreground galaxies, *lensing*, is another powerful probe of their matter distribution. This is most commonly done using the light from background galaxies. Strong lensing occurs when the lensing mass is substantial, and the alignment between the background source, lens and observer is close to perfect. The

distortions are readily apparent, with multiple images, lenses or arcs easily visible. Future surveys such as Euclid will detect statistical samples of strong lenses. Weak lensing is a much more common phenomena, where the background light is deflected too weakly for the effect to be detected in an individual galaxy. However it is possible to infer the mass distribution of the lens from the statistical distribution in the shapes of many background sources (e.g. Geiger & Schneider, 1998). A recently developed probe for constraining cluster masses is CMB lensing (e.g. Baxter et al., 2018), where the subtle imprint of the deflection of CMB photons is identifiable in skymaps. An advantage of lensing is that it can be measured more readily at higher redshifts compared to other methods.

Stellar streams are a probe of the dark matter distribution that has benefited from the recent influx of Local Group data from instruments such as Gaia. When a globular cluster or dwarf galaxy is accreted by a larger galaxy, their stars are gradually stripped in the tidal interaction, forming a stream that roughly traces out the path of the orbit (e.g. Johnston et al., 1995). The shape and density of the stream is sensitive to the gravitational field, and hence can be used to constrain the matter distribution of the Milky Way (e.g. Koposov et al., 2022) and nearby galaxies (e.g. Pearson et al., 2022) in which the streams are visible.

The density profile of dark matter is usually constrained by fitting parameterised functions (e.g. Navarro et al., 1997; Burkert, 1995; Di Cintio et al., 2014; Read et al., 2016) to the inferred circular velocity profile, or by forward modelling an observable for varying assumed mass distributions. The halo parameters, which we refer to as the *properties* of the halo, are typically the virial mass, the concentration and sometimes additional parameters describing the shape of the profile, such as the steepness of the inner slope, or halo ellipticity.

1.2.4 Physical models of galaxy formation

As previously discussed, a key motivation for constraining the galaxy-halo connection is to guide the development of physical models of galaxy formation, which we now review briefly.

1.2.4.1 Hydrodynamical simulations

Hydrodynamical simulations (e.g. Vogelsberger et al., 2020) attempt to self-consistently follow the complex processes involved in galaxy formation: the cooling of gas, the formation and death of stars, the formation and growth of black holes and the injection of energy and momentum by the possible feedback processes discussed above. However this is challenging due to the enormous dynamic range required. Galaxies are strongly affected by material brought to them from by large scale cosmic flows with characteristic length scales of megaparsecs. Star formation and feedback however involve phenomena such as accretion discs and shocks with sub-parsec scales. These small-scale effects are modelled using *sub-grid* recipes, analytic prescriptions that are intended to propagate the outcome of the unresolved processes onto the resolution scale of the simulation.

Many of the small scale processes are not well understood, and therefore the parameters of the analytic prescriptions are either explicitly tuned so that the output of the simulations matches some set of observations, or have been adjusted over time in order to produce realistic galaxies. One example of this is supernova feedback, which is believed to drive strong outflows in the gas. As well as reducing star-formation efficiency, it was found that these outflows were also required to drive low angular momentum gas out of the disc, allowing higher angular momentum gas to be accreted, and allowing stable discs to form (thus avoiding the "angular momentum catastrophe", Couchman & Thacker 2003). In spite of this lack of predictivity, modern cosmological simulations are able to produce galaxies that are similar to observed galaxies in mass and luminosity distribution, colours and morphology, with relatively few parameters given the myriad processes involved.

There has been much recent work on characterising the galaxy-halo connection in simulations, where halo and galaxy properties are known exactly. Often this involves using supervised machine learning techniques to map out all the correlations of the galaxy-halo connection as well as their scatter (e.g. Kamdar et al., 2016; Stiskalek et al., 2022; Lovell et al., 2023). This theoretical galaxy-halo connection can then be compared to the

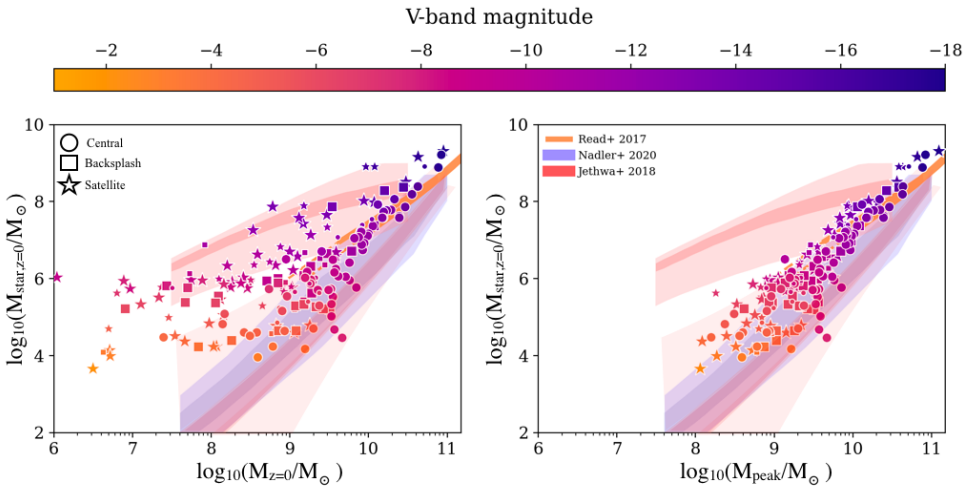

Figure 1.4: The stellar-mass-to-halo mass relationship of simulated galaxies (circles, stars and squares) is compared to those derived from abundance matching-based models of the galaxy-halo connection (Nadler et al., 2020; Jethwa et al., 2018) and rotation curve modelling (Read et al., 2017). The left panel shows the relationship for z=0 halo mass and the right panel shows peak halo mass. A number of tensions between the simulation and the inferred galaxy-halo connections are visible. For example, the simulated galaxies are in apparent tension with Nadler et al., who find the scatter in stellar mass is small at all halo masses contrary to the simulations. The tension may indicate missing physics from the simulations and/or a deficiency in model of Nadler et al.. *Figure reproduced from Munshi et al. (2021).*

observed one in order to identify the correct galaxy formation model. However due to the difficulty in measuring halo properties, the observed galaxy-halo connection is characterised comparatively weakly, with comparisons typically focusing on the stellar-to-halo mass relationship and its scatter. We show an example of such a comparison from Munshi et al. (2021) in fig. 1.4.

1.2.4.2 Semi-analytical models

Another approach is semi-analytical modelling (SAMs) (e.g. Somerville & Primack, 1999), where instead of tracking the distribution and evolution of individual elements of dark matter, stars and gas, all relevant astrophysical processes are parameterised by equations (e.g. gas accretion, outflows), which are then evolved numerically with time. Due to relatively low computation cost, the full parameter space of the model can be efficiently

explores and its values constrained using observations. As higher level models, constructing analytical prescriptions also tests our physical understanding of the relevant processes.

The backbone of SAMs are dark matter only simulations, and their halo catalogues and merger trees. Their parameterisations assume relationships between accreted dark matter and baryons. However this has its limitations. To give one example, models have historically assumed proportionality between the angular momentum of a halo and the galaxy angular momentum (Mo et al., 1998), which has subsequently found not to hold in both data (Desmond et al., 2019; Behroozi et al., 2022) and numerical simulations (e.g. Jiang et al., 2019; Stiskalek et al., 2022; Karmakar et al., 2023). Instead the complexity of gas dynamics mean the correlation of angular momentum and dark matter is quickly loosened, even before halo collapse (e.g. Cadiou et al., 2022). Hence although semi-analytical models may be able to statistically reproduce the properties of galaxies, they are unable to predict the properties of a galaxy that will form in a particular simulated dark matter halo due to the incomplete information considered.

Due to the simplifying assumptions required and the cheapness of modern computation, hydrodynamical simulations have gained in popularity relative to SAMs in recent years.

1.2.5 Small-scale tensions

There are various disagreements between the predictions of ΛCDM and observations at small scales (Bullock & Boylan-Kolchin, 2017a), which may provide evidence in favour of non-cold dark matter models. These include the cored dark matter density profiles observed in some galaxies (*the cusp-core problem*) and possible tensions in the abundance/kinematics of observed galaxies compared to simulated halos (*the missing satellites problem/too-big-to-fail*). However, at these small scales it is hard to disentangle the underlying dark matter physics from the effect of baryonic physics. The missing satellites problem, too-big-to-fail and cusp/core are all sensitive to the assumed galaxy-halo connection, which is not as well constrained at low mass.

Several mechanisms have been proposed for baryon-induced core formation, such as gravitational potential fluctuations associated with stellar feedback (e.g. Pontzen & Governato, 2014), dynamical friction from dense clumps of baryons (El-Zant et al., 2001; Nipoti & Binney, 2015), mergers (Orkney et al., 2021) and dynamical coupling to galactic bars. The prevalence of each mechanism in the real world is still uncertain. Correlating dark matter halo profiles with galaxy properties connected to each core-formation mechanism (such as star formation, redshift or the presence of a bar or AGN) is important to identify the correct mechanism(s) (e.g. Read & Erkal, 2019).

An extension of cusp/core is the diversity of rotation curve problem (reviewed in Sales et al., 2022): observed dwarf galaxies of similar mass show variation in their inner halo shape, which is not found in current simulations, where supernova feedback seems to form a core (or not) too reliably at a given galaxy mass. The combination of supernova feedback and self-interacting dark matter has been advocated as a solution (Ren et al., 2019).

Another interesting tension at small-scales are the properties of the bars observed in late-type galaxies. Roshan et al. (2021); Kashfi et al. (2023) argue the prevalence of fast rotating bars in observations is incompatible with ΛCDM simulations, in which dynamical friction from the dark matter halo decelerates bars. However Chiba et al. (2021a) claim to have detected the deceleration of the Milky Way's bar by dynamical friction. Obtaining improved knowledge of the dark matter distribution around statistical samples of galaxies is important for resolving this issue.

Finally there is the planes of satellites problem: nearly all Milky Way satellites and about half of Andromeda satellites are observed to be in a thin, kinematically coherent plane, behaviour that is not readily apparent in cosmological simulations where satellite distributions are more isotropic (reviewed in Pawlowski, 2018; Boylan-Kolchin, 2021; Sales et al., 2022). Proposed solutions have focused on the numerical modelling of satellite distributions and the Local Group's position in the cosmic web. Some evidence for coherent structures has also been found in external galaxies, but these are less well established due

to the limited data available.

1.3 Thesis Overview

As outlined above, constraining the galaxy-halo connection is an important step to constructing a complete theory of galaxy formation, as well as constraining cosmology and dark matter models. The core motivation of the thesis is this: to achieve a precise enough knowledge of the galaxy-halo to accomplish these goals it will be necessary to synthesise diverse data types that *in combination* are able to satisfy the following three requirements:

1. The must probe from the inner regions of the galaxy all the way to the halo virial radius.

2. They must be available for the full range of galaxy types.

3. They must be measureable for cosmological volumes of galaxies, including at higher redshift.

Therefore, in this thesis I will study combinations of four different types of constraint on the galaxy-halo connection: photometry (through empirical models), stellar kinematics, HI kinematics and weak lensing. Between them they trace varying regions from the very centre of the galaxy out to the virial radius (Fig. 1.5). Although we focus on late-type galaxies in this thesis, all methods except HI kinematics are equally applicable to early-types. Finally through current and forthcoming large-surveys, including Rubin, SKA, EUCLID, MaNGA and 4MOST, they will be measurable for cosmological volumes of galaxies and as a function of redshift. Through this work, I aim to establish a framework for maximimising the information on dark matter halos extracted from forthcoming surveys, and in doing so lay the foundation stone for a comprehensive knowledge of the galaxy-halo connection.

In Chapters 3, 4 and 5 I focus on the HI-rich galaxies that will be observed in vast quantities in forthcoming surveys such as the SKA. In Chapter 3 I constrain the halo mass

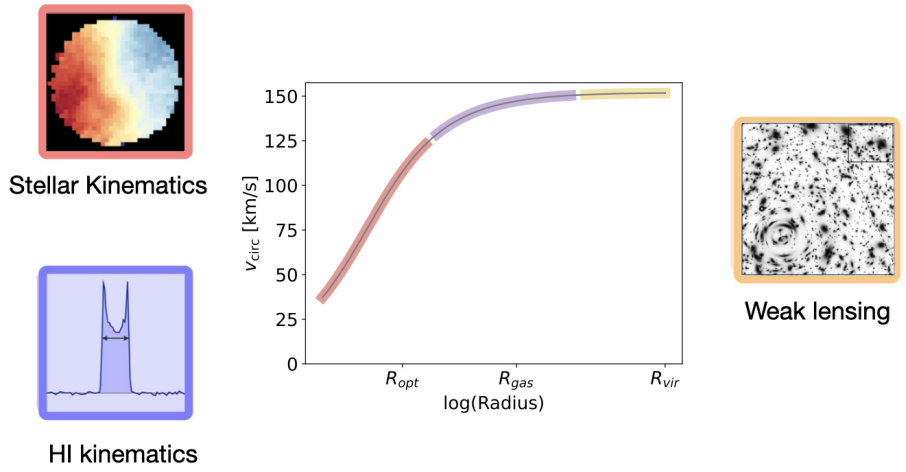

Figure 1.5: A cartoon showing the circular velocity as a function of radius from the galaxy/halo centre, with the region of the circular velocity curve constrained by each of stellar kinematics (red), HI kinematics (blue) and weak lensing (yellow) highlighted. The optical disc scale length ($R_{\rm opt}$), HI disc scale length $R_{\rm gas}$ and the halo virial radius $R_{\rm vir}$ are labelled. Only combinations of these data types are able to constrain a significant portion of the circular velocity curve. Empirical models of the galaxy-halo connection, which are not shown, use photometry to constrain global halo properties.
Adapted from Taranu et al. (2017)

and concentration of the ~22,000 galaxies visible in both the radio (in ALFALFA) and the optical (in SDSS) by combining two Bayesian models: one for the total baryonic mass of the galaxy using abundance matching (which requires only photometry), and one for the HI linewidth using kinematic modelling. In Chapter 4 I study the constraining power on dark matter halos afforded by different types of spectroscopic observations of late-type galaxies, with the aim of informing the design of forthcoming surveys. In Chapter 5 I combine IFU stellar kinematics with HI data to constrain the halo properties of galaxies in MANGA survey. In Chapter 6 I carry out a preliminary investigation on using weak lensing data to help achieve precision constraints on the galaxy-halo connection. I conclude in Chapter 7.

Chapter 2

Methods

2.1 Statistical methods

2.1.1 Bayesian statistics

We wish to constrain a set of physical parameters θ which describe a physical model $\mathcal{M}$ through comparison to a set of data D. The desired quantity is $\mathcal{P}(\theta|D, \mathcal{M})$, the posterior probability distribution on the model parameters given the data (e.g. Saha, 2003; Trotta, 2008). Physical models however typically only give us means to calculate the likelihood $\mathcal{P}(D|\theta, \mathcal{M})$, the probability of the observed data for each set of model parameters θ. The posterior distribution can be calculated from the likelihood using Bayes theorem

$$\mathcal{P}(\theta|D, \mathcal{M}) = \frac{\mathcal{P}(D|\theta, \mathcal{M})\mathcal{P}(\theta|\mathcal{M})}{\mathcal{P}(D|\mathcal{M})}, \tag{2.1}$$

where we have introduced the prior $\mathcal{P}(\theta|\mathcal{M})$, which describes our $apriori$ knowledge of the probability distribution on θ. The normalising term is the probability of the data given the model, which is known as the Bayesian evidence ($\mathcal{Z}$). It can be calculated by marginalising the likelihood over the model parameters

$$\mathcal{Z}(D) = \int \mathcal{P}(D|\theta, \mathcal{M})\mathcal{P}(\theta|\mathcal{M})d\theta. \tag{2.2}$$

However this is generally a very expensive quantity to calculate due to the large number of likelihood evaluations required.

2.1.2 Sampling techniques

Techniques have been developed to instead draw random samples from $\mathcal{P}(\theta|D, \mathcal{M})$. Using these samples (and the requirement that the distribution is normalised) the posterior probability distribution or its summary statistics can be reconstructed to some precision, which is determined by the number of samples. Although much more efficient than explicitly evaluating equation 2.1, evaluating large numbers of samples is still required, especially in higher dimensions.

2.1.2.1 Metropolis-Hastings

The main algorithm we use in this thesis is Metropolis-Hastings, which is a type of Markov Chain Monte Carlo (MCMC) algorithm. A Markov Chain is a stochastic sequence of states where the next state in the chain only depends on the previous event, and so is uniquely defined by $P(x'|x)$, the probability of transitioning from a given state x to another state x'. MCMC algorithms specifically construct Markov Chains that at equilibrium output random samples from a desired probability distribution $P(x)$.

The construction of the Metropolis-Hastings algorithm begins by requiring detailed balance: the probability of being in state x and transitioning to state x' must be equal to the inverse

$$P(x' \mid x)P(x) = P(x \mid x')P(x'). \tag{2.3}$$

The algorithm breaks the transition between states into two stages. In the first a move $g(x'|x)$ is proposed from x to a possible new state x'. In the second the proposal is either accepted or rejected with probability given by $A(x'|x)$; if the proposal is rejected then the

old state is simply repeated. This makes the total probability to transition

$$P(x' \mid x) = g(x'|x)A(x'|x). \tag{2.4}$$

Inserting into equation 2.3 gives

$$\frac{A(x', x)}{A(x, x')} = \frac{P(x')}{P(x)} \frac{g(x \mid x')}{g(x' \mid x)}, \tag{2.5}$$

which can be satisfied by choosing

$$A(x', x) = \min\left(1, \frac{P(x')}{P(x)} \frac{g(x \mid x')}{g(x' \mid x)}\right). \tag{2.6}$$

As the chain becomes longer it approaches the desired probability distribution $P(x)$, which for us is the likelihood multiplied by the prior. Therefore at each step, first $g(x'|x)$ is evaluated, and then $A(x'|x)$, which requires a likelihood evaluation, which for non-simple models is expensive part of the procedure.

The choice of $g(x'|x)$ is problem specific. Its choice is a balance between avoiding wasted likelihood evaluations by maintaining a high acceptance fraction and allowing efficient exploration of the target distribution. In this thesis we predominantly use `EMCEE` (Foreman-Mackey et al., 2013), which is the Python implementation of the affine-invariant ensemble sampler proposed by (Goodman & Weare, 2010). Affine-invariant here means its performance is unchanged under affine transformations (transformations that preserves lines and parallelism) of the target distribution, so it is insensitive to covariances between parameters. It achieves this by generating proposals for each walker based on a linear combination of its current position and that of another randomly chosen walker. Qualitatively, in doing this the sampler is using the covariances of the distribution, learnt from the positions of the ensemble, to inform the proposals. Hence it can efficiently sample distributions with strong covariances without loss of performance. However it will still suffer performance loss if the target proposal cannot be transformed into a simple distribution by an affine transformation (e.g. a curved distribution).

A common way to ascertain whether a MCMC chain has converged to it has reached and explored equilibrium distribution is by calculating the autocorrelation length of the chain.

2.2 Simulation methods

2.2.1 Cosmological simulations

N-body simulations are an important tool in computational astrophysics. They are used to study the behaviour of systems, such as the stars in a galaxy or dark matter, that are well represented as a collection of gravitationally interacting particles. For computational efficiency in galaxy-scale or cosmological simulations of dark matter, each simulated particle represents a much larger ensemble of dark matter particles. An alternative is to treat dark matter in the fluid approximation and solve the Vlassov-Poisson equations, but this is unattractive for most purposes due to the high computation expense (Rampf, 2021). There are various schemes to more efficiently solve for the evolution of N-body systems by making approximations that remove the need to explicitly evaluate the force between all particle pairs. Tree methods group particles that are far enough away into larger "pseudo-particles" who's collective influence can be more quickly computed (Barnes & Hut, 1986) . Particle-mesh methods (PM) map the particles onto a grid and efficiently calculate the gravitational force in Fourier space (Hockney & Eastwood, 1981).

In this thesis we use the 140 Mpc/h "Shin-Uchuu" box of the Uchuu suite of cosmological N-body simulations[1] (Ishiyama et al., 2021). Shin-Uchuu contains 6400^3 particles, with a particle mass of $8.97 \times 10^5 M_\odot/h$ and force softening length of $0.4h^{-1}$kpc. The simulation uses the GreeM N-body code (Ishiyama et al., 2009, 2015), which is a hybrid code using the Tree method for short-range interactions and PM for long-range interactions. It uses the 2018 Planck flat ΛCDM cosmology (Planck Collaboration et al., 2020): $H_0 = 67.74\,\mathrm{km\,s^{-1}\,Mpc^{-1}}$; $\Omega_0 = 0.3089$; $\lambda_0 = 0.6911$, scalar spectral index $n_s = 0.9667$; root-mean-square matter fluctuation on 8 Mpc/h scales $\sigma_8 = 0.8159$.

This simulation box was chosen because it is the publicly available simulation box with the smallest particle mass, that still has large enough volume to adequately sample the high

[1] http://skiesanduniverses.org/Simulations/Uchuu/

mass end of the halo mass function (which is important for abundance matching, which populates halos in order of descending mass/luminosity). This was tested by checking that the high mass end of the abundance matching-derived SHMR found using Shin-Uchuu is consistent with larger volume boxes, showing convergence.

2.2.2 Halo finders and catalogues

Halo finders are used to identify halos from snapshots of the simulation at different timesteps, and merger trees are generated to track halos and mergers across the timesteps. Halo finding is both a difficult and ambiguous task (Knebe et al., 2011; Behroozi et al., 2013a). The ambiguity lies in e.g. defining the centre of the halo and deciding which particle belongs to two overlapping halos. The difficulty lies in imperfect information e.g. because of the limited resolution due to the finite dark matter particle mass or the limited number of snapshots.

There are two main approaches. The first is density-based methods (e.g. Knollmann & Knebe 2009), which calculate the density on a grid and identify the centre of halos as the centres of overdense regions. Particles are then added outwardly in spheres until a boundary condition such as the minimum overdensity condition is reached. The second is friends-of-friends based algorithms (e.g. Eisenstein & Hut 1998), which iteratively groups particles based on a minimal linking length. Phase-space algorithms add velocity information, for example by defining a linking length in 6D position-velocity space rather than 3D space. We use catalogues of halos generated by the phase-space based friends-of-friends Rockstar halo finder (Behroozi et al., 2013a) and the Consistent Trees Merger Tree Code (Behroozi et al., 2013b).

Once the particles belonging to each halo are calculated, their properties such as their mass and concentration can be calculated, along with a wealth of other information on the the distribution of particles and their dynamical state. Rockstar calculates the halo mass in a profile-independent manner by simply summing the mass of the particles belonging to each

halo using the overdensity condition $\Delta_{\rm vir} = 178$ discussed previously. To calculate the NFW scale length of the halo r_s, the Rockstar algorithm fits an NFW profile to a mass profile generated by dividing the particles into radial bins. In this thesis we use a trimmed version of the Shin-Uchuu catalogue of halos with $M_{\rm vir} > 10^9\,{\rm M}_\odot$, which means each halo has a minimum of 1100 particles and is therefore well-resolved. The cutoff of $M_{\rm vir} > 10^9\,{\rm M}_\odot$ is chosen as halos below this are too low mass to be populated by the galaxies studied with our abundance matching model.

2.3 Galaxy surveys

2.3.1 Luminosity and mass functions

Over the past few decades large-scale galaxy surveys have transformed our understanding of the structure and evolution of the universe by mapping the position and properties of vast numbers of objects. In particular the data from blind surveys, which systematically map large areas of the sky (as opposed to targetting previously known objects), can be used calculate the statistical properties of unbiased, random samples of galaxies. Prominent among these are the Sloan Digital Sky Survey (SDSS, Margon 1999) and The Arecibo Legacy Fast ALFA survey (ALFALFA, Haynes et al. 2011). SDSS has observed millions of galaxies in the optical, and ALFALFA has observed $\sim 30,000$ galaxies in the radio, at a wavelength of 21cm where it detects emission from the hyperfine transition of the galaxies' neutral hydrogen.

Both surveys are used to generate galaxy luminosity functions, the number density of galaxies as a function of luminosity, in their respective tracer. These are well described by Schechter functions (Schechter, 1976), which has a power law at low luminosity and an exponential cut-off at high luminosity. Malmquist bias, the fact that brighter objects are observed out to larger distances, must be corrected for through methods such as the $1/V_{\rm max}$ method (Schmidt, 1968), which weights observed objects by the inverse of the maximum

distance an object of that luminosity could be observed to in the survey.

Stellar Population Synthesis models (Tinsley, 1980; Bruzual & Charlot, 2003) are used to calculate the mass of the stars in a galaxy, by inferring its star-formation history from its observed spectrum. These models are defined by a star-formation history (SFH), an initial-mass function (IMF, the distribution of masses for a population of stars at the time of their formation, which is generally assumed to be universal) and models for the spectrum of a star as a function of its age, metallicity and mass. From these a model galaxy's total stellar content (including stellar metallicities) and its total emitted spectrum can be calculated as a function of time, with the best fit model constrained using the observed galaxy spectrum. In practice this procedure has reasonably large uncertainties, as the final stellar mass depends on the choice of IMF, whose exact form and universality is still an open question (reviewed in Bastian et al., 2010). Additional difficulties including modelling the effect of dust on the observed spectrum (e.g. Calzetti et al., 2000).

2.3.2 Correlation functions

Empirical models of the galaxy halo connection such as HOD and SHAM are constrained by forward modelling the clustering of galaxies. This is quantified by correlation functions (Peebles, 1980), which give the excess probability of finding two galaxies at a given separation compared to that found for a random distribution of galaxies. Here we consider the correlation function ξ as a function of comoving distance r,

$$dP = \rho(1 + \xi(r))dV, \tag{2.7}$$

where P is probability, ρ the galaxy comoving number density, and V the comoving volume. The abundance matching model used in this thesis is constrained using the projected two-point correlation function (2PCF) calculated in bins of galaxy mass/luminosity. The 2PCF w_p is the integral of the full correlation function along the line-of-sight, given by

$$w_p(r_p) = 2\int_0^\infty \xi\left(\sqrt{r_p^2 + \pi^2}\right) d\pi = 2\int_{r_p}^\infty \frac{\xi(r)}{\sqrt{r^2 - r_p^2}} dr \tag{2.8}$$

where r_p is the projected distance between galaxies and π is distance along the line-of-sight. In practice it is calculated using pair-counting techniques that compare the number of observed galaxy pairs at different separations to the number found in randomized catalogues (Landy & Szalay, 1993).

2.3.3 Rotation curves

The gas of late-type galaxies is ideal for studying dark matter due to the simplicity of its dynamics: as it can cool, it quickly settles into a thin disc with nearly circular orbits. As the rotational velocity is much greater than the velocity dispersion, the pressure support is insignificant. Therefore the acceleration is given by $g = v_c^2/r$, where v_c is the circular velocity at radius r from the galactic centre. The potential Φ can then be found by solving $\partial\Phi/\partial r = v_c^2/r$. This is in contrast to the stars of galaxies, which have significant pressure support. In that case circular velocity can be obtained by solving the Jeans equation, which either requires full 6D phase space information (e.g. Nitschai et al. 2020) or assumptions about the anisotropy of the velocity dispersion tensor (e.g. Cappellari 2008).

Extracting rotation curves from raw gas data was recently reviewed in (Lelli, 2023). The gas disc is assumed to be optically and geometrically thin. In this case the projected line-of-sight velocity $V_{\rm los}$ at sky position (x, y) is given by

$$V_{\rm los}(x, y) = V_{\rm sys} + V_{\rm rot}(R)\sin(i)\cos(\theta), \tag{2.9}$$

where $V_{\rm sys}$ is the recession velocity, $V_{\rm rot}$ the rotation velocity of the gas at radius r, i the galaxy inclination and θ the azimuthal angle in the disc plane

$$\cos(\theta) = \frac{-(x - x_0)\sin(P.A.) + (y - y_0)\cos(P.A.)}{R}, \tag{2.10}$$

where (x_0, y_0) are the coordinates of the galaxy's centre and $P.A.$ is the position angle of the major axis. The 2D velocity field $V_{\rm los}(x, y)$ is calculated across the disc by spectral line fitting in small bins. $V_{\rm rot}$ is calculated using using *tilted ring modelling* (Rogstad et al., 1974;

Begeman, 1989), which divides the 2D velocity field into N rings with a width determined by the spatial resolution of the data. Equation 2.9 is then fit to each ring independently. Typically a first run is performed, whose output is used to calculate a mean $V_{\rm sys}$ and (x_0, y_0) which is then fixed in subsequent fits. $P.A.$ and i are estimated in the same way, unless the disc is warped, in which case their values are fitted with a smooth function, which is then used as input to a final fit to constrain $V_{\rm rot}$ for each ring. The uncertainty on the inclination is taken to be the scatter in the values of i. The procedure is carried out seperately for the approaching and receeding side of the disk, with their average taken to be $V_{\rm rot}$ and half their difference the systematic uncertainty (which is combined with the statistical uncertainty from the fit).

As an alternative to tilted-rings, parametric approach (Courteau, 1997a) assume a functional form for the rotation curve (as well as additional quantities such as $i(R)$), whose parameters are directly constrained by the data. However these approaches impose a smoothness on the rotation curve which may eliminate physical features.

Fitting the 2D velocity field works well when the data has high spatial resolution. However when the resolution is lower it is preferable to forward model the 3D datacube (with wavelength the third axis).

The most detailed modern studies of this type use radio interferometry to measure the rotation curves (RCs) of galaxies, the rotational velocity of the gas as a function of radius (e.g. Walter et al. 2008; Lelli et al. 2016a). This has allowed detailed comparison between different halo models (Katz et al., 2017; Li et al., 2020), provided insights into the scaling relationships between galaxies (e.g. Lelli et al. 2019; Desmond et al. 2019) and afforded tests of modified gravity (Burrage et al., 2017; Naik et al., 2019; Chae et al., 2021).

However, due to the observational expense, even the largest collations of RCs only contain hundreds of galaxies, with ongoing surveys such as MIGHTEE-HI (Maddox et al., 2021) and APERTIF (Oosterloo et al., 2010) aiming to extend this to thousands.

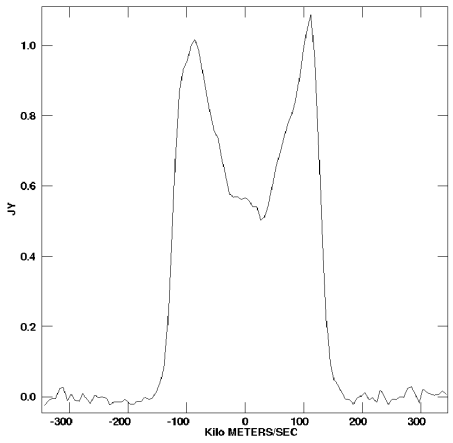

Figure 2.1: The HI line profile of NGC2977, with flux plotted against radial velocity relative to the galaxy's kinematic centre. *Reproduced from Hess et al. (2009).*

2.3.4 HI Linewidths

The HI line profile, the spatially integrated flux of the 21-cm emission line (Fig. 2.1), also provides information on the kinematic status of a galaxy. In particular, the width of the emission line (henceforth W_{50}) is a readily observable kinematic tracer and has already been derived for tens of thousands of galaxies. The current state of the art is the ALFALFA survey (Haynes et al., 2018), which has produced a catalogue of W_{50} for ~30,000 galaxies out to $z \sim 0.06$ using a blind drift scan with the ARECIBO telescope. Future single dish and interferometric surveys such as WALLABY (5×10^5 galaxies; Koribalski et al. 2020) and the SKA ($\sim 10^9$ galaxies out to $z \sim 2$; Yahya et al. 2015) will increase the number of W_{50} observations by orders of magnitudes while extending to significantly higher redshift.

The drawback of using W_{50} rather than resolved RCs to localise dark matter is that it lacks spatial information within the galaxy, instead providing a weighted average across the RC. In particular, W_{50} is dependant on both the spatial distribution of HI gas in the galaxy and the velocity profile that traces the total gravitational potential. If the HI gas disc extends into the flat part of the RC with speed $V_{\rm flat}$, the HI spectral profile takes the form of the classic symmetric two-horned shape, due to flux building up at the wavelengths equivalent to the Doppler shifting of the HI line by $\pm V_{\rm flat}$. In this case the inclination-corrected line

width $W_{50}/\sin i$ is approximately $2V_{\rm flat}$, which is typically dominated by the gravity of the dark matter halo. However, depending on the HI distribution, W_{50} can either be weighted towards the inner parts of the galaxy where the baryonic contribution is important, causing it to be closer to twice the peak velocity $V_{\rm max}$, or to lower values if the rotation curve is still rising or observed close to edge-on, causing a single peaked profile. W_{50} can also be affected by morphological asymmetries caused by environmental interactions or internal processes (Bok et al., 2019; Reynolds et al., 2020; Watts et al., 2020). Despite these complexities W_{50} contains a large amount of potential information about the dynamical mass of a galaxy. Lelli et al. (2019) find that for the SPARC sample W_{50} from archival single-dish data give a tighter Baryonic Tully–Fisher Relation than all velocity summary statistics ($V_{\rm max}$, V_{2R_e},$V_{2.2}$) other than $V_{\rm flat}$.

Early studies attempting to compare HI linewidths to ΛCDM expectations used naive models in which the linewidth was directly equated to the maximum circular velocity of the underlying halo. However due to the finite extent of the gas disc, this is not expected to be accurate (Brook & Shankar, 2016). For example, Sardone et al. (2023) carry out long integration observations of a small number of galaxies, enabling them to measure the width of the HI line defined at smaller and smaller fractions of the peak flux. They find that the linewidth defined as the width at 10% of the peak flux is closer to the expected maximum circular velocity of the dark matter halo than the width at 50% of peak flux. Clearly more sophisticated modelling that accounts for both the finite extent of the HI disc and the expected mass distribution of the dark matter halo is necessary when comparing linewidths to ΛCDM expectations. In Chapter 3 I develop such a model and apply it to data.

Chapter 3

Inferring dark matter halo properties for HI-selected galaxies

In this chapter we set constraints on the dark matter halo mass and concentration of ~22,000 individual galaxies visible both in HI (from the ALFALFA survey) and optical light (from the SDSS). This is achieved by combining two Bayesian models, one for the HI line width as a function of the stellar and neutral hydrogen mass distributions in a galaxy using kinematic modelling, and the other for the galaxy's total baryonic mass using the technique of inverse subhalo abundance matching (SHAM).

To analyse the linewidth, we develop a Bayesian forward-modelling framework: we first construct models for the full HI line profile of a galaxy for given baryonic and dark matter mass distribution and then compress this to the W_{50} statistic. Unlike models that simply equate W_{50} to some summary statistic of the rotation curve (typically $V_{\rm flat}$ or $V_{\rm max}$), possibly with empirical corrections for the effects described above, our method naturally takes full account of the HI distribution and shape of the rotation curve based on the available observational data. We test the accuracy of our method, which uses survey data and empirical relationships to construct the distribution of baryons, using the resolved spectroscopy and photometry of the SPARC data set.

SHAM assigns galaxy masses based on the virial mass or rotation velocity of their halo, with some scatter to allow for stochasticity in the galaxy–halo connection (Kravtsov et al., 2004; Conroy et al., 2006; Behroozi et al., 2010; Guo et al., 2010; Moster et al., 2010). The ALFALFA survey has revealed that HI-selected samples are much more weakly clustered than optically-selected (Li et al., 2012; Martin et al., 2012; Papastergis et al., 2013), and recent work has shown that reproducing their clustering signal requires performing SHAM on a subset of the simulated halo population selected on properties that have a similar clustering bias, such as formation time (Guo et al., 2017; Stiskalek et al., 2021).

SHAM, along with the similar empirical technique of Halo Occupation Distribution modelling, are commonly combined with the halo model or DMO simulations to construct mock catalogues for the massive volumes of the sky probed by cosmological surveys. They can also be applied in the inverse direction: using photometric observations of galaxies to map out the dark matter distribution (e.g. Desmond et al., 2018b). Therefore it is vital that these empirical methods are validated by independent tests, especially at low masses where clustering constraints become weak or unavailable.

In this work we use the SHAM prescription of Stiskalek et al. (2021) (henceforth ST21), which is specifically tailored to the HI-selected galaxies of the ALFALFA sample, to construct an inverse SHAM method which produces a Bayesian posterior on the halo properties of a galaxy given its baryonic mass as observational input. Comparing the independent constraints on halo properties from HI kinematics and SHAM will allow us to answer the following questions:

- What is the DM content of HI-selected galaxies and how does this correlate with galaxy variables at both the population and individual galaxy levels?
- To what extent are the halo properties implied by kinematics and photometry consistent?
- How much information on the DM distribution is contained in cheaper photometric

observations of a galaxy, versus the more expensive W_{50}?

- Does combining kinematic and abundance matching posteriors give us tighter constraints on halo properties than either one alone?

The paper is structured as follows. Section 3.1 describes the observed and simulated data we use. Section 3.2 describes our Bayesian models and inference for W_{50} and SHAM, and the metrics we use to characterise the posteriors of individual galaxies. In Section 3.3 we present the constraints on halo properties obtained by the two models for our sample of HI-selected galaxies, their summary metrics and their correlation with galaxy properties. We expand on the implications of our results, discuss potential systematic errors and compare to the literature in Section 3.4, and conclude in Section 3.5. We assume $H_0 = 70\,\mathrm{km\,s^{-1}}$, and all logarithms are base-10.

3.1 Data

3.1.1 ALFALFA

We take HI line widths, HI masses and distances from the ALFALFA[1] (Haynes et al., 2018) data set. This contains HI line sources in 7000 deg^2 of high Galactic latitude out to a redshift of 0.06 generated from a blind survey using the Arecibo telescope. The complete $\alpha.100$ catalogue contains ~31500 extragalactic sources with HI masses ranging from 10^6 to 10^{11} $M_\odot$. We use the W_{50} line width measurement, which is the velocity width measured at 50% of the peak flux. This is calculated by identifying the two peaks of the classic twin horned HI line profile, then fitting polynomials to the data between the peak and zero flux on each side. W_{50} is corrected for instrumental broadening, as described in Springob et al. (2005), but not for turbulent motion, disk inclination or cosmological effects. The catalogue also contains W_{20}, the velocity width measured at 20% of the peak flux. Theoretically this is

[1] http://egg.astro.cornell.edu/alfalfa/data/index.php

expected to be a better tracer of the dark matter-dominated outskirts of the galaxy. However Haynes et al. (2018) find the measurement less robust, and its errors harder to quantify, and so only an error on W_{50} is provided.

The catalogue also contains distances. For objects with $cz > 6000$ km/s this is cz, where z is the redshift in the CMB frame measured from the centroid of the HI line. For objects closer than this a distance is calculated using the local peculiar velocity model of Masters (2005). This is based on a multiattractor model, which models the effect of structures such as the local supercluster on the Hubble flow by fitting multiple parameterised spherical attractors to large samples of observed galaxy velocities. The Masters model is fit to the velocities of the SFI++ sample of 5000 spiral galaxies with Tully-Fisher distances. Primary distances are used if they are available in the literature. The HI mass $M_{\rm HI}$ is provided, calculated from the total integrated HI flux and the assumed distance. A code indicates the reliability of each detection based on the signal-to-noise ratio (SNR) and other observational criteria. Code 1 sources (of which there are 25,434) are the highest-quality observations, whilst code 2 sources may have lower SNR, but have been successfully crossmatched with known optical counterparts at the same redshift as the HI line. We use both in our fiducial analysis.

Yu et al. (2022) perform a reanalysis of the ALFALFA raw spectra, including calculating a different, integrated definition of the line width using the "curve of growth" method of Yu et al. (2020). Their measurement (henceforth $W_{\rm Yu85}$) is defined as the velocity width enclosing 85% of the total flux. We use $W_{\rm Yu85}$ in a non-fiducial model to test for possible systematics due to the ALFALFA data reduction.

3.1.2 NASA-Sloan Atlas

We use the NASA-Sloan Atlas (NSA) to obtain stellar masses and optical axis ratios (used to derive inclinations) for the ALFALFA galaxies. The NSA consists of images and parameters of local galaxies derived from Sloan Digital Sky Survey (SDSS) imaging

data, with the addition of *Galaxy Evolution Explorer* (GALEX) (Martin et al., 2005) data. We use NSA v1_0_1[2] which is based on SDSS DR13 (Albareti et al., 2017) and contains ~640,000 galaxies out to redshift $z = 0.15$. The image analysis pipeline utilises enhanced object detection, deblending and other improvements over standard SDSS processing, which improves its performance for larger and brighter galaxies (Blanton et al., 2011). The catalogue contains both elliptical Petrosian and Sérsic aperture photometry fits, with the former considered more reliable. The fits are K-corrected to $z = 0.0$ using the `kcorrect code v4_2` (Blanton & Roweis, 2007), which also estimates the stellar mass. A Chabrier initial mass function (IMF) is assumed and spectral energy distributions (SEDs) are fitted to the broadband optical SDSS fluxes as well as ultraviolet fluxes from *GALEX* when available.

To crossmatch the NSA catalogue with ALFALFA we follow ST21 by requiring a 5 arcsecond skymatch between NSA galaxies and the ALFALFA×SDSS optical counterparts of Durbala et al. (2020), and a maximum line-of-sight distance of 10 Mpc. These criteria should yield a low number of mismatches. There are 21,776 galaxies in our final ALFALFA×NSA catalogue. We note that the ALFALFA × SDSS catalogue of Durbala et al. (2020) contain estimates of stellar mass for ~30,000 galaxies, but we prefer to use NSA's improved image analysis pipeline, which also improves consistency with ST21.

3.1.3 SPARC

SPARC[3] (Lelli et al., 2016a) is a database of 175 late-type galaxies for which both high quality HI rotation curves and near-infrared Spitzer photometry are available. We use SPARC's publicly available resolved rotation curves, detailed mass models and W_{50} measurements, as well as the HI surface density as a function of radius (F. Lelli, private communication) in our analysis. The high resolution SPARC data is used as a truth against which we test the approximations that allow us to model the much larger ALFALFA data set. A caveat to

[2] https://www.sdss.org/dr13/manga/manga-target-selection/nsa/
[3] http://astroweb.cwru.edu/SPARC/

this approach is that it is still possible for HI inferences to be biased even in the presence of very high quality data (e.g. Collins & Read, 2022), so the SPARC dataset is not a perfect ground truth. Such biases have been studied extensively in simulations (e.g. Oman et al., 2020). The strongest biases result from non-circular gas motions and the geometry of the HI distribution, which are highly dependent on the implementation of feedback and gas cooling prescriptions, as well as resolution. The strongest biases also occur in low mass dwarf galaxies, few of which are present in our sample. Therefore we choose to use observational data as the ground truth, although exploring biases in HI inferences in recent cosmological simulations which produce realistic late-type galaxies with thin gas discs (e.g. Dubois et al., 2021) would be interesting future work.

The sample spans a large range in luminosity (10^7 to $10^{12} L_\odot$), surface brightness (~5 to ~5000 $L_\odot \mathrm{pc}^{-2}$), gas mass (~10^7 to $10^{10.6} M_\odot$) and morphology (S0 to Im/BCD). The advantage of Spitzer photometry is that at 3.6μm the mass-to-light ratio of galaxies is relatively constant, which helps to break the degeneracy between the velocity contribution from the stars and the dark matter. We perform a crossmatch between ALFALFA and SPARC using the same procedure as for the NSA, which yields 45 matches.

Lelli et al. (2019) compile HI line widths from various sources in the literature and for various definitions for the SPARC galaxies. The closest line width definition they include to ALFALFA's W_{50} is $W_{50\mathrm{Mc}}$: the width at 50% flux of the mean flux, where the mean flux is taken across the whole line width, with corrections for instrumental resolution and relativistic broadening. As we find the two measures are very similar for galaxies that have both, we test our W_{50} model using the 125 galaxies in SPARC for which there is either an ALFALFA W_{50} or a SPARC $W_{50\mathrm{Mc}}$.

Table 3.1: The free parameters in our abundance matching and kinematic models, their physical definitions and their Bayesian priors. All parameters are sampled in logarithmic space except inclination and distance.

	Parameter	Units	Definition	Prior
AM	$M_{\rm vir}$	$M_\odot$	Virial mass	2D halo probability density from Uchuu simulation
	$c_{0.1}$		Custom halo concentration, defined in Eq. (3.11)	
Kinematics	$M_{\rm vir}$	$M_\odot$	Virial mass $M_{\rm vir} = M_{\rm halo} + M_{\rm bar}$ (see Section 3.2.1)	Flat in range $\log(M_{\rm bar}/\,{\rm M}_\odot) < \log(M_{\rm vir}/\,{\rm M}_\odot) < 15.5$
	$c_{0.1}$		Custom halo concentration, defined in Eq. (3.11)	Flat in range $0.5 < \log c_{0.1} < 2$, or halo mass–concentration relationship
	$M_{\rm HI}$	$M_\odot$	HI mass	Gaussian prior from ALFALFA observed value and its uncertainty
	M_*	$M_\odot$	Stellar mass	Gaussian prior from NSA observed value with adopted 0.2 dex uncertainty
	$r_{\rm HI}$	kpc	Scale length of exponential gas disc	Gaussian prior from Wang et al. (2016) mass–size relationship
	$r_{\rm disk}$	kpc	Scale length of exponential stellar disc	Gaussian prior from empirical relationship based on M_* (Dutton et al., 2011)
	$r_{\rm bulge}$	kpc	Half light radius of stellar bulge	Gaussian prior from empirical relationship based on M_* (Dutton et al., 2011)
	D	Mpc	Physical distance to galaxy	Gaussian prior from ALFALFA value and its uncertainty
	i	deg	Inclination (0° face on; 90° edge on)	Equation (3.13) with NSA $b/a \pm 10\%$, and a flat prior on q in the range 0.15 to b/a.

3.2 Methodology

3.2.1 Overview and verification with SPARC

For each galaxy in our sample we have two separate Bayesian models: the kinematic model, for which the observable is the ALFALFA W_{50}, and the SHAM model, for which the observable is the galaxy's baryonic mass $M_{\rm bar}$. Our kinematic model also contains nuisance parameters describing the galaxy, the priors of which are informed by the NSA and ALFALFA data. The free parameters and their priors for each model are listed in Table 3.1.

DMO simulations (on which our SHAM model is based) implicitly assume that baryons and dark matter behave identically and hence are perfectly mixed. The virial halo masses listed in their halo catalogues (which we label $M_{\rm vir}$) are therefore different to the masses inferred from fitting parameterised halo profiles to kinematic data (which we label $M_{\rm halo}$) according to $M_{\rm vir} = M_{\rm halo} + M_{\rm bar}$ where $M_{\rm bar}$ is the mass of *observed* stars and cold gas. $M_{\rm halo}$ therefore includes DM as well as any unobserved baryons, which are inferred indiscriminately in the kinematic analysis. We assume that the sum of these components follows a standard density profile (Section 3.2.2.1), e.g. because they have the same distribution. In reality, the distribution of hot gas around galaxies and its association with the dark matter is poorly known. Hafen et al. (2019) found that $f_{\rm b}$ can vary substantially

between galaxies, as part of the circumgalactic medium can be accreted from the intergalactic medium and other galaxies. However, this potential systematic uncertainty in $M_{\rm vir}$ of up to $\sim 15\%$ (for a halo completely stripped of baryons) is still small compared to the typical uncertainties on our derived halo masses. We do not modify halo concentrations to account for the fact that a fraction of $M_{\rm halo}$ is in baryons (see also Sec. 3.4.2.1).

In our kinematic model we sample $\log M_{\rm vir} = \log(M_{\rm halo} + M_{\rm bar})$ rather than $M_{\rm halo}$ itself, setting the lower bound on its flat prior to be $\log M_{\rm bar}$. We find some galaxies to have non-zero posterior probability at $M_{\rm halo} = 0$, so this parameterisation aids sampling by raising the lower limit of the posterior to a finite value. We could perform the SHAM inference with the same parameterisation as the kinematics, but it is unnecessary. Our SHAM posterior does not approach $M_{\rm halo} = 0$, so we can simply convert to or from $M_{\rm vir}$ in post-processing.

In Fig. 3.1 we show relationship between our observed and simulated input quantities and our Bayesian models, as well as the verification of the W_{50} model using the SPARC data. In Section 3.2.2 we describe our kinematic model and its verification using SPARC, and in Section 3.2.3 our SHAM model.

3.2.2 Kinematic model

The kinematic model puts constraints on halo parameters by combining a parameterised form for the halo density profile with a baryonic mass distribution to forward-model W_{50} for comparison with the ALFALFA data. The forward-model consists of three steps:

1. Calculate the model rotation curve $V_{\rm c}(r)$ and HI surface density $\Sigma_{\rm HI}(r)$ for the galaxy for a given set of model free parameters.

2. Construct the model HI line profile from $\Sigma_{\rm HI}(r)$ and $V_{\rm c}(r)$.

3. Calculate W_{50} from the line profile and compare to the observed value.

As SPARC has mass models for the HI and stars of each galaxy, as well as the observed RC, we can use it to carry out checks on our model:

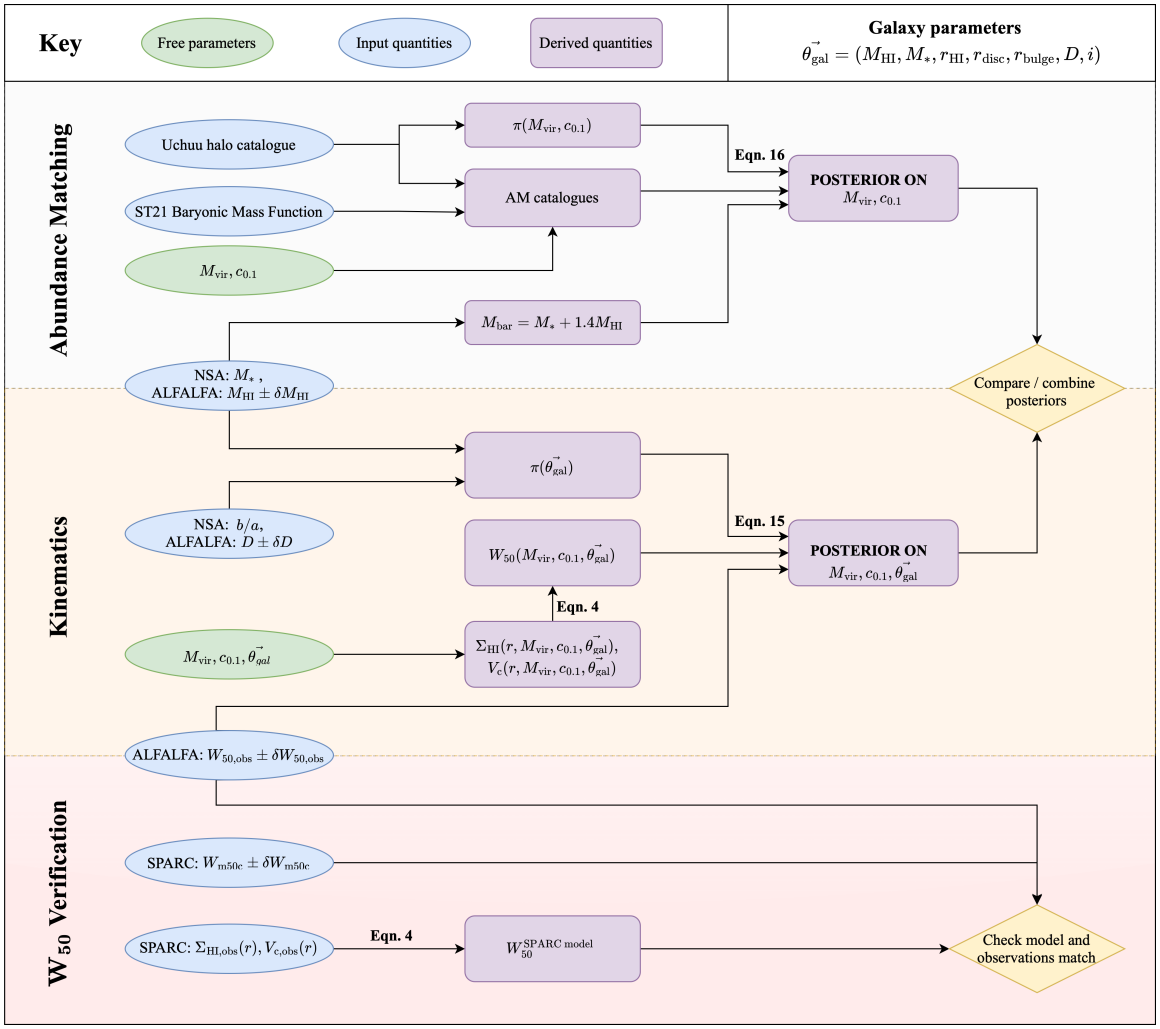

Figure 3.1: Schematic of our workflow for constraining halo mass and concentration from abundance matching and kinematics. The kinematics observable is the ALFALFA W_{50}. Observations of galaxy parameters from the NSA and ALFALFA inform the priors on the free parameters in the kinematic inference. The observed $M_{\rm HI}$ and M_* are also used to calculate the galaxy's baryonic mass $M_{\rm bar}$, which is the observable in the subhalo abundance matching model. The resolved rotation curves ($V_{\rm c,obs}$) and HI surface density observations ($\Sigma_{\rm HI,obs}$) from the SPARC data set are used to verify that the model for calculating W_{50} (equation 3.4) can match observations.

1. Are the observed W_{50} of real galaxies well modelled as a product of their azimuthally averaged RC and HI surface density?

2. How much do our simple mass models based on empirical relations and non-resolved observations bias line widths compared to the detailed mass models in SPARC?

3. How accurate are optical inclinations from SDSS photometry compared to those derived from tilted-ring fits to spatially resolved velocity fields?

The HI spectrum is a spatially integrated quantity, so to calculate W_{50} we must first model the full RC. We assume the rotational speed is equal to the circular speed (we discuss the validity of this in Sec. 3.4.2.2). The total circular speed, $V_c(r)$, is the sum in quadrature of the circular speed due to each of the galaxy's components (dark matter, stellar bulge, stellar disc, gas disc),

$$V_c^2(r) = V_{DM}|V_{DM}| + V_{bulge}|V_{bulge}| + V_{disc}|V_{disc}| + V_{gas}|V_{gas}|, \tag{3.1}$$

where V_x is also a function of r. To construct the HI spectrum from $V_c(r)$ and $\Sigma_{HI}(r)$ we follow the method of Obreschkow et al. (2009), by considering the gas disc as a series of flat rings each with a constant circular speed V_c. The flux of the HI spectrum at a given wavelength λ corresponds to HI gas with radial velocity V_λ, which we define relative to the galaxy's systemic velocity so the midpoint of the spectrum is at $V_\lambda = 0$. The flux at wavelength λ due to a single, infinitely thin ring of gas is given by

$$\tilde{\psi}\left(V_\lambda, V_c\right) = \begin{cases} \frac{1}{\pi\sqrt{V_c^2 - V_\lambda^2}} & \text{if } |V_\lambda| < V_c \\ 0, & \text{otherwise} \end{cases} \tag{3.2}$$

The singularity is smoothed by introducing a velocity dispersion σ_{HI} for the gas, which models its random motion. We fix the dispersion to be 10 km/s, based on observations of nearby galaxies (Leroy et al., 2008; Mogotsi et al., 2016). This broadens the flux from the ring:

$$\psi\left(V_\lambda, V_c\right) = \frac{\sigma_{HI}^{-1}}{\sqrt{2\pi}} \int_{-\infty}^{+\infty} dV \exp\left[\frac{(V_\lambda - V)^2}{-2\sigma_{HI}^2}\right] \tilde{\psi}\left(V, V_c\right). \tag{3.3}$$

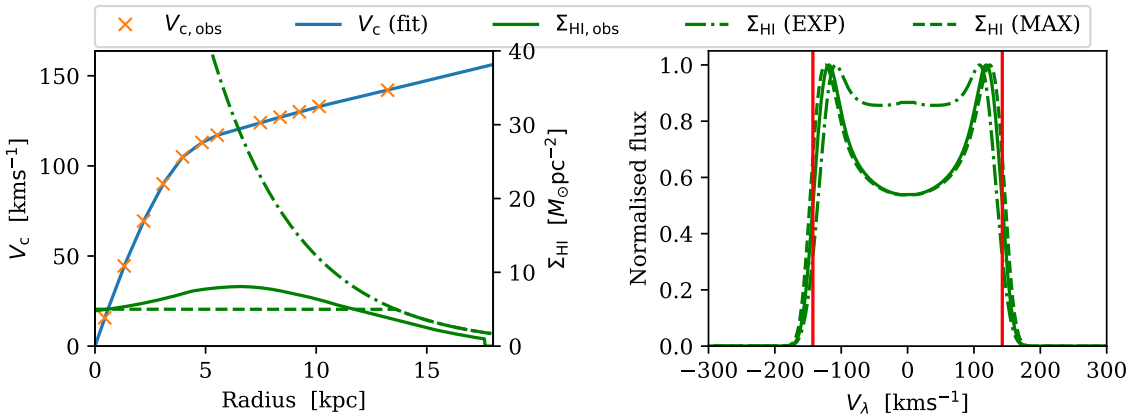

Figure 3.2: *Left panel*: For the low surface brightness galaxy F568-1 we plot the circular velocity $V_{c,obs}$ from SPARC (orange) and its fit (blue) with linear extrapolation (*left y-axis*) . The observed $\Sigma_{HI,obs}$ from SPARC is shown (*right y-axis*), as well as the untruncated exponential model (EXP) and the truncated model (MAX) with $\Sigma_{MAX} = 5 M_\odot pc^{-2}$ (see Section 3.2.2.2). The model Σ_{HI} are based on the mass-size relationship of Wang et al. (2016).
Right panel: The green lines are the HI flux profiles calculated by applying equation 3.4 to V_c (fit) and each of the three Σ_{HI} shown in the left panel with the corresponding line style. V_λ is the observed radial velocity relative to the galaxy's systemic velocity. The resulting W_{50} are: 285.4 km s^{-1} for $\Sigma_{HI,obs}$ (shown in red); 271.2 km s^{-1} for EXP; 287.3 km s^{-1} for MAX. The untruncated model produces lower values of W_{50} generally. This galaxy is an example where even though the MAX model does not provide a perfect fit to Σ_{HI}, it is still capable of reproducing W_{50}.

The total flux observed at λ is then obtained by integrating over the galaxy:

$$\Psi_{HI}(V_\lambda) = \frac{2\pi}{M_{HI}} \int_0^\infty dr\, r \Sigma_{HI}(r) \psi(V_\lambda, V_c(r)) \,. \tag{3.4}$$

As our model profiles are symmetrical, W_{50} is calculated by identifying the peak flux and then finding the outermost point where the flux is 50% of the maximum.

To check the accuracy of modelling W_{50} in this way, we calculate a "SPARC model W_{50}" by applying equation (3.4) to $V_{c,obs}$, the observed inclination-corrected RC, and $\Sigma_{HI,obs}$, the observed HI surface density profile, of the SPARC galaxies. For some SPARC galaxies the HI surface density observations extend beyond the final data point of the RC. We extrapolate the RC as V_{flat} if it is defined for the galaxy (Lelli et al., 2015), or linearly extrapolate the RC if it is not. We show this procedure for a single galaxy in Fig. 3.2. To approximate uncertainties on the SPARC model W_{50} we use the maximum and minimum W_{50} generated

by combinations of the observational errors on the RC and $V_{\rm flat}$, and extrapolating linearly or with $V_{\rm flat}$.

In Fig. 3.3 we compare the SPARC model W_{50} to the observed W_{50} for the 125 galaxies in the SPARC data set with either an ALFALFA W_{50} or the very similar SPARC $W_{50\rm Mc}$ (described in Section 3.1.3). Although the uncertainties on the SPARC model W_{50} are crude, there are only 3 galaxies for which there is $> 3\sigma$ tension between the model and observed value. It is interesting that the model W_{50} on average slightly underpredicts the observed value across a large range, suggesting it cannot be due to a constant effect such as instrumental broadening. A possible cause is non-circular motions such as outflows. We conclude that the model works well for $W_{50} \gtrsim 200\,{\rm km\,s^{-1}}$. The scatter between model and observations increases at lower W_{50}, but this can be explained by the increased uncertainty in the extrapolation of the RC.

To apply the W_{50} model to the ALFALFA galaxies, we now need to construct model $\Sigma_{\rm HI}(r)$ and $V_{\rm c}(r)$ for the ALFALFA sample.

3.2.2.1 Dark matter distribution

The circular speed contribution from the DM is calculated by assuming a halo profile, with the halo mass $M_{\rm halo}$ and its concentration as free parameters. There are a large number of different halo profiles in literature (see e.g. Li et al. 2020). We perform our analysis for the cuspy Navarro-Frenk-White (NFW) (Navarro et al., 1997) and the cored Burkert (Burkert, 1995) profiles as representatives of cusped and cored profiles respectively. We caution that neither of these is likely to be entirely accurate after accounting for baryonic feedback, as we discuss further in Section 3.4.2.

NFW: NFW found that the haloes in cosmological DMO simulations are well fit by a universal density profile

$$\rho_{\rm NFW}(r) = \frac{\rho_s}{\left(\frac{r}{r_s}\right)\left[1+\left(\frac{r}{r_s}\right)\right]^2}, \tag{3.5}$$

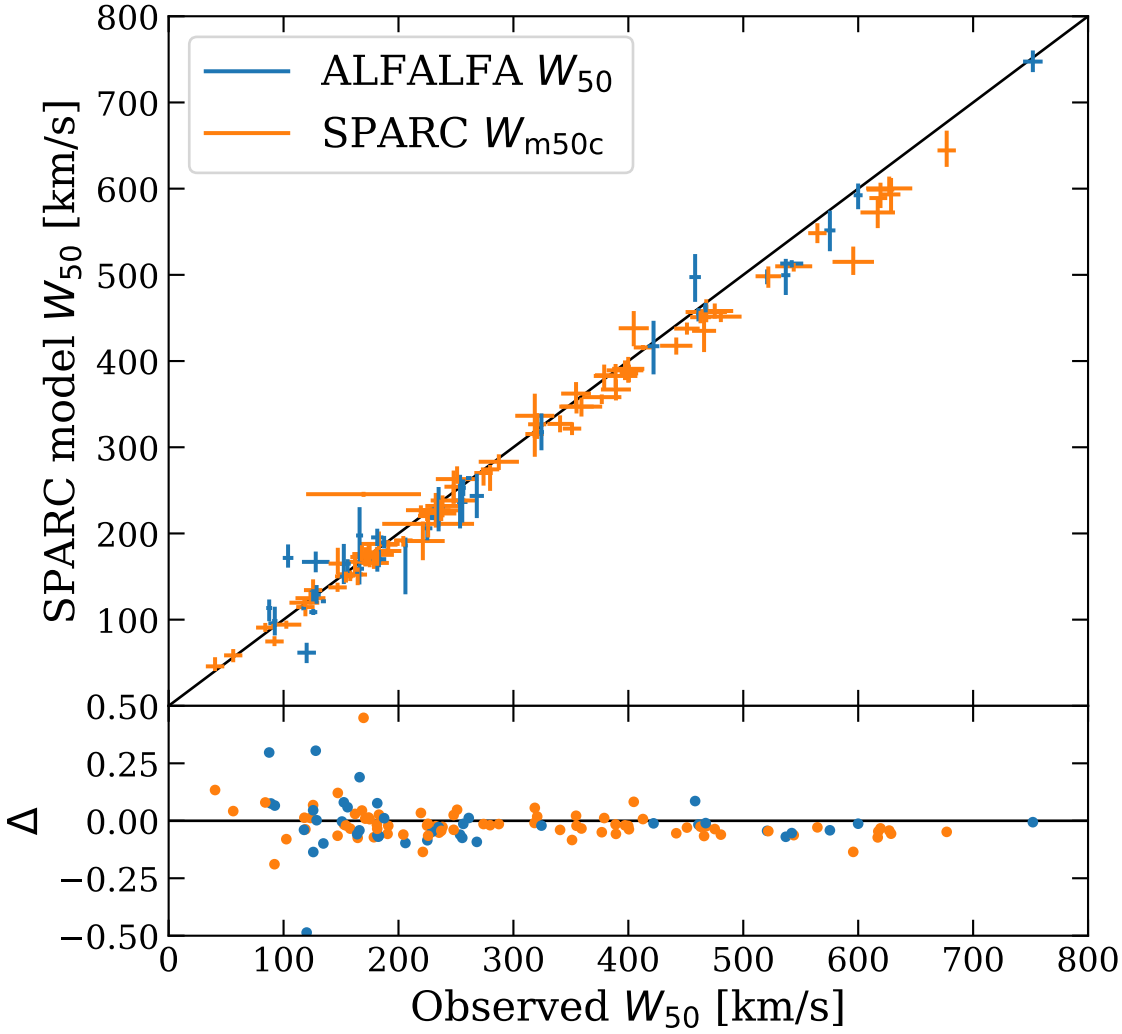

Figure 3.3: The SPARC model W_{50} (calculated from the observed SPARC HI surface density and RC using equation 3.4) plotted against the observed W_{50}, for the 125 galaxies in SPARC with either an ALFALFA W_{50} or SPARC W_{50Mc} (see Section 3.1.3). The subplot shows the relative differences $\Delta = \frac{\text{Model}-\text{Observed}}{\text{Observed}}$. The model and observations are in good agreement, although there is increasing scatter in the residuals at lower values. Both quantities are calculated/corrected using the inclinations from the SPARC kinematic fitting.

where r_s is a scale radius and ρ_s a characteristic density. The enclosed mass at radius r is

$$M_{\rm NFW}(r) = 4\pi\rho_s r_s^3 \left[\ln(1+x) - \frac{x}{1+x}\right], \tag{3.6}$$

where $x \equiv r/r_s$.

Burkert: The Burkert profile was proposed as a modification to the PISO profile in order to improve the fit to observations of dwarf spheroids at larger radii. The density profile is

$$\rho_{\rm Burkert}(r) = \frac{\rho_s}{\left(1+\frac{r}{r_s}\right)\left[1+\left(\frac{r}{r_s}\right)^2\right]}, \tag{3.7}$$

and the enclosed mass is given by

$$M_{\rm Burkert}(r) = 2\pi\rho_s r_c^3 \left[\frac{1}{2}\ln\left(1+x^2\right) + \ln(1+x) - \arctan(x)\right]. \tag{3.8}$$

It should be noted that whilst differing at small radii, at large radii both NFW and Burkert profiles have the same slope $\rho \propto 1/r^3$. Therefore the large extrapolation necessary to calculate the halo's total mass (the virial radius lies far outside the radius probed by W_{50}) is similar for both. The contribution of the halo to the circular speed at radius r is $V_{\rm DM} = \sqrt{GM_{\rm DM}(r)/r}$. It is most convenient to calculate relative to the virial quantities

$$\frac{V_{\rm DM}(r)}{V_{\rm halo}} = \sqrt{\frac{M_{\rm DM}(r)}{M_{\rm halo}}\frac{R_{\rm halo}}{r}}. \tag{3.9}$$

where $V_{\rm halo} \equiv \sqrt{GM_{\rm halo}/R_{\rm halo}}$ is the circular speed at the virial radius $R_{\rm halo}$ (which is inferred from $M_{\rm halo}$).

Traditionally, concentration is defined as

$$c_{\rm halo} = \frac{R_{\rm halo}}{r_{-2}}, \tag{3.10}$$

where r_{-2} is the radius at which the slope of the logarithmic density profile is equal to -2 (for NFW $r_s = r_{-2}$). We instead use a new concentration definition

$$c_{0.1} = \frac{R_{\rm halo}}{r_{0.1}}, \tag{3.11}$$

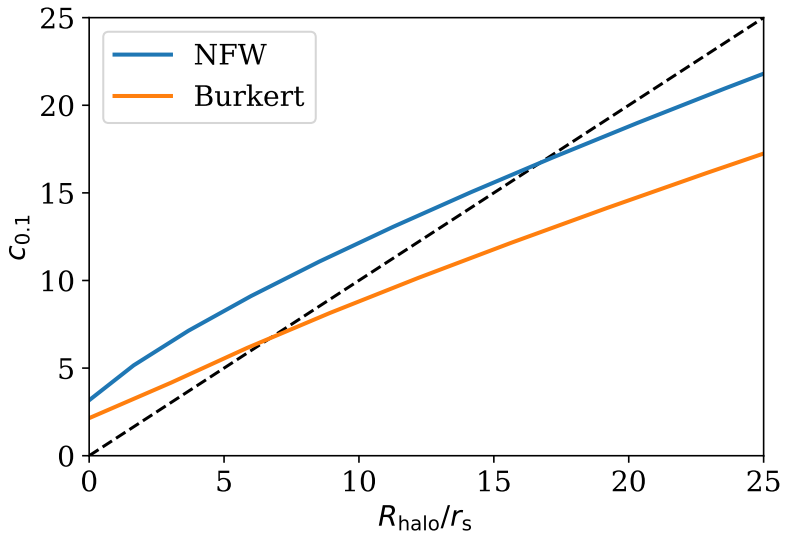

Figure 3.4: The mapping between $R_{\rm halo}/r_s$ (where $R_{\rm halo}$ is the virial radius) and our new concentration definition $c_{0.1}$ (equation 3.11). The scale length r_s is defined separately for the NFW (equation 3.5) and Burkert (equation 3.7) profiles. For the NFW profile $r_s = r_{-2}$.

where $r_{0.1}$ is the radius enclosing 10% of the halo mass. This new definition has three advantages: 1) unlike r_{-2}, $r_{0.1}$ is defined for all halo profiles; 2) $r_{0.1}$ can be calculated from haloes in simulations without assuming a profile but just counting particles in spheres grown from the centre; 3) it is easier to interpret, as it does not depend on the profile shape. In Fig. 3.4 we show the mapping between $c_{0.1}$ and $R_{\rm halo}/r_s$, which we calculate numerically.

3.2.2.2 Baryon distribution

We set the prior on M_* to be a Gaussian with mean equal to the NSA M_* and a scatter of 0.2 dex for all galaxies, as a representative value of uncertainty on the mass-to-light ratio. We compare the NSA M_* to the GALEX-SDSS-WISE Legacy Catalog (Salim et al., 2018) values; this is a smaller sample than NSA, but all galaxies have SDSS spectra and WISE photometry which are used in their alternative SED fitting pipeline. For the ~11,000 galaxies in both catalogues and ALFALFA, the mean difference in M_* is 0.04 dex, with a standard deviation of 0.19 dex. With 0.2 dex uncertainty, the NSA M_* are also consistent with those from SPARC (adopting $\Upsilon_* = 0.5\,{\rm M}_\odot/L_\odot$ as per Lelli et al. 2016a). We scale the

NSA M_* according to the distances listed in ALFALFA.

We use $M_{\rm HI}$ and its uncertainty from ALFALFA. McGaugh et al. (2020) find that the molecular gas mass for late-type galaxies is around 7% of the stellar mass. This correction is minor for most of our sample. Therefore to be consistent with ST21 we set the total baryonic mass to be simply $M_{\rm bar} = M_* + 1.4M_{\rm HI}$, where the factor of 1.4 accounts for cosmological helium and metals.

To estimate the spatial distribution of the stars we use the empirical relationships of Dutton et al. (2011), who use the GIM2D software (Simard et al., 2002) to perform two-component bulge and disc fits to r-band and g-band images and hence derive structural properties of ~200,000 late and early type galaxies from SDSS DR7. They find empirical relationships for $M_* - r_{\rm disc}$ and $M_* - r_{\rm bulge}$, and the bulge fraction. We use their relationships for late-type galaxies, as these comprise the bulk of our sample. We fix the bulge fraction to the mean relationship and set the Bayesian priors on $r_{\rm disc}$ and $r_{\rm bulge}$ to be a Gaussian with mean given by Dutton et al. (2011) and a scatter of 0.5 dex (estimated from their fig. 4).

For the model HI surface density $\Sigma_{\rm HI}(r)$ we use the empirical relationship of Wang et al. (2016, henceforth W16), based on a sample of 500 mainly late-type galaxies with spatially resolved HI observations. They find

$$\log\left(D_{\rm HI}/{\rm kpc}\right) = 0.51\log\left(M_{\rm HI}/M_\odot\right) - 3.29, \tag{3.12}$$

with 0.06 dex of scatter, where $D_{\rm HI}$ is the diameter of the $1M_\odot/{\rm pc}^2$ isophote of $\Sigma_{\rm HI}$. W16 also find that for late-type galaxies, there is a homogeneous exponential profile in the outer parts with scale length $r_{\rm HI} = 0.1D_{\rm HI}$. Adopting this and equation (3.12) specifies the full $\Sigma_{\rm HI}(r)$. We also fit exponential profiles to the outer radii of the SPARC galaxies, and find a similar relationship.

Observed HI discs are not exponential all the way to the centre (Leroy et al., 2008; Wang et al., 2014, 2016). Many galaxies have HI cores or holes as the high density HI converts to H_2. The conversion is also dependant on metallicity and temperature, so varies

between galaxies (Bigiel & Blitz, 2012). Therefore we truncate $\Sigma_{\rm HI}(r)$ to have a maximum value $\Sigma_{\rm max}$, which is set by the requirement to reproduce the observed $M_{\rm HI}$. For the W16 model this gives $\Sigma_{\rm max} \approx 5\,{\rm M}_\odot$, which is consistent with observations. This truncated model is better at handling slowly rising RCs, where an unrealistic central peak in HI could overweight the velocities at low radius and thus cause W_{50} to be underestimated. However it is not very sensitive to the precise value of $\Sigma_{\rm max}$. Fig. 3.2 compares the model $\Sigma_{\rm HI}(r)$ to SPARC observations for a particular galaxy. Although the model is not a precise match, we see that this does not cause a large shift in W_{50} for a galaxy with a slowly rising RC. This is because the HI density towards the centre changes the flux and shape, but does not shift the position of W_{50}, which is mainly set by the outer, flatter part of the RC that forms the horns.

3.2.2.3 Inclination

The model circular speed $V_{\rm c}(r)$ must be corrected for inclination ($i = 0°$ face on); $i = 90°$ edge on) by a factor of $\sin(i)$. As ALFALFA does not resolve the HI disc, inclination is derived from optical photometry. Assuming axisymmetry, the relationship between intrinsic relative thickness q, observed axis ratio b/a and inclination is

$$\cos^2 i = \frac{(b/a)^2 - q^2}{1 - q^2}. \tag{3.13}$$

Typically b/a is obtained from infrared photometry, due to the lower extinction. However this light predominantly comes from older stars that do not reside in a thin disc. There is much discussion on q in the literature, and its variation with galaxy type. It is common to simply assume $q = 0.2$ for line width surveys (Zwaan et al., 2010), based on population studies of late-type galaxies (e.g. Unterborn & Ryden 2008). Based on colour, bulge fractions and Sérsic index the majority of the ALFALFA sample are late-type. However as baryonic mass increases (above $\sim 10^{10}\,{\rm M}_\odot$), there is an increasing population of galaxies in ALFALFA with properties more consistent with early-type galaxies. Dwarf galaxies are also observed to have thicker discs (Méndez-Abreu et al., 2010).

In view of the importance of, and uncertainty in, inclinations we consider three different models for it, ordered from least to most conservative:

1. Assume q=0.2 and derive i from equation (3.13) using the observed b/a and its uncertainty $\sigma_{b/a}$.

2. Give q a flat prior between 0.15 (the lowest b/a in the NSA) and the observed b/a of the galaxy. Then the prior on inclination is $\pi(i|b/a \pm \sigma_{b/a})$, as calculated from equation (3.13). We use this prior in our fiducial analysis as it is more conservative. However, assuming the true distribution of q for our sample is peaked at lower values, it will bias our results towards higher i and hence lower dynamical mass. This is because $b/a \leq 1$, so changing q has a bigger effect on the numerator of Eq. 3.13 than the denominator.

3. Simply assume the galaxies are randomly oriented. The angle between two random vectors in 3D is distributed as $\sin(i)$, so the prior on inclination is then $\pi(i) = \frac{1}{2}\sin(i)$.

For b/a we use the SERSIC_BA value from the NSA, which is calculated from single-component two-dimensional Sérsic fits to r-band photometry. In Fig. 3.5 we plot the SPARC kinematic inclinations against the NSA optical inclinations (with $q = 0.2$), for the 84 galaxies in both SPARC and the NSA. The kinematic inclinations are obtained from tilted-ring fits to the velocity fields, and so are expected to be more accurate.

There are a couple of extreme outliers. The optical inclination of UGC 07261 severely overpredicts the kinematic inclination. On inspection, its SDSS image shows it to be heavily barred, causing it to have a far lower b/a that does not reflect the stellar disc itself, which appears to be nearly face on. This could be mitigated by calculating b/a using outer isophotes only. However we find all other measures of b/a in the NSA, such as those based on Petrosian fits at radii containing 50% and 90% of the total light, produce less plausible inclinations across the whole sample.

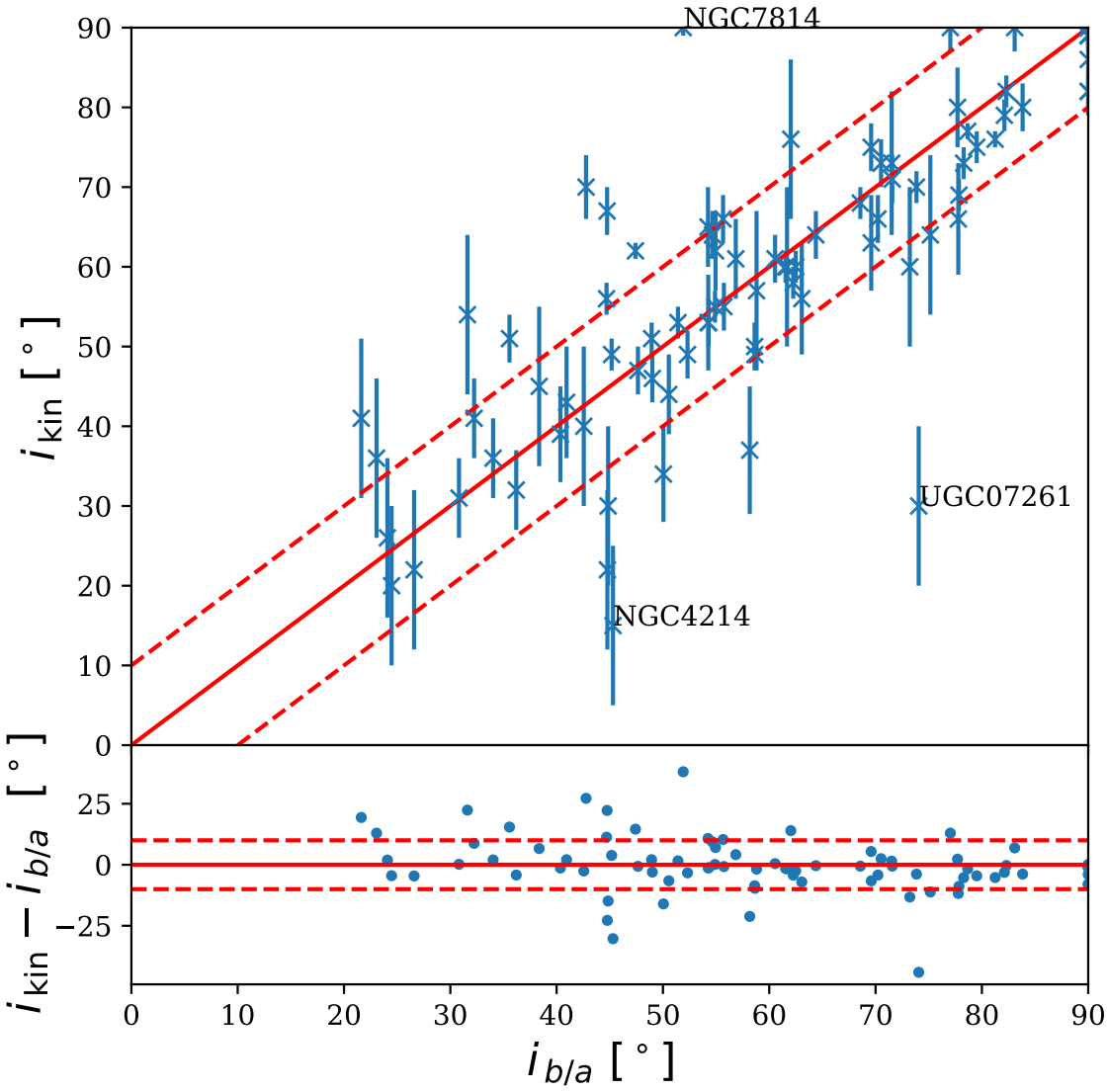

Figure 3.5: The inclinations from NSA r-band optical axis ratios assuming $q = 0.2$ ($i_{b/a}$) plotted against inclinations obtained from tilted ring fits to the resolved HI velocity field ($i_{\rm kin}$) for the SPARC sample. The solid red line shows equality, and the dashed red lines $\pm 10°$ disagreement. The subplot shows their residuals. Our fiducial model has a flat prior on q, so galaxies above the solid red line are accounted for in the scatter of the posterior probability on halo properties. We account for galaxies below the red line by adopting a 10% uncertainty on b/a.

The optical inclination of NGC 7814 is a severe underestimate of the kinematic value. The SDSS image reveals it to be an edge-on thin disk with an extremely prominent bulge, resulting in a high b/a. The flat prior on q in our fiducial model accounts for this, as $q = 1$ is appropriate for a bulge. In fact our fiducial model is flexible enough that it can account for any case where the optical inclination is an underprediction of the true value.

NGC 4214 is the most severe example of a galaxy where the inclination is overpredicted by the optical b/a due to the irregularity of the light distribution in its SDSS image. Irregularity has a tendency to make circular objects appear to have a lower b/a. To account for these galaxies, we adopt an uncertainty of 10% on b/a, which makes the SPARC kinematic and optical inclinations consistent within 2σ for all galaxies where the optical b/a overpredicts inclination, except for UGC 07261.

3.2.2.4 Likelihood

We compare our model line width to the observed line width by using Bayes' theorem to calculate the probability for the parameters θ given model $\mathcal{M}$ and data D,

$$\mathcal{P}(\theta|D,\mathcal{M}) = \frac{\mathcal{P}(D|\theta,\mathcal{M})\mathcal{P}(\theta|\mathcal{M})}{\mathcal{P}(D|\mathcal{M})}. \tag{3.14}$$

We choose the likelihood to be

$$\mathcal{P}(W_{50,\mathrm{obs}}|\theta,\mathcal{M}) = \frac{\exp\{-(W_{50,\mathrm{obs}} - W_{50})^2/(2\delta W_{50,\mathrm{obs}}^2)\}}{\sqrt{2\pi}\delta W_{50,\mathrm{obs}}}. \tag{3.15}$$

We also repeat the same inference, but imposing the mass–concentration relation (converted to $c_{0.1}$) derived from the Uchuu simulations (Ishiyama et al., 2021, equation 2) as a prior, with 0.11 dex log-normal scatter. This breaks the degeneracy between mass and concentration.

3.2.3 Abundance matching

In its simplest form, SHAM posits that the most massive (or brightest) galaxy forms in the most massive halo or subhalo, the second most massive galaxy in the second most

massive halo and so on (Kravtsov et al., 2004). When applied to a galaxy survey and an equivalently sized simulation box this yields a monotonic relationship between halo mass and galaxy mass. Conroy et al. (2006) showed that this simple non-parametric model could produce an excellent fit to galaxy clustering from the present day up to $z = 5$. The model has been extended to allow stochasticity through the SHAM scatter parameter σ_{AM}, which models both intrinsic scatter in the galaxy–halo connection and scatter from observational uncertainties in the galaxy mass or luminosity (Behroozi et al., 2010, henceforth BCW10). Halo assembly bias can be included in the SHAM framework by allowing secondary halo parameters such as concentration to affect the order in which galaxies are assigned to haloes (Reddick et al., 2013; Lehmann et al., 2016; Chaves-Montero et al., 2016; Stiskalek et al., 2021).

In SHAM the property used to rank galaxies is traditionally luminosity or stellar mass, as these quantities are readily available for the large samples required to calculate accurate abundance and correlation functions. In this work we use a SHAM model from ST21 (section 4.2) that is based on a sample of HI-selected galaxies, and instead ranks galaxies using their baryonic mass. This is possible as the galaxy sample is a crossmatch of NSA and ALFALFA, and hence contains both a stellar mass and HI mass for each galaxy. Baryonic mass is expected to be more fundamentally related to halo mass than stellar mass as star formation has only an indirect effect on galaxies' baryonic mass fractions. This is implied empirically by the Tully–Fisher relation and radial acceleration relation, both of which are tighter and more regular when plotted in terms of total cold baryonic mass rather than stellar mass.

To construct the galaxy baryonic mass function (BMF) we fit a Schechter function (Schechter, 1976)

$$\phi\left(M_{\rm bar}\right) = \ln(10)\phi_* \left(\frac{M_{\rm bar}}{M_*}\right)^{\alpha+1} e^{-\left(\frac{M_{\rm bar}}{M_*}\right)}, \tag{3.16}$$

where the fit parameters are M_*, ϕ_* and α, to the ALFALFA×NSA BMF of ST21 (plotted in their fig. 2). We remove the four lowest mass data points, as ST21 suggest that the

Table 3.2: The statistics we use to characterise and compare the 2D posteriors in halo mass and concentration from kinematics and AM.

Metric	Definition	Interpretation
$\mathcal{F}$	The fraction of the marginalised 1D $\log(M_{\rm vir})$ posterior probability from kinematics that lies in the region $\log(M_{\rm vir}) < \log(M_{\rm bar}) + 0.2$.	The extent to which a galaxy is compatible with having $M_{\rm vir} = M_{\rm bar}$ (i.e. $M_{\rm halo} = 0$). Galaxies with large observational uncertainties will have higher $\mathcal{F}$. We interpret $\mathcal{F} > 0.01$ as $M_{\rm halo} = 0$ not being excluded by W_{50}.
$\mathcal{O}$	The fraction of the marginalised 2D $\{M_{\rm vir}, c_{0.1}\}$ posterior probability from kinematics that lies inside the 2σ contour of the SHAM posterior.	The level of agreement between SHAM and kinematics. We interpret $\mathcal{O} < 0.01$ as the two models being in tension.
$\mathcal{I}$	$\left[\frac{\sigma_{\rm AM}}{\sigma_{\rm AM+KIN}} - 1\right]$, where $\sigma_{\rm AM}$ is the size of the 1σ contour of the marginalised 1D $M_{\rm vir}$ posterior for AM, and $\sigma_{\rm AM+KIN}$ is the same quantity for the combined posterior of SHAM and kinematics.	The improvement in the constraint on $M_{\rm vir}$ obtained when combining kinematics with SHAM, compared to SHAM alone. $\mathcal{I} = 0$ corresponds to no improvement and $\mathcal{I} = 1$ to a constraint that is twice as tight.

faint end is biased by incomplete treatment of selections effects. The derived BMF, which we plot in Fig. 3.6, has parameters $\alpha = -1.24 \pm 0.02$, $\log(M_* h^2/M_\odot) = 10.20 \pm 0.02$ and $\phi^* = 3.3 \pm 0.2 \times 10^{-3} h^3 \mathrm{Mpc}^{-3} \mathrm{dex}^{-1}$ (with α and ϕ_* anti-correlated with M_*). The uncertainty on the BMF (which is dominated by α) does not significantly impact the assignment of galaxies to haloes in the mass range probed by ALFALFA, and so is not propagated through our analysis. We find the fitted value of α is in good agreement with that of the ALFALFA HIMF derived by Jones et al. (2018), which is unhampered by selection effects induced by the ALFALFA×NSA crossmatch.

For the SHAM proxy, haloes are first selected that have a peak-mass redshift below a certain value $z_{\rm cut}$, and then ranked by their present-day $M_{\rm vir}$. The $z_{\rm cut}$ parameter allows the model to reproduce the weaker clustering of HI-selected samples with lower $\sigma_{\rm AM}$. ST21 found $z_{\rm cut} = 0.22^{+0.4}_{-0.2}$ and $\sigma_{\rm AM} = 0.42^{+0.8}_{-0.2}$ dex from clustering constraints. We use these maximum likelihood values in our fiducial model. These uncertainties are also not propagated, as discussed further in Section 3.4.3.

The basic abundance matching procedure links each halo in the catalogue to a galaxy baryonic mass as follows:

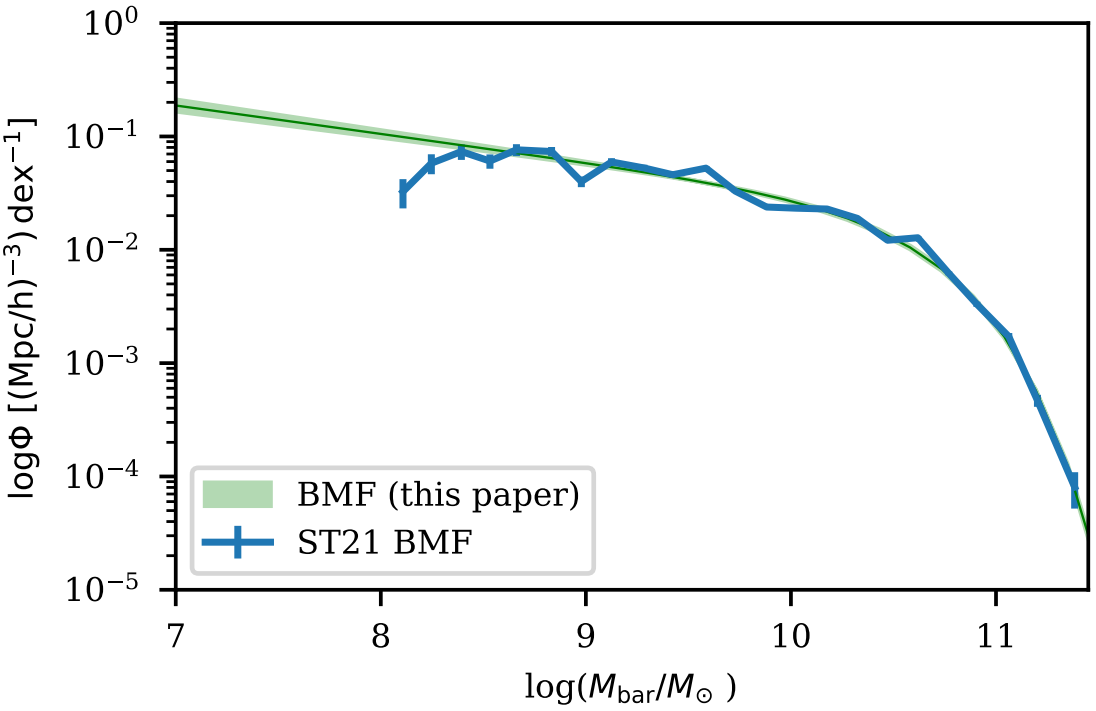

Figure 3.6: The baryonic mass function (BMF) used in the abundance matching analysis (green line), derived by fitting a Schechter function to the ST21 BMF (blue). The four lowest mass data points are not included in the fit, as the faint end is potentially biased by incomplete treatment of selection effects (ST21). The shaded band shows the 1σ uncertainty.

1. Deconvolve the galaxy mass function with the chosen SHAM scatter (BCW10).

2. Remove haloes with a peak formation time before the redshift $z_{\rm cut}$.

3. Rank haloes by the proxy (in our case $M_{\rm vir}$).

4. Assign a baryonic mass to each halo by matching abundances as described above.

5. Add the SHAM scatter according to the prescription of BCW10.

We repeat this process 500 times, thereby assigning 500 $M_{\rm bar}$ to each halo in the catalogue. We bin the haloes onto a grid of $M_{\rm vir}$ and $c_{0.1}$, and use kernel density estimation to calculate the 1D probability distribution $P(M_{\rm bar}|M_{\rm vir}, c_{0.1})$ for each bin. The probability distributions are then interpolated over the entire space of $\{M_{\rm vir}, c\}$. As our proxy is simply $M_{\rm vir}$ after $z_{\rm cut}$ preselection, the probability is actually independent of $c_{0.1}$ here. We show examples in Fig. 3.7. The posterior probability that the halo of a galaxy has parameters $\{M_{\rm vir}, c_{0.1}\}$, given that it is observed to have baryonic mass $M_{\rm bar,obs} \pm \delta M_{\rm bar,obs}$, is

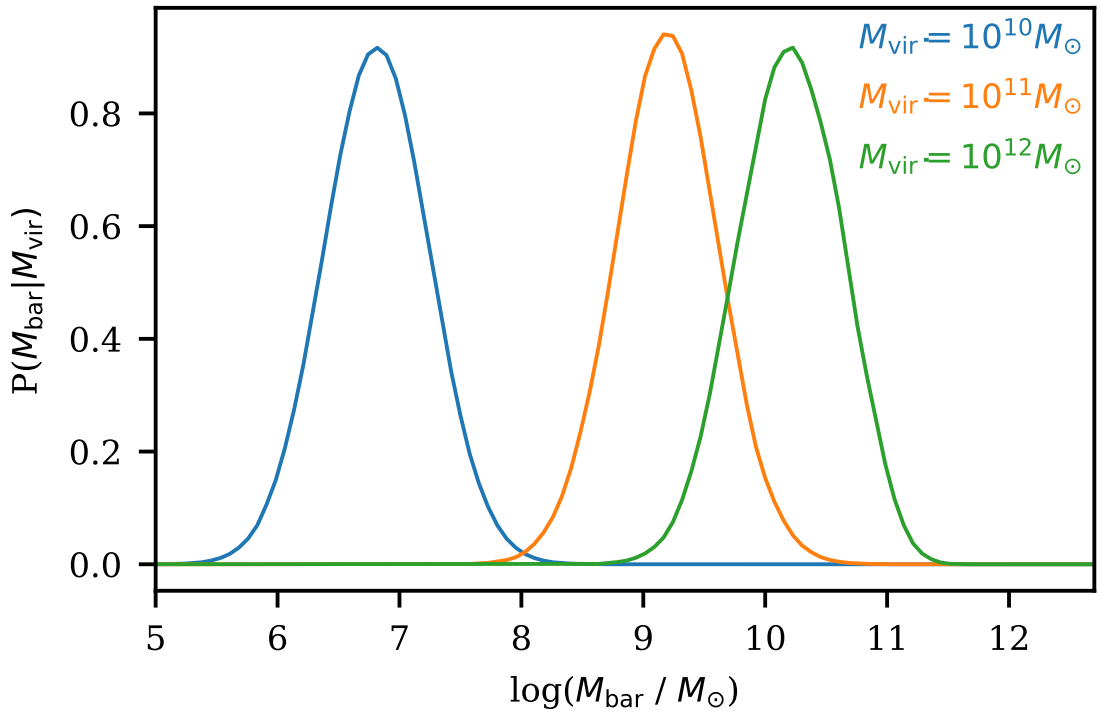

Figure 3.7: Probability distributions $P(M_{\rm bar}|M_{\rm vir})$ for different values of $M_{\rm vir}$, calculated from an ensemble of abundance matching catalogues. These form the likelihood in our Bayesian inverse abundance matching method (Section 3.2.3). The width of the distributions corresponds to the scatter in baryonic mass at fixed halo mass, which is ~ 0.4 dex in our model (which is higher than in canonical AM models based on optically-selected samples). The $M_{\rm vir} = 10^{12}\,{\rm M}_\odot$ distribution is slightly skew, as this mass samples the turnover in the stellar-mass-to-halo mass relationship.

$$P(M_{\rm vir}, c_{0.1}|M_{\rm bar,obs}) = \frac{P(M_{\rm bar,obs}|M_{\rm vir}, c_{0.1})P(M_{\rm vir}, c_{0.1})}{P(M_{\rm bar,obs})}. \tag{3.17}$$

The likelihood for the observed baryonic mass is connected to the likelihood for the "true" $M_{\rm bar}$ from abundance matching by

$$P(M_{\rm bar,obs}|M_{\rm vir}, c_{0.1}) = \int_0^\infty P(M_{\rm bar,obs}|M_{\rm bar})P(M_{\rm bar}|M_{\rm vir}, c_{0.1})\, dM_{\rm bar}, \tag{3.18}$$

where

$$P(M_{\rm bar,obs}|M_{\rm bar}) = \frac{1}{\sqrt{2\pi}(\delta M_{\rm bar,obs})} e^{-\frac{(M_{\rm bar,obs}-M_{\rm bar})^2}{2(\delta M_{\rm bar,obs})^2}}. \tag{3.19}$$

The prior $P(M_{\rm vir}, c_{0.1})$ is the 2D probability density function in $\{M_{\rm vir}, c_{0.1}\}$ for all haloes in the simulation.

3.2.4 Inference methods and analysis of posteriors

We generate the posterior probability distributions using the `emcee` ensemble sampler (Foreman-Mackey et al., 2013). We initiate the sampler with 200 walkers and use the stretch move $a = 2$. We run a small sample of galaxies until the strict $\tau > 50$ autocorrelation time convergence condition is reached. For the whole sample we use only 10,000 steps, which for most galaxies does not reach $\tau = 50$, but we check our posteriors are unaffected using the galaxies with fully converged chains. We remove the first 5000 steps as burn-in. The acceptance fraction is ~0.15. We rerun a subsample of galaxies with `Multinest` to check our results are not dependant on the choice of sampler. We place a flat prior on $\log(M_{\rm vir}/\,{\rm M}_\odot)$ between $\log(M_{\rm bar})$ and 15.5, corresponding to an extremely massive cluster. We sample in $\log(c_{0.1})$, with a flat prior between a lower bound corresponding to the smallest value $c_{0.1}$ can take for an NFW halo, and an upper bound of 2, as there are extremely few haloes in the Uchuu simulation with higher concentration.

In Table 3.2 we define a number of metrics to summarise and compare the posteriors produced by SHAM and kinematics. We quantify the extent to which the posterior is compatible with $M_{\rm halo} = 0$ using the $\mathcal{F}$ metric. It is defined as the fraction of the posterior

for which $\log(M_{\rm vir}) < \log(M_{\rm bar}) + 0.2$, with 0.2 chosen because it is the uncertainty on M_*, which is typically much larger than the uncertainties on $M_{\rm HI}$ and so is roughly the maximum uncertainty on $M_{\rm bar}$.

The tension between the SHAM and kinematics posteriors is quantified by the the overlap metric O, the fraction of the kinematics posterior that lies inside the 2σ contour of the SHAM posterior. We interpret two posteriors as being in tension if O¡0.01, roughly corresponding to a 2σ disagreement. We choose 0.01 (rather than 0.05) so small posteriors that overlap with much larger posteriors are not considered to be in tension. This statistic is easy to calculate from the posteriors and can easily handle a variety of shapes of the kinematics posterior, at the price of a nontrivial interpretation. Like other assessments of tension such as the Bayesian evidence, this method is sensitive to the choice of prior. Two posteriors that overlap perfectly will also be considered more in tension if one of them is very wide. In this sense O measures the similarity of the two posteriors along the lines of the Bhattacharyya distance (Bhattacharyya, 1946). We avoid using Bayes factors to evaluate tension, because commonly used samplers may not evaluate the evidence correctly for posteriors with plateaus and shallow likelihoods, which are common for our kinematic model (Schittenhelm & Wacker 2021; Fowlie et al. 2020; although see Fowlie et al. 2021 for a solution). To ensure O is calculated accurately we check that the 2σ contours have converged with respect to chain length, and we use a large number of samples (1,000,000) so the tails of the distributions are well resolved.

The metric $\mathcal{I}$ quantifies the tightening of the constraint on $M_{\rm vir}$ from combining kinematics with SHAM. It is defined relative to the SHAM constraint alone because this tends to be significantly tighter than the kinematic constraint, and because it is more common to have photometric than spectroscopic measurements. We compare in $M_{\rm vir}$ rather than $M_{\rm vir}$–$c_{0.1}$, because $M_{\rm vir}$ and $c_{0.1}$ are highly degenerate in the kinematic inference. We check that using a different contour, e.g. 2σ, or using the Kullback–Leibler divergence as a measure of information content, leads to the same conclusions. We redefine the SHAM likelihood to

include the prior, so it can have the same flat prior on $M_{\rm vir}$ and $c_{0.1}$ as the kinematic model. Then the combined posterior can be obtained by direct multiplication of the two separate posteriors, due to the assumption of independence.

3.3 Results

3.3.1 Individual posteriors

3.3.1.1 Idealised dark matter-only inference

To understand the posterior shapes for the kinematic model, it is instructive to consider first the case of a single galaxy where we assume the potential is sourced purely by the dark matter, and the galaxy parameters (i, M_*, $r_{\rm HI}$ etc.) are perfectly known. This leaves $M_{\rm vir}$ and $c_{0.1}$ as the only free parameters and δW_{50} the only source of uncertainty. We apply this to AGC 742791 and show the posterior in Fig. 3.8 for different assumed values of $r_{\rm HI}$ and i. The elongated posterior is due to the perfect degeneracy between mass and concentration; the same line width can be sourced by a high mass halo with a low concentration or vice versa. What matters to first order is the dynamical mass contained within the gas disc that contributes to the rotational velocity. As there are no additional parameters to marginalise over, the posteriors are the locus in the mass–concentration plane required to produce the observed W_{50}, broadened by the observational error δW_{50}.

The naive model $W_{50} = 2V_{\rm max}$, where $V_{\rm max}$ is the maximum circular speed of the halo, is only equal to our full model for values of $c_{0.1}$ where $V_{\rm max}$ occurs at a similar radius to $r_{\rm HI}$. When $V_{\rm max}$ occurs at a larger radius than $r_{\rm HI}$ more halo mass is required to produce the same W_{50}, so our model posterior curves to the right of the $2V_{\rm max}$ posterior. This effect is more pronounced at low values of $r_{\rm HI}$ and $c_{0.1}$, where $V_{\rm max}$ occurs at a larger radius. Conversely, when $V_{\rm max}$ occurs at a much smaller radius than $r_{\rm HI}$ there is a large contribution to the HI spectral line from the gradually decreasing part of the rotation curve beyond $V_{\rm max}$, which

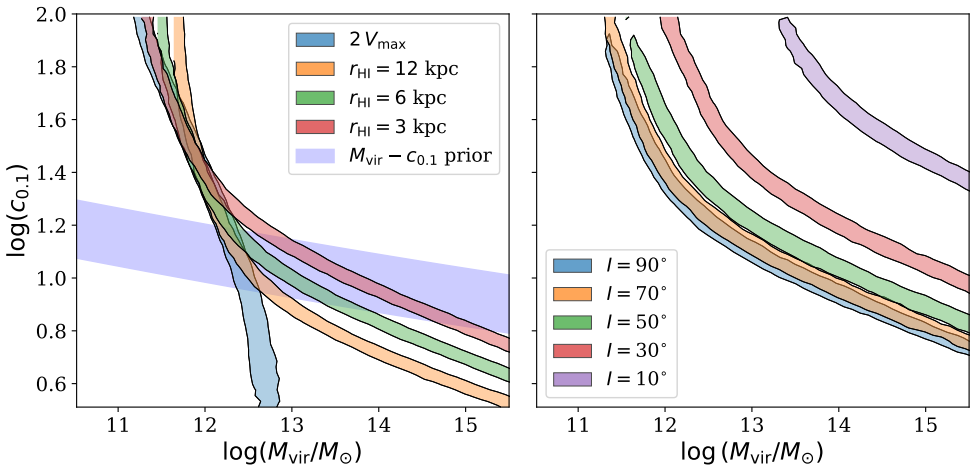

Figure 3.8: The posterior for AGC 742791 ($W_{50} = 428 \pm 25$ km s^{-1}), obtained by assuming the line width is only sourced by the DM, and with no uncertainty on inclination or the gas disc size r_{HI}. The contours show the 1-sigma region, which has width only due to the uncertainty on the line width. In the left panel r_{HI} is varied. We also show the simple model where $W_{50} = 2\,V_{max}$, where V_{max} is the maximum circular velocity of the dark matter halo, and the mass–concentration prior. As the size of the gas disc decreases and probes a smaller radius, the posterior deviates further from the $2\,V_{max}$ model. In the right panel r_{HI} is fixed and the inclination i is varied.

biases W_{50} to lower values. More mass is required at a given concentration to produce the observed W_{50}, so once again our posterior curves to the right of the $2V_{max}$ case, with the effect more pronounced for higher values of r_{HI} and $c_{0.1}$ (the effect is only significant at extreme $c_{0.1}$). Adding baryons to the idealised model would shift the posteriors to the left, as less DM is required to generate the observed W_{50}.

The right hand panel of Fig. 3.8 shows the posterior for our idealised model at different assumed inclinations. At high inclination the $\sin i$ correction to W_{50} is slowly changing, so as inclination decreases the posterior slowly sweeps to higher mass/concentration. As i decreases the posterior sweeps to higher mass and concentration at an increasing rate. Therefore our 'randomly distributed' inclination model (3) would have a posterior with have a sharp peak at the $i = 90°$ region, with a long tail all the way to the high M_{vir} and $c_{0.1}$ prior boundary at low values of i. For our fiducial inclination model (2), with a flat prior on intrinsic relative thickness q, the minimum inclination occurs at $q = 0.15$, where the inclination probability also peaks. Hence there is a competing effect between the peak

in inclination probability at the lowest value of inclination, and the peak in the 2D posterior corresponding to $i = 90°$ described above. For the simple $q = 0.2$ model (1), the uncertainty on inclination is only due to the uncertainty on b/a, so the posterior is a band.

3.3.1.2 The full model

The output of our model for a single galaxy is the posterior probability distribution on the two halo parameters $M_{\rm vir}$ and $c_{0.1}$ for both the SHAM and kinematic model, as well as the six galaxy parameters for kinematics (listed in Table 3.1). We also calculate the joint posterior of both models. Our kinematic model puts Gaussian priors on all galaxy parameters (except inclination), with the width set by the observational or empirical model uncertainty. The line width does not further constrain these galaxy parameters beyond their priors in most cases, so only the 2D and 1D posteriors on $M_{\rm vir}$ and $c_{0.1}$ are of primary interest. Inclination i is sometimes prevented from taking on very low values (face-on) if this would cause too high an intrinsic line width, requiring a dark matter halo with $M_{\rm vir}$ or $c_{0.1}$ beyond the prior boundaries. It can also be prevented from taking on high values (edge-on), as for some galaxies this would make the intrinsic line width so low that the circular velocity from the baryons alone exceeds it. However the galaxy parameters are still important, as the uncertainty on them broadens the posteriors on halo properties, often dramatically. For example the high-end tail of the prior on M_* can cause the $M_{\rm vir}$ posterior to have a significant tail to low values.

When we apply the real kinematic model to the whole ALFALFA sample, the resulting 2D posteriors on $M_{\rm vir} - c_{0.1}$ vary greatly between galaxies. In Fig. 3.9 we show the posteriors for a selection of galaxies to illustrate this diversity, as well as their $\mathcal{F}, O$ and $\mathcal{I}$ metrics (see Table 3.2 for definitions). The kinematics posterior of AGC 724223 (first panel) is most similar to the theoretical example above. Its W_{50} is large enough relative to $M_{\rm bar}$ that the baryonic contribution to the dynamical mass within the gas disc is subdominant to DM across the whole range of galaxy priors. Its b/a is small, so there is a narrow prior on

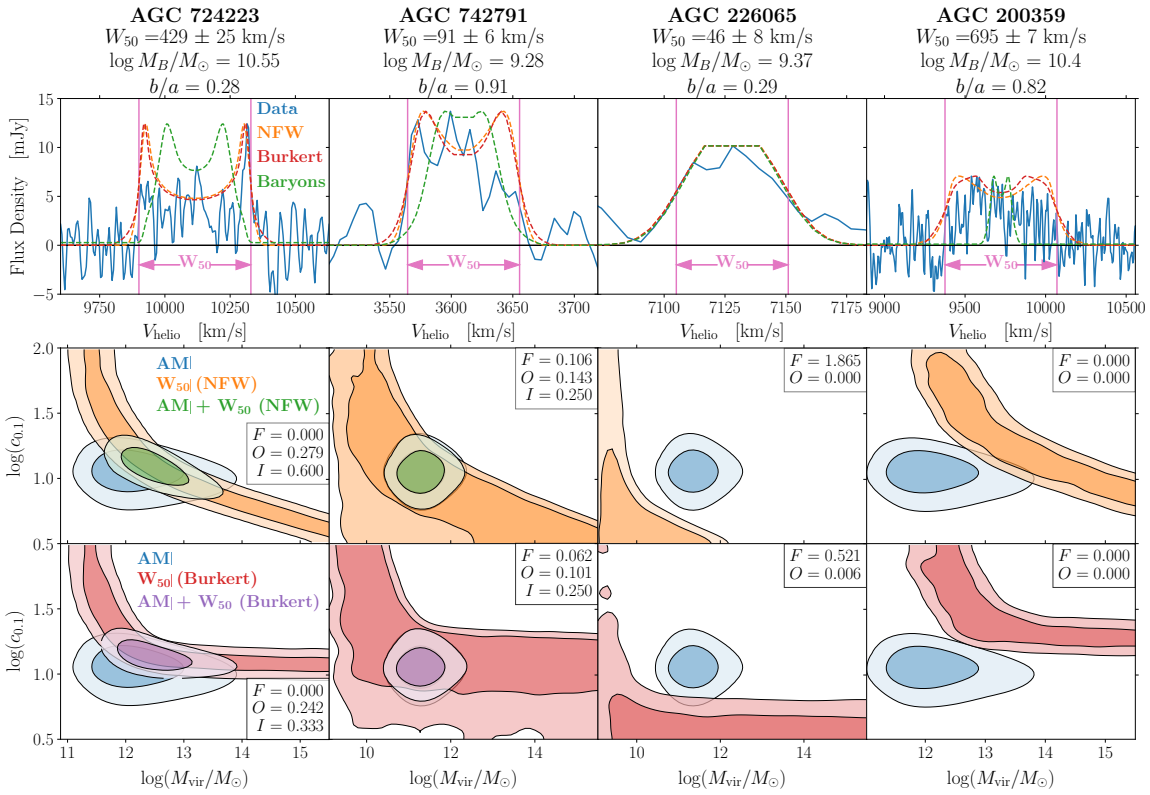

Figure 3.9: Results for four representative galaxies. From left to right: i) one with a well-constrained DM distribution from kinematics consistent with SHAM, ii) a poorly-constrained distribution consistent with SHAM, iii) an apparently DM-free galaxy and iv) a galaxy with a more massive halo predicted from W_{50} than expected from SHAM. *Top:* The raw ALFALFA spectra, with our best-fit model using an NFW and Burkert halo profile. We also show the line profile generated by the baryons only, which is calculated using the mean of the priors on the galaxy parameters. The normalisation of the model fluxes is arbitrary. As we are only fitting to W_{50} (and not the full flux profile), the best fit model is not necessarily a good match to the spectrum, often due to asymmetries. In Chapter 5 we investigate fitting the full spectrum. *Bottom:* Posteriors on halo mass and concentration from SHAM, kinematics assuming NFW (upper) or Burkert (lower) profiles, and their combination (1 and 2σ isoprobability contours shown). The inset lists the $\mathcal{F}$, $\mathcal{O}$ and $\mathcal{I}$ summary statistics (see Table 3.2). We only combine the kinematics and SHAM posteriors in the first two cases where they are not in tension.

inclination that does not greatly broaden the posterior. It has $\mathcal{F} = 0$, because $M_{\rm halo} = 0$ is strongly disfavoured. AGC 742791 (middle right panel) is the opposite case – the observed W_{50} can be explained with negligible DM within the priors on the baryonic component; it can only have a DM halo of significant mass if $c_{0.1}$ is so low that most of the halo mass sits outside of the gas disc. This results in much higher values of $\mathcal{F}$. AGC 742791 is an example between these two extremes. Some region of the priors on galaxy parameters are compatible with having little DM within the gas disc, as shown by the 2σ contour extending down to the baryonic mass of the galaxy. The weak constraints are in large part driven by its high b/a, which results in a broad prior on inclination. AGC 200359 (far right panel) also has a high b/a, but its W_{50} is very large relative to $M_{\rm bar}$, so the kinematic constraints are still relatively tight. The posterior strongly disfavours $M_{\rm halo} = 0$, so $\mathcal{F} = 0$.

Fig. 3.9 also shows the difference between the NFW and Burkert profiles. A higher halo mass is required for the cored Burkert profile to generate the same W_{50} as the cuspy NFW profile. The bend in the banana shape is much more pronounced for the Burkert profile, going almost completely horizontal below a certain concentration for each galaxy, meaning a large range of halo masses generates the same line width at a fixed concentration. The cored Burkert profile has a much more slowly rising circular velocity profile than NFW, so for typical concentrations the larger halo mass does not become apparent until radii larger than the extent of the gas disc. This effect is illustrated in Fig. 3.10.

For all galaxies, the SHAM posterior occupies a constrained region with a defined peak. Towards low mass there is a sharp drop to zero probability, with longer tails to high $M_{\rm vir}$, high $c_{0.1}$ and low $c_{0.1}$. The SHAM posteriors vary smoothly with $M_{\rm bar}$, as it is the only galaxy property that the model depends upon (the additional scatter on halo parameters due to the observational uncertainty on $M_{\rm bar}$ is subdominant to the SHAM model's intrinsic scatter). In particular the posterior smoothly decreases in size in the $M_{\rm vir}$ dimension as $M_{\rm bar}$ decreases (compare the third and fourth columns of Fig. 3.9). This is due to the differing slopes of the BMF and HMF, meaning that the scatter $\sigma(M_{\rm vir}|M_{\rm bar})$ increases towards higher mass,

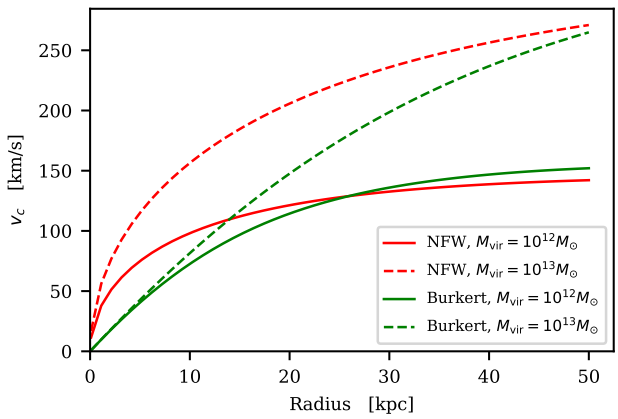

Figure 3.10: The circular velocity of a dark matter halo with $c_{0.1} = 10$ for difference masses and halo profiles. For the Burkert profile, increasing the halo mass by a factor of 10 results in very little change in circular speed within 20 kpc. For NFW the difference is much more pronounced. This explains why increasing the mass of Burkert haloes that are below a certain concentration only slowly increases the predicted line width, and hence why Burkert masses are poorly constrained.

even though the SHAM scatter parameter $\sigma_{\rm AM} = (M_{\rm bar}|M_{\rm vir})$ is constant. This also results in an asymmetric posterior: a galaxy of a given $M_{\rm bar}$ is assigned to a long tail of high mass haloes. We discuss the effect of SHAM scatter further in Section 3.4.3. The distribution of $c_{0.1}$ in the SHAM posterior corresponds to the mass–concentration relationship of haloes that survive the formation time cut, which have a lower mean concentration at a given mass than the whole catalogue.

The galaxies in Fig. 3.9 are ordered from least in tension to most in tension. For the first two panels SHAM and kinematics are in good agreement, so $\mathcal{O}$ is high. Therefore we combine the SHAM and kinematic posteriors, which leads to a significant tightening in the constraints for AGC 724223 due to its tighter kinematic constraint (and wider SHAM constraint due to the higher $M_{\rm bar}$), whereas there is no improvement for AGC 742791. For AGC 226065 a very low dynamical mass is inferred from W_{50}, causing tension with AM. The tension is less severe with the Burkert profile, as it is possible to have a larger $M_{\rm vir}$ whilst keeping the dynamical mass inside the gas disc the same. For cases where SHAM and kinematics are in tension ($\mathcal{O}$¡0.01), we do not combine the posteriors.

3.3.2 Population behaviour

3.3.2.1 $M_{\rm bar} - M_{\rm vir}$ relationship

We now derive a $M_{\rm bar} - M_{\rm vir}$ relationship from our modelling of the HI line width and AM. We do this by stacking the 1D posteriors on $M_{\rm vir}$ in bins of $M_{\rm bar}$ with 0.25 dex width, applying the mass–concentration prior to break the degeneracy of those parameters. The result is shown in Fig. 3.11. The previously discussed gradual variation in the size and asymmetry of the AM posterior in $M_{\rm vir}$ as $M_{\rm bar}$ changes is clearly visible. The kinematic relations have high scatter due to the significant fraction of galaxies for which there is very little constraint on $M_{\rm vir}$ (e.g. the second panel of Fig. 3.9). For the Burkert profile the stacked posteriors extend all the way to the upper limit of the prior, due to the cored profile causing a long tail to high mass in most galaxies (e.g. the right panel of Fig. 3.9), which overlaps with the mass–concentration prior.

Despite the large scatter, the mode of the posterior contains important information about the $M_{\rm bar} - M_{\rm vir}$ relationship implied by HI kinematics. It is stable to random resampling for bins with more than ~150 galaxies. Above $M_{\rm bar} = 10^{9.5}\,{\rm M}_\odot$, the NFW and Burkert relationships modes are similar, while towards lower mass the NFW mode diverges from the SHAM mode to a much lower $M_{\rm vir}$. The Burkert bends away from the SHAM mode in the other direction, but becomes extremely close to it again for the lowest $M_{\rm bar}$ bins. For NFW the slope of the $M_{\rm bar} - M_{\rm vir}$ relationship is much shallower than for AM, and is even compatible with a constant $M_{\rm bar}/M_{\rm vir}$. For NFW, the mean and median of the distribution in each bin are similar to the mode. However due to the long tail to high $M_{\rm vir}$ for Burkert, the mean and median are different to the mode, and are dependant on the upper bound of the prior. This makes the mode the more robust statistic.

The stacked intervals are very wide for Burkert kinematics, as many individual galaxies have $M_{\rm vir}$ that are poorly constrained by W_{50}. The divergence between NFW kinematics and SHAM at low baryonic mass is caused by the substantial population of galaxies with low

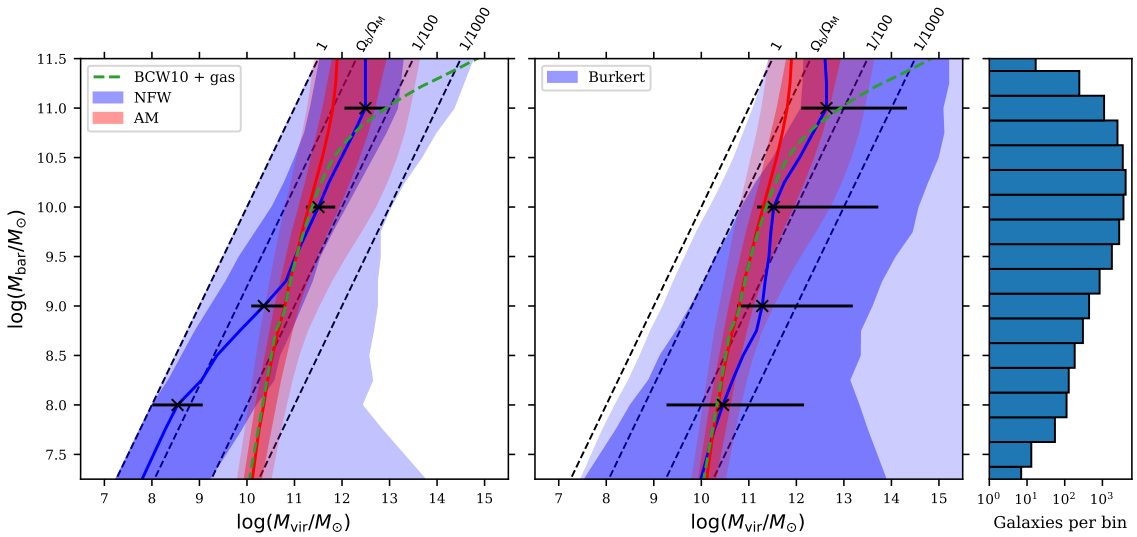

Figure 3.11: The baryonic mass–halo mass relation formed by stacking the 1D marginalised posteriors on $M_{\rm vir}$ in 0.25 dex bins of baryonic mass, for kinematics (blue) and SHAM (red). For kinematics, the mass–concentration prior is applied. The solid line shows the mode of the stacked distribution in each bin, and the shaded regions the 1 and 2σ isoprobability contours. 'BCW10+gas' shows the best-fit SHAM relationship from Behroozi et al. (2010), which is derived for optically-selected galaxies, converted to baryonic mass using the mean gas fraction in each bin for the ALFALFA galaxies. Black points show the average per-galaxy uncertainties $M_{\rm vir}$ at given $M_{\rm bar}$; that these errorbars are much smaller than the width of the blue band shows that this is driven mainly by variations between galaxies in a bin. The diagonal dashed lines show constant $M_{\rm bar}/M_{\rm vir}$ as indicated at the top.

line widths given their baryonic mass, which seem to have little if any dark matter within the radius probed by their gas disc (e.g. 3rd column of Fig. 3.9).

The large scatter of the kinematic relations derive from a combination of per-galaxy uncertainty on M_{vir} and an offset of the M_{vir} posteriors of different galaxies in a given M_{bar} bin. To investigate this, we show in black in Fig. 3.11 the per-galaxy uncertainties for four M_{bar} bins: the points are at the stacked modal M_{vir} and the errorbars show the average over all galaxies in the bin of the distance between the mode and the lower/upper 1σ interval of each individual galaxy posterior. Their size is a much weaker function of M_{bar} than the stacked intervals, showing that the flaring in the blue band at low M_{bar} is driven by increased scatter in M_{vir} *between* galaxies at fixed M_{bar}, rather than increased uncertainties for particular galaxies.

To see how much the relationship is tightened when the galaxies with the weakest constraints are removed, and to check its robustness, we consider a quality cut to the data (Code 1 galaxies only; SNR $>$ 10; $\delta W_{50}/W_{50} < 0.1$; $b/a < 0.7$, which corresponds to $i \approx 45$ for $q = 0.2$), and recalculate $M_{bar} - M_{vir}$ using the remaining 4232 galaxies. The mode and shape of the confidence intervals are unchanged, except for bins with few galaxies after the cut ($M_{bar} < 10^{8.25}\,M_\odot$). The mean width of the 1σ region is 30% smaller for NFW after the cut, but the posterior still reaches the prior bound for Burkert.

3.3.2.2 Compatibility with $M_{vir} = 0$

60% of galaxies in the sample have $\mathcal{F} < 0.01$ for both Burkert and NFW; the other 40% have posteriors that are compatible with $M_{halo} = 0$. To investigate which galaxy properties this depends upon, we trained a Random Forest Classifier (Pedregosa et al., 2011) on the sample for the binary classification $\{\mathcal{F} < 0.01, \mathcal{F} > 0.01\}$, optimising its hyperparameters using 3-fold cross-validation. As our labels are roughly balanced, we assess accuracy using the fraction of correctly predicted labels. To select important features we use the method of Stiskalek et al. (2022, section 3.6), in which galaxy properties are added sequentially to the

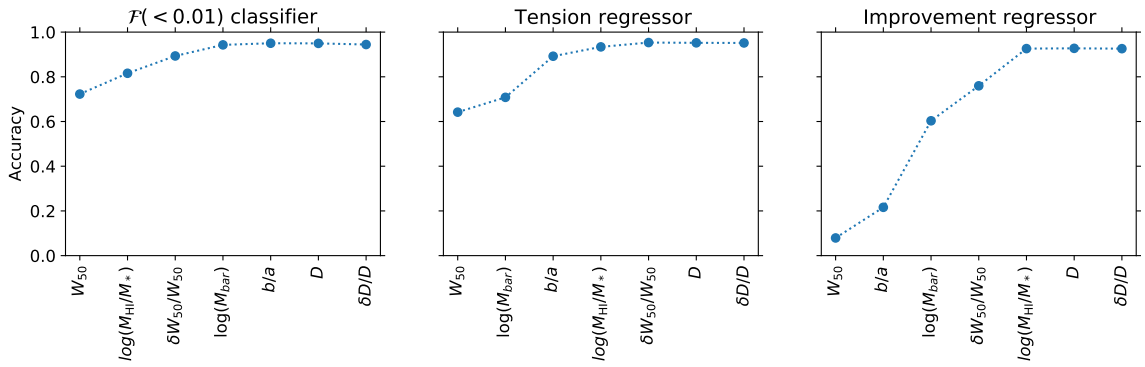

Figure 3.12: The test set accuracy of the random forest as a function of the cumulative number of features used to predict the posterior metrics $\mathcal{F}$ (left column), tension $\mathcal{O}$ (middle) and improvement $\mathcal{I}$ (right column) (see Table 3.2 for definitions). We use random forest regressors for $\mathcal{O}$ and $\mathcal{I}$, and a binary classifier for $\mathcal{F}$ on the condition $\mathcal{F}(< 0.01)$, because its distribution is sharply peaked at $\mathcal{F} = 0$. Features are added from left to right in the order that maximises the increment in accuracy, as described in section 3.3.2.2. Accuracy is measured by the fraction of correctly predicted labels for the classifier, and by R^2 (equation 3.20) for the regressors. We see that W_{50} is the most predictive galaxy property for $\mathcal{F}$ and $\mathcal{O}$, giving reasonable accuracy even when it alone is used to the train the random forest. No galaxy property is predictive on its own for $\mathcal{I}$, but together W_{50}, b/a, $M_{\rm bar}$, $\delta W_{50}/W_{50}$ and $M_{\rm HI}/M_*$ yield good accuracy. D and its fractional error add no new information in any case, as would be expected. The results shown are for the NFW profile, but very similar results are obtained with the Burkert profile.

set of features used to train the random forest. At each increment, the next feature added is the one that generates the greatest improvement in accuracy when combined with the current set of features. This produces a list of features, ordered from most to least important, and the new accuracy after their inclusion. This method of identifying important features avoids ambiguities associated with highly correlated features because the improvement is conditioned on some set of features already being used. The result is shown in the left panel of Fig. 3.12. For the $\mathcal{F}$ statistic the most important galaxy property is W_{50}, with a much smaller dependence on $\delta W_{50}/W_{50}$, $\log(M_{\rm HI}/M_*)$ and $M_{\rm bar}$.

The top panel of Fig. 3.13 correlates $\mathcal{F}$ with various galaxy properties, and the bottom panel correlates these properties with W_{50}. $\mathcal{F}$ is a strong function of W_{50}, with $\mathcal{F} > 0.01$ for nearly all galaxies in the lowest W_{50} bin. We use the reduced residual method to remove the dependence on W_{50}, and find the residuals of $\delta W_{50}/W_{50}$, $M_{\rm bar}$, b/a, n correlate positively

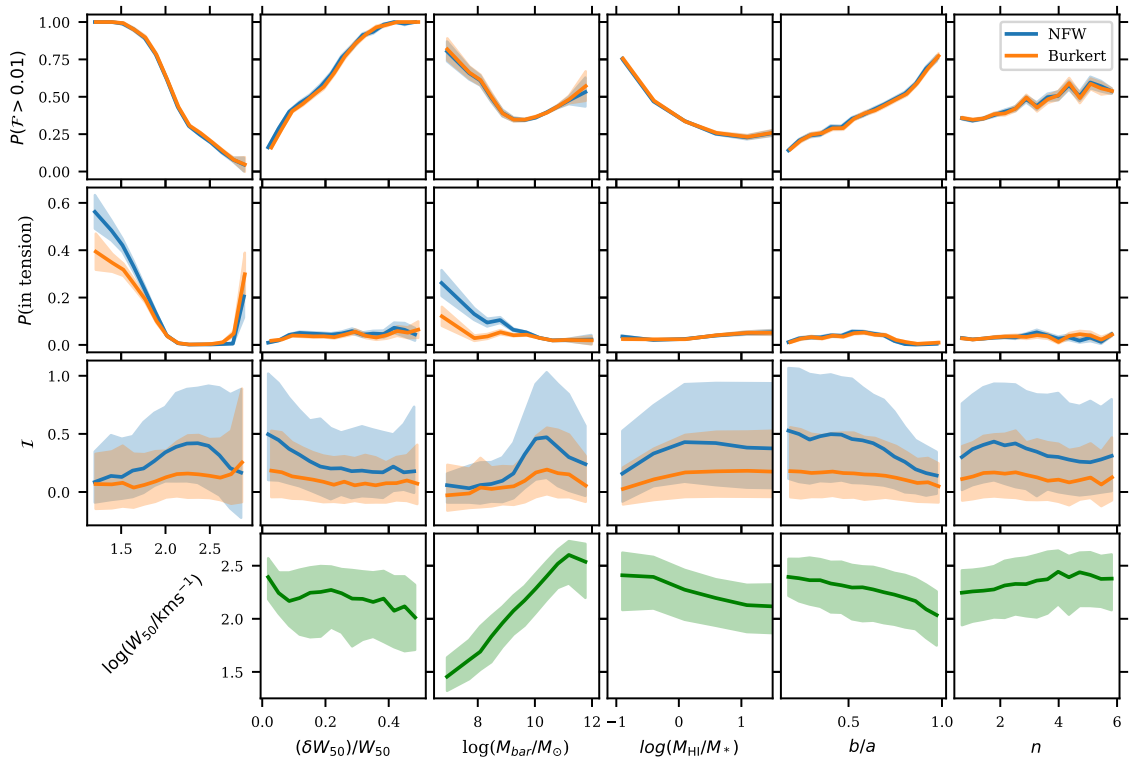

Figure 3.13: The correlation of galaxy parameters with the $\mathcal{F}$, $\mathcal{O}$ and $\mathcal{I}$ metrics, and with the ALFALFA line width W_{50}. The top two panels show the fraction of galaxies in each bin for which $M_{\rm halo} = 0$ is not excluded by kinematics ($\mathcal{F} > 0.01$, top panel) or exhibit tension between SHAM and kinematics ($\mathcal{O} < 0.01$, second panel). The shaded bands show the 1σ uncertainties calculated by bootstrap resampling each bin. The bottom two panels show the median (solid line) of $\mathcal{I}$ and $\log W_{50}$, with the shaded region showing the 1σ variation between the galaxies in each bin. We initially set 15 bins in each plot, then merge the outermost bins if there are fewer than 10 galaxies in one of them. We show the correlation of each quantity with W_{50} because we saw in Fig. 3.12 that this was the most important quantity for determining $\mathcal{F}$, $\mathcal{O}$ and $\mathcal{I}$. Galaxy parameter values that give tighter constraints (low δW_{50}, high gas fraction, low b/a, high W_{50}) produce low values of $\mathcal{F}$ and high values of $\mathcal{I}$. Tension is most prevalent at low W_{50} and low $M_{\rm bar}$, and is higher for NFW than Burkert.

with $P(\mathcal{F} < 0.01)$, and the residuals of $\log(M_{\rm HI}/M_*)$ anti-correlate. These are all as expected: higher values of $\delta W_{50}/W_{50}$ and b/a give weaker constraints and therefore higher $\mathcal{F}$; higher gas fractions result in tighter constraints and hence lower $\mathcal{F}$, as a larger $M_{\rm HI}$ means a larger $r_{\rm HI}$, so W_{50} probes further into the halo at fixed $M_{\rm bar}$; higher $M_{\rm bar}$ galaxies have a lower mean gas fraction and higher n, leading to weaker constraints.

3.3.2.3 Agreement between SHAM and kinematics

In Fig. 3.14 we show the distribution of our tension metric O (described in Table 3.2). Around 1000 galaxies are in tension ($O < 0.01$) for both halo profiles. The second peak in O corresponds to galaxies where the SHAM posterior lands exactly on the kinematics posterior, such as the left panel of Fig. 3.9. Most cases of tension are due to kinematics predicting too little dynamical mass relative to AM, as in the third column of Fig. 3.9. Nearly all these galaxies are also compatible with $M_{\rm halo} = 0$ according to our $\mathcal{F}$ statistic. There is a smaller population of galaxies where the dynamical mass inferred from the kinematic model is higher than SHAM (as in the right column of Fig. 3.9).

We correlate tension with galaxy properties in Fig. 3.13. The too low/too high dynamical mass populations are visible in the two peaks in the correlation with W_{50}, with a higher peak at low W_{50} than high W_{50}. There is higher tension for NFW than Burkert at low W_{50}, and also at low $M_{\rm bar}$, which is also seen in the stacked $M_{\rm vir} - M_{\rm bar}$ relationship. There are slightly more galaxies for Burkert that overpredict the dynamical mass than for NFW. It is harder for kinematics to be in tension with SHAM from predicting too high a $M_{\rm vir}$ due to the SHAM posterior's long tail to high $M_{\rm vir}$, especially at high $M_{\rm bar}$.

We apply a random forest regressor to our O metric to assess its dependence on galaxy properties, once again optimising hyperparameters using 3-fold cross-validation. We use the same importance ranking procedure as before, but this time assessing accuracy using the coefficient of determination

$$R^2 = 1 - \frac{\sum_i (y_{i,\rm test} - y_{i,\rm pred})^2}{\sum_i (y_{i,\rm test} - \hat{y}_{\rm test})^2}, \tag{3.20}$$

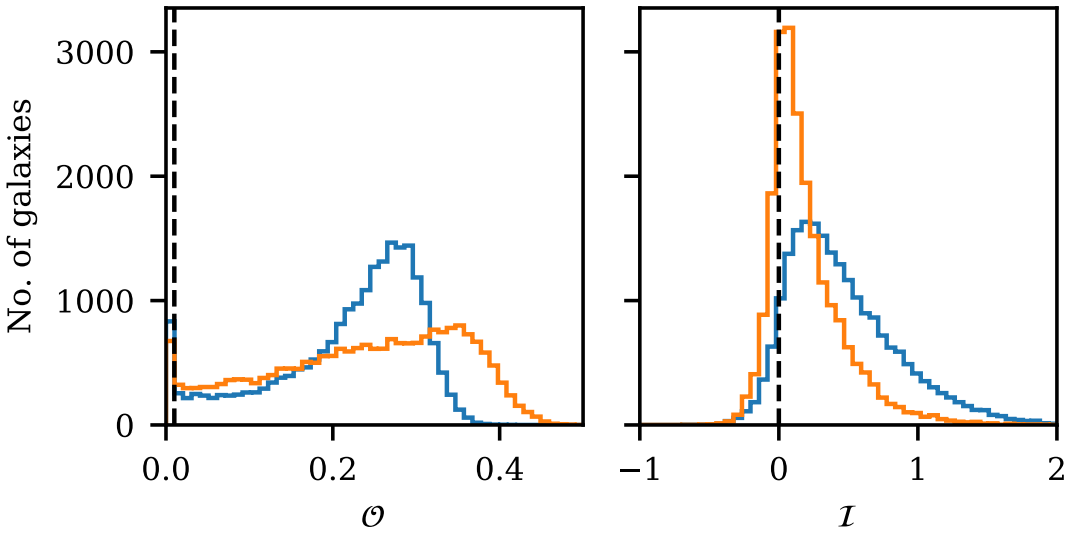

Figure 3.14: Distribution of the overlap metric $\mathcal{O}$ and improvement metric $\mathcal{I}$ over all galaxies in the sample (see Table 3.2). SHAM and kinematics are in tension for galaxies with $\mathcal{O}$ to the left of the vertical dashed line. For those with $\mathcal{I}$ to the right of the vertical dashed line, the constraint on $M_{\rm vir}$ from SHAM is tightened when combined with the constraint from kinematics. For $I = 1$ the constraint on $M_{\rm vir}$ is twice as tight.

where $y_{i,\rm test}$ is the test set value, $y_{i,\rm pred}$ the corresponding prediction and $\hat{y}_{\rm test}$ the mean test set value. $R = 1$ is perfect prediction, and $R = 0$ is given by a model that always predict $\hat{y}_{\rm test}$, disregarding the input data. We find O is most dependant on W_{50}, and to a lesser extent on $M_{\rm bar}$ and b/a (Fig. 3.12, middle panel).

In Fig. 3.15 we plot the 2D $W_{50} - M_{\rm bar}$ distribution of the ALFALFA sample, which shows clearly that tension primarily occurs when W_{50} is low for a given $M_{\rm bar}$. The split is very clean in the $\log W_{50} - \log M_{\rm bar}$ plane and the $M_{\rm bar} - W_{50}$ relationship from the SPARC sample lies within it. The scatter in the ALFALFA data is much greater than in SPARC. We see from the relatively similar scatter of the ALFALFA and SPARC data describing the same galaxies (red and white dots) that the ALFALFA data is reasonably accurate for the SPARC sample. Therefore the increased scatter is due to systematics in the ALFALFA×NSA data that are not present for galaxies that are also in SPARC and/or because the ALFALFA×NSA sample has a different intrinsic $\log W_{50} - \log M_{\rm bar}$ distribution to SPARC e.g. we do not

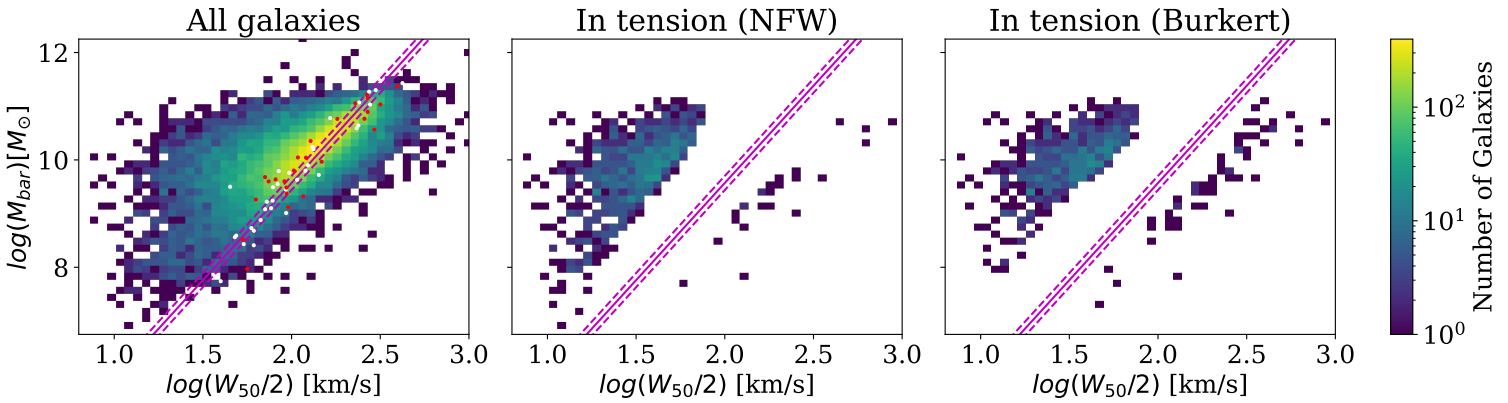

Figure 3.15: A heat map of the distribution of W_{50} and $M_{\rm bar}$ for the whole ALFALFA sample, and for galaxies where SHAM and kinematics are in tension. The W_{50} have been corrected for inclination assuming the intrinsic relative thickness $q = 0.2$. The $M_{\rm bar} - W_{50}$ relationship from SPARC (Lelli et al., 2019) is shown (magenta line) with its 3σ intrinsic scatter (dashed lines). The 25 galaxies that are in SPARC×ALFALFA×NSA are plotted both using their ALFALFA data (red dots) and their SPARC data (white dots) in the left panel. For the latter we use the $W_{\rm m50}$ line width measure and kinematic inclinations, as these were used to derive the SPARC $M_{\rm bar} - W_{50}$ relationship.

expect the entire sample to be rotationally supported and in equilibrium. We discuss potential systematics extensively in Section 3.4.2.

We repeat the random forest regressor procedure for the improvement statistic $\mathcal{I}$, and find that it is dependant on a greater number of features than $\mathcal{F}$ and $\mathcal{O}$ (Fig. 3.12, right panel). The improvement $\mathcal{I}$ is much greater for NFW than Burkert due to the Burkert posterior's long tail to high mass, which for many galaxies aligns with the high mass of tail of the SHAM posterior. We correlate $\mathcal{I}$ with galaxy properties in Fig. 3.13. The positive correlation of $\mathcal{I}$ with $M_{\rm bar}$ is because the SHAM constraint is much weaker at high $M_{\rm bar}$ due to the increasing scatter $\sigma(M_{\rm vir}|M_{\rm bar})$. The correlations with other galaxy parameters are for the same reasons as discussed for the $\mathcal{F}$ statistic, as I is strongly correlated with the tightness of the kinematic constraint.

3.4 Discussion

3.4.1 Interpretation of the results

3.4.1.1 Abundance matching vs. kinematic constraints

Our W_{50}-based kinematic model and our abundance matching (AM) model produce Bayesian posteriors on the mass and concentration of individual galaxies. The constraints offered on halo mass by kinematics are reasonably strong (¡1 dex with the mass–concentration prior applied) for around 40% of galaxies when assuming a cuspy profile. When assuming a Burkert profile the constraints are much weaker, often only providing a lower limit on mass, as the more slowly rising circular velocity profiles due to the core mean that haloes with vastly different masses can have relatively minor differences in rotational velocity within the gas disc. The model is flexible enough that the mode of the posterior produces a W_{50} within 2σ of the observed value for all galaxies. Thus it is not possible for the constraints to be artificially tightened by a poor fit, which is a concern when fitting resolved rotation curves.

In general the constraints offered by SHAM are tighter than for kinematics. When assuming an NFW profile, combining SHAM with kinematics yields stronger constraints on halo mass for a majority of galaxies, with a 1-sigma constraint that is twice as tight for around 1/5 of the sample. The improvement is more pronounced at the high mass end, where the SHAM constraints are weaker. Our analysis therefore shows that SHAM can be augmented with the abundant HI line widths of future large scale surveys to constrain better the distribution of dark matter, especially for haloes with cuspy profiles.

The improvement from combining probes may in fact be even stronger, as the tightness of our SHAM constraints are likely overestimated because our analysis does not account for the uncertainties on the SHAM model itself (e.g. in the proxy and scatter). This is especially true at the low-mass end, where there is no clustering data to constrain the SHAM parameters. We discuss the uncertainty on the SHAM model further in Section 3.4.3.

3.4.1.2 Tension

Overall we do not find significant tension between kinematics and SHAM when comparing the posteriors of individual galaxies, apart from a population of galaxies for which the line width predicts too small a dynamical mass relative to AM, and a smaller population of galaxies for which the inverse is true. The lack of tension is to some extent unsurprising given the weak constraints on halo properties from kinematics for many galaxies. For our SHAM model the mean $M_{\rm vir}$ changes by only 2 dex over 4 dex in baryonic mass, which is comparable to the scatter in $M_{\rm vir}$ from kinematics for a substantial fraction of our sample even with the mass–concentration prior applied.

Although more individual galaxies are in tension between SHAM and kinematics for both profiles at lower baryonic mass (in part due to the tighter constraints from SHAM at low mass), fewer are in tension with Burkert than NFW. This is also clearly visible in the stacked $M_{\rm bar} - M_{\rm vir}$ relationship: the mode of the stacked posterior lies at much lower $M_{\rm vir}$ when assuming an NFW profile, compared to both SHAM and the Burkert profile, which are in good agreement with each other. Therefore both individual and stacked posteriors suggest that at low mass NFW underpredicts halo mass relative to AM/Burkert. This is expected when fitting a cuspy profile to a cored halo (Trujillo-Gomez et al., 2022). Therefore the disagreement may imply that core formation is a decreasing function of mass, and/or that SHAM needs further refining for HI-selected samples.

There is much literature, both theoretical and observational, on dark matter core formation (see Del Popolo & Le Delliou 2021 for a review). A popular hypothesis is that core formation proceeds through the kinematic heating of the dark matter in galactic centres by supernova driven cycles of gas inflows and outflows (Read & Gilmore, 2005; Pontzen & Governato, 2014). Some simulations (e.g. Di Cintio et al., 2014) and analytic calculations (Peñarrubia et al., 2012) have found core formation to be a function of $M_*/M_{\rm vir}$, with M_* a proxy for the energy available to drive gas outflows with supernovae, and $M_{\rm vir}$ related to the amount of DM that needs to be removed and the depth of the potential well that it needs

to be removed from. Read et al. (2019) find observational evidence for this in local dwarf galaxies. From our stacked $M_* - M_{\rm vir}$ relationship (which is qualitatively very similar to our $M_{\rm bar} - M_{\rm vir}$ relationship), we see no such correlation with $M_*/M_{\rm vir}$: SHAM is most in agreement with cored halos relative to cusps at low M_*, rather than at some value of $M_*/M_{\rm vir}$, as suggested by the above models. However our results in this regard are weak, and do not rule out any scenario. The disagreement between kinematics with NFW and SHAM at low mass could also be resolved by haloes expanding to lower concentrations than in DMO simulations. Semi-analytical studies based on SHAM have found some evidence that this is necessary to explain the Tully–Fisher (Desmond & Wechsler, 2015) and radial acceleration (Desmond, 2017a) relations. Both these papers use a relaxation model in which the halo as a whole can expand or contract relative to its pristine NFW profile (Dutton et al., 2007), finding mild evidence for expansion. However, applying a different relaxation model to the radial acceleration relation, Paranjape & Sheth (2021) found evidence for expansion only in the outer halo.

The $M_{\rm bar}-W_{50}$ relationship for the SPARC galaxy sample (Lelli et al., 2019) is extremely tight (see Fig. 3.15). Papastergis et al. (2016) take an extremely restricted sample of only 90 ALFALFA galaxies and construct a similarly tight relationship: their criteria are edge-on, high gas fraction and $W_{50} > 100\,{\rm km\,s^{-1}}$, and they inspect each spectrum for residual noise. They find a correlation between increasing offset of a galaxy from their mean relationship to lower W_{50} and the degree to which the HI spectrum only has a single peak (measured by kurtosis). The offset also increases at lower baryonic mass. Our full ALFALFA×NSA sample is a very different population of galaxies compared to these two studies, so it is expected that the $M_{\rm bar} - W_{50}$ distribution will differ. However with such a large sample based on unresolved observations, some of our galaxies will inevitably have biased halo properties due to systematic uncertainties. Galaxies that lie far from the literature relations fall under particular suspicion. We consider potential systematics in the kinematic modelling in detail in Section 3.4.2, but we note here that our results are robust to basic quality cuts on

SNR and b/a, such as the one used to test the $M_{\rm bar} - M_{\rm vir}$ relationship in Section 3.3.2.1.

3.4.1.3 $M_{\rm bar} - M_{\rm vir}$ relationship

A key result is the $M_{\rm bar} - M_{\rm vir}$ relationship derived from HI kinematics (Fig. 3.11), which we find to be roughly linear in log-space. This is reminiscent of the baryonic Tully–Fisher relation (BTFR) between $M_{\rm bar}$ and $V_{\rm rot}$, which is linear over six decades in mass. Canonical optically-selected SHAM relationships such as that of BCW10, however, display a break in the stellar mass–halo mass relation (SHMR) around the Milky Way mass. Generating a linear BTFR from such SHAM relationships is non-trivial (Desmond, 2017b). Observations of massive spirals have also failed to detect the SHMR break expected from SHAM (Li et al., 2020; Posti & Fall, 2021; Mancera Piña et al., 2022), and McGaugh & van Dokkum (2021) pointed out that the halo mass predictions for the Milky Way and Andromeda from kinematics lie well below the SHAM prediction. Neither the $M_* - M_{\rm vir}$ or $M_{\rm bar} - M_{\rm vir}$ relationship from our kinematic model display a break, but continue approximately linearly with a mode close to the cosmic baryon fraction at the highest masses. This result is robust to quality cuts in the data. Although for the Burkert profile the relationship is very wide, the modal relation is still linear.

Posti & Fall (2021), also applying the mass–concentration relationship as a prior in their kinematic analysis, argue for a linear SHMR relationship for late-type galaxies, with elliptical galaxies displaying the expected break. Unlike Posti & Fall, we do not have a clean sample of late-type galaxies. When assessed by standard cuts on colour and Sérsic index (n) it appears the majority of galaxies in our sample above $10^{10.5}\,{\rm M}_\odot$ are early-type. When we split our sample using a crude cut on morphological type ($n < 2$ for late-type, $n > 3$ for early-type) we do not find differing relationships in $M_{\rm bar} - M_{\rm vir}$. Multiple empirical studies using different methods have attempted to measure the SHMR for passive and star forming galaxies separately, but no consensus has yet been reached on whether they differ (Wechsler & Tinker, 2018).

Our fiducial SHAM model, based on HI-selected galaxies, has a scatter of $\sigma_{\rm AM}$ = 0.42 dex, whereas the scatter for optically-selected galaxies is well constrained to ~0.2 dex (at least under the assumption that $\sigma_{\rm AM}$ is not a function of mass; e.g. Reddick et al. 2013). As $\sigma_{\rm AM}$ increases the highest mass galaxies are increasingly assigned to the much more numerous lower mass haloes, washing out the characteristic break in the mean $M_{\rm bar} - M_{\rm vir}$ relationship, as can be seen in Fig. 3.11. However there is still an increasing scatter $\sigma(M_{\rm vir}|M_{\rm bar})$ towards high mass, with the posterior extending to high $M_{\rm vir}$. There is also still a break in galaxy formation efficiency as a function of halo mass. The fiducial model is in better agreement with our kinematic relationship than BCW10, but we caution that $\sigma_{\rm AM}$ is very poorly constrained for HI-selected galaxies. The model also assigns around a third of the most massive galaxies into haloes such that $M_{\rm bar}/M_{\rm vir} > \Omega_{\rm b}/\Omega_{\rm M}$, suggesting SHAM models with scatter this high may not produce realistic galaxy populations, even if they reproduce the clustering signal.

3.4.2 Kinematic modelling caveats

3.4.2.1 Baryonic effects on halo density profiles

We have studied the NFW and Burkert profiles as representative cases of a cusped and cored profile respectively. However previous studies have shown that no halo profile is a good fit to all observations (Katz et al., 2017; Li et al., 2020). This may be explained by the difficulty in calculating baryon-induced modifications to haloes, due to the uncertainty in the numerical implementation of baryonic physics and resolution constraints. Initially haloes are expected to contract adiabatically from baryonic infall as galaxies form. The subsequent expulsion of gas from galaxies by star-formation is then expected to expand the halo. Recently Velmani & Paranjape (2022) studied halo relaxation in large volume hydrodynamical simulations and found it to vary substantially with halo mass and concentration, and star formation rate. Paranjape et al. (2021) demonstrated that changes to halo relaxation physics can significant alter W_{50}. Li et al. (2022b) incorporate adiabatic contraction into their halo fitting procedure,

although only using an iterative fitting method that starts with an abundance matched halo rather than a full parameter space exploration.

Any baryonic effect that modifies halo density profiles would be expected to alter our mass and concentration constraints, and thus our analysis would need to be repeated for halo profiles inspired by hydrodynamical simulations (e.g. Di Cintio et al. 2014). As there is currently no convergence in the precise effects of baryons on dark matter across a range of galaxy scales, this is left for future work. Ultimately, theoretical and observational progress in understanding the net effect of feedback processes is required before the modification of haloes by baryons can be robustly accounted for in kinematic analyses.

3.4.2.2 Modelling the line width

Our model assumes the line width is the product of a galaxy's azimuthally-averaged rotation curve and HI surface density, with a HI velocity dispersion of 10km/s. We tested this using the SPARC sample and found good agreement. However very few of these galaxies had observed line widths $< 100\,\mathrm{km\,s^{-1}}$, which is the region in which most of the tension is found. Furthermore we see a trend in Fig. 3.3 where towards lower line width there is weaker agreement between model and observations, although this could be explained by uncertainty in the extrapolation of RCs.

Pressure support has the effect of reducing the rotational velocity below the circular velocity, causing the dynamical mass to be underestimated (Bureau & Carignan, 2002; Oh et al., 2015; Iorio et al., 2016). This "asymmetric drift" correction becomes important in galaxies where $V_{\rm rot}$ is comparable to the gas dispersion, and becomes more important at larger radii. Our models for $\sigma_{\rm HI}$ and $\Sigma_{\rm HI}$ do not capture the galaxy-to-galaxy variation required to sensibly apply the correction, which is challenging even with resolved data. As a simple test of the sensitivity of our results to asymmetric drift, we rerun our inference replacing the assumption that $V_{\rm rot}(r) = V_{\rm c}(r)$ with $V^2_{\rm rot}(r) = V^2_{\rm c}(r) - \sigma^2_{\rm HI}$, with $\sigma_{\rm HI} = 10$km/s. We find that for our stacked $M_{\rm bar} - M_{\rm vir}$ relationship the mode of $M_{\rm vir}$ is increased by 0.5

dex for NFW and 0.15 dex for Burkert in the lowest mass bin ($M_{\rm bar} = 10^{7.25}\,{\rm M}_\odot$), where the effect is greatest. At $M_{\rm bar} = 10^{8.5}\,{\rm M}_\odot$ the difference with our fiducial model is less than 0.15 dex for both haloes. We conclude that, although there is an increasing number of galaxies towards lower mass and W_{50} that are affected by asymmetric drift, our overall conclusions are likely robust to it.

Non-equilibrium motions are also expected to be increasingly important towards lower mass, due to supernovas driving gas out of the plane of the disc, and radial outflows (e.g. Verbeke et al. 2017). Asymmetries due to the increasing irregularity of galaxies may also cause W_{50} not to reflect the dynamical mass (Reynolds et al., 2020). High velocity clouds in the observed galaxy can also create high velocity wings in the flux profile, leading to W_{50} overpredicting the rotational velocity (Schulman et al., 1994).

3.4.2.3 Measuring the line width

Extracting the line width from often noisy spectra is a difficult process. We investigate the difference between the base ALFALFA catalogue W_{50} line width measurement and the $W_{\rm Yu85}$ measurement from the Yu et al. (2022) reanalysis. $W_{\rm Yu85}$ implies a slightly lower mass for most galaxies, but there is a significant population for which it infers a much higher mass. The strength and trends of tension with galaxy properties are the same for both line width measures, although there is not good agreement on which specific galaxies are in tension. $W_{\rm Yu85}$ produces a very similar stacked $M_{\rm bar} - M_{\rm vir}$ relationship to W_{50}, with the mode not different by more than 0.4 dex in any bin.

Haynes et al. (2018) caution that at low SNR, radio frequency interference can cause the line width to be underestimated. This could potentially explain the population of galaxies with extremely low W_{50} relative to their baryonic mass. However we find that galaxies with HI code 2 are not overrepresented among in-tension galaxies, and we do not find a trend between SNR and tension above SNR = 6, suggesting this cannot be the sole cause. Yu et al. (2022) provide a different cut on galaxies more vulnerable to RFI. Again we found these galaxies were not overrepresented among the in-tension galaxies. Another potential

source of error is confusion, where the separation between two galaxies is smaller than the beam width. Jones et al. (2016) show that the impact of confusion for the catalogue as a whole is not significant, although they say it is easy to identify specific examples. Using the flag for crowding in the reanalysis of Yu et al. (2022), we found that crowded galaxies are not over-represented among the in-tension galaxies.

Ball et al. (2022) present an ALFALFA reanalysis that utilises a similar curve-of-growth based algorithm and crowding analysis to Yu et al., with the aim of minimising the BTFR scatter by removing outliers. Future work may benefit from testing their methods and sample selections in the mass-modelling context.

3.4.2.4 Inclination

As discussed in Section 3.2.2.3, the gas disk inclination calculated from the observed optical axis ratio can be highly inaccurate. The most troubling potential inclination systematic is when the measured b/a is biased low, leading to too high (edge-on) an inclination, too low an inferred intrinsic W_{50} and hence too low a dynamical mass within the gas disc. The majority of our in-tension galaxies are of the type where the dynamical mass inferred from W_{50} is lower than the SHAM expectations, with the frequency of tension increasing at lower $M_{\rm bar}$. In our SPARC sample we find a single severe underestimation of b/a in the optical, for a heavily barred face-on galaxy. As bars are most prevalent in galaxies with stellar masses $10^9 < M_*/\,\mathrm{M}_\odot < 10^{11}$ (Méndez-Abreu et al., 2010), this is unlikely to explain the increasing tension that we observed towards even lower $M_{\rm bar}$.

Several irregular galaxies in the SPARC sample had a NSA b/a that was somewhat too low (given both their kinematic inclination and visual appearance), which we accounted for by adopting a 10% error on b/a. This sample was too small to look for a correlation between mass or flux and disagreement with kinematic inclination, to see if the effect increases towards lower mass, as does the tension. In general we expect irregularity to increase towards low $M_{\rm bar}$, as the weaker self-gravity of the system makes it more susceptible to

internal and environmental effects.

Applying a flat prior on q, when the true distribution for the sample is likely peaked at $q \approx 0.2$, will cause the inferred masses to be biased low. We calculated the $M_{\rm bar} - M_{\rm vir}$ relationship for the $q = 0.2$ inclination model, and found it made little difference in the lowest and highest mass bins, where it raises $M_{\rm vir}$ somewhat. However it is in these bins that we expect q to be higher than 0.2.

Finally, Almeida & Filho (2019) have argued that low dynamical masses may be caused by ignoring triaxiality when calculating inclination using the optical b/a. We also neglect triaxiality, so our results are subject to the same potential bias. A more sophisticated analysis could use the expected population distribution of inclination to infer the distribution of axial ratios as a function of galaxy properties (Putko et al., 2019). However this is complicated for ALFALFA, as the selection function of blind spectroscopic HI surveys is dependant on inclination (Lang et al., 2003).

3.4.2.5 Baryonic mass

Using an erroneously high $M_{\rm bar}$ will cause $M_{\rm vir}$ to be underestimated. The uncertainties on $M_{\rm HI}$ are smaller than those on M_*. We verified the NSA M_* in two ways. Firstly we compared it to the GALEX survey and found consistency within the uncertainties. Secondly we compared the NSA to SPARC, and also found good agreement on the whole, but with increasing disagreement towards low mass ($< 10^9\,{\rm M}_\odot$). However low mass galaxies tend to be more gas-dominated, so the bias on $M_{\rm vir}$ from M_* will be less important, suggesting it is unlikely to be the cause of the observed trend of tension with mass. Ball et al. (2022) also identified foreground stars as a potential source of overestimated stellar masses, finding this pathology in 11% of the most extreme BTFR outliers in their data.

HI self-absorption has not been accounted for in HI masses. Depending on the model used, the correction can range from insignificant except for the most edge-on galaxies, to a 30% correction for all galaxies (see Jones et al. 2018 for a thorough discussion).

Underestimating the HI mass causes the halo circular velocity to be overestimated, and the size of the HI disc to be underestimated. Both of these result in too high a halo mass being inferred. Applying the inclination-based correction from Jones et al. ($\Delta \log M_{\rm HI} = 0.13 \log(b/a)$) results in insignificant differences to our results above $M_{\rm bar} = 10^9\,{\rm M}_\odot$. However at lower mass, where galaxies are more gas-rich, the effect is significant, with the mode of the stacked $M_{\rm vir}$ distribution 0.4 dex lower at $M_{\rm bar} = 10^{7.5}\,{\rm M}_\odot$ for NFW, putting more galaxies in tension. As the Jones et al. model is based on thin disc galaxies, the true effect may be larger for thicker dwarf galaxies. Future work may benefit from improved modelling of HI self-absorption.

3.4.2.6 Gas distribution

The adopted gas model from Wang et al. (2016) is based on a sample of 500 dwarf and spiral galaxies, with masses down to $M_{\rm HI} = 10^7\,{\rm M}_\odot$. They find that early-type galaxies, although still lying on the $M_{\rm HI} - D_{\rm HI}$ relation, tend to have flatter gas profiles, with a larger fraction of their gas lying outside of $D_{\rm HI}$. Adopting too low an $r_{\rm HI}$ causes $M_{\rm vir}$ to be overestimated. On the other hand, explaining the tension between SHAM and kinematics at the low mass end would require that the true size of the gas disc be smaller than in the model. The $M_{\rm HI} - r_{\rm HI}$ relationship of W16 shows no evolution towards lower mass. The most in-tension galaxies in this regime, for which the baryonic mass alone is enough to generate the observed line width, are little sensitive to changes in gas distribution as both the stars and gas are contained within the gas disc.

3.4.3 Abundance matching caveats

The abundance matching relationship for gas-selected galaxies is constrained by clustering only for $\log M_{\rm B} > 9.4$, and even for those ranges it is poorly constrained (see fig. 14 of ST21) due to the weaker clustering of HI-selected samples and the comparatively small sample size of HI surveys.

Rather than sample from the entire posterior of ST21, which includes regions with extremely high $\sigma_{\rm AM}$ for which the galaxy–halo connection is essentially fully randomised, we adopted their maximum likelihood point under the assumption that the SHAM parameters are independent of mass (although this was strongly ruled out for optically-selected samples by ST21). As discussed previously, the high mass end is particularly sensitive to $\sigma_{\rm AM}$. We find far weaker dependence on the $z_{\rm cut}$ parameter.

The extrapolation of the baryonic mass function becomes important for galaxies with $\log M_{\rm bar} < 10^{8.5} M_{\odot}$. However the trends in our results are not noticeably different in the extrapolated regime. The only way to increase the baryon fraction for SHAM at the low mass end (hence reducing tension with kinematics) is to strongly increase the steepness of the baryonic mass function.

Finally, at the faint end it is possible that a qualitatively different SHAM prescription is required to deal with the different formation scenarios of lower mass galaxies. ST21 showed that fainter optically-selected samples require higher scatter, and argue that low mass galaxies may require a different set of SHAM assumptions, such as increased galaxy formation bias or a difference between satellite and central galaxies. On the other hand, Nadler et al. (2020) find an upper limit $\sigma_{\rm AM} = 0.2$ for Milky Way satellites.

3.4.4 Comparison to literature

Previous studies, most notably of the SPARC galaxies, have used resolved rotation curves to infer halo properties (Katz et al., 2017; Li et al., 2020). The advantage of resolved rotation curves is that they are able to provide much more information on density profiles than a summary statistic that effectively samples the RC at a single radius. Li et al. (2020) tested a wide variety of rotation curves, and found that in general cored profiles such as Burkert provided better fits than cuspy profiles such as NFW, with many galaxies favouring cores even at higher mass. Even with the full rotation curve, the constraints on halo properties are weak in some cases. For example Li et al. (2020) find many galaxies for which the

1σ halo mass constraint spans over two orders of magnitude. However for many of the galaxies they recover a good constraint without any prior applied, as the shape of the rotation curves is enough to break the degeneracy between mass and concentration. Our approach is complementary, sacrificing precision of the dynamical measurements for a much larger sample size and thus trading potential systematic error in relating the small SPARC sample to the entire halo population for weaker galaxy-by-galaxy constraints. For us, robust conclusions are available only statistically across the full sample.

Our analysis sheds light on the "small-scale problems" of ΛCDM (Bullock & Boylan-Kolchin, 2017b). The Too-Big-to-Fail problem (TBTF) is the observation that the kinematically-inferred halo masses of the Milky Way's satellites are much lower than the masses of the largest subhaloes of Milky Way-sized haloes in N-body simulations (Boylan-Kolchin et al., 2011). This was later generalised to populations of field galaxies that were found to have kinematics that implied a lower halo mass than predicted by abundance matching (Ferrero et al., 2012). Papastergis et al. (2015) studied the problem in a sample of ALFALFA isolated dwarfs for which resolved rotation curves also exist, using a SHAM procedure that ranks galaxies by their line width. Fitting an NFW profile, they found that haloes with resolved outer rotational velocities of less than 25km/s are incompatible with the haloes implied by AM. They find that fitting a halo profile with a mass-dependant core reduces the tension, but does not fully alleviate it. Although we do not separate satellite and field galaxies, or restrict our sample to galaxies with resolved rotation curves (and hence more robust kinematic halo masses), our results are similar to the above studies: we also find a population of dwarf galaxies for which the halo mass inferred from kinematics is significantly below the SHAM prediction, such that the two measurements are in statistical tension. The disagreement is partially alleviated by fitting a Burkert profile instead of NFW. There is much literature on proposed solutions to TBTF for both satellite and field galaxies, including modelling and observational uncertainties, and new dark matter physics (see Papastergis & Shankar 2016 for a review).

A related small-scale problem is the observed diversity of rotation curves at fixed galaxy mass, which does not appear in ΛCDM simulations (Oman et al., 2015). Baryonic models which solve small scale problems such as TBTF through core-formation create cores too uniformly, and therefore fail to generate this rotation curve diversity (Sales et al., 2022). In our sample we observe great diversity in W_{50} at fixed $M_{\rm bar}$ at lower mass, where the gas disc does not probe so far into the halo. This could be indicative of different arrangements of the baryons and/or different DM central densities at fixed halo mass, assuming the abundance matching relation does not flare at low mass. However, as we do not have accurate baryonic distributions we cannot provide more concrete results.

We find a significant number of ALFALFA galaxies are dark matter-deficient according to our model, as their line width is completely explained by the baryons alone. The existence of apparently dark matter-deficient galaxies has been previously noted for the ALFALFA sample by Guo et al. (2020), using a simple method where the dynamical mass is estimated from the gas disc scale length and the observed line width without full modelling. They apply quality cuts to the sample and find 19 dark-matter deficient galaxies (14 of which are isolated) out of a sample of 324 (although Almeida & Filho 2019 argue this may due to neglected triaxiality, see Section 3.4.2.4).

Mancera Piña et al. (2019) study a sample of six ALFALFA galaxies with low linewidths for their baryon masses using HI interferometric data, deriving resolved RCs (with 2-3 resolution elements per galaxy side) which support the galaxies being baryon-dominated. Furthermore, using higher resolution observations, Mancera Piña et al. (2021) identified an apparently "dark matter-free" isolated galaxy in the sample, although the inclination is still a potentially significant systematic uncertainty and its stability in the absence of dark matter has been contested (Sellwood & Sanders, 2022). Two dark matter-free dwarf galaxies have also been identified using globular cluster dynamics (van Dokkum et al. 2018, 2019, although see Saifollahi et al. 2021) speculated to have formed from gas stripped in a galaxy–galaxy collision (van Dokkum et al., 2022).

In general, claimed observational detections of dark-matter deficient galaxies tend to be controversial due to modelling uncertainties, even with far better data than our unresolved observations. It is interesting to speculate, however, whether the galaxies we identify as being plausibly dark matter-deficient would remain so given more precise measurements. Jackson et al. (2021) and Moreno et al. (2022) find dark matter-free galaxies produced in tidal interactions in simulations, the latter predicting that 30% of central galaxies host at least one dark matter-free satellite.

Another approach to comparing HI kinematics with ΛCDM expectations is to forward model the line width velocity function using either semi-analytical models (Chauhan et al., 2019; Paranjape et al., 2021) or hydrodynamical simulations (Dutton et al., 2018; El-Badry et al., 2018). This does not require the inclinations of individual galaxies, avoiding a major source of uncertainty. Dutton et al. (2018) find that the velocity function for dwarf galaxies in the hydrodynamical NIHAO simulations are in good agreement with ALFALFA line widths in the range $10 < W_{50}/2 < 80\,\mathrm{km\,s^{-1}}$. They identify turbulent motions, projection effects due to intrinsic HI disc thickness and flattened DM distributions as important factors in lowering the observed line widths relative to expectations. We do not properly account for turbulent motions (although we test our model sensitivity to them) and we assume an infinitely thin HI disc. We find less tension at low line width when fitting a Burkert profile, but our inferred core-formation dependence is in disagreement with the $M_*/M_{\rm vir}$ dependence seen in their simulation. It is plausible that the turbulent motions, HI disc thickness and feedback physics in their simulation account for the differences with our results.

Dutta et al. (2022) use an abundance matching-based method to extract $M_{\rm HI}$–$M_{\rm vir}$–$V_{\rm rot}$–W_{50} scaling relations for the ALFALFA sample. They use group finder-based halo masses to obtain a reduced halo mass function corresponding to the ALFALFA sample, which they abundance match to the ALFALFA HIMF. The resulting HI-selected HI-to-halo mass relationship (their fig. 7) is similar to the mean of our stacked abundance matching

HI-to-halo mass relationship at low mass, but at high mass has a much stronger break. This is largely driven by the lack of AM scatter in their model (compared to 0.42 dex in ours), which prevents an apples-to-apples comparison.

3.4.5 Future work

This paper presents a first attempt to compare the halo properties inferred from abundance matching and HI line widths for an entire population of HI-selected galaxies. Future HI surveys will improve the constraints on SHAM models for HI-selected galaxies by reducing the uncertainty on galaxy clustering and extending it to lower masses, allowing a more robust assessment of the agreement between the two methods and their relative constraining power.

The increased precision and reduction in systematics on W_{50} of future surveys should also improve the constraints from kinematics. The increasing number of observed line widths will also increase the statistical power at the low and high mass ends. Future surveys will also allow both HI line width and abundance matching studies to be extended to higher redshifts. Ponomareva et al. (2021) have already used line widths from MeerKAT to study the BTFR out to z=0.081. Glowacki et al. (2021) predict evolution in the BTFR with redshift from the SIMBA simulation.

More information is contained in the HI flux profile, of which W_{50} is a summary statistic. Exploiting this would increase the precision of halo parameter inference. Using a similar model as this work, Paranjape et al. (2021) showed this by performing a full spectrum fitting for some nearby galaxies with very well resolved ALFALFA spectra. This method is potentially very powerful if it can be applied to whole populations of galaxies. A potential problem is the uncertainty in the detailed HI distribution, which may have cores, holes or asymmetries. These may bias the inferred halo properties if not adequately modelled.

Finally, other methods of inferring the properties of DM haloes could potentially be combined, which could probe the DM distribution at different radial distances from the halo

centre. The HI line width probes the central region of the halo, but weak lensing measures the acceleration towards the outskirts of stacked galaxies. The velocity dispersions of stars in early-type galaxies (or of galaxies in groups or clusters) could also be used. For example, Schulz et al. (2010) used weak lensing to measure the dark matter halo profile in the outskirts of massive elliptical galaxies, extrapolated it to the centre assuming an NFW halo and then compared the resulting central dynamic mass to the SDSS velocity dispersion, finding evidence for halo contraction.

3.5 Conclusions

We have compared the constraints on halo mass and concentration inferred from the kinematic modelling of the HI line width with those inferred from an (inverse) abundance matching model specifically tailored to HI-selected galaxies, for the ~22,000 galaxies in the ALFALFA×NSA data set. Our conclusions are as follows:

- The two methods produce consistent halo constraints galaxy-by-galaxy in most cases, with the kinematics posterior broader and requiring a mass–concentration prior for bounded constraints on either quantity.

- The halo posteriors of SHAM can be augmented with information from the HI line width to produce tighter constraints on the dark matter distributions of individual galaxies. The gains are greater when assuming a cuspier halo profile.

- Towards low baryonic mass there is an increasing population of galaxies with smaller line widths than expected from abundance matching. For some galaxies this implies a dynamically insignificant amount of dark matter within their gas disc, leading to extremely high baryon fractions when the halo is extrapolated to the virial radius. The disagreement with abundance matching is more severe when fitting an NFW halo than Burkert, which we interpret as weak evidence for a cored central DM density at low baryonic mass. There is a smaller population of galaxies for which SHAM and

kinematics disagree because the dynamical mass inferred from kinematics is higher than from AM.

- The $M_{\rm bar} - M_{\rm vir}$ relation reconstructed from HI kinematics is in statistical agreement with that from SHAM (Fig. 3.11). It is however closer to a power-law, with a deviation (especially assuming an NFW profile) towards lower $M_{\rm vir}$ at fixed $M_{\rm bar}$ at the faint end. When assuming a Burkert profile there is less information to be gleaned on $M_{\rm vir}$ from the line width, resulting in a very uncertain relation.

- We formulate statistics to quantify whether a galaxy i) exhibits tension between its kinematics and SHAM modelling results, ii) affords a strong improvement in halo constraints by combining the two methods, and iii) has $M_{\rm halo} = 0$ excluded by the kinematic modelling. We also develop a machine learning-based method for assessing the extent to which these statistics correlate with various galaxy properties, finding line width to be the most important feature in each case.

Our analysis demonstrates the potential for combined photometric and spectroscopic constraints on the galaxy–halo connection, even when using low-resolution spectroscopic products such as HI line widths. With future surveys set to improve dramatically our knowledge of the HI universe, we anticipate that our framework will be useful for inferring DM distributions, constraining kinematic and empirical models, and advancing understanding of the physical processes that underlie galaxy formation.

Chapter 4

The information on dark matter halo profiles contained in spectroscopic observations of late-type galaxies

4.1 Introduction

In resolved studies, the density profile of dark matter is usually constrained by fitting parameterised functions (e.g. Navarro et al., 1997; Burkert, 1995; Di Cintio et al., 2014; Read et al., 2016) to the measured rotation curve (RC). The parameters, which we refer to as the *properties* of the halo, are typically the virial mass, the concentration (a measure of the autocorrelation of dark matter within the halo) and sometimes additional parameters describing the shape of the profile, such as the steepness of the inner slope. The tightness of the constraints on the free parameters is a complex function of the properties of the measurements (e.g. the number of measured RC data points, the uncertainties on the measured velocities, the maximum radius probed), properties of the galaxy (e.g. stellar surface density, gas fraction) and the precision of auxiliary data on the galaxy (inclination, distance, baryon content).

Rotation curves can be measured using a variety of kinematic tracers. Radio telescopes, in either single dish or interferometer configurations, probe atomic hydrogen (HI), which has the advantage of extending far beyond the optical disc for late-type galaxies, into the region where dark matter dominates. The SPARC (Lelli et al., 2016a) database, the largest of its type, contains HI rotation curves for 175 late-type galaxies. Collated from archival observations, the measurement properties vary greatly between different RCs. For example, the best sampled RC has 120 data points, and the worst sampled has 5. In this paper we use SPARC to study the precision of constraints on halo parameters as a function of measurement and galaxy properties. This will reveal the ways in which future surveys ought to be designed to maximise their constraining power on the dark matter distributions around galaxies.

Other tracers do not probe as far as HI, but have their own advantages. Optical IFU surveys such as DiskMass (Martinsson et al., 2013), MaNGA (Bundy et al., 2014) and SAMI (Croom et al., 2021) use optical emission from ionised gas or stars, which extends only as far as the galaxy's stellar component, although the resolution is higher than HI surveys. Sub-mm telescopes (again either in single dish or interferometric configurations) can be used to probe the molecular CO gas disk, which usually extends to 50-70% of the radius of the stellar disc (e.g. Lang et al., 2020).

Future and current surveys HI are seeking to study larger, statistically representative samples of galaxies (e.g. Maddox et al., 2021; Oosterloo et al., 2010) and galaxies at larger distances. For example, MIGHTEE-HI is an ongoing blind survey that will measure RCs out to $z = 0.5$. Due to the further distances, the RCs are sampled more coarsely than in nearby catalogues such as SPARC (Ponomareva et al., 2021). RCs can be measured to lower radius but higher redshift using optical (Stott et al., 2016; Di Teodoro et al., 2016) and sub-mm (Jones et al., 2021; Lelli et al., 2021, 2023) instruments. Strongly lensed galaxies can also be used to increase the distance probed (e.g. Rizzo et al., 2021).

Finally all of the methods described above can be used to obtain spatially integrated

spectra, which requires significantly less integration time and so can be obtained for orders of magnitude more galaxies. Current surveys such as ALFALFA (Haynes et al., 2018), and future surveys such as WALLABY (Koribalski et al., 2020; Deg et al., 2022), CRAFTS (Zhang et al., 2020, undertaken on FAST) and the SKA (Yahya et al., 2015) will measure the spatially integrated HI emission for cosmological volumes of galaxies.

These different observational techniques and tracers will measure rotation velocities with varying precision and will probe different parts of the RC. The constraining power of these different types of kinematic measurement on halo properties has never been studied in detail. To begin investigation of this question, we study here the information content contained in different parts of the RCs of the SPARC galaxies. This is achieved by constraining halo properties using the RC summary statistics recorded in SPARC, each of which characterise a particular part of the RC. These statistics are $V_{\rm flat}$, the speed of the flat part of the rotation curve, $V_{\rm max}$, the peak rotational speed and $V_{2.2}$, the circular velocity at 2.2 times the disc exponential scale length and $W_{\rm p20}$ the width of the spatially integrated HI line profile at 20% of the peak flux.

RC summary statistics have previously been utilised extensively in the study of the Tully–Fisher relation (TFR), the tight empirical relationship between the mass or luminosity of a galaxy and some measure of its rotational velocity. The TFR was first defined using HI linewidth (Tully & Fisher, 1977), and later studies have used $V_{\rm max}$ (Conselice et al., 2004), $V_{2.2}$ (Courteau, 1997b) or $V_{\rm flat}$ (McGaugh, 2005; Ponomareva et al., 2018). Recently Lelli et al. (2019) (henceforth L19) compared the baryonic TFR (McGaugh et al., 2000; McGaugh, 2005; Lelli et al., 2016b; Iorio et al., 2016) produced by different summary statistics of the RC, as well as the HI line width, for the SPARC galaxies. The study of the dark matter halo constraints offered by these summary statistics is also interesting in this context.

A velocity summary statistic is sensitive only to the enclosed dynamical mass within the radius it probes (which can be estimated as $M \sim V^2 R/G$, Caserano & Shostak 1980).

Hence, although summary statistics do provide information on halo mass and concentration (once a profile is assumed), the constraints are relatively weak due to the degeneracy between the two parameters: the same enclosed mass can be generated by either a high mass, low concentration or a low mass, high concentration halo. The degeneracy can be broken to some extent by assuming a halo mass–concentration relation from simulations (e.g. Posti et al., 2019), but the extent to which these relationships are obeyed by real halos is uncertain (Dutton & Macciò, 2014; Katz et al., 2017; Li et al., 2020; Mancera Piña et al., 2022). For example, due to assembly bias (Dalal et al., 2008), we do not expect a population of relatively isolated, late-type galaxies such as those found in SPARC to follow an identical mass–concentration relationship to that of all the halos in a simulation.

Without an informative prior linking mass and concentration, the kinematic data alone can sometimes not exclude unphysical scenarios such as low mass galaxies having cluster mass halos. Studying the degenerate posterior in mass–concentration can still yield insight however. The constraints from summary statistics can be compared and/or combined with other pieces of information, such as abundance matching (Yasin et al., 2022), optical kinematics (proposed by Taranu et al., 2017) or weak lensing data (Shajib et al., 2021, for SDSS velocity dispersions). Therefore in this study we choose to analyse the constraining power in the mass–concentration plane offered by the different types of measurements without applying a mass–concentration prior, although we discuss the effects this would have in Sec. 4.4.1.

We quantify the precision of constraints on halo properties using the Kullback–Leibler divergence (D_{KL}, Kullback & Leibler, 1951) of the posterior from the prior, a measure of information gain based on information theory. We study the information gain of the 2D total mass–concentration posterior (where total mass is equal to the halo mass plus the galaxy mass). We use total mass rather than halo mass, because the lower bound of the prior on total mass can be naturally set to the galaxy mass, whereas the halo mass, when sampled logarithmically (as is computationally necessary), has no natural lower bound. Our method

could equally be applied to additional parameters describing shape. By quantifying the information gain on these halo properties when using either the full RCs, HI line widths or summary statistics to constrain the kinematic model, we aim to answer the following questions:

- How does the information content depend on properties of the measurement such as velocity uncertainties, the minimum HI surface density probed and auxiliary data on galaxy parameters.
- How does the information content depend on galaxy properties?
- How much information is contained in different summary statistics compared to the full RC?
- How much information is there in integrated HI measurements relative to more expensive, spatially resolved measurements?

To answer the first two questions we will construct a predictive model for $D_{\rm KL}$ given the galaxy and measurement properties as input. The paper is structured as follows. Section 4.2 describes the the SPARC data. Section 4.3 describes the Bayesian models for inferring halo properties from the observations. In Section 4.4 we present the information content as a function of different types of observations, measurement properties and galaxy properties. We discuss the implications of our results in Section 4.5, and conclude in Section 4.6. We define the halo mass $M_{\rm vir}$ using the overdensity condition $\Delta_{\rm vir} = 178$ of Bryan & Norman (1998). All logarithms are base-10 unless stated otherwise.

4.2 Observational data

In addition to the main SPARC database, we use data from L19. L19 calculate the RC summary statistics $V_{\rm flat}$, $V_{\rm max}$, $V_{2.2}$ and their associated errors for a subsample of 153 (out of

Table 4.1: The summary statistics of the full rotation curve and HI linewidth definition used in this paper.

Measurement	Interpretation	Sample size
Full RC	The full rotation curve.	175
$V_{\rm flat}$	The velocity of the flat part of the rotation curve. The algorithm to identify the flat part of the rotation curve is listed in Section 4.3.2 and differs slightly from the definition used in the SPARC database.	123
$V_{\rm max}$	The maximum velocity of the rotation curve. If the rotation curve is continuously rising in the observed range then this is the outermost measured point	175
$V_{2.2}$	The velocity at twice the exponential stellar disk scale length. This is found by linearly interpolating between datapoints on either side of the required radius.	167
$W_{\rm p20}$	The width of the global HI 21-cm emission line of a galaxy measured at 20% of the peak flux.	148

175) SPARC galaxies (most of the galaxies are cut due to either low i or few of data points). We use their definitions to calculate $V_{\rm max}$ and $V_{2.2}$ for the whole sample, but we calculate $V_{\rm flat}$ using our own definition, which we describe in Section 4.3.2. The definitions of the velocity measurements are summarised in Table 4.1. L19 also compile HI linewidths from archival data for various different definitions. We choose to use $W_{\rm p20}$, the width at 20% of the peak flux, as it is available for the most galaxies. Unlike L19, we do not include the contribution from inclination to the observational uncertainties on the summary statistics and $W_{\rm p20}$, as inclination is a free parameter in our inference.

4.3 Methods

4.3.1 Rotation curve model

Dark matter halo properties are inferred by fitting a parameterised halo profile to the observational data. Different halo profiles has been studied extensively in literature but

Table 4.2: The free parameters in our kinematic model, their physical definitions and their Bayesian priors. We sample all parameters in logarithmic space except inclination and distance.

	Parameter	Units	Definition	Prior
	$M_{\rm tot}$	$M_\odot$	Total mass $M_{\rm tot} = M_{\rm halo} + M_{\rm bar}$	Flat in range $\log(M_{\rm bar}/\,{\rm M}_\odot) < \log(M_{\rm tot}/\,{\rm M}_\odot) < 15.5$
	$c_{0.1}$	-	Halo concentration, as defined in Eq. (3.11)	Flat in range $0.5 < \log c_{0.1} < 2$
	$\Upsilon_{\rm disc}$	$\rm M_\odot/L_\odot$	Disc mass-to-light ratio	Lognormal ($\mu = \log(0.5), \sigma = 0.1$)
	$\Upsilon_{\rm bulge}$	$\rm M_\odot/L_\odot$	Bulge mass-to-light ratio	Lognormal ($\mu = \log(0.7), \sigma = 0.1$)
	D	Mpc	Physical distance to galaxy	Gaussian prior from SPARC value and its uncertainty
	i	deg	Inclination (0° face on; 90° edge on)	Gaussian prior from SPARC value and its uncertainty

a clear picture has yet to emerge of the relationship between the properties of a galaxy and the shape of its halo (Katz et al., 2017; Li et al., 2020). The haloes in dark matter-only simulations were found to have a universal profile dubbed Navarro-Frenk-White (NFW) (Navarro et al., 1997), but profiles motivated by hydrodynamical simulations, that interpolate between a cusp and a core based on galaxy/halo properties (Di Cintio et al., 2014; Read et al., 2016), have been found to fit the SPARC data better than the NFW profile (Katz et al., 2017; Li et al., 2020). However cores have been observed in high mass systems (Collett et al., 2017), including for the SPARC galaxies (Li et al., 2019, 2022a), which is against the mass-dependant behaviour of the supernova-induced core flattening predicted by the aforementioned hydrodynamical simulations. On the other hand many studies have found NFW haloes to be good fits to clusters and weak lensing data for high mass galaxies (e.g. Mandelbaum et al. 2016), and some have argued that the inference of cores from 21-cm rotation curve observations may be due to systematics (Roper et al., 2022). In light of this uncertainty we choose to study the NFW and Burkert (Burkert, 1995) profiles as representative examples of a cusped and cored profiles respectively. Due to the preference of most SPARC galaxies for cores using our modelling procedure (in agreement with Li et al. 2020, although see Posti et al. 2019 for a different analysis), we present our results primarily for the Burkert profile.

We define baryonic mass $M_{\rm bar}$, dark matter halo mass $M_{\rm halo}$, concentration $c_{0.1}$, and the NFW and Burkert profiles in the same way as in Chapter 3 (Section 3.2.2.1). We define total mass $M_{\rm tot} = M_{\rm halo} + M_{\rm bar}$ (this is the same as $M_{\rm vir}$ in Chapter 3). We now also analyse

how well observations can constrain a shape parameter for the inner halo by studying the generalised-NFW profile (gNFW, e.g. Umetsu et al. 2011), with density

$$\rho_{\rm gNFW}(r) = \frac{\rho_s}{\left(\frac{r}{r_s}\right)^{\alpha}\left[1+\left(\frac{r}{r_s}\right)\right]^{3-\alpha}}. \tag{4.1}$$

This reduces to NFW for $\alpha = 1$. The mass enclosed is given by

$$M_{\rm gNFW}(r) = 4\pi\rho_s r_s^3\left[B(x/(1+x), 3-\alpha, 0)\right], \tag{4.2}$$

where $B(z;a,b) \equiv \int_0^z u^{a-1}(1-u)^{b-1}du$ and $x = r/r_s$.

Our Bayesian fitting procedure is similar to those of Katz et al. (2017); Li et al. (2020). As the late-type galaxies studied are rotationally dominated, we assume the rotational speed is equal to the circular speed. We try a non-fiducial model where we add 10km/s in quadrature to all velocities as a crude "asymmetric drift" correction, and find it does not affect our results (see Bureau & Carignan 2002; Oh et al. 2015; Iorio et al. 2016 for a full discussion of asymmetric drift). The total circular speed, $V_{\rm c}(r)$ is equal to the sum in quadrature of the circular speed due to the dark matter and each baryonic component (dark matter, gas, stellar disc, stellar bulge)

$$V_{\rm c}^2(r) = V_{\rm DM}|V_{\rm DM}| + \Upsilon_{\rm bulge}V_{\rm bulge}|V_{\rm bulge}| + \Upsilon_{\rm disc}V_{\rm disc}|V_{\rm disc}| + V_{\rm gas}|V_{\rm gas}|, \tag{4.3}$$

where each V is also a function of r, and $\Upsilon_{\rm bulge/disc}$ is the mass-to-light ratio of the bulge or disc. The latter are tabulated in the SPARC database for each galaxy. The baryonic mass models depend on the assumed distance as

$$V_{\rm disc,bulge,gas}(r) \propto \sqrt{D}, \tag{4.4}$$

and the radius depends on the assumed distance as

$$r \propto D. \tag{4.5}$$

The model prediction for the line-of-sight rotational speed is found by correcting $V_{\rm c}(r)$ for the inclination i of the galaxy ($i = 0°$ face-on; $i = 90°$ edge-on)

$$V_{\rm pred}(r) = V_{\rm c}(r)\sin i. \tag{4.6}$$

D, i, Υdisk and $\Upsilon_{\rm bulge}$ are free parameters in the inference. When fitting to the full RC, $V_{\rm pred}(r)$ can be compared directly to the observed RC. For the summary statistics, $V_{\rm pred}(r)$ is evaluated at the same radii as the observed data points, and then the same algorithm that was used to calculate each summary statistic from the observed RC is applied.

4.3.2 Definition of $V_{\rm flat}$

The algorithm to calculate $V_{\rm flat}$ in the SPARC database (see Lelli et al. 2015) starts by defining the outermost observed data point as being the flat part of the RC, and then adds additional points to it iteratively. At each step the next innermost data point at radius r_{i-1} is added if its speed is within 5% of the mean of the data points already included:

$$\Delta \equiv \frac{|\overline{V} - V_{i-1}|}{\overline{V}} < 0.05. \tag{4.7}$$

If the difference is greater than 5% the process terminates, and $V_{\rm flat}$ is the mean of the points already included. A galaxy is only considered to have a defined $V_{\rm flat}$ if the flat part constitutes at least three points when the algorithm terminates. The definition depends on the distance between the points, which means finely sampled RCs can still be considered flat even if they are much steeper than less finely sampled RCs. To lessen this bias we change the condition to a limit on Δ per stellar disk scale length ($R_{\rm disc}$),

$$\frac{\Delta}{(R_i - R_{i-1})/R_{\rm disc}} < 0.10. \tag{4.8}$$

The condition is set to 10% per disc scale length so $V_{\rm flat}$ is defined for a similar number of galaxies (123) as the original definition (133). Our results are not sensitive to the exact value. For galaxies which meet both the old and new $V_{\rm flat}$ definition, the difference between the two values is negligible.

4.3.3 HI linewidth model

The summary statistics $V_{\rm max}$,$V_{2.2}$ and $V_{\rm flat}$ can be calculated from the RC alone. To calculate a model $W_{\rm p20}$ that can be compared to the observed value, we must calculate a model HI

integrated spectrum from the RC and the HI surface density profile. which we do using the model developed in Chapter 3. The model $W_{\rm p20}$ summary statistic can be trivially calculated by finding a peak of the distribution, and moving outwards to larger speed until until the flux drops to 20% of the maximum.

4.3.4 Inference

Bayes' theorem is used to calculate the probability of our parameters θ condition on our data D given the model $\mathcal{M}$,

$$\mathcal{P}(\theta|D,\mathcal{M}) = \frac{\mathcal{L}(D|\theta,\mathcal{M})\pi(\theta|\mathcal{M})}{p(D|\mathcal{M})}, \tag{4.9}$$

where $\mathcal{L}(D|\theta,\mathcal{M})$ is the likelihood of the data, $\pi(\theta|\mathcal{M})$ is the prior probability density and $p(D|\mathcal{M})$ the marginalised likelihood. For $V_{\rm flat}$,$V_{\rm max}$,$V_{2.2}$,$\rm W_{p20}$, which consist of a single observation, the likelihood of the data is

$$\mathcal{L}(W_{\rm obs}|\theta,\mathcal{M}) = \frac{\exp\{-(W_{\rm obs}-W_{\rm pred})^2/(2\delta W_{\rm obs}^2)\}}{\sqrt{2\pi}\delta W_{\rm obs}}, \tag{4.10}$$

where $W_{\rm obs}$ is the observed velocity summary statistic and $W_{\rm pred}$ the model prediction. For the full rotation curve the likelihood is

$$\mathcal{L}(D|\theta,\mathcal{M}) = \prod_i \frac{\exp\{-(V_{\rm i,obs}-V_{\rm pred}(r_{\rm i}))^2/(2\delta V_{\rm i,obs}^2)\}}{\sqrt{2\pi}\delta V_{\rm i,obs}}. \tag{4.11}$$

When fitting with summary statistics we find some galaxies have non-zero posterior probability at $M_{\rm halo} = 0$. Therefore in order to raise the lower limit of the posterior to a finite value we sample $\log M_{\rm tot} = \log(M_{\rm halo} + M_{\rm bar})$ rather than $M_{\rm halo}$ itself, setting the lower bound on its flat prior to be $\log M_{\rm bar}$. A minimum baryonic content for each galaxy regardless of Υ is ensured by the HI mass, which is relatively well constrained by observations and so is not allowed to vary in our model (apart from through its dependence on distance).

The total free parameters are $\{M_{\rm tot}, c_{0.1}, \Upsilon_{\rm disc}, \Upsilon_{\rm bulge}, i, D\}$ (summarised in Table 4.2). The priors on $\Upsilon_{\rm disc}$ and $\Upsilon_{\rm bulge}$ are lognormal with means of $\log(0.5)$ and $\log(0.7)$ respectively, and 0.1 dex scatter (following Li et al., 2020). The priors on i and D are normal with mean given by the observed values and scatter by the observational uncertainties from SPARC. The posterior is sampled using the `emcee` ensemble sampler (Foreman-Mackey et al., 2013). We set the number of walkers to 200 and the stretch move to $a = 2$. To ensure the chain is converged we run the sampler until the chain is at least 50 times the autocorrelation length (Goodman & Weare, 2010) in all parameters, or a minimum of 10,000 steps to ensure the posterior is densely sampled to aid in the calculation of $D_{\rm KL}$. The first 25 autocorrelation lengths are discarded as burn-in.

4.3.5 Goodness-of-fit

We wish to examine the dependence of constraining power on the type and precision of the measurements. A nuisance effect is that constraints can be very tight for models that are a poor fit to the data, as a small fraction of parameter space can still have high likelihood relative to the rest of it, even if the absolute value of the likelihood is low for that region (a problem previously identified for rotation curves, e.g. Li et al. 2020).

To exclude galaxies that are poor fits to a particular profile, we examine the distribution of normalised residuals

$$\mathcal{R}_i = \frac{V_{\rm i,obs} - V_{\rm pred}(r_{\rm i})}{\delta V_{\rm i,obs}}, \tag{4.12}$$

evaluated for the i RC datapoints of a galaxy. The set of $\mathcal{R}_i$ should be drawn from a standardised normal distribution if the model is perfect (Andrae et al., 2010; Zentner et al., 2022). We identify galaxies as having poor fits if the probability that the distribution of residuals is drawn from a standardised normal is $p_{\rm fit} < 0.05$, as calculated by the Kolmogorov–Smirnov test (Massey, 1951). The probabilistic nature of the test means it is more stringent for better sampled rotation curves, which is desirable as better sampled

rotation curves generally give stronger constraints on halo properties. We define a galaxy as overfit if $p_{\rm fit} < 0.05$ and the standard deviation of their residuals is less than 1, and underfit if $p_{\rm fit} < 0.05$ and the standard deviation of residuals is greater than 1. This procedure finds 23 (14) galaxies to be underfit and 8 (11) overfit for the NFW (Burkert) profile in the fiducial model. These are removed from the sample.

We find that the galaxies for which Burkert is underfit have higher than average mass, but for NFW there is no clear trend with any galaxy property (including inclination). There is no clear trend for overfitting using either halo profile. Finally, removing under/overfit galaxies does not significantly impact the distribution of $D_{\rm KL}$ for the sample. This suggests that whether or not the above procedure has identified all poor fits, the issue of poorly fitting galaxies having tight constraints is unlikely to bias our subsequent analysis of $D_{\rm KL}$.

4.3.6 Abundance matching

For reference we also show the information gain on halo properties from abundance matching, an empirical model that matches the haloes in simulations to observed galaxies by positing an approximately monotonic relationship between a halo property (the *proxy*) and a galaxy observable (e.g. Kravtsov et al. 2004; Conroy et al. 2006). In the simplest model the proxy is halo mass and the galaxy observable is stellar mass or luminosity. We use the proxy of Lehmann et al. (2016) which models assembly bias through the hybrid proxy $v_\beta := V_{\rm halo} \left(\frac{v_{\rm max}}{V_{\rm halo}}\right)^\beta$, where $v_{\rm max}$ is the maximum circular velocity of the halo, and $V_{\rm halo}$ is the velocity at the virial radius. The free parameters in the model are the AM scatter $\sigma_{\rm AM}$ and β, which they constrain by clustering to $\beta = 0.57^{+0.20}_{-0.27}$ and $\sigma_{\rm AM} = 0.17^{+0.03}_{-0.05}$. We calculate the posterior on mass–concentration using the Bayesian inverse subhalo abundance matching scheme developed in Chapter 3, sampling over $\sigma_{\rm AM}$ and β.

4.3.7 The Kullback–Leibler divergence

The Kullback–Leibler divergence (Kullback & Leibler, 1951) can be used to quantify the information gain in an experiment in going from the prior distribution to the posterior in units of bits

$$D_{\mathrm{KL}}(P \parallel \pi) = \int_{\theta} \mathcal{P}(\theta) \log_2 \left(\frac{\mathcal{P}(\theta)}{\pi(\theta)} \right) \mathrm{d}\theta. \tag{4.13}$$

It quantifies the similarity between $\mathcal{P}(\theta)$ and the reference distribution $\pi(\theta)$. In information theory terms it is the excess surprise when using $\mathcal{P}(\theta)$ compared to $\pi(\theta)$. More intuitively it can be interpreted as the expectation of the logarithm of the ratio of the posterior and prior with respect to the posterior . This integral over a measure of difference between the two distributions is a more appropriate quantity than simply calculating the difference in information between the two distributions ($\int_{\theta}[\mathcal{P}(\theta) \log_2 (\mathcal{P}(\theta)) \ - \pi(\theta) \log_2 (\pi(\theta)) \ ] \mathrm{d}\theta$), which can still be zero even if the posteriors are not identical (e.g. if one is a translation in θ of the other). Formally it can be shown that the Kullback-Leibler divergence is the only quantity that satisfies a number of desiderata required for a measure of information gain (Hobson, 1969), which are generalisations of the axioms used for defining Shannon information (e.g. Shannon & Weaver, 1949).

It is the appropriate metric to use when comparing the improvement on precision in constraints between two experiments (Buchner, 2022), as it takes into account the full probability distributions, as opposed to comparing a summary statistic such as the 2σ credible interval. However this comes at the expense of ease of interpretation. An intuitive example is an experiment with a flat prior that produces a flat posterior that has a k times smaller hypervolume. In this case $D_{\mathrm{KL}} = \log_2(k)$.

To calculate D_{KL}, kernel density estimation (KDE) is used to estimate the posterior probability distribution. We use the fastKDE algorithm (O'Brien et al., 2014, 2016), which selects the kernel and bandwidth based on the criteria of Bernacchia & Pigolotti (2011). We ensure that D_{KL} is converged with respect to the number of MCMC samples by checking

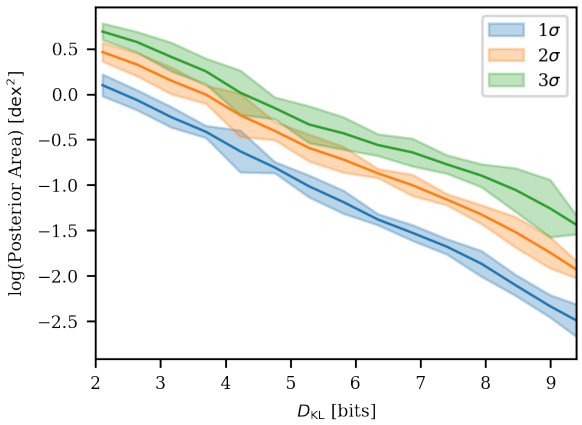

Figure 4.1: The correlation between the KL divergence ($D_{\rm KL}$) of the posterior from the prior in $M_{\rm tot} - c_{0.1}$ space and the area of the 2D posterior (for varying confidence intervals) from fitting Burkert haloes to the full RC for the whole sample of galaxies. The solid lines show the mean posterior area in bin of $D_{\rm KL}$ (15 bins total), with the band showing the 1σ spread in each bin. $D_{\rm KL}$ and posterior size are strongly correlated, with a small scatter due to changing shapes of the posteriors and the prior on $M_{\rm tot}$ that is a function of the galaxy's $M_{\rm bar}$.

that our results do not change when using a shorter or longer chain.

In Fig. 4.1 we plot $D_{\rm KL}$ against the 2D credible interval size for one of our runs, showing the strong correlation between them. Two factors cause a scatter between $D_{\rm KL}$ and the size of a contour. Firstly two posteriors with the same size 2σ contours will have a different $D_{\rm KL}$ if the rest of their contours are different. The prior on $M_{\rm tot}$ is also a function of the galaxy's $M_{\rm bar}$. $D_{\rm KL}$ is dependent on the size of the prior. Our prior bounds are well motivated for mass, and the lower bound of concentration. However the upper bound of concentration is arbitrary. However we are interested in the relative $D_{\rm KL}$ between different measures, so our conclusions are not sensitive to the choice of prior.

4.3.8 A predictive model for $D_{\rm KL}$

We aim to study the dependence of $D_{\rm KL}$ on the properties of the measurement and the properties of the galaxy. To do this we build a predictive model for $D_{\rm KL}$ using the `ExtraTrees` algorithm (Pedregosa et al., 2011). We optimise the hyperparameters through a grid search

with 5-fold cross-validation (see Kohavi, 1995). The features are the set of galaxy properties listed in the SPARC database. In addition, when fitting using the full RC, we add the following features that describe the details of the galaxy and RC: N (the number of RC data points); $R_{\rm out}$ (the radius of the outermost data point); $R_{\rm out}/R_{\rm eff}$ (the ratio of the radius of the outermost data point to the effective radius of the galaxy); $\frac{1}{N}\sum_i V_{\rm obs,i}/V_{\rm bar,i}$ (the mean ratio of the observed velocity to the baryonic circular velocity, which quantifies the mean dark matter dominance); $V_{\rm obs}(r)/V_{\rm bar}(r)$ at the radii $R_{\rm out}$, $R_{\rm disk}$ and $R_{2.2}$ (this quantifies the dark matter dominance at different points in the galaxy); the summary statistics and their uncertainties; $\delta V_{\rm out}/V_{\rm out}$ (the uncertainty on the outermost data point); $\frac{1}{N}\sum_i \delta V_{\rm obs,i}/V_{\rm obs,i}$ (the mean velocity uncertainty). When fitting using individual summary statistics, as most of the above features are not relevant, we only add the summary statistic and its uncertainty, as well the ratio of the summary statistic to the baryonic circular velocity at the corresponding radius e.g. $V_{\rm max}/V_{\rm bar}(R_{\rm max})$.

To find which features are most important in determining $D_{\rm KL}$, we use the feature importance analysis method of Chapter 3 (defined in section 3.3.2.2), assessing the accuracy of the model's predictions are assessed using the coefficient of determination.

4.4 Results

4.4.1 Summary statistics

4.4.1.1 Overview

In our primary analysis we wish to study the dependence of the KL divergence ($D_{\rm KL}$) on the type of measurement, properties of the measurement, and properties of the galaxy. In Fig. 4.2 we show the distribution of $D_{\rm KL}$ when fitting to the different types of measurement in the kinematic inference: the full RC, $W_{\rm p20}$, or the summary statistics (see Table 4.1). The full rotation curve produces the tightest constraints, with a fairly flat distribution of

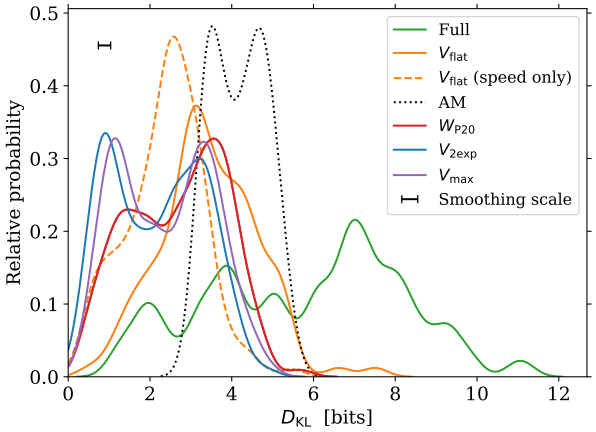

Figure 4.2: Kernel density estimation plots showing the distribution of the Kullback–Leibler divergence ($D_{\rm KL}$) for the different types of measurement, smoothed with a Gaussian kernel with a standard deviation of 0.3 $D_{\rm KL}$ to remove unphysical small-scale noise. The full rotation curve ("Full") contains the most information. The single point summary statistics ($W_{p20}/V_{max}/V_{2.2}$) contain much less information and are similar to each other. $V_{\rm flat}$ has much less information than the full RC, albeit more than other summary statistics, showing the importance of the inner parts of the RC in constraining the shape of the halo and breaking the degeneracy between mass and concentration. Abundance matching has more information than any measure except the full RC.

$D_{\rm KL}$ between 4 and 10 bits (corresponding roughly to posteriors that are 16 and 1000 times smaller than the prior). The broad distribution of $D_{\rm KL}$ is due to the massive variation both in measurement properties and galaxy properties across the sample. The summary statistics and W_{p20} produce similar distributions in $D_{\rm KL}$, with a minimum of close to 0 bits (meaning the posterior is similar to the prior) and a maximum of 6 bits (approximately half that of the full RC fits). $V_{\rm flat}$ has a higher mean $D_{\rm KL}$ than the other summary statistics. We also show the distribution of $D_{\rm KL}$ from abundance matching, which is narrow and has a mean 1-2 bits higher than the summary statistics.

We use the `ExtraTrees` algorithm to construct a predictive model for $D_{\rm KL}$ and carry out a feature importance analysis (as described in Section 4.3.8) and show the results in Fig. 4.3. The model is moderately predictive, with an accuracy of $R_2 = 0.77$. The most important features for predicting $D_{\rm KL}$ are, in descending order of importance: the number of data points N, the uncertainty on the outermost measured velocity $\delta V_{\rm out}/V_{\rm out}$, the fractional

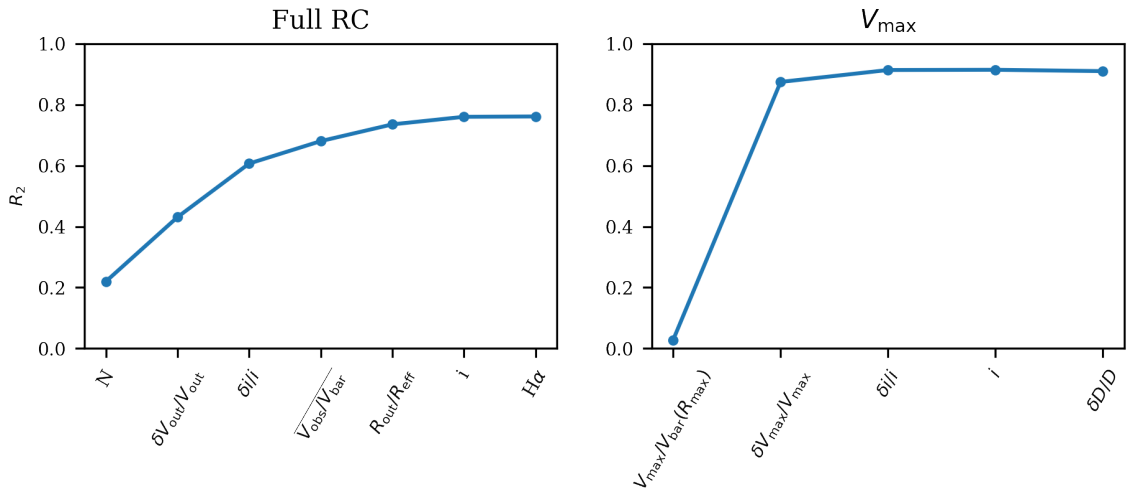

Figure 4.3: The important features for predicting the KL divergence ($D_{\rm KL}$) from fitting to the full rotation curve (*left panel*) and fitting to $V_{\rm max}$ (*right panel*) using an ExtraTrees regressor. Features are added left to right in the order which maximises accuracy at each increment, as described in Section 4.3.8. No features are predictive on their own, but for the full rotation curve the combination of number of data points N, the fractional uncertainty on the outermost measured velocity $\delta V_{\rm out}/V_{\rm out}$, the fractional uncertainty on inclination $\delta i/i$, and the mean ratio of observed rotational velocity to baryonic circular velocity $\overline{V_{\rm obs}/V_{\rm bar}}$ (a measure of dark matter dominance) give reasonable accuracy, with $R_2 = 0.77$. For $V_{\rm max}$ a combination of $V_{\rm max}/V_{\rm bar}(R_{\rm max})$ and the fractional uncertainty $\delta V_{\rm max}/V_{\rm max}$ give good accuracy ($R^2 = 0.9$). The full list of features used in our analysis are described in Sec. 4.3.8, but includes all galaxy properties (such as stellar mass) given in the SPARC database, as well as additional features characterising the rotation curve (such as Hα, a binary variable for whether or not a galaxy has Hα kinematic data.)

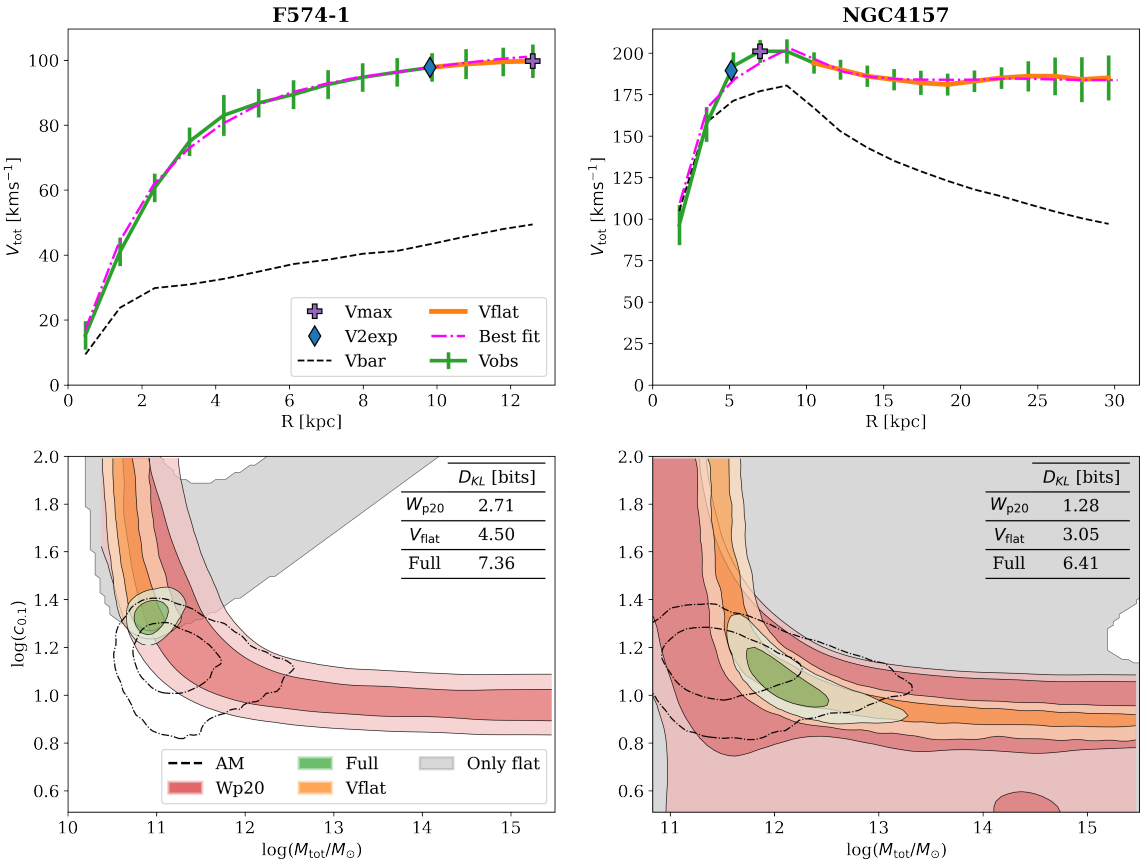

Figure 4.4: Comparison between observed and model rotation curves (*top panels*), and the posteriors in mass–concentration space for F574-1 (*left panel*), a low-surface brightness galaxy, and NGC4157 (*right panel*), an intermediate mass spiral galaxy. Different colours in the bottom panel show posteriors computed from fitting to the full rotation (green), fitting to the HI linewidth W_{p20} (red) and fitting to the V_{flat} summary statistic (orange, see Section 4.3.2). The grey shows the posterior from just requiring that the rotation curve flatness condition be met, without matching the actual value of V_{flat}. The D_{KL} of each posterior is shown on the right. The posteriors for V_{max} and $V_{2.2}$ are not shown, but are similar to W_{p20}. The abundance matching posterior for each galaxy is also shown for comparison.

uncertainty on inclination $\delta i/i$, the mean ratio of the observed velocity to baryonic circular velocity $\overline{V_{\rm obs}/V_{\rm bar}}$ and the ratio of the radius of the outermost data point to the effective radius $R_{\rm out}/R_{\rm eff}$. We reiterate that the uncertainties on $V_{\rm obs}$ do not include a contribution from inclination - which is treated separately.

As illustrative examples, in Fig. 4.4 we show the RCs and posteriors of F574-1, a low surface-brightness galaxy, and NGC4157, an intermediate mass spiral galaxy. F574-1 is an example of a galaxy that is dark matter dominated. Its RC gradually rises and levels off to a flat part close to the last measured point. NGC4157 is baryon-dominated in its inner parts, with a RC that sharply rises to a maximum velocity that corresponds to the peak in the stellar velocity, before declining slightly to the flat part. Both galaxies have a similar number of data points, and uncertainties on observed distance and inclination. In general dark matter dominated galaxies have tighter constraints on halo properties, as when $V_{\rm bar}$ is low relative to $V_{\rm obs}$, the uncertainties on $V_{\rm bar}$ (which are set by the uncertainties on the mass-to-light ratios) are less important. The RC of F574-1 is also sampled further out into the halo (relative to the virial radius) than NGC4157, contributing to its tighter constraints.

We note that stellar mass and surface brightness, which were input features to our feature importance analysis, do not appear among the features identified as important for predicting $D_{\rm KL}$. This is because, although they are correlated with the dark matter fraction, they do not themselves directly impact the strength of the constraints on halo properties. Once $\overline{V_{\rm obs}/V_{\rm bar}}$ (when fitting to the full RC) or $V_{\rm max}/V_{\rm bar}(R_{\rm max})$ (when fitting to $V_{\rm max}$) are selected, adding stellar mass or surface brightness does not improve predictivity further.

4.4.1.2 $\mathbf{W_{p20}}$, $\mathbf{V_{2.2}}$, $\mathbf{V_{max}}$

Using either $W_{\rm p20}$, $V_{2.2}$ and $V_{\rm max}$ in the inference produces posteriors that are very similar in shape for most galaxies. We show the posteriors for $W_{\rm p20}$ in Fig. 4.4. As we have assumed the halo is spherically symmetric, the circular velocity due to the halo depends solely on its enclosed mass. This results in a complete degeneracy between the halo mass and

concentration for $W_{p20}/V_{2.2}/V_{max}$, which do not constrain the shape of the RC. For the dark matter dominated F574-1, the posteriors are simply a band corresponding to the additional circular velocity required from the dark matter to generated the observed $W_{p20}/V_{2.2}/V_{max}$, thickened by the its observational uncertainty and the uncertainties on i, D and $\Upsilon_{disk/bulge}$.

For NGC4157 the constraints on halo properties from $W_{p20}/V_{2.2}/V_{max}$ are extremely weak, as the baryons alone can generate the observed values of these summary statistics. Therefore a large range of haloes are compatible with observation, as long as they do not significantly change: the mass enclosed within the HI disk for W_{p20}; the maximum observed velocity for V_{max}; the velocity at $R_{2.2}$ for $V_{2.2}$. These three criteria result in similar constraints: a halo must have mass or concentration low enough such that there is no significant halo mass at lower radii. In the case of W_{p20}, the degeneracy between mass and concentration can be broken by fitting the full HI flux profile rather than just the linewidth, as an extended, flat RC produces a very different HI profile to a RC that peaks and then declines (as occurs with very low mass / concentration haloes). We leave this to future work.

The mean D_{KL} for $W_{p20}/V_{max}/V_{2.2}$ is 2.76/2.41/2.27. In Fig. 4.3 we present the D_{KL} feature importance analysis for V_{max} only. V_{max} is chosen because it is available for more galaxies than W_{p20} and $V_{2.2}$, but all three give similar results. The important features are, in descending order: $V_{max}/V_{bar}(R_{max})$ (which measures the dark matter-dominance at R_{max}), $\delta V_{max}/V_{max}$, its fractional uncertainty, and $\delta i/i$. We interpret the ordering of the mean D_{KL} for the three measurements as being due to the dark matter dominance of the region probed by each quantity. The HI disc extends beyond $R_{2.2}$, and so probes the RC in the more dark matter-dominated outer regions. For most galaxies in our sample, V_{max} coincides with the outer point of the RC (as in F574-1), which is typically beyond $R_{2.2}$. However for the galaxies with baryon-dominated inner regions such as NGC4157 V_{max} roughly coincides with $R_{2.2}$. Hence the mean D_{KL} for V_{max} is between W_{p20} and $V_{2.2}$.

4.4.1.3 $V_{\mathbf{flat}}$

$V_{\rm flat}$ has higher mean $D_{\rm KL}$ than $W_{\rm p20}$, $V_{\rm max}$ and $V_{2.2}$. Its posteriors (see Fig. 4.4) are either a band similar to $W_{\rm p20}$ (NGC4157) or a truncated band (F574-1). There are two distinct contributors to the constraining power on halo properties from the $V_{\rm flat}$ statistic. The first is that $M_{\rm vir}$ and $c_{0.1}$ must generate a RC that meets the flatness criterion. If this is met, then the velocity of the flat part of the model RC must also be equal to the observed $V_{\rm flat}$. The second criteria is similar to the summary statistics $V_{2.2}$ and $V_{\rm max}$, in that it simply requires one part of the RC to be a certain value, resulting in a degenerate band posterior. It is the flatness criterion that can truncate the band, as it does for F574-1.

To demonstrate the behaviour of the flatness criterion in isolation, in Fig. 4.4 we show the regions for which the RC is considered flat in grey. The shape of the RC depends on the parameters describing the baryons, so we consider a given $M_{\rm tot}, c_{0.1}$ to meet the flatness criterion if the probability of the RC being flat is $> 34\%$ (i.e. 1σ) when marginalising over D and Υ. A much smaller region of the $M_{\rm tot}, c_{0.1}$ prior is considered flat for F574-1 than NGC4157. This is because for NGC4157 the RC with baryons alone is considered flat, as it is gently declining over many disc scale lengths. But generating a flat RC for F574-1 requires a dark matter halo that is both dominant over the baryonic component and has high enough concentration to have reached the gently declining "flat" part by the outer most RC point.

To separate the second criteria out from the flatness requirement, we calculate $D_{\rm KL}$ for a new summary statistic: V_{flat} *(speed only)*. This is a single data point that is the mean speed of the flat part of the RC, occurring at its mean radius, without any flatness requirement. We see in Fig. 4.2 that the $D_{\rm KL}$ for $V_{\rm flat}$ (speed only) are similar to $W_{\rm p20}$,$V_{\rm max}$ and $V_{2.2}$. This exercise demonstrates the extra constraining power that comes from observing a flat rotation curve over its length, compared to just measuring a single point from it.

We train an `ExtraTrees` regressor on $D_{\rm KL}$ for $V_{\rm flat}$, but found it to be poorly predictive. This is due to difficulty in predicting the size of the region for which the flatness criterion

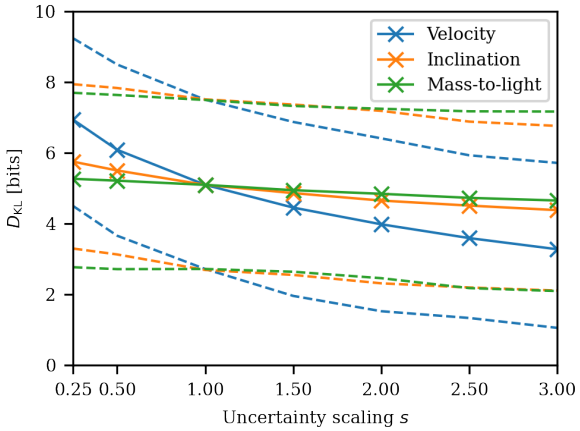

Figure 4.5: The dependence of D_{KL} on the uncertainties on velocity, inclination and mass-to-light ratio. At each point, the uncertainties are scaled on either the velocities, the inclination, or the mass-to-light ratios on the bulge and disk by a constant factor s (such that $\delta' = s\delta$) and the D_{KL} from fitting to the full rotation curve is recalculated for each galaxy. Any galaxy that is considered underfit (see 4.3.5) for any value of s for any of velocity/inclination/mass-to-light is excluded from this analysis. Therefore D_{KL} is calculated for the same sample of 98 galaxies for all points. The solid lines show the mean of D_{KL} at each value of s (marked by crosses), and the dashed lines show the 16th and 84th quantiles of the distribution. D_{KL} is most dependent on the velocity uncertainties.

is met, which depends on the detailed shape of the circular velocity due to the baryons.

4.4.2 D_{KL} as a function of measurement properties

In the feature importance analysis the uncertainties on inclination and velocity were found to be important predictors of D_{KL}. We now isolate their effect on D_{KL} for the full RC by scaling their uncertainties by a constant factor s, i.e. $\delta V_{\mathrm{obs,scaled}} = s\delta V_{\mathrm{obs}}$ or $\delta i_{\mathrm{obs,scaled}} = s\delta i_{\mathrm{obs}}$, and repeating the inference. We do this for δV_{obs} and δi separately, for a range of values of s. We also apply the same procedure to the scatter on the prior of $\Upsilon_{\mathrm{disc/bulge}}$ (changing it for both disc and bulge simultaneously).

We exclude bad fits using the residual analysis described in Section 4.3.5. To ensure we use the same sample for all three quantities, galaxies are only included if they are not bad fits for any value of s for all of V_{obs}, i and $\Upsilon_{\mathrm{disc/bulge}}$. With a minimum value of $s = 0.25$ (the fits are worst for lower s), this leaves 98 galaxies in the sample. We show their D_{KL} as a

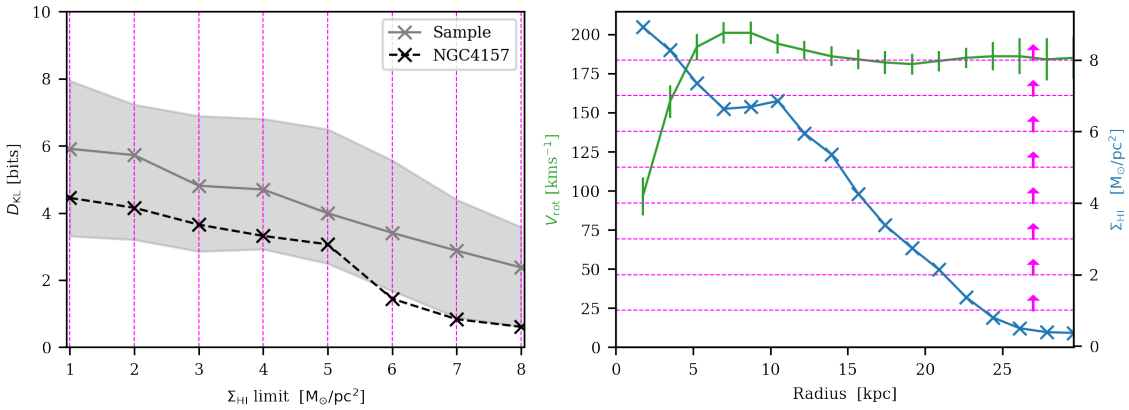

Figure 4.6: The dependence of D_{KL} (grey line, sample mean; band, 16th and 84th quantiles) on the minimum HI surface density probed $\Sigma_{\mathrm{HI,min}}$ (left panel). The procedure for varying $\Sigma_{\mathrm{HI,min}}$ is illustrated for a single galaxy (NGC4157) in the right panel: for each value of $\Sigma_{\mathrm{HI,min}}$ (pink lines), only the data points of the rotation curve (blue) at radii where $\Sigma_{\mathrm{HI}} > \Sigma_{\mathrm{HI,min}}$ (i.e. green > pink) are used in the inference. The D_{KL} for NGC4137 is shown as a dashed line in the left panel. This analysis is only applied to the subsample of 54 galaxies that each have an HI surface density profile that spans all the way from 1 to 8 $\Sigma_{\mathrm{HI}}/M_\odot\mathrm{pc}^{-2}$. For this sample, D_{KL} increases strongly (with an approximately linear relationship) as $\Sigma_{\mathrm{HI,min}}$ is reduced and the lower surface density regions towards the outskirts of the galaxy are added to the observation.

function of s in Fig. 4.5. D_{KL} shows the greatest dependence on the velocity uncertainties, and is relatively flat for the rest. The rate of increase in D_{KL} steepens as s decreases for δV_{obs} and i.

R_{out} was identified as an important feature for predicting D_{KL}. It is set by the minimum HI surface density probed by the observation. We study the effect of varying the minimum HI density on D_{KL}, by repeating the inference with modified RCs that only include data points at radii where the HI surface density is above a chosen minimum value, which we vary. In this analysis we include only galaxies that each have a $\Sigma_{\mathrm{HI}}(r)$ that fully spans the range 1 to 8 $\mathrm{M}_\odot/\mathrm{pc}^2$, and which do not have $H\alpha$ observations, leaving 45 galaxies. The D_{KL} for this sample is shown in Fig. 4.6. If one knew the uncertainty on Σ_{HI}, an alternative approach would be to vary the minimum signal-to-noise ratio rather than the surface density.

In Fig. 4.6 we notice a sharp gain in D_{KL} that corresponds to the rotation curve reaching the flat part for NGC4157. This could indicate the important thing is to reach the flat part of

the RC, and the information gain is lower afterwards. To investigate this for our subsample of galaxies, we calculate the radius corresponding to the largest increase in $D_{\rm KL}$ with radius ($R_{\rm gain}$), and plot it against the radius at which the rotation curve reaches its flat part. We define $R_{\rm flat}$ as the radius of the innermost datapoint that is considered to be in the flat part of the RC (as defined in 4.3.2). We show the result in Fig. 4.7. We notice that although there is no strong correlation, $R_{\rm gain}$ does not occur much beyond $R_{\rm flat}$ for any of the galaxies. This suggests that significant gains in information tend not to come after the RC flattens, although the largest gain in information does not necessarily come on reaching the flat part, mostly occurring at lower radii. It is however possible the lack of correlation stems from the ambiguity in defining where the flat part of the rotation curve begins.

4.4.3 Halo profile comparison

We now study the constraining power of observations on whether a halo has a cusp or a core. In contrast to $D_{\rm KL}$, we found that it was not possible to generate a decently predictive model for the precision of the inner slope constraints from the galaxy/RC features. This is likely because the relationship between galaxy/RC properties and the precision of inner slope constraints is more complicated than for $D_{\rm KL}$, and so a larger sample size is required to generate a predictive model. Therefore we instead focus on analysing how varying individual features affects the the precision of the inner slope constraints.

In the $D_{\rm KL}$ analysis $\delta V_{\rm obs}$ was found to be the most important measurement uncertainty. Therefore we study the dependence of the likelihood ratio test between a NFW and Burkert profile on $\delta V_{\rm obs}$, using the same uncertainty scaling procedure as above. We plot the resulting distribution of likelihood ratios in Fig. 4.8. We interpret a likelihood ratio greater than 100 as one halo profile being significantly favoured over the other. For $s = 1$ (no scaling) this occurs for around 30% of galaxies, with most favouring Burkert. For $s = 2$ this drops to 15%, and for = 0.5 it rises to 70%.

Another way of looking at this is to examine how much constraining power an obser-

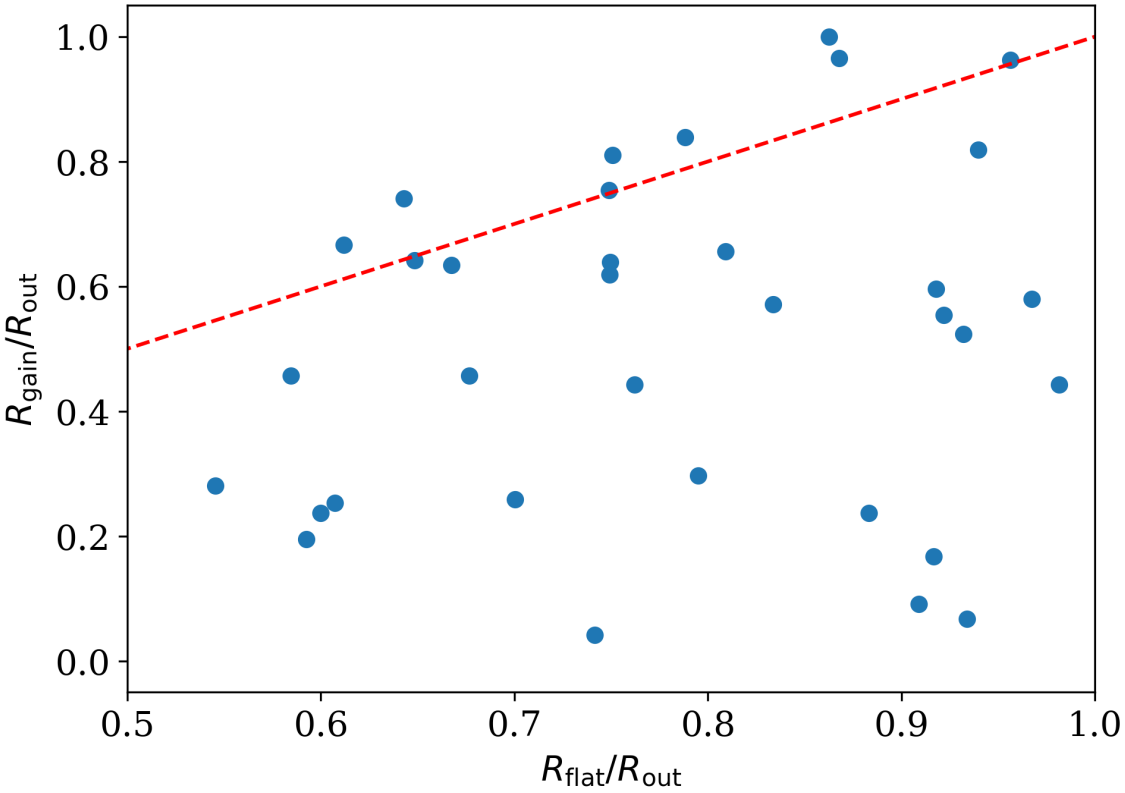

Figure 4.7: The radius at which the increase in D_{KL} is greatest (R_{gain}) plotted against the radius at which the rotation curve becomes flat (R_{flat}), with both radii normalised by the radius of the outermost data point (R_{out}). The line of equality is shown in red. R_{gain} does not occur at values much larger than R_{flat} for any galaxy, suggesting the largest gains in information do not come after the RC flattens out. However for most galaxies the largest gains in information actually occur at lower radii.

vation has on the shape parameter of 3 parameter halo profiles. The α parameter of the gNFW profile controls to the gradient of the inner slope. A cusped profile has $\alpha = 1$ and a cored profile $\alpha = 0$. We repeat the uncertainty scaling procedure above, but this time fitting a gNFW profile instead. The uncertainty on the marginalised α parameter (which we take to be its standard deviation, std(α) measures how well the inner slope is constrained. A galaxy with a smaller uncertainty on α has a better known inner halo shape, with $\Delta\alpha = 1$ the difference between a cored and a cusped $(1/r)$ inner profile. We study the distribution of std(α) for the sample as a function of s in Fig. 4.8. The mean scatter on α only drops below 0.2 for $s \sim 0.6$. In the right column of Fig. 4.8, we repeat the same halo profile comparison analysis as above, but this time varying the minimum HI density instead s. We find the dependence is much weaker than for $\delta V_{\rm obs}$.

Another possibly important factor for determining the inner slope constraints is whether or not a galaxy has $H\alpha$ observations. We split the sample in two, and find galaxies with $H\alpha$ have a mean std(α) of 0.23, but those without have a mean of 0.3. We have checked the two populations of galaxies do not significantly differ with respect to other variables that drive the constraints on $D_{\rm KL}$, and so conclude that adding $H\alpha$ observations moderately reduces the uncertainty on the inner slope (comparable to halving the velocity uncertainties from their fiducial values).

4.5 Discussion

4.5.1 Predicting information gain

Constraining halo mass and concentration from fits to rotation curve data is routine procedure in the study of late-type galaxies. However, to our knowledge, this study is the first to formally quantify the precision of the constraints and study their variation with galaxy and measurement properties. For the SPARC sample, we found massive variation in precision on $M_{\rm tot}$ and $c_{0.1}$ when fitting to the full RC, ranging from 1 to 11 bits of information gain.

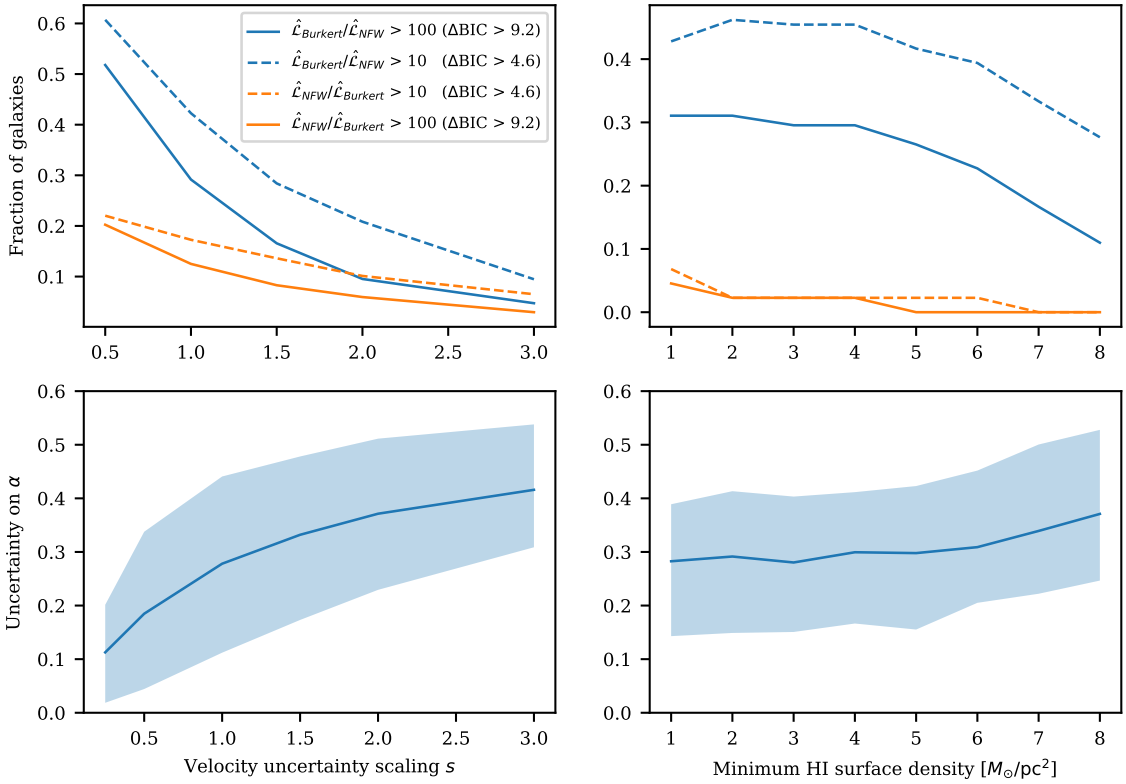

Figure 4.8: *Top panels:* The fraction of galaxies in the sample for which the ratio of the maximum likelihood estimates of the two profiles $\hat{\mathcal{L}}_{\rm Burkert}/\hat{\mathcal{L}}_{\rm NFW}$ (or the inverse) is above a certain value, as a function of a multiplicative scaling s of the velocity uncertainties (*left panels*, see Fig. 4.5) and the minimum HI surface density probed (*right panels*, see Fig. 4.6). We interpret $\hat{\mathcal{L}}_{\rm Burkert}/\hat{\mathcal{L}}_{\rm NFW} > 100$ (10) as strongly (moderately) favouring Burkert over NFW (and vice-versa). At $s = 1$ (no scaling) one halo is strongly favoured over another in around ~40% of galaxies, with most favouring Burkert. If the velocity uncertainties are halved ($s = 0.5$), this rises to 70%. For reference we also show the corresponding difference in Bayesian Information Criterion.
Bottom panels: The distribution of the uncertainties on the α shape parameter from fitting a gNFW halo to the full rotation curve (solid line, mean; band, 16th and 84th quantiles in bins of s). Both the uncertainties on α and the likelihood ratios show a strong dependence on the velocity uncertainties, but a weaker dependence on the HI surface density.

This range is equivalent to the difference between a flat prior shrinking to a flat posterior by only a factor of 2 (2^1) compared to $\sim$ 2000 (2^{11}). We created a predictive model for $D_{\rm KL}$ using the `ExtraTrees` algorithm, and conducted a feature importance analysis to identify the galaxy and measurement properties that are the strongest predictors of information gain. The measurement properties are, in descending order of importance: the number of data points N, the fractional uncertainty on the outermost measured velocity $\delta V_{\rm out}/V_{\rm out}$, the fractional uncertainty on inclination $\delta i/i$, and the radius of the outermost measured velocity normalised by the effective radius $R_{\rm out}/R_{\rm eff}$. The only important galaxy property is $\overline{V_{\rm obs}/V_{\rm bar}}$, a measure of the dark matter dominance. N ranks more highly than both the the maximum radius of the RC (although the two are positively correlated, with a Spearman coefficient of 0.58) and whether or not a galaxy has Hα data. This shows the importance of sampling at many points across the RC to constrain the shape.

The moderate predictivity of our model ($R^2 = 0.77$) is part due to the small sample size, and part due to the input features not fully capturing the full details of the RC and the distribution of the baryons. For example N does not account for the autocorrelation of the RC, and $\overline{V_{\rm obs}/V_{\rm bar}}$ is only an average. Our model is more predictive for the fits to the single data point summary statistics, $\rm W_{p20}$, $V_{2.2}$ and $V_{\rm max}$, with the latter giving R^2=0.9 and depending only on the uncertainty on $V_{\rm max}$ and $V_{\rm max}/V_{\rm bar}(R_{\rm max})$, a measure of dark matter dominance.

Our feature importance analysis only ranks the measurement properties by importance. In order to quantify the size of their effect on $D_{\rm KL}$, we varied the uncertainties on velocity and inclination whilst holding the rest of the inference constant. We also varied uncertainties on the mass-to-light ratios $\Upsilon_{\rm disc}$ and $\Upsilon_{\rm bulge}$, applied in our model through the priors. We find that the constraints are most dependent on the velocity uncertainties, with the inclination and mass-to-light showing only weaker dependence. In Fig. 4.6 we calculated the dependence of $D_{\rm KL}$ on the minimum HI density probed (which sets the maximum radius of the RC). Reducing the minimum density by $1\,{\rm M_\odot/pc^2}$ yields an additional 0.4 bits of information

gain. In order to investigate whether this dependence on the minimum HI density simply mirrors the strong dependence on N found earlier (Fig. 4.3), we also plotted $D_{\rm KL}$ / N for the different runs (not shown), and found no strong trend with the minimum HI density. This suggests that the observed trend in $D_{\rm KL}$ with minimum HI density is driven primarily by N, rather than say the points in the outer RC (where the HI density is lowest) yielding disproportionately more information. This concurs with our earlier finding that $R_{\rm out}/R_{\rm eff}$ is a less important feature than N.

Our results can inform future survey design, by highlighting which features of the measurement should prioritised for optimisation. The main way to improve constraints is of course to use longer integration times or higher instrument sensitivity, which would increase the number of data points (Staveley-Smith & Oosterloo, 2015). However specific optimisations are possible. The beam size sets the maximum resolution. At fixed sensitivity/integration time, there is a trade off between minimum HI density that can be probed (i.e. the maximum radius) and resolution, although this can be altered with adaptive smoothing techniques in post-processing (Briggs, 1995). Reducing the velocity uncertainties would require improving the model used to determine the velocities and/or increasing the spectroscopic resolution. SPARC inclinations are produced as output of the fits to the 2D velocity field (Lelli et al., 2016a), so the uncertainties would be reduced by improving the velocity map. Inclination can also be calculated using the ellipticity of the HI zeroth-moment map (Ponomareva et al., 2021), including forward modelling it to the datacube (Mancera Piña et al., 2021), or more imprecisely using optical data. Kourkchi et al. (2022) recently used a combination of machine learning and citizen science to improve inclinations from optical data. Schombert et al. (2022) use stellar population models to study the variation of the uncertainty on Υ with the passband, and the available morphology and colour information.

4.5.2 Summary statistics

We compared the information gain when constraining halo parameters using the full RC, summary statistics or the HI linewidth W_{p20}. Our feature importance analysis found the degree of dark matter dominance at the radius of the velocity measurement was the most important factor in determining D_{KL}. The ranking of mean D_{KL} for the summary statistics from highest to lowest is $\{V_{flat}, W_{p20}, V_{max}, V_{2.2}\}$, which reflects how far out into the halo each measurement probes, and hence the degree of dark matter domination. L19 calculated the intrinsic scatter of the BTFRs constructed using the different summary statistics as the velocity measure. For the ones studied in this paper, they found $\{V_{flat}, W_{p20}, V_{max}, V_{2.2}\}$ had an intrinsic orthogonal scatter of $\{0.026, 0.035, 0.040, 0.070\}$ respectively, which is the inverse ordering of D_{KL}. L19 interpret the amount of scatter to be negatively correlated with the closeness of the summary statistic to the true flat value of the rotation curve (as opposed to the observed V_{flat}, which is limited by maximum radius probed in some galaxies). Hence it is not surprising that the mean information content on halo properties from each measurement is negatively correlated with the scatter of their respective BTFRs.

In this work we chose not to apply a prior based on the mass–concentration relationship from dark matter-only simulations. Although this would have helped break the degeneracy between mass and concentration (see also Sec. 4.1), it would also have imported assumptions from N-body simulations and galaxy formation theory (assembly bias) which we prefer to avoid. However we now qualitatively discuss the effect this prior would have on our results. Applying the mass–concentration prior increases D_{KL} significantly for all galaxies, with the effect greatest when using relatively weak data such as summary statistics for which the mass–concentration degeneracy is especially pronounced. Applying the prior whilst assuming a cuspy profile leads to a finite constraint on halo mass even when using such summary statistics (this is studied for linewidths in more detail in Yasin et al. 2022). However for many galaxies, even with the mass–concentration prior applied there is still a strong remaining degeneracy (e.g. NGC4157 in the right panel of Fig. 4.4), especially

when assuming a cored profile. Nevertheless D_{KL} still increases significantly compared to the no-prior case, even when the degeneracy is not fully broken. It is important to bear in mind however that in this case the information gain is not purely from the kinematic data.

4.5.3 Constraining the inner halo shape

We studied the ability of observations to constraint the inner halo shape in two ways. Firstly we studied the impact of the δV_{obs} uncertainties on the ability to distinguish between the cored Burkert profile and cusped NFW profile using a likelihood ratio test. We found that with the unmodified velocity uncertainties, one profile was decisively favoured over another in 40% of cases, with this rising to 70% when the uncertainties are halved. On the other hand, when the uncertainties are doubled, one halo is only strongly favoured in only 20% of galaxies. We also studied the uncertainty of the inner slope parameter α when fitting a 3-parameter generalised NFW profile. With the normal SPARC uncertainties the mean std(α) is ~0.3 (the change in α is 1 between a cored gNFW profile and a normal NFW profile), but there are a significant number of galaxies with std(α) > 0.5. This suggests a survey with velocity measurements more precise than SPARC is necessary to precisely constrain the inner halo shape for whole samples of galaxies. We repeated the analysis varying the minimum HI density probed, and found a much weaker dependence. This demonstrates the importance of obtaining kinematic datasets with precise velocity uncertainties when targetting the cusp-core problem (see Del Popolo & Le Delliou, 2021, for a review) relative to probing lower HI surface densities.

4.5.4 Comparison to literature

Saburova et al. (2016) used a sample of 14 galaxies from the THINGS survey (Walter et al., 2008) to study the size of the uncertainties on halo parameters derived from rotation curve fitting, in particular identifying the halo concentration as often poorly constrained. The main differences to this paper are our quantification of the constraining power using the Kullback–

Leibler divergence, our focus on the constraining power in the mass–concentration plane rather than the uncertainty on individual parameters, our study of the constraining power as a function of measurement and galaxy properties, and our Bayesian fitting procedure that propagates the uncertainties on galaxy parameters into the constraints on halo properties. In agreement with Saburova et al. we find that for many galaxies the constraining power offered by rotation curves can still be relatively weak (as evidenced by the long tail to low D_{KL} for the full RC in Fig. 4.2).

We have highlighted the important measurement properties which should be targeted by future surveys. Identifying the observational parameters (such as integration time) required to achieve the desired measurement properties is beyond the scope of this work. Recent work has simulated spectroscopic HI observations of simulated late-type galaxies (Oman, 2019), which in theory allows an end-to-end determination of the effect of observational properties such as integration time on the constraints on halo properties. However, our analysis of real observations is an important complementary approach, as simulations still struggle to produce realistic samples of rotation curves (Roper et al., 2022).

In light of increasingly expensive observations, but comparatively cheap computational resources, there are an increasing number of studies examining optimal observational strategies. For example, two recent studies have used the Fisher-matrix formalism to quantify the information content in stellar streams (Bonaca & Hogg, 2018) and the cosmic web (Kostić et al., 2022) in order to identify the best observational strategy.

4.6 Conclusion

We have used the Kullback–Leibler divergence (D_{KL}) of the posterior on total mass–concentration (where total mass is equal to the halo mass plus the galaxy mass) from the prior to quantify the gain in information obtained from spectroscopic observations of the late-type galaxies of the SPARC database. We set the observable in the kinematic

inference to be either the full rotation curve, summary statistics of the rotation curve ($V_{\rm max}$, $V_{2.2}$, $V_{\rm flat}$), or the linewidth of the integrated 21-cm spectrum, $W_{\rm p20}$, in order to quantify the information contained in different parts of the rotation curve and different types of measurement. Further, to determine the properties of the measurements that are most important for the information gain, we study the variation on $D_{\rm KL}$ as we modify properties of the rotation curve observations such as the uncertainties on velocity or the minimum HI surface density probed. Our conclusions are as follows:

1. The full RC fitting offers a wide range of information gain for the SPARC galaxies, ranging from ∼1 bit to ∼11 bits. This is predominantly due to the massive range in the number of data points each rotation curve has, and the large variation in velocity uncertainties.

2. Fits to the summary statistics of the RCs offer much smaller gains, ranging from ∼0 to ∼6 bits, as the posteriors are degenerate in mass–concentration and run up against the prior bounds. $V_{\rm flat}$ offers a modest increase due to the flatness constraint. For most SPARC galaxies $W_{\rm p20}$, $V_{\rm flat}$, $V_{2.2}$ and $V_{\rm max}$ all probe regions of the rotation curve which are dark matter dominated, and hence contain similar information on the halo.

3. We measured $D_{\rm KL}$ as a function of the minimum HI surface density probed, and the uncertainties on velocity, inclination and mass-to-light ratios. Its dependence is strongest on the minimum surface density and the velocity uncertainties. These results can be used to weigh up the increase in precision on halo constraints afforded by improving each aspect of the measurement against the associated cost.

4. The tightness of the constraints on the inner halo shape are strongly dependent on the velocity uncertainties, but have a much weaker dependence on the minimum HI surface density. This suggests that whilst both sensitivity and velocity uncertainties are important for obtaining tight constraints on halo properties, surveys specifically targeting e.g. the cusp-core problem should prioritise the latter.

Our study has identified the most important variables for improving the constraints on dark matter halo properties from spectroscopic observations of late-type galaxies. With forthcoming instruments set to greatly enhance our ability to probe the dark matter distribution around galaxies, in terms of number of galaxies, increasing redshift and measurement precision, these results should inform future survey design to maximise the return of knowledge on the galaxy–halo connection.

Chapter 5

Combining HI linewidths with IFU data

5.1 Introduction

As we have shown in Chapter 3, the integrated HI line profile is an observationally abundant probe of the dark matter halo. We now investigate the potential of combining integrated HI observations with stellar kinematics to increase the precision of constraints on halo properties. Over the past two decades studies of stellar kinematics have been revolutionised by the advent of large integral Field Unit (IFU) galaxy surveys such SAURON (Tim de Zeeuw et al., 2002), ATLAS^{3D} (Cappellari et al., 2011), CALIFA (Sánchez et al., 2012), SAMI (Bryant et al., 2015) and MaNGA (Bundy et al., 2014). The extra spatial dimension of information compared to long-split spectroscopy allows sophisticated dynamical modelling methods to be applied to constrain both the orbit structure of the galaxies and the mass distribution of the different components.

There are a variety of different mass-modelling methods available, differing in sophistication and prior assumptions. These include action-angle modelling e.g. (Binney, 2010), Schwarzchild orbit superposition modelling (Schwarzschild, 1979) and its extension made-to-measure modelling (Syer & Tremaine, 1996) and Jeans Anisotropic Modelling (Cappellari, 2008, 2020b). The applicability of each method depends on the sophistication

of the data available. Jeans Anisotropic Modelling places stronger assumptions on the data compared to these other methods, namely axisymmetry and additional assumptions on the orientation of the vellocity ellipsoid. However these have been validated in many studies of large samples of galaxies with high quality data (Cappellari, 2016). The JAM method has also been validated in both N-body and hydrodynamical simulations (Li et al., 2016), and has been found to perform favourably against Schwarzchild modelling on real data (Leung et al., 2018, using CO rotation curves as the ground truth).

Recently (Zhu et al., 2023b) have applied JAM modelling to all 10,000 galaxies in the final data release of the MaNGA survey (Abdurro'uf et al., 2022), which span a broad range in properties such as morphology, stellar mass and kinematic structure. Their library of dynamical properties has enabled population studies of mass-to-light ratios, the fundamental plane, dark matter fractions, total density-gradients (Zhu et al., 2023a) and their correlations with stellar populations (Lu et al., 2023a). However, as previously discussed, due to the limited extent of the optical light they are only able to constrain the dark matter fraction within the stellar disc, with constraints on the total halo mass/concentration unavailable.

Fortunately the MANGA-HI survey (Masters et al., 2019) is in the process of obtaining integrated HI observations for most of the 10,000 galaxies, with all MaNGA galaxies outside the ALFALFA footprint undergoing fresh observation with the Green Bank Telescope. In this Chapter we will combine JAM stellar-kinematic modelling with our previously developed model of the integrated HI spectral line in order to constrain global halo properties for galaxies in the MaNGA survey.

5.2 Data

5.2.1 MaNGA

The SDSS-IV MANGA survey (Bundy et al., 2014) is an IFU survey targetting ~10,000 nearby galaxies using the BOSS spectrographs (Smee et al., 2013) and the Sloan 2.5m

telescope at the Apache point observatory. It has obtained spatially resolved spectra for the primary sample (∼2/3 of the galaxies) out to 1.5 effective optical scale lengths (R_e) and for the secondary, higher redshift, sample (∼1/3 of galaxies) out to 2.5 R_e (Law et al., 2015). The spectra sample the wavelength range 3600 - 10300 angstrom at a spectral resolution of 72 km/s. The spaxel size is 0.5" with a g-band PSF full-width half maximum (FWHM) of ∼ 2.54 arcsec (Law et al., 2015). The distribution in galaxy stellar mass is roughly flat from 10^9 to 10^{11} $M_\odot$. The Data Analysis Pipeline derives stellar kinematics by fitting absorption lines using `PPXF` software (Cappellari & Emsellem, 2004) with the MILES-HC stellar library (Falcón-Barroso et al., 2011). Each spaxel is Voronoi binned (Cappellari & Copin, 2003) to a minimum 10 S/N before fitting the spectrum. The stellar velocity dispersions are corrected for instrumental resolution (Westfall et al., 2019). We use the SDSS r-band PSF FWHM values from the MaNGA main catalogue[1] to correct for beam smearing when modelling the stellar kinematics.

DynPop (Zhu et al., 2023b, henceforth DynPop23) provide quality-checked multi-gaussian expansions (Cappellari, 2002) for the entire MaNGA sample, derived from SDSS r-band images, and quality flags[2] for each galaxy based on visual inspection of the kinematic best fit models. The flags are designed to identify galaxies for which JAM modelling is not suitable, due to either the assumptions being broken due to the presences of asymmetries (e.g. bars) or the lack of steady-state (e.g. due to an ongoing merger). As our purpose is inferring the dark matter content, we only use the three best quality flags (1,2 and 3). Flag 1 indicates that the JAM best fit model is able to acceptably reproduce the shape of $V_{\rm RMS}$, but not the line-of-sight velocity V. Flag 2 indicates an acceptable reproduction of both $V_{\rm RMS}$ and V. Flag 3 indicates a good fit to both $V_{\rm RMS}$ and V. For Flags 1 and 2 the decomposition between dark and luminous matter can be trusted if both cylindrical and spherical assumptions for the velocity ellipsoid agree. For Flag 3 all quantities are regarded as reliable.

[1]https://www.sdss.org/dr17/manga/manga- data/data- access/
[2]https://manga-dynpop.github.io

5.2.2 MaNGA-HI

The MaNGA-HI survey (Masters et al., 2019) is observing all MaNGA observed galaxies with $cz < 15,000 \mathrm{kms}^{-1}$ and not in the footprint of the ALFALFA survey. This cut is designed to reduce the number of non-detections due to distance, but also acts as a cut on stellar mass due to the selection criteria of the MaNGA survey (larger galaxies are selected at higher redshift to optimally fill the IFU). As shown in fig. 1 of (Masters et al., 2019), above $M_* = 10^{10.25}\,\mathrm{M}_\odot$ progressively fewer MaNGA galaxies are selected for MaNGA-HI observation. The observations are designed to reach comparable rms noise to the ALFALFA survey. We use the most recent MANGA-HI data release (DR2, Stark et al. 2021) which combines observations for 1191 Green Bank Telescope (GBT) detections with an ALFALFA crossmatch for a total of 2901 galaxies. The derived quantities provided in the catalogue are very similar to the ALFALFA data described in Chapter 3. We make use of the HI mass and the width of the 21-cm spectral line measured at 50% of the peak flux density on either side of the profile (W_{F50}). This is subtly different from the W_{p50} measurement used in Chapter 3, which is measured at 50% of the overall peak flux density. We adopt W_{F50} because, unlike W_{p50}, it is provided for all galaxies in the MaNGA-HI catalogue. As our linewidth model is symmetric the procedure to calculate W_{F50} from the model flux profile is unchanged.

We only keep sources that are marked as uncrowded, have a S/N > 6.5 and have less than 20% uncertainty on W_{F50}. In our final MaNGA/MaNGA-HI sample there are 399 sources with a DynPop23 quality flag of 1 or higher, and 99 with flag 3.

5.3 Methods

5.3.1 Jeans Anistropic Modelling

Our Jeans Anisotropic modelling for the stellar kinematics exactly follows the procedure of (Zhu et al., 2023b). We begin with a brief review of Jeans Anisotropic Modelling (Cappellari, 2008, 2020a). Assuming a steady-state axisymmetric system, the Jeans equations in the cylindrical coordinate system (R, z, ϕ) is (Binney & Tremaine, 2008):

$$\frac{\partial(n\overline{v_r^2})}{\partial r} + \frac{(1+\beta_r)\, n\overline{v_r^2} - n\overline{v_\phi^2}}{r} = -n\frac{\partial \Phi}{\partial r} \tag{5.1a}$$

$$(1-\beta_r)\frac{\partial(n\overline{v_r^2})}{\partial \theta} + \frac{(1-\beta_r)\, n\overline{v_r^2} - n\overline{v_\phi^2}}{\tan\theta} = -n\frac{\partial \Phi}{\partial \theta}, \tag{5.1b}$$

where Φ is the gravitational potential, n is the number density of the tracer group from which the kinematics are measured, with moments of the velocities given by

$$n\overline{v_k v_j} \equiv \int v_k v_j f \, \mathrm{d}^3\mathbf{v}, \tag{5.2}$$

where f is the stellar distribution function. As these solutions contain more unknowns than equations, a unique solution is not available. To find solutions it is necessary to make assumptions about the orientation of the velocity ellipsoid. Cappellari (2008) posited that the velocity ellipsoid aligns with the cylindrical coordinate system, with a constant velocity anisotropy in the meridional plane which is written as:

$$\beta_z \equiv 1 - \frac{\overline{v_z^2}}{\overline{v_R^2}} = 1 - \frac{\sigma_z^2}{\sigma_R^2} \equiv 1 - \frac{1}{b}. \tag{5.3}$$

Under these conditions, the Jeans equations simplify to (Cappellari, 2008, eq. 8,9):

$$\frac{b\, n\overline{v_z^2} - n\overline{v_\phi^2}}{R} + \frac{\partial(b\, n\overline{v_z^2})}{\partial R} = -n\frac{\partial \Phi}{\partial R} \tag{5.4}$$

$$\frac{\partial(n\overline{v_z^2})}{\partial z} = -n\frac{\partial \Phi}{\partial z}, \tag{5.5}$$

These equations yield a unique solution for $\overline{v_z^2}$ and $\overline{v_\phi^2}$, using the boundary condition $n\overline{v_z^2} = 0$ as z approaches infinity.

An alternative approach to solving the Jeans equations was introduced by Cappellari 2020a. This method assumes alignment of the velocity ellipsoid with the spherical coordinate system (r, θ, ϕ) with a spatially constant velocity anisotropy defined as

$$\beta_r \equiv 1 - \frac{\overline{v_\theta^2}}{\overline{v_r^2}} = 1 - \frac{\sigma_\theta^2}{\sigma_r^2}. \tag{5.6}$$

Using this assumption (and converting to spherical coordinates), the Jeans equations can be rewritten as:

$$\frac{\partial(n\overline{v_r^2})}{\partial r} + \frac{(1+\beta_r), n\overline{v_r^2} - n\overline{v_\phi^2}}{r} = -n\frac{\partial\Phi}{\partial r} \tag{5.7a}$$

$$(1-\beta_r)\frac{\partial(n\overline{v_r^2})}{\partial\theta} + \frac{(1-\beta_r), n\overline{v_r^2} - n\overline{v_\phi^2}}{\tan\theta} = -n\frac{\partial\Phi}{\partial\theta}, \tag{5.7b}$$

With boundary condition $n\overline{v_r^2} = 0$ as r approaches infinity, these equations give unique solutions for $\overline{v_r^2}$ and $\overline{v_\phi^2}$.

Given the gravitational potential Φ, the tracer density distribution n, and the velocity anisotropy (β_z or β_r), the intrinsic second velocity moments can be deduced by solving the above equations. Subsequently, the projected second velocity moments, represented by $\overline{v_{\rm los}^2}$, can be obtained by integrating the intrinsic moments along the line-of-sight direction and fitted to the data to constrain model parameters. The projected second velocity moment is calculated as $V_{\rm RMS} = \sqrt{V^2 + \sigma^2}$, where V is the line-of-sight velocity and σ is the stellar velocity dispersion provided by the MaNGA DAP.

In a galaxy, the gravitational potential is related solely to the even moments of velocity. This occurs because, for specific density and tracer distributions, one can always reverse the direction of rotation (altering the sign of velocity) of an arbitrary number of tracer stars, without the need to modify either the density or the tracer. Consequently only the second

velocity moments $V_{\rm RMS}$ are used to constrain model parameters in the JAM procedure. We use the `JamPy` (Cappellari, 2008) to solve the Jeans equations, project the second moment and perform the convolution with instrumental PSF.

The stellar distribution n is expressed using the Multi-Gaussian Expansion (MGE; Cappellari 2002). We use those provided by the DynPop23 library, which are calculated from SDSS r-band images. The surface brightness is expressed as a sum of Gaussians

$$\Sigma\left(x', y'\right) = \sum_{k=1}^{N} \frac{L_k}{2\pi\sigma_k^2 q_k'} \exp\left[-\frac{1}{2\sigma_k^2}\left(x'^2 + \frac{y'^2}{q_k'^2}\right)\right], \tag{5.8}$$

with L_k the total luminosity, σ_k dispersion along the major axis, q_k' the axial ratio of k-th Gaussian component, and (x', y') the plane-of-sky coordinates centred on the galaxy. By assuming the galaxies are oblate axisymmetric, the 2D MGE can be deprojected to 3D, and the density written as (Cappellari, 2008, eq. 13):

$$v(R, z) = \sum_{k=1}^{N} \frac{L_k}{\left(\sqrt{2\pi}\sigma_k\right)^3 q_k} \exp\left[-\frac{1}{2\sigma_k^2}\left(R^2 + \frac{z^2}{q_k^2}\right)\right], \tag{5.9}$$

where q_k is the 3D intrinsic axial ratio of the k-th Gaussian component. The smallest intrinsic axial ratio $q'_{min} = min(q_k^{'})$ a set to be a free parameter in the model fit. The inclination can be calculated from q'_{min} using

$$\tan^2 i = \frac{1 - q'^2_{\rm min}}{q'^2_{\rm min} - q^2_{\rm min}}, \tag{5.10}$$

which is used to deproject the rest of the Gaussian components.

Following DynPop23 we use the kinematic position angle, except for galaxies with highly disturbed kinematics (for which a flag is provided). The MGE surface brightness is corrected by a factor of $(1 + z)^3$ to account for cosmological dimming and redshift. Due to the low redshift, K-correction is not applied.

Following DynPop23, we assume a spatially constant anisotropy to simplify the model, and impose an upper limit on anisotropy. The limit is based on the known approximate upper limit on anisotropy for fast rotators (Cappellari, 2016), which it has been argued results from a physical limit on high-anisotropy equillibrium configurations in disc galaxies (Wang et al.,

2020a), although it appears valid for both cyclindrical and spherical alignments. The limit is given by (Cappellari, 2016)

$$\beta, \lesssim 0.7 \times \varepsilon_{\rm intr}, \tag{5.11}$$

This translates to a lower bound on the velocity dispersion ratio :

$$\mathcal{R}(q) = \sqrt{0.3 + 0.7q}, \qquad \sigma_z/\sigma_R \gtrsim \mathcal{R}(q), \qquad \sigma_\theta/\sigma_r \gtrsim \mathcal{R}(q), \tag{5.12}$$

where q is the intrinsic axial ratio of the galaxy.

The likelihood for the stellar kinematics is

$$\mathcal{L}_{\rm stars}(D|\theta, \mathcal{M}) = \prod_i \frac{\exp\{-((\overline{V^2_{\rm LOS,i}})^{1/2} - V_{\rm RMS,i})^2/(2\delta V^2_{\rm RMS,i})\}}{\sqrt{2\pi}\delta V_{\rm i,obs}}, \tag{5.13}$$

where $\overline{V^2_{\rm LOS,i}}$ is the model projected second velocity moment of the i-th Voronoi bin and $V_{\rm RMS,i}$ is the corresponding observed root-mean-square velocity.

5.3.1.1 Initial fit to stellar kinematics

DynPop23 perform an initial fit using a mass-follows-light model (MFL), with no dark matter halo, in order to remove outlying pixels, calculate the intrinsic axis ratio q for the anisotropy prior, and modify the uncertainties in a way that approximately accounts for systematic errors. We adopt the same procedure, which we now describe for completeness.

Outlier pixels are removed by iteratively fitting the kinematics and removing pixels whose deviation from the best fit model is greater than the 3σ, where σ is the noise calculated from the differences between model and data using a bi-weight estimate (Hoaglin et al., 1983). Surviving bins are utilized in subsequent optimisations until convergence is reached.

To prevent the inner high-S/N Voronoi bins exerting too strong an influence on the fit, the actual observed kinematic errors are not used. Instead the errors on the velocity (ε_V)

and velocity dispersion (ε_σ) are initially set to $\varepsilon_V = 5$ km s^{-1} and $\varepsilon_\sigma = 0.05\sigma$. The initial fractional error on Vrms is obtained through error propagation

$$\varepsilon^{\rm init} V_{\rm rms} = \frac{1}{V_{\rm rms}} \sqrt{(V\ \varepsilon_V)^2 + (\sigma \varepsilon_\sigma)^2}. \tag{5.14}$$

The errors are further modified using the method of Mitzkus et al. (2017). Following a initial fitting stage with $\varepsilon^{\rm init} V_{\rm rms}$, we calculate the χ^2 and increase the uncertainties using:

$$\varepsilon_{V\rm rms} = \varepsilon^{\rm init} V_{\rm rms} \times \sqrt{\chi^2/{\rm DOF}} \times (2N_{\rm bins})^{1/4}, \tag{5.15}$$

where χ^2/DOF represents the reduced chi-square value from the initial fit, and $\rm N_{bins}$ refers to the count of kinematic bins left post-initial fitting. The two scaling components of $\sqrt{\chi^2/{\rm DOF}}$ and $(2N_{\rm bins})^{1/4}$ increase the kinematic errors to obtain $\chi^2/{\rm DOF} = 1$ and approximately account for potential systematic uncertainties (Mitzkus et al., 2017). This methodology is based on the approach proposed for confidence intervals based on χ^2 by van den Bosch & van de Ven (2009), and subsequently adopted in numerous papers IFU kinematic studies. This method of approximating the uncertainties is not statistically justified, which we discuss in Section 5.5.

The trimmed kinematic maps, the updated kinematic errors $\varepsilon_{V\rm rms}$ and the intrinsic axial ratio obtained from this initial MFL fit are then used in the rest of the mass models we present.

5.3.2 HI modelling

We forward model the HI flux profile using the same model as in Chapters 3 and 4. For the W_{50} summary statistic the likelihoood is the same as before

$$\mathcal{L}_{HI}(W_{\rm obs}|\theta, \mathcal{M}) = \frac{\exp\{-(W_{\rm obs} - W_{\rm pred})^2/(2\delta W_{\rm obs}^2)\}}{\sqrt{2\pi}\delta W_{\rm obs}}, \tag{5.16}$$

where $W_{\rm obs}$ is the observed linewidth and $W_{\rm pred}$ the model prediction.

We now also try a separate inference where we instead fit to the full HI flux profile $\Psi_{\rm HI}(V_\lambda)$ (still defined as the flux of the HI spectrum at a given wavelength λ corresponding

to HI gas with radial velocity V_λ, which we define relative to the galaxy's systemic velocity so the midpoint of the spectrum is at $V_\lambda = 0$). The likelihood is (dropping the HI subscript from $\Psi_{\rm HI}$)

$$\mathcal{L}_{HI}(D|\theta, \mathcal{M}) = \prod_i \frac{\exp\{-(\Psi_{\rm i,obs} - \Psi_{\rm pred}(V_{\lambda,i}))^2/(2\delta\Psi^2_{\rm i,obs})\}}{\sqrt{2\pi}\delta\Psi_{\rm i,obs}}, \tag{5.17}$$

where $\Psi_{\rm i,obs}$ is the observed HI flux in each of the i velocity bins, and $\Psi_{\rm pred}(V_{\lambda,i}))$ is the model prediction at the corresponding velocity. We take the observational uncertainty $\delta\Psi_{\rm i,obs}$ to be the rms noise provided for each galaxy in the MaNGA-HI catalogue.

We now also convolve the model flux profile with a Gaussian of width 10km/s to account for instrumental broadening (unlike the ALFALFA catalogue values, the MaNGA-HI W_{50} are not corrected for instrumental broadening).

5.3.2.1 Modelling the HI surface density

As we are now using the full HI flux profile, and not just W_{50}, our model is now more sensitive to the inner HI distribution. Rather than use a fixed HI profile as in Chapter 3, we develop a Bayesian prior for the HI profile based on resolved observations of other galaxies.

Stevens et al. (2019), in exploring the origin of the HI mass-size relationship, tested three analytic profiles for the HI surface density on a sample of 110 galaxies from the THINGS, LITTLE THINGS, LVHIS, and Bluedisk surveys, finding all three were a good fit to observations. We adopt their "model 2", which was found to be the best-fit to the most galaxies. Towards the centre the profile has a core with variable size, and at large radius it falls off exponentially with radius squared (a Gaussian),

$$\Sigma_{\rm H\,I}(r) = \begin{cases} \Sigma_0, & r \leq r_b \\ \Sigma_0 \exp\left[-r_S^{-2}(r - r_b)^2\right], & r > r_b \end{cases}, \tag{5.18}$$

where Σ_0 is the central surface density, r_b is the core size, and r_S is the scale length of the exponential decline. We define normalised lengths and surface densities

$$\bar{r}_x \equiv r_x/r_{\rm H\,I}\,, \tag{5.19a}$$

$$\bar{\Sigma}_x \equiv \Sigma_x / \left(1\,\mathrm{M}_\odot\,\mathrm{pc}^{-2}\right)\,, \tag{5.19b}$$

where $r_{\mathrm{H\,I}}$ is the radius at which the gas drops to $\left(1\,\mathrm{M}_\odot\,\mathrm{pc}^{-2}\right)$. The radius $r_{\mathrm{H\,I}}$ can then be written as

$$r_{\mathrm{H\,I}} = \sqrt{\frac{m_{\mathrm{H\,I}}}{\pi\,\Sigma_0\,\left[\bar{r}_b^2 + \bar{r}_S\,(\bar{r}_S + \sqrt{\pi}\bar{r}_b)\right]}}\,, \tag{5.20a}$$

and

$$\bar{r}_S = \frac{1 - \bar{r}_b}{\sqrt{\ln(\bar{\Sigma}_0)}}\,. \tag{5.20b}$$

We fit equation 5.18 to the HI surface density profiles of the SPARC galaxy, and find a similar distribution in model parameters to Stevens et al. (their fig. 5). Following Stevens et al. we assume Σ_0 and $\bar{r}_b$ are independent of other galaxy properties (i.e. self-similar density profiles). We check this is a reasonable assumption using SPARC, finding the strongest correlation is a weak (Pearson correlation coefficient of 0.26) and not quite statistically significant (p-value of 0.08) correlation between Σ_0 and M_{HI}. We make Σ_0 and $\bar{r}_b$ free parameters in our MaNGA/MaNGA-HI inference, with a prior given by the 2D distribution of (Σ_0,$\bar{r}_b$) for the SPARC galaxies, which together with the observed M_{HI} of each galaxy specifies the HI surface density in full. To smooth and interpolate the distribution we fit a Gaussian Mixture Model, using the number of Gaussians that minimises the Bayesian Information Criterion.

For computational efficiency we do not include the mass contribution from the HI gas in the JAM fit (as its contribution to the enclosed mass is insignificant within the range of the IFU data). We calculate the contribution of the gas to the circular velocity used to calculate the HI flux profile by solving Poisson's equation for an infinitely thin disk (Binney & Tremaine, 2008). The circular velocity for the stars and dark matter is calculated by `JamPy`. We do not include an asymmetric drift correction, as our galaxies are all high mass and therefore rotationally dominated.

5.3.2.2 Inference

In this Chapter we only consider the gNFW profile

$$\rho_{\rm gNFW}(r) = \frac{\rho_s}{\left(\frac{r}{r_s}\right)^{\alpha}\left[1+\left(\frac{r}{r_s}\right)\right]^{3-\alpha}}. \tag{5.21}$$

We also revert to using the standard definition of halo concentration ($c = R_{\rm vir}/r_s$), and $M_{\rm vir}$ now refers to the dark matter mass only. We now have the r-band mass-to-light ratio as the free parameter governing the total stellar mass, with its prior based on the NSA value with an assumed 0.2 dex uncertainty (equivalent to the prior on M_* in Chapter 3).

The combined likelihood from the gas and stars is simply

$$\mathcal{L} = \mathcal{L}_{\rm stars}\mathcal{L}_{HI}. \tag{5.22}$$

The fitting is done with MultiNest using 500 active points and 0.8 sampling efficiency. MultiNest is chosen over `emcee` because of its faster convergence rate, which is preferred due to the computational expense of solving the Jeans equation. The free model parameters are summarised in Table 5.1. In this work we use the cylindrically oriented velocity-ellipsoid assumption, and leave testing the spherically-aligned assumption to future work.

Table 5.1: The free parameters in the inference, their physical definitions and their Bayesian priors. $\mathcal{U}$ and $\mathcal{N}$t denote a uniform and truncated normal distribution respectively.

	Parameter	Units	Definition	Prior
	$M_{\rm vir}$	$M_\odot$	Virial mass	Loguniform(8,15)
	c		Halo concentration $R_{\rm vir}/r_s$	Loguniform(0,2) (or DMO simulation prior)
	σ_z/σ_R		Stellar anisotropy	$\mathcal{U}(\mathcal{R}(q), 1)$
	M_*/L	$M_\odot$	r-band mass-to-light ratio	Lognormal(NSA M_*/L,0.2)
	$q_{\rm min}$		Intrinsic b/a of thinnest MGE Gaussian.	$\mathcal{U}(0.05, q_{\rm min'})$
	$i_{\rm gas}$	deg	HI disc inclination (0° face on; 90° edge on)	$\mathcal{N}$t($i_{\rm stars}$, 10; 0, 180°)
	$\bar{r}_{\rm b}$		Normalised HI core radius $r_b/r_{\rm HI}$ (equation 5.19)	2D distribution of ($\bar{r}_{\rm b}$,Σ_0) of SPARC galaxies
	Σ_0	$M_\odot/{\rm pc}^2$	Maximum HI surface density	
	α		Halo inner slope	$\mathcal{U}(0, 1.6)$

5.4 Results

5.4.1 Linewidth fit

We first carried out the fitting procedure using the stellar kinematics and W_{50} as constraints (not the full flux profile), with the mass-concentration prior applied. However we found that this gave us extremely weak constraints on $M_{\rm vir}$, with only an upper limit for most galaxies. The is due to the fact that the galaxies with a DynPop23 quality flag greater than 0 are nearly all high stellar mass galaxies, for which the peak in circular velocity of the stellar mass is nearly equal to the maximum circular velocity across the whole rotation curve. As we discussed in Chapter 4 (right panel of Fig. 4.4), for this type of galaxy the constraints on $M_{\rm vir}$ are weak, as the linewidth can be generated by the baryons alone. The constraining power of the linewidths in this MaNGA(-HI) analysis are actually generally weaker than those presented in Chapter 4, because our knowledge of the mass-to-light ratio and inclination is weaker than for the SPARC galaxies.

5.4.2 Full flux profile

As the linewidth provides very little additional information compared to the IFU data for the galaxies in our sample, we instead try fitting to the full flux profile (we refrained from doing this in our ALFALFA study due to the poorer knowledge of the stellar mass distribution and inclination, both of which are ameliorated by the IFU data).

5.4.2.1 With mass-concentration prior, NFW halo

We first carry out the fit with the mass-concentration prior applied and an NFW halo profile ($\alpha = 1$). In Fig. 5.1 onwards we show constraints for some example galaxies when fitting to both the stellar kinematics and HI flux profile ("HI + stars"), or each individually. Most galaxies in our sample are similar to Figs. 5.1 and 5.2, where the circular velocity is constrained by the linewidth to be approximately flat, leading to strong constraints on the $M_{\rm vir}$. The model can reproduce the shape of the HI flux profile well, and the fit to the stellar kinematics is not significantly worsened by the addition of HI. The HI density parameters Σ_0 and $\bar{r}_b$ are constrained to a somewhat smaller region than their prior.

Figs. 5.3 and 5.4 are two examples of galaxies for which a smaller $M_{\rm vir}$ than expected is favoured. In both cases the flux profile shape is somewhat reproduced by the model, even without dark matter. Both galaxies prefer (Σ_0,$\bar{r}_b$) values that are towards the edge of their priors. The low values of $M_{\rm vir}$ are favoured by the HI alone for both galaxies. The inclination of both galaxies is fairly high, suggesting this is unlikely to be the problem. The mass-to-light ratios for both galaxies are towards the upper end of the prior, but not in disagreement with the values preferred by the stellar kinematics. $\sim$ 10% of galaxies in the sample have a 2-σ lower bound on $M_{\rm bar}/M_{\rm vir}$ greater than the cosmologically available fraction of baryons.

Figs. 5.5 show an example galaxy for which a larger $M_{\rm vir}$ than expected is favoured. Within the HI disc, the circular velocity does not exceed the linewidth. However a steeply rising circular velocity is strongly preferred, which requires a large $M_{\rm vir}$. The HI flux profile is roughly flat, which is not well produced by our model. The closest our model can get to producing a flat "top-hat" flux profile is by having a steeply rising rotation curve, which results in only a small dip in the centre of the flux profile as the lack of flatness suppresses the formation of the double horns. We find this behaviour mostly occurs for close to face-on galaxies. We suspect the noisy flux profiles combined with the few velocity bins at low inclination, and the large inclination corrections, may be amplifying the effects of

unmodelled systematics in the HI spectrum (such as correlated noise). 6% of galaxies have a 2-σ lower bound on $M_{\rm vir}$ greater than 10^{13} $M_\odot$.

Some galaxies have unusual HI flux shapes that are not well described by the either the double horn or Gaussian profile. In a couple of cases, but not all, this is because the galaxy does not appear to be a rotating disc.

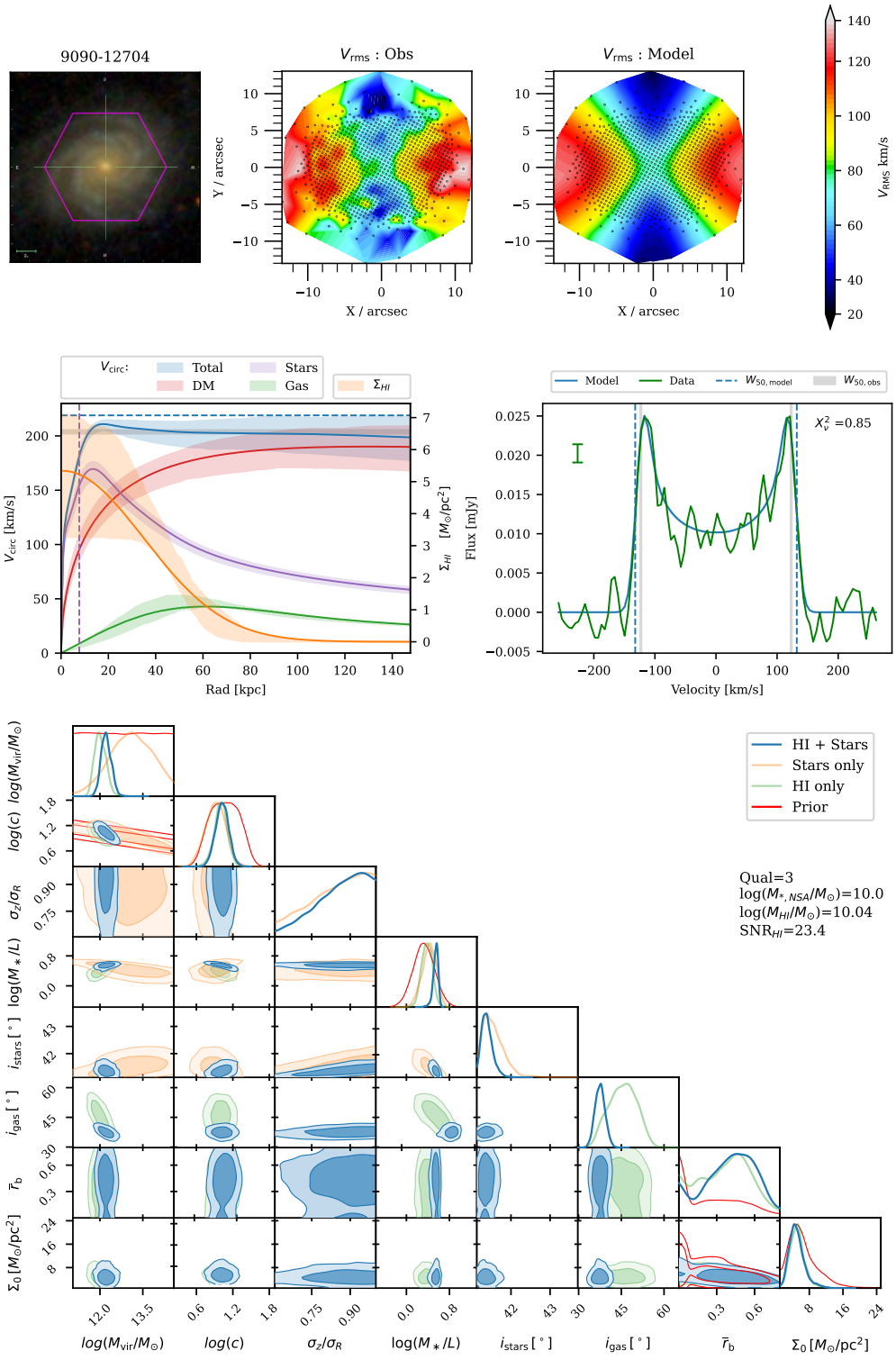

Figure 5.1: *Top*: The SDSS composite image, the observed V_{rms} and the best fit JAM model from fitting to the stellar kinematics and full HI profile (HI + stars) for galaxy 9090-12704. The mass-concentration prior is applied and the halo is fixed to NFW ($\alpha = 1$). The dots show the Voronoi bin centroids.
Middle: The best fit model circular velocities for each mass component and the HI surface density (*left panel*), and the observed and model HI flux profile (*right panel*) for the HI + stars fit. The shaded bands show the 1σ confidence intervals. The vertical dashed purple line shows the maximum radius of the IFU data. The horizontal/vertical dashed blue line (grey band) shows the model (observed) W_{50} (although it is not used as a constraint); in the left panel these quantities are inclination-corrected. The uncertainty on the flux is shown (green error bar). *Bottom:* Corner plot of the model parameters inferred by the HI and/or stars fits and the parameter priors (red). For this galaxy the circular velocity curve is well constrained to be approximately flat, resulting on a tight constraint on $M_{\rm vir}$.

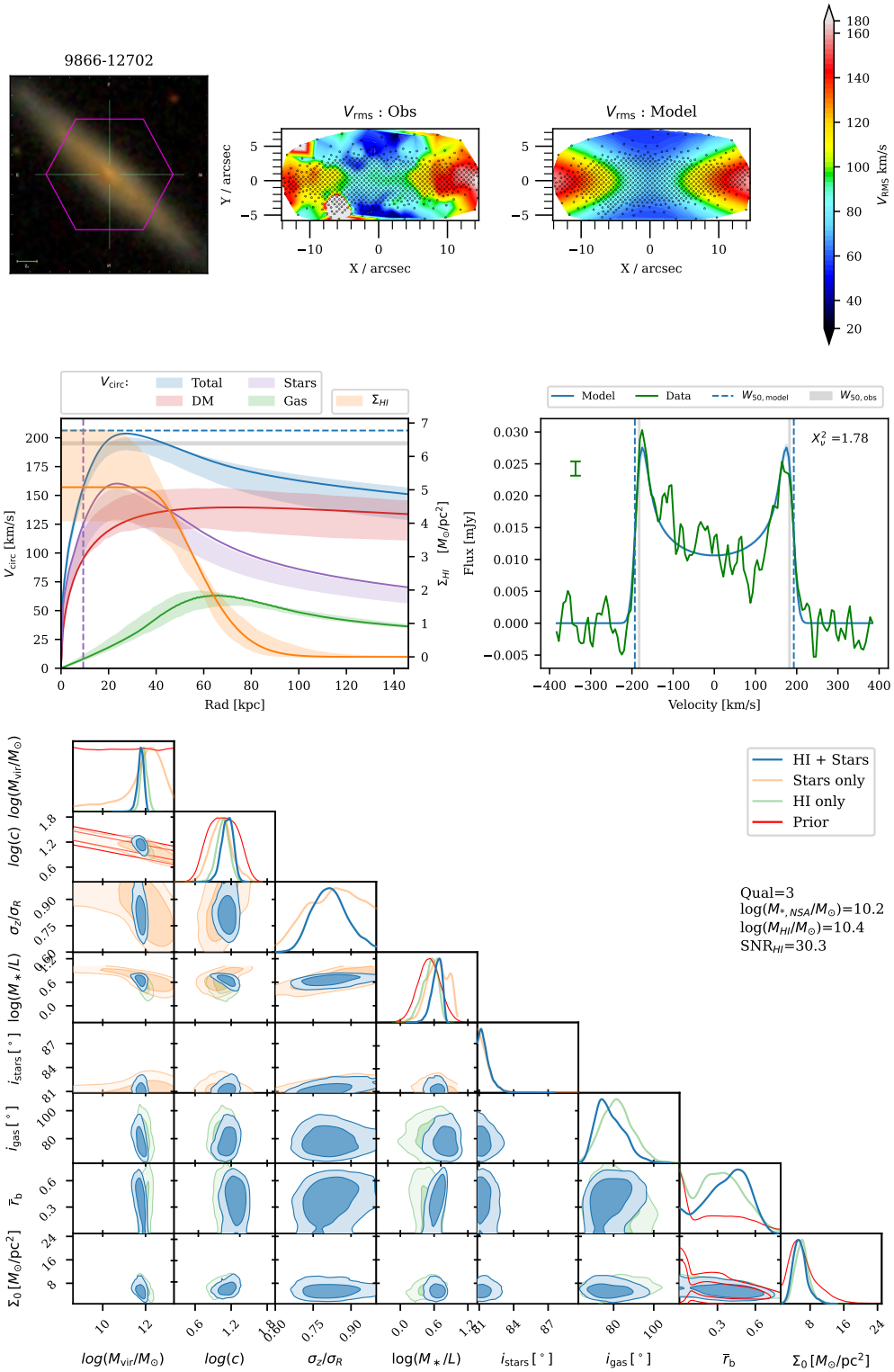

Figure 5.2: Same as Fig. 5.1, but for 9866-12702. Here the rotation curve rises steeply and then gently declines until approximately flat. Again M_{vir} is well constrained.

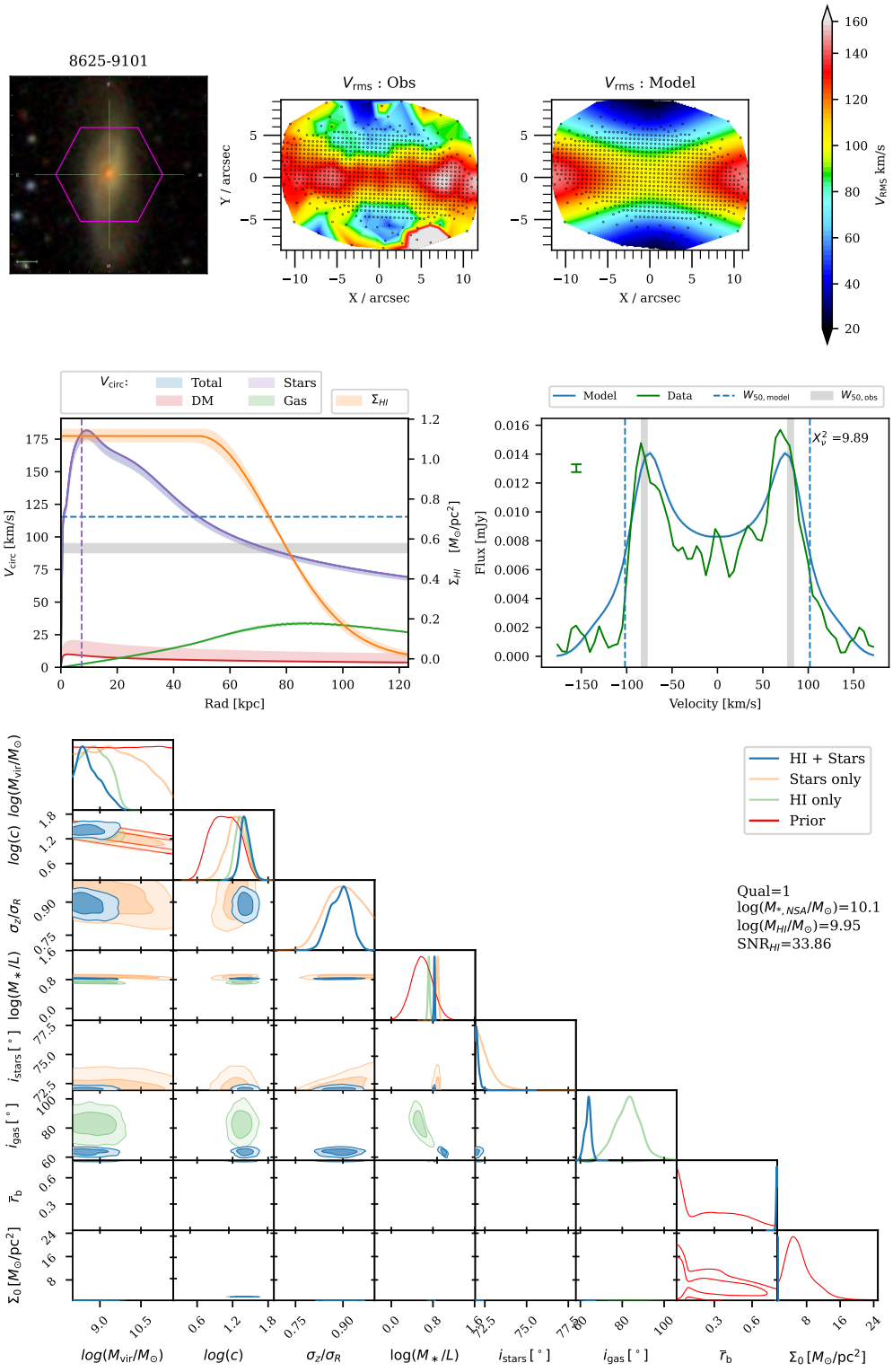

Figure 5.3: Same as Fig. 5.1, but for 8625-9101. The dark matter mass is favoured to be small, and the best fit circular velocity is completely dominated by the stars: it rises quickly and then has a Keplerian decline. The model HI profile roughly matches the shape: however $\bar{r}_b/\Sigma_0$ are tightly constrained to the largest/smallest values allowed by the prior, suggesting that they are being used to compensate the shape of the flux profile for the lack of dark matter.

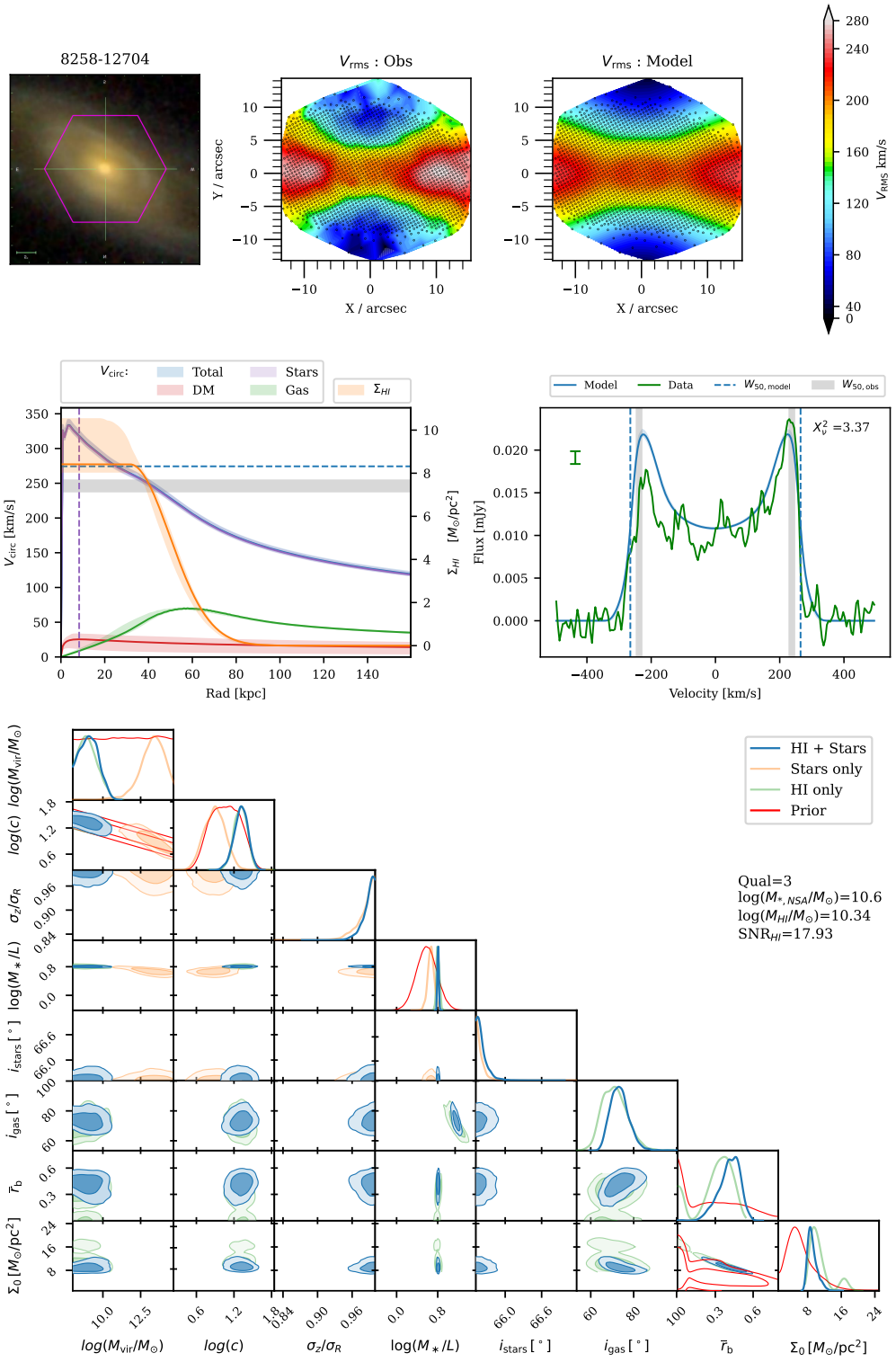

Figure 5.4: Same as Fig. 5.1, but for 8258-12704. As in the previous figure, $M_{\rm vir}$ is constrained to be much smaller than expected. The model flux profile approximately matches the shape of the data, and $\bar{r}_b/\Sigma_0$ are again towards the edge of the prior. The stars only fit favours a much higher $M_{\rm vir}$.

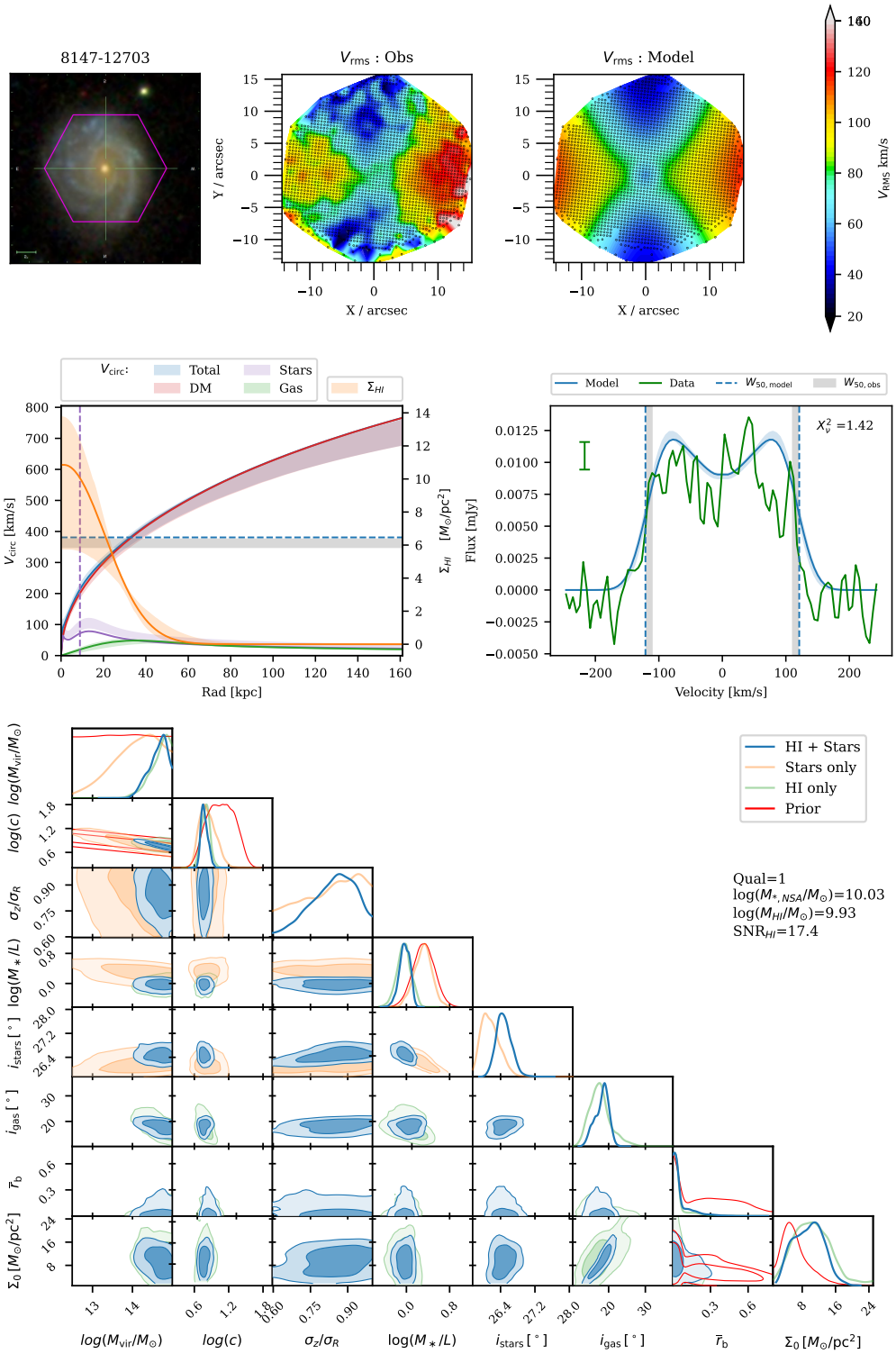

Figure 5.5: Same as Fig. 5.1, but for 8147-12703. A very high $M_{\rm vir}$ is favoured, with the circular velocity quickly rising past the velocity corresponding to the linewidth. The model flux profile does not reproduce the shape of the data, which seems almost flat in its centre rather than the double-horned shape. This flat shape is generally most closely reproduced by a constantly rising circular velocity. The galaxy is at a very low inclination, leading to large corrections to the observed velocities that may amplify systematics.

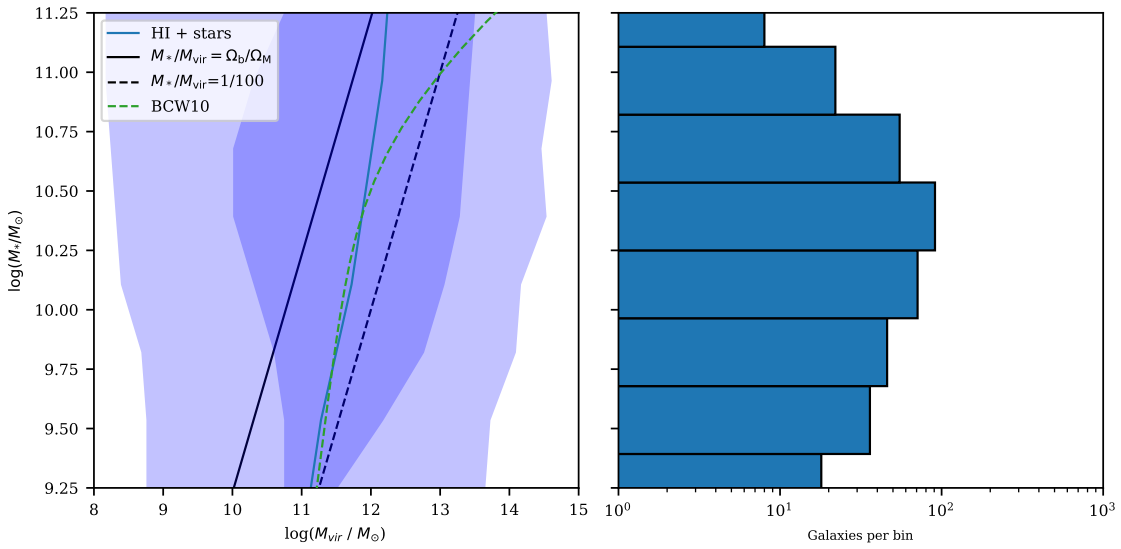

Figure 5.6: The stellar mass–halo mass relation formed by stacking the 1D marginalised posteriors on $M_{\rm vir}$ in 0.25 dex bins of stellar mass from fitting to the stellar kinematics and HI full flux profile (blue). The mass–concentration prior is applied. The solid line shows the mode of the stacked distribution in each bin, and the shaded regions the 1 and 2σ isoprobability contours. 'BCW10' shows the best-fit SHAM relationship from Behroozi et al. (2010), which is derived for optically-selected galaxies. The diagonal dashed and solid lines show constant $M_{\rm bar}/M_{\rm vir}$ as indicated in the caption.

In Fig. 5.6 we present the stacked stellar-to-halo mass relationship for the sample. Despite the different sample and inference methods, both the SHMR and BHMR (not shown) are similar to those obtained by our ALFALFA analysis in Chapter. 3 (in the overlapping mass range). At lower mass the mode of the distribution matches abundance matching relationships. At higher mass however the kinematically inferred SHMR continues as a power law and doesn't show the break expected from abundance matching models. The width of the 1 and 2 sigma regions are similarly large to our ALFALFA analysis, and hence cannot rule out the existence of a break.

5.4.2.2 Without mass-concentration prior, NFW halo

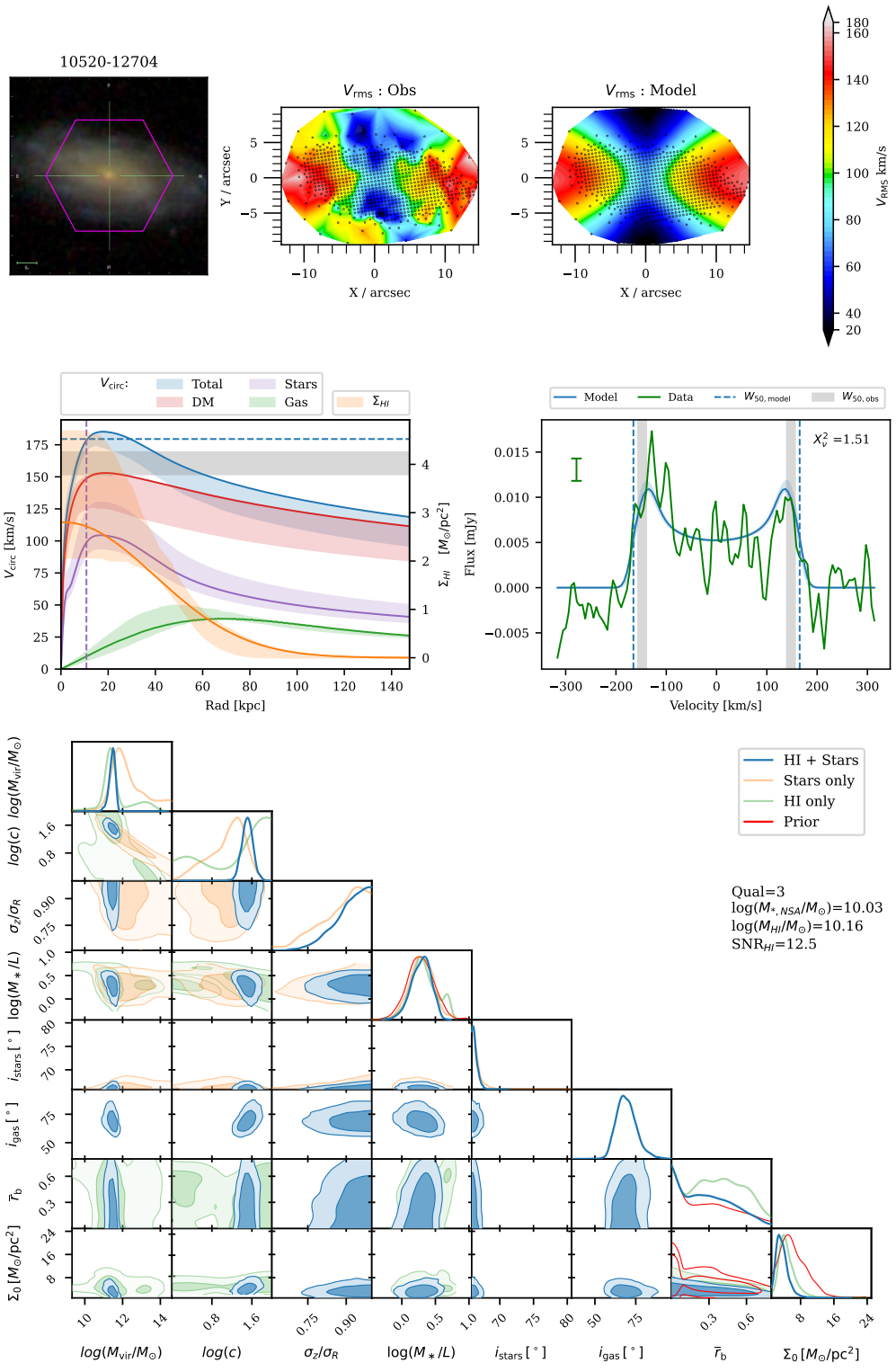

Figure 5.7: Same as Fig. 5.1, but for galaxy 10520-12704 and without the mass–concentration prior applied.

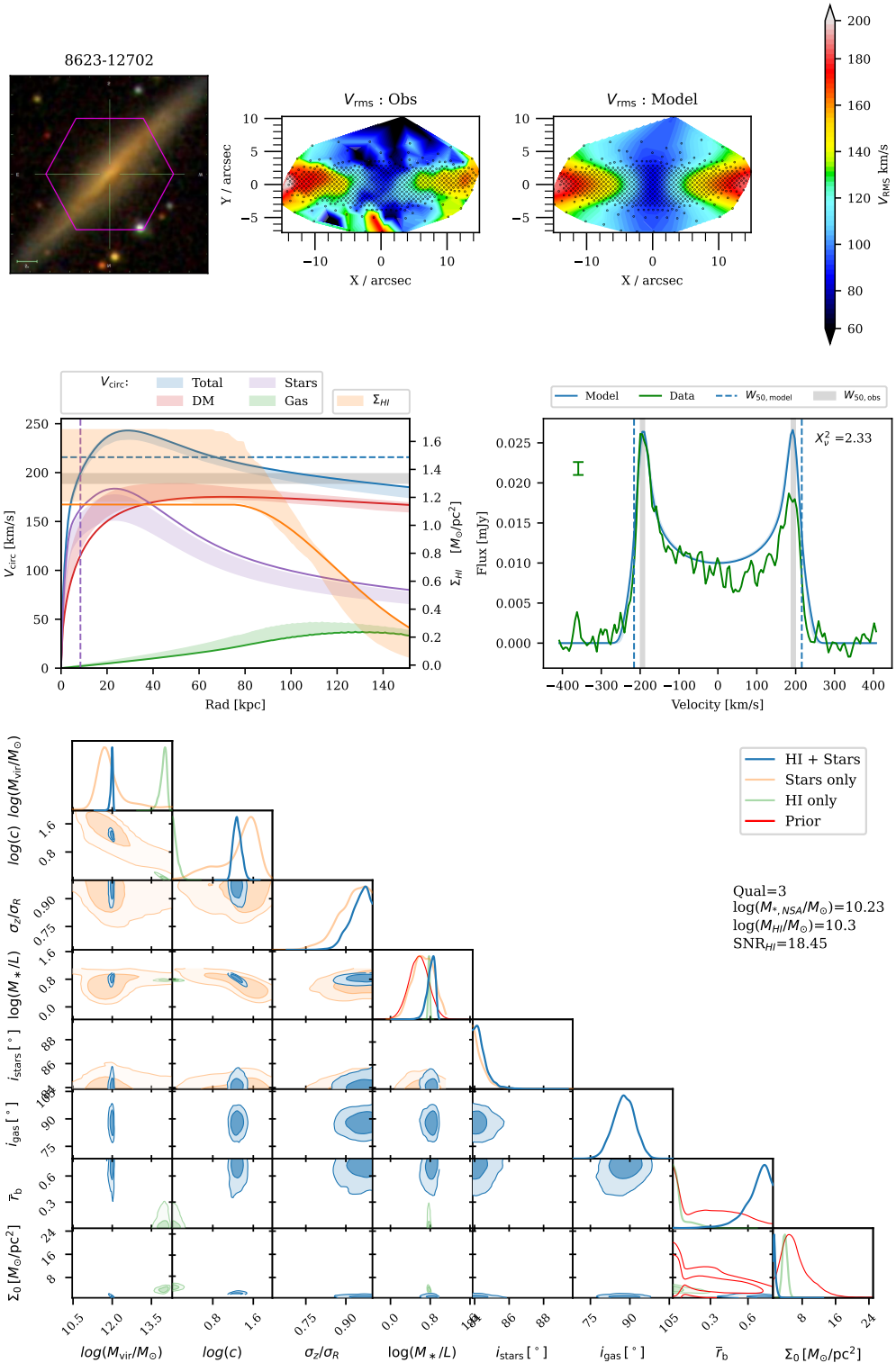

Figure 5.8: Same as Fig. 5.1, but for galaxy 8623-12702 and without the mass–concentration prior applied.

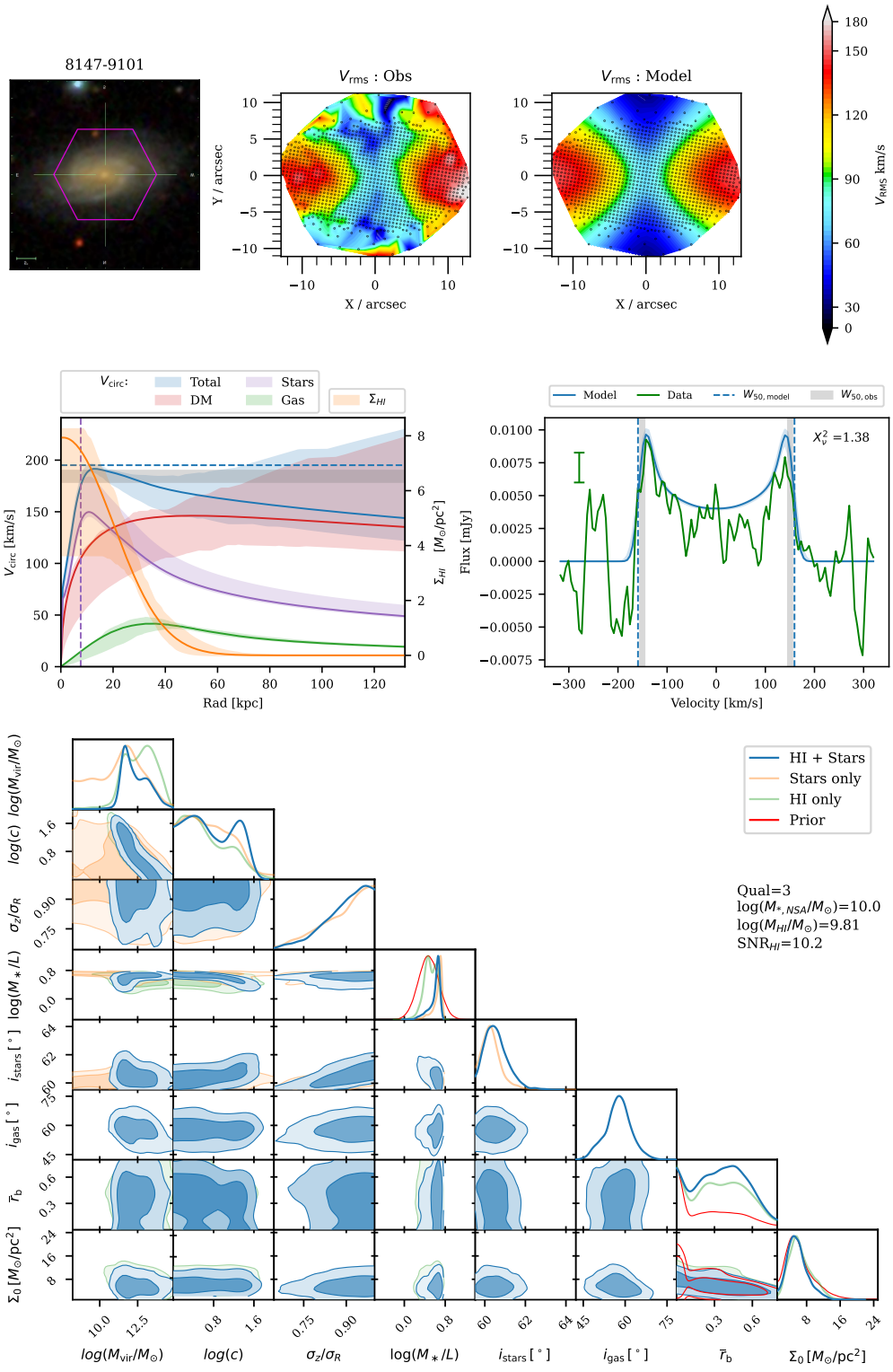

Figure 5.9: Same as Fig. 5.1, but for galaxy 8147-9101 and without the mass–concentration prior applied.

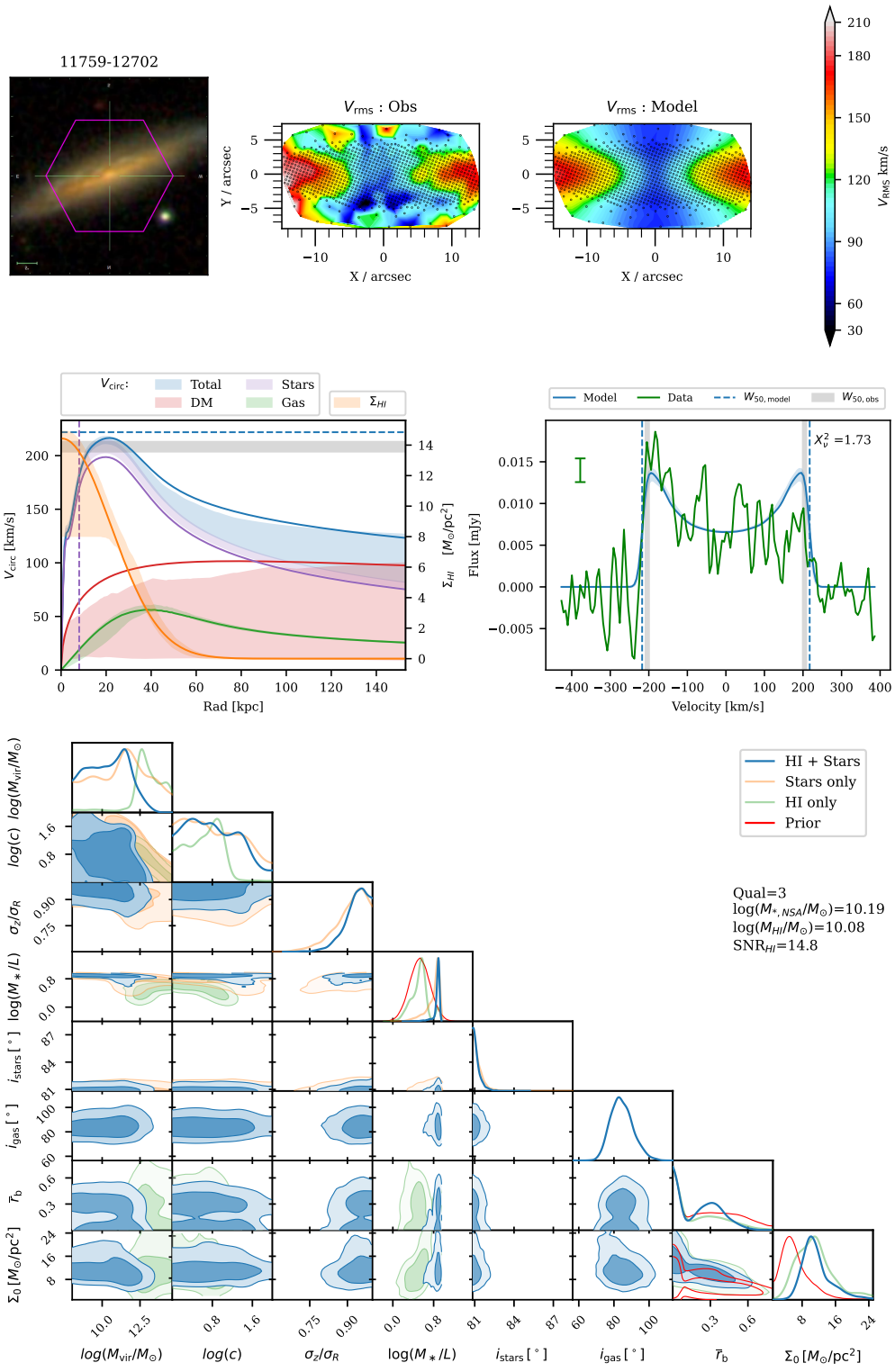

Figure 5.10: Same as Fig. 5.1, but for galaxy 11759-12702 and without the mass–concentration prior applied.

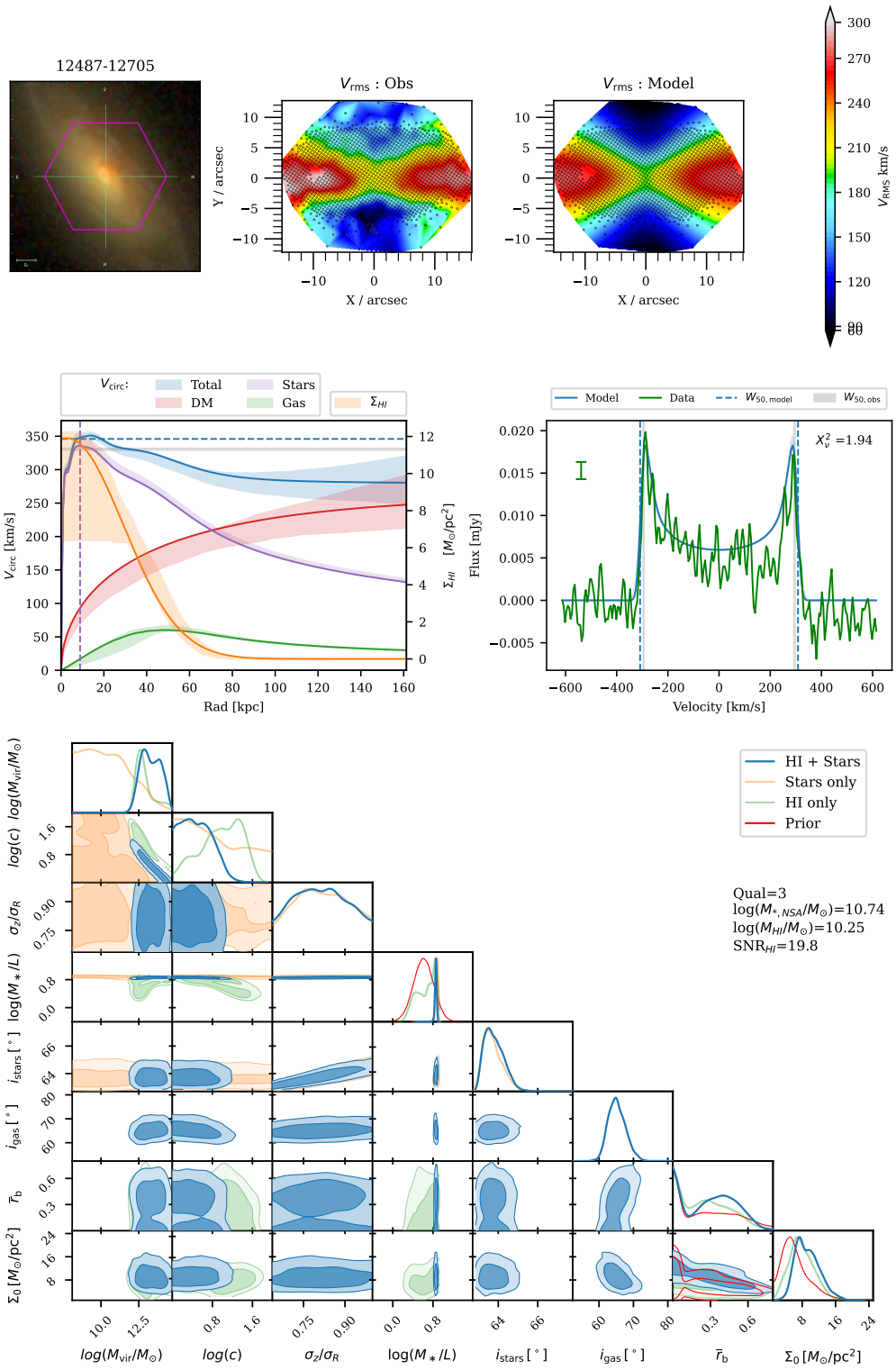

Figure 5.11: Same as Fig. 5.1, but for galaxy 12487-12705 and without the mass–concentration prior applied.

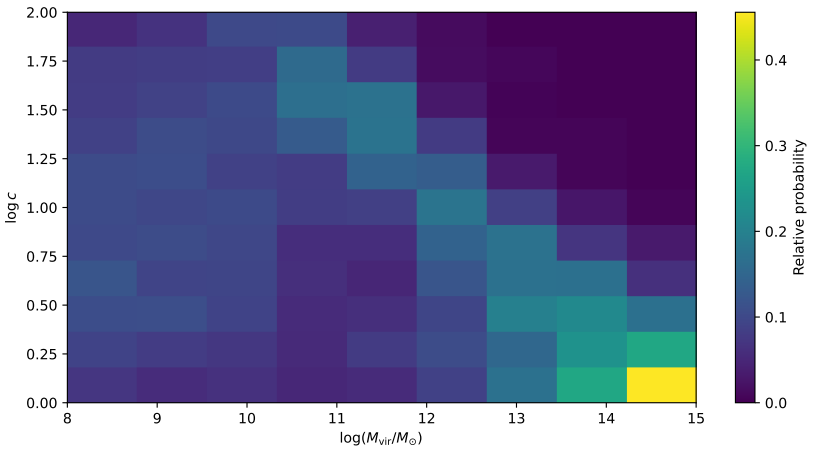

Figure 5.12: The stacked mass–concentration relationship from an NFW fit (with no mass–concentration prior applied), created by stacking the posteriors in 2D bins of mass and concentration, and then normalising each *mass bin*. The steep shape and tail to very high mass/low concentration reflects the fact that for many galaxies the degeneracy between them isn't broken.

We next repeat the inference without the mass–concentration prior. We find that whilst for most galaxies an approximately flat circular velocity curve is still favoured, the number of galaxies where either a very small or very large $M_{\rm vir}$ is favoured is increased somewhat. However due to the weaker constraints on $M_{\rm vir}$ we find that the number of galaxies where the bound on $M_{\rm vir}$ is 2σ discrepant with the implied cosmologically available baryons, or where $M_{\rm vir} > 10^{13}\,{\rm M}_\odot$ is slightly less than when the mass–concentration prior was applied.

The posteriors show a range wide of behaviours. About about a third of galaxies now have both well constrained mass and concentration (e.g. Figs. 5.7 and 5.8). For many galaxies the concentration is still poorly constrained in spite of the combination of stellar and HI data (e.g. Figs. 5.9,5.10,5.11), often as a result of strong degeneracy between mass and concentration. Almost unconstrained concentrations are also observed in studies with resolved rotation curves such as SPARC (e.g. Li et al. 2020). Unlike in our ALFALFA study, very few galaxies now have completely unconstrained $M_{\rm vir}$ even without the mass–concentration prior. In many galaxies the posteriors from inferences with either gas or stars alone are in tension with the combined inference (seen in Fig 5.8).

We stack the posteriors to form a mass–concentration relationship (Fig. 5.12), which is much steeper in the data than the relationship from DMO simulations (outside of the region of the plot with very small halo masses). This is also seen with SPARC resolved rotation curves (Katz et al., 2017, fig. 3), and is due to the degeneracy between mass and concentration still not being broken for many galaxies due to the limited extent of the HI. The absence of posterior mass in the upper right half of the plot compared to the lower left is because the line profile can confidently rule out very high masses/concentrations (as these generate too broad a line profile), but not low mass/concentrations as the baryons alone generate a profile of a similar width (although a different shape) to when these amounts of dark matter are present.

5.4.2.3 Free α

Next we let α be free, whilst fixing the mass-concentration relationship to prevent too much degeneracy. We only use galaxies with a DynPop23 quality flag of 3. In Fig. 5.13 we see the galaxies have a mean α of around 0.75 (weighted by the uncertainty), which is shallower than the NFW halo profile. There is no statistically significant correlation with M_*. It should be cautioned that α is a difficult quantity to measure as most galaxies in the sample are "maximal discs", and therefore have little dark matter in the inner region.

5.5 Discussion

In this Chapter we have debuted two new methods to constrain dark matter halo properties with kinematic observations compared to our linewidth study in Chapter 3. Firstly we have fitted to the full flux profile rather than just the linewidth summary statistic. Secondly we have added IFU data to the inference, modelled using the JAM procedure. The stellar kinematics provide an additional dynamical constraint towards the centre, and the improved knowledge of galaxy inclination and the stellar mass distribution compared to the simple

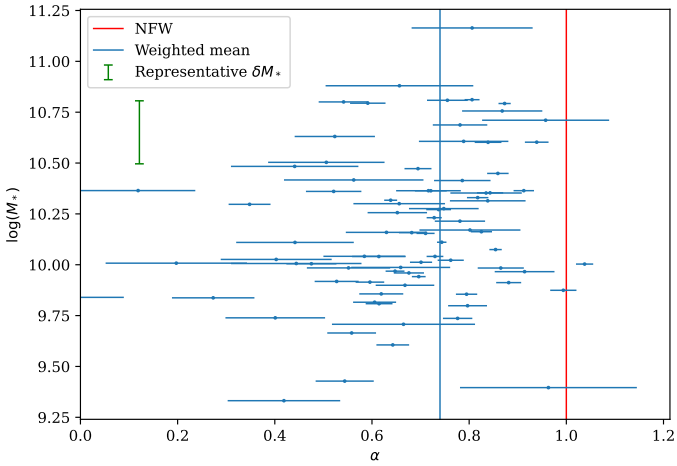

Figure 5.13: The gNFW logarithmic inner slope (α) inferred from a fit to stellar kinematics and HI with the mass–concentration prior applied, plotted against M_*, with 1σ symmetrised errorbars. The sample consists of the 99 galaxies with $Qual = 3$ (and that pass the HI quality cuts, see Section 5.2). The NFW slope is $\alpha = 1$ (red), whereas the weighted mean for the sample is slightly shallower ~ 0.75 (blue).

models used in Chapter 3 boosts the constraining power of the HI data.

The use of the full flux profile was motivated by the degeneracy between the linewidth generated by the baryons alone and the linewidth generated with additional dark matter halo for high surface brightness galaxies where the peak in the baryonic circular velocity is close to $V_{\rm flat}$, which results in weak constraints. We found the combination of HI (with the full flux profile) and stars is able to help break the degeneracy between halo mass and concentration and provide stronger constraints than linewidth modelling alone. These constraints can be compared to abundance matching and their strength and correlations characterised using the tools developed in Chapter 3.

When fitting to the HI flux profile we find for most galaxies our inferences give sensible constraints on the RC. However there are a minority for which, contrary to expectations, either the halo mass is constrained to be less than the baryonic mass or to be the mass expected from a large group or cluster. This may be because our empirical mode for the HI surface density does not reflect the true HI surface densities of our sample, either because

the functional form we used does not adequately describing the SPARC data or MaNGA galaxies having intrinsically different HI distributions. One obvious shortcoming is that our model does not allow holes in the HI. A hole may occur at only the very centre of the galaxy where velocities are low, and hence a hole would tend to decrease the flux towards the centre of the line profile, making it more horned, which is the same effect that dark matter has. Therefore this can plausibly explain galaxies which have too little dark matter. We also see the galaxy in Fig. 5.3 prefers a solution with minimum Σ_0 and maximum $\bar{r}_b$, which may be an attempt to to mimick a core. However its preferred solution is less horned than the data, arguing against this solution.

Another possibility is that the measured flux is incorrect - it is apparent from the best fit figures that for many galaxies the total flux of the model appears to be slightly higher than the data (even though by construction they are the same, as the mass of our HI disc is equal to the HI mass reported in the catalogue). This could be an artefact of the smoothing procedure used to calculate the flux from the data by the MaNGA-HI survey, or from including contributions away from the HI emission line. To test this we let the flux be a free parameter with uncertainty given by that reported in MaNGA and repeated the inference for a few galaxies with extreme halo masses. However we found it did not make a difference. Nevertheless in the future the inference should marginalise over the uncertainties on both the HI flux and distance.

We considered possible problems in IFU data/modelling, but most outlier halos remain outliers even when only the HI data is used in the inference. We investigate whether quality cuts on the HI data are able to remove these outliers, focusing on the SNR, inclination and asymmetry of the flux profile (quantified as the ratio of flux on each side of line profile centre). We define outliers as galaxies constrained by 2σ to have a halo mass less than the baryonic mass, or to have a halo mass greater than $10^{13}\,\mathrm{M}_\odot$. We find that only SNR cuts can remove a significant fraction of outliers. However a minimum SNR of 18 is required to remove all outliers, at which point our sample is non-statistical (12 galaxies). This may

indicate that high SNR is important to enable accurate inferences using the full flux profile. We discuss how to test our HI model more systematically using resolved HI data in section 5.5.1.1.

We also presented a stacked SHMR (Fig. 5.6), finding a deviation from abundance matching relationships consistent with our ALFALFA study. Perhaps surprisingly the 1 and 2σ confidence regions are similar in width in $M_{\rm vir}$ to our ALFALFA analysis, despite the increasingly powerful data being used. There are two main causes. Firstly there are now more outliers (where either a very small or very large halo mass is favoured) in our MaNGA sample compared to the ALFALFA galaxies (at fixed stellar mass), increasing the scatter in the stacked posterior. Secondly we find that for MaNGA our inferences prefer values of M_*/L that are consistently towards the upper end of the prior, suggesting the NSA M_*/L (which were used in our ALFALFA analysis, in which M_* was not constrained beyond its prior) may be underestimated. A lower M_*/L increases the dark matter dominance towards the centre and hence improves the constraints on $M_{\rm vir}$ (as discussed in Chapter 4). The distribution of baryons in the MaNGA sample may also be intrinsically more concentrated than in ALFALFA due to differences between the two populations; for example the ALFALFA galaxies may be more gas-rich on average (at fixed baryonic mass), or have less concentrated stellar distributions. Finally we have also switched to a more sophisticated gas model, which gives a weaker prior on the HI distribution and hence weaker constraints on $M_{\rm vir}$.

Finally we let the inner slope parameter α vary in an inference using only the highest quality IFU data, and found α to be slightly shallower than that of an NFW halo, which may be due to dynamical heating of the dark matter. Previous studies such as SPARC (Li et al., 2019, figure A4) have found evidence for non-NFW inner slopes in high mass galaxies (using the Einasto halo profile). However Li et al. find much greater variation, with many high-mass galaxies with both flatter cores than we find or steeper slopes than NFW. Theory/simulations (e.g. Di Cintio et al., 2014) argue for a dependence on $M_*/M_{\rm vir}$.

However it is not easy to study in data due to the poor constraints on many $M_{\rm vir}$ for many galaxies. As the theoretical models also predict strong correlation of coredness with M_* due to their tight SHMR, we instead plot M_* against α, finding no statistically significant correlation. Moreover for high mass discs theory predicts adiabatic contraction should steepen the slope to above NFW. Therefore we conclude the observed inner slopes are in disagreement with theory, although we again caution that the low dark matter fraction makes it difficult to measure. Dynpop23 advocate the total (dark plus light) inner density slope as a more reliable quantity to measure, albeit less related to the dark matter.

The validity of JAM models has been extensively studied in simulations and mock data (e.g. Li et al., 2016; Wang et al., 2022). The core assumptions of JAM are that the galaxy is steady-state, axisymmetric and the velocity ellipsoid is orientated as described in Section 5.3. Li et al. also find having high enough resolution data is required to obtain an unbiased inference. The by-eye quality cuts of Dynpop23 are meant to be identify galaxies that are clearly non-axisymmetric, out of equilibrium, or have low quality data. However it is possible that more subtle departures from these assumptions remain even in galaxies assigned a high quality flag. Wang et al. find non-equilibrium motion caused by galactic winds in star-forming systems can cause biases in JAM modelling. However, like with HI, the validity of this statement depends on the ability of simulations to produce realistic galaxies, which depends on the galaxy formation model as well as the numerical implementation. Some current generation simulations do not produce late-type galaxies with discs as thin as observed (Peebles, 2020). In our model for simplicity we assume a constant anisotropy and mass-to-light ratio across the galaxy, which is an approximation that could bias inferences on the dark matter content. Relaxing these assumptions (e.g. by using stellar population models to find a radially-dependent mass-to-light ratio) would be an interesting future investigation.

5.5.1 Future work

5.5.1.1 Validating the modelling

A priority is to test our full flux profile model using a sample for which both resolved and integrated HI observations are available. If outlier cases (with either very low or high halo masses) no longer appear once the true resolved HI surface density is used to generate the flux profile in the inference, then our empirical model is insufficient. Otherwise the problem must be with the HI data or other modelling assumptions. The outlier cases can also be correlated with galaxy/measurement properties such as inclination, SNR and goodness-of-fit statistics to establish any underlying cause and enable principled cuts to exclude them from the analysis.

The results so far have been derived using the cylindrically alligned-velocity ellipsoid. The inferences should also be carried out using the spherically-aligned assumption for the velocity ellipsoid. DynPop23 argue that for quality flag 1 galaxies, derived quantities can only be trusted if both the cylindrical and spherical assumptions are in agreement, whereas for quality flag 3 galaxies all quantities can be trusted. We have already checked that there are not clear systematic differences in the results presented here between quality 1/2 and quality 3 galaxies.

5.5.1.2 Model improvements

The outliers in halo mass may be caused by the SPARC HI density profiles not being representative of the MaNGA galaxies. Larger samples of resolved HI density profiles will enable construction of more sophisticated empirical models for the HI surface density profiles using machine learning methods such as symbolic regression (e.g. La Cava et al., 2021; Bartlett et al., 2023), which do not require a particular functional form for the profile to be assumed.

5.5.1.3 Improved data

The completed MaNGA-HI survey will provide data for three times as many galaxies, strengthening the statistical power of this study. It is important to note (based on Chapter 4) that the high-surface brightness galaxies in our sample are the worst for constraining dark matter halo profiles due to their baryon-dominated inner regions. Whilst MANGA does have significant numbers of lower mass galaxies down to $M_* = 10^{8.5}\,M_\odot$, the majority are assigned low quality flags by DynPop23. Future IFU surveys that focus on obtaining better data for lower mass galaxies would enable our method to be applied to galaxies across a larger mass range. The MaNGA Dwarf galaxy survey (MaNDala, Cano-Díaz et al. 2022) has recently observed 136 bright field dwarves with $M_* < 10^9\,M_\odot$.

It may also be possible to use a simpler model on lower mass galaxies that is more suited for the lower quality data, or to use rotation curves derived from H-α to probe the inner regions instead of/in addition to the stellar kinematics.

Many galaxies were also cut from the sample as they were observed with too low SNR by the MANGA-HI survey. Future HI with surveys such as MIGHTEE, ASKAP and the SKA will be able to deliver integrated HI observations out to higher redshift, with less noise and with fewer systematics than single dish experiments. This will not only provide increased constraining power but may reduce the presence of outliers if systematics in the HI flux profile are producing biases.

5.5.1.4 Uncertainties

A weakness in our method is the "estimated" uncertainties on the stellar kinematics, which is in tension with our Bayesian approach, This method of estimating uncertainties is used because using the reported uncertainties (or even the initial larger estimates for the kinematic uncertainties) results in unrealistically tight constraints. A natural solution to this is to use a more flexible model. However even studies using the more flexible Schwarzchild modelling still run into the same problem and adopt similar procedures to modify their uncertainties

(van den Bosch & van de Ven, 2009). The most flexible form of modelling that can account for any feature is distribution function (DF) modelling. DF models are often constructed for the Milky Way and nearby galaxies (e.g. Gherghinescu et al. 2023). However it will be difficult to construct bespoke models for large surveys such as MaNGA.

5.6 Conclusion

We have presented a novel approach to combine integrated HI observations with IFU stellar kinematics to constrain dark matter halo properties, and applied it to a sample of 399 high mass late-type galaxies observed by the MaNGA/MaNGA-HI survey. Our main findings are as follows:

- For this population of galaxies, combining IFU and HI data is able to provide strong constraints on halo mass for most galaxies when the mass–concentration relationship from DMO simulations is applied as a prior.
- Without the prior applied, around 1/3 of galaxies still have both both mass and concentration well constrained. For the rest there is still strong degeneracy between mass and concentration, although interesting parts of the parameter space are excluded.
- Consistent with other studies, we find evidence that high-mass late-type galaxies have on average very high star-formation efficiencies, converting nearly all of their cosmologically available baryons to stars.
- We find evidence the inner slope parameter of our sample is slightly shallower (~ 0.75) than an NFW halo, in disagreement with expectations from simulations.

The completion of current and future IFU and HI surveys will enable our method to be applied to larger numbers of galaxies with a broader range of properties. Moreover the rich auxiliary data available from combined IFU and HI surveys, including spatially resolved

star formation histories, will enable the relationship between halo properties and a galaxy's gas content and star formation to be disentangled over the coming years. Our method of forward modelling spatially integrated flux profiles can be applied at redshifts inaccessible to resolved studies and adapted to other tracers such as CO, enabling studies of how the dark matter content of galaxies evolves over cosmic time, and its consistency with ΛCDM galaxy formation.

Chapter 6

Weak lensing: a preliminary investigation

6.1 Introduction

Weak lensing is a powerful probe of the galaxy-halo connection. It only requires photometric observations, and hence is available for large quantities of galaxies. Unlike kinematic methods, the analysis does not vary with galaxy type: galaxies with diverse properties can be analysed homogeneously, lessening the risk of inferring spurious variation of the galaxy-halo connection with galaxy type. Lensing is also easier to measure out to higher redshift than kinematics.

The drawback, of course, is that weak lensing is a weak effect, with the shape distortion of a source galaxy typically 1-10% the dispersion in the observed ellipticities of unsheared galaxies. Therefore weak lensing analyses must statistically combine large numbers of lensing galaxies in order to derive precise halo masses for populations of galaxies. This is usually achieved through stacking: the mean weak lensing signal is calculated in radial bins around a set of galaxies with similar observed properties (e.g. Mandelbaum et al., 2016). Then either a parameterised halo profile is constrained using each bin of galaxies, or the

population can be forward modelled assuming a stellar-to-halo mass relationship (SHMR).

A weakness of the stacking methodology is that when combining galaxies in a bin, one is essentially assuming all galaxies/halos in the bin are identical. This results in loss of information on the variation within the bin, making it difficult to infer the intrinsic scatter in properties between halos. It is also not possible to select galaxies with exactly the same properties: the galaxies in each bin will have a wider than intended distribution in the property they were selected on due to observational uncertainties.

Stacking also makes it difficult to explore the dependency of halo mass on more than one parameter, as this requires splitting the sample in two-dimensional bins. This can work when the second parameter is binary, but when it is continuous it is difficult to sufficiently populate all bins with galaxies. Properly modelling observational and intrinsic scatter is also important for the accurate inference of secondary properties in the SHMR (Sonnenfeld & Leauthaud, 2018).

An alternative approach is to use a Bayesian formulation of weak lensing (Lieu et al., 2017; Sonnenfeld & Leauthaud, 2018). Here rather than stacking galaxies, a likelihood is used for the probability of the shear of each background galaxy. This likelihood can then be used to constrain parameterised relationships between galaxy and halo properties, along with their intrinsic scatter. The Bayesian formalism also offers a natural way to combine lensing constraints with kinematic data or empirical methods. Whilst the Bayesian approach has previously been applied to clusters and massive ellipticals, here we briefly discuss its potential application to constrain the galaxy-halo connection across a wide range of galaxy masses and types.

6.2 Methods

In weak lensing the observable is the observed tangential shear $\epsilon_t^{(\mathrm{obs})}$. The predicted tangential shear $g(\boldsymbol{\theta}, z_s)$ of a background galaxy around a foreground lens for a given mass

model/position $\boldsymbol{\theta}$ and source redshift z_s is the *reduced-shear*

$$g(\boldsymbol{\theta}, z_s) = \frac{\gamma(\boldsymbol{\theta}, z_s)}{1 - \kappa(\boldsymbol{\theta}, z_s)}. \tag{6.1}$$

where $\kappa(\boldsymbol{\theta}, z_s)$ is the dimensionless surface mass density (*convergence*) and $\gamma(\boldsymbol{\theta}, z_s)$ is the complex shear due to the lens at the image position.

The convergence κ is the ratio between the surface mass density, $\Sigma(r)$, and the critical surface mass density, $\Sigma_{\rm cr}$

$$\kappa = \frac{\Sigma(r)}{\Sigma_{\rm cr}}, \tag{6.2}$$

where

$$\Sigma_{\rm cr} = \frac{c^2}{4\pi G} \frac{D_S}{D_L D_{LS}}, \tag{6.3}$$

with D_S, D_L, and D_{LS} the angular diameter distances between the observer and the source, the observer and the lens, and between the lens and the source, respectively, and c the speed of light. The shear $\gamma(\boldsymbol{\theta}, z_s)$ at a radius r is the difference between the average surface mass density within that radius ($\overline{\Sigma}(< r)$), and the actual surface mass density:

$$\gamma = \frac{\overline{\Sigma}(< r) - \Sigma(r)}{\Sigma_{\rm cr}}. \tag{6.4}$$

The values of Σ and $\overline{\Sigma}$ are determined by integration of the 3D density model profile in the direction of the line of sight (e. Lieu et al., 2017, appendix A).

Using this formalism, and parameterising each lens galaxy and halo through their stellar mass (M_*), halo mass ($M_{\rm vir}$) and concentration (c), the likelihood of observing a source galaxy with observed shear $\epsilon_t^{(\rm obs)}$ around a given lensing galaxy is

$$\mathrm{P}(\epsilon_t^{(\rm obs)} | M_*, M_h, c_h) = \frac{1}{\sqrt{2\pi}\sigma_\epsilon} \exp\left\{ -\frac{(g(\boldsymbol{\theta}, z_s) - \epsilon_t^{(\rm obs)})^2}{2\sigma_\epsilon^2} \right\}, \tag{6.5}$$

with σ_ϵ the uncertainty on the observed tangential shear. Here we are assuming that the sampling distribution for the shear is a Gaussian with width equal to σ_ϵ, which (Lieu et al., 2017) argue is a reasonable assumption for the shear uncertainties reported in weak lensing

catalogues. The shear sampling distribution is generated by two effects: the true variation in galaxy shapes and the uncertainty in measuring a galaxy's shape from photometry, with the former typically dominating.

For a given galaxy-halo pair, the likelihood of the halo/galaxy mass and concentration are the product of the likelihoods of the j source galaxies

$$\mathrm{P}(\{\mathrm{WL}\}\,|M_h, c_h, M_*) = \prod_j \mathrm{P}(\epsilon_{t,j}^{(\mathrm{obs})}|M_*, M_h, c_h). \tag{6.6}$$

The ensemble of galaxies can then be used to constrain parameterised relationships such as the SHMR in a hierarchical model. For demonstration purposes we use a simple power law SHMR

$$\mu_h(M_*) = \mu_{h,0} + \beta(\log M_* - \log M_*^{\mathrm{piv}}) \tag{6.7}$$

where $\mu_h(M_*)$ is the mean log halo mass for a galaxy with intrinsic stellar mass M_*, $\mu_{h,0}$ is the mean log halo mass at a chosen stellar mass M_*^{piv} and β is the slope. We allow a constant Gaussian scatter in halo mass at fixed stellar mass σ_h. To account for difference between the observed and intrinsic distribution of stellar masses (which is important due to the slope of the stellar mass function), the distribution of intrinsic galaxy stellar masses can be parameterised and constrained as part of the inference. For simplicity we not include it here, and set intrinsic stellar masses to be equal to the mean observed value. We assume the halos follow an NFW profile, with halo concentration which follows the mass–concentration relationship from DMO simulations (Dutton & Macciò, 2014).

We select lens galaxies from the GAMA spectroscopic dataset (Baldry et al., 2012). The GAMA survey contains 300,000 galaxies observed over $\sim$ 300deg^2 down to a magnitude limit of 19.8 mag, with many galaxies observed out to a redshift of 0.5. In common with the optically-selected NSA and MaNGA samples, it contains a mix of early and late-type galaxies. This is in contrast to the HI-selected samples analysed Chapters 3,4 and 5 which consisted almost exclusively of late-type galaxies. GAMA has excellent statistics down a stellar mass of around 10^8 M$_\odot$.

In its current form the method cannot differentiate between shear due to the mass of the galaxy/halo of interest, and shear from other nearby galaxies. Therefore to make sure we only have central or isolated galaxies in our sample, we select galaxies which have the highest stellar mass in a 1 Mpc spherical region (we check are results are not strongly sensitive to this value), following Mandelbaum et al. (2016). We put a redshift-dependent cut on stellar mass to ensure that for a chosen lens galaxies, nearly all nearby galaxies of similar mass are also detected (even if they have a lower mass-to-light ratio).

For our source galaxies we use the KiDS-1000 catalogue (Giblin et al., 2021), applying the same quality cuts as Brouwer et al. (2021). The KiDS-1000 catalogue provides a measurement and uncertainty for the shear of each galaxy derived from the `lensfit` code (Miller et al., 2007, 2013). The `lensfit` code was the first Bayesian model-fitting algorithm for measuring weak gravitational lensing shear from survey images. The method fits two-component models (consisting of a disk and a bulge), which are convolved with the point spread function to determine the ellipticity of each galaxy. Marginalisation over nuisance parameters accounts for uncertainties in the galaxy's position, size, luminosity, and the bulge fraction, enabling an accurate measurement from multiple dithered photometric exposures with image distortion and misalignment.

6.3 Results

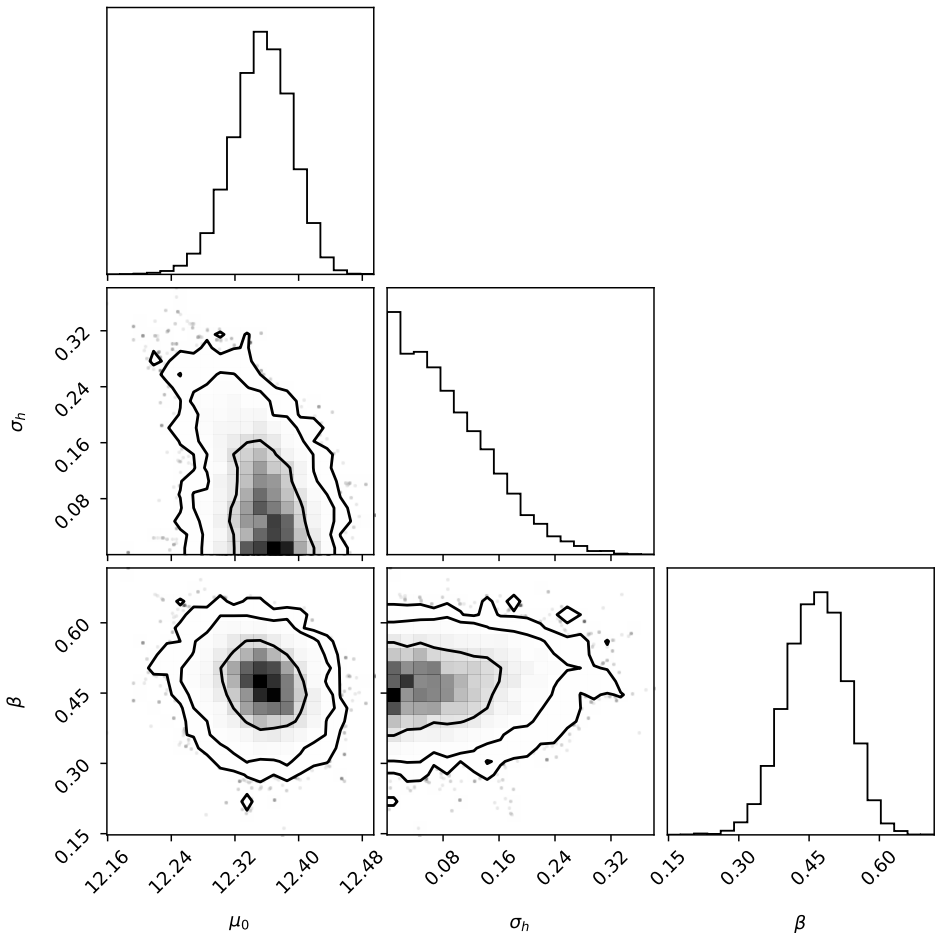

Figure 6.1: The inferred parameters of the SHMR (equation 6.7) for our sample of isolated/central galaxies (with contours marking the 1,2 and 3 σ intervals). The preferred value of the scatter in halo mass at fixed stellar mass (σ_h) is 0, contrary to expectations.

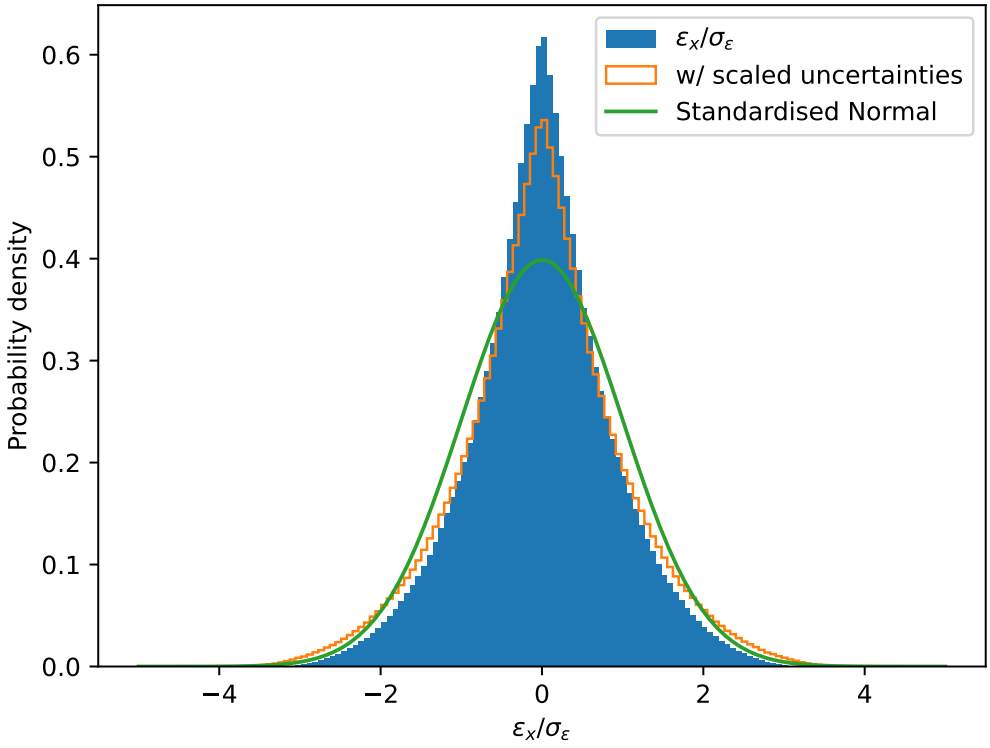

Figure 6.2: A histogram of the distribution of the residuals of the cross shear $\epsilon_x/\sigma_\epsilon$ (blue), as well as the new residuals when the uncertainties σ_ϵ have been reduced by 17% in order to make variance of the residuals equal to 1 (orange). A standardised normal distribution is also shown for comparison (green). The distribution of residuals is significantly non-Gaussian.

In Fig. 6.1 we present the inferred parameters of the SHMR for our sample (using flat priors on all parameters). The preferred value of the scatter in halo mass at fixed stellar mass σ_h is 0, the mean halo mass of a galaxy with $M_* = 10^{11}\,\mathrm{M}_\odot$ is $\sim 10^{12.35}\,\mathrm{M}_\odot$ and the power law slope is 0.45. That $\sigma_h = 0$ is highly suspicious. To diagnose the problem we consider the residuals of the cross shear $\epsilon_x/\sigma_\epsilon$. The uncertainty on the cross shear is equal to that of the tangential shear. As the cross-shear is unaffected by the lens galaxies, its residuals should have the distribution of a standardised normal under the modelling assumption that the sampling distribution of the shear is a Gaussian with width given by σ_ϵ. We plot the residuals in Fig. 6.2, and find this not to be the case.

In particular we find that the distribution is narrower than a standardised normal, which would explain the overly low value of σ_h. We attempt to crudely correct for this by increasing all shear uncertainties σ_ϵ by 17% so the variance of the residuals becomes 1. However we find that this dramatically increases σ_h to a preferred value of ~ 0.7.

6.4 Discussion

We have found strong evidence that a standard modelling assumption in Bayesian hierarchical lensing: that the sampling distribution of the shear is a Gaussian with width given by the `lensfit` uncertainties, leads to a biased inference of model parameters. We attempt to correct for this using a simple rescaling of the uncertainties, but find the inferred model parameters are very sensitive to this. We find other cases in the literature where a suspiciously low σ_h has been found using the Bayesian weak lensing method (e.g. Sonnenfeld et al., 2022).

Investigating further, we find that the intrinsic distribution of galaxy ellipticities used in the calculation of `lensfit` uncertainties is non-Gaussian. Our conclusion is that in order to make unbiased inferences using the Bayesian weak lensing method, it is necessary to better model the uncertainties in the tangential shear and use a non-Gaussian likelihood. Unfortu-

nately due to the complexity of deriving these uncertainties (which are a combination of the distribution of intrinsic galaxy ellipticities and galaxy shape measurement uncertainties), this is not a simple task.

Moreover it is possible that the current method of using the intrinsic ellipticity distribution of bright nearby galaxies as the distribution of intrinsic ellipticities for source galaxies may not be accurate enough due to evolution in galaxy properties with redshift. A better approach would be to infer the intrinsic distribution of source galaxy ellipticities as a part of the hierarchical inference. Such an approach has been developed by Schneider et al. (2015) in the context of cosmic shear, but involves pixel level forward modelling and has yet to be applied to real data. It may be possible to adapt some aspects of this method to infer the distribution of source galaxy intrinsic ellipticities along with an unbiased SHMR. We leave this to future work.

Chapter 7

Conclusions

In this thesis I have developed methods to maximise the information extracted on the galaxy-halo connection from forthcoming large-scale surveys. In particular I have focused on combining photometric and kinematic constraints on the galaxy-halo connection.

In Chapter 3 I presented two main novel developments. Firstly I developed a Bayesian formulation of the inverse abundance matching method that enables efficient calculation of posteriors on halo properties for large samples of galaxies. This Bayesian formulation could also be applied to any method that generates statistical samples of galaxy-halo pairs such as hydrodynamical simulations or semi-analytic models to calculate their prediction for P(halo properties|galaxy properties) efficiently along with the Bayesian evidence.

Secondly I developed a Bayesian forward model for the HI linewidth. Historically HI mass-modelling has been carried out for hand-selected samples of galaxies, imbuing the samples with an unknown selection function and raising questions about how representative they are of the wider population of late-type galaxies. By analysing the linewidth I was able to carry out the first comparison between HI kinematics and abundance matching for a statistical volume-limited samples of galaxies generated from a blind survey with known selection function, and was able to establish a number of interesting results in this domain. This includes the general agreement between halo masses inferred from abundance

matching and kinematics, evidence for core formation in low mass halos and the apparent power-law behaviour of the baryonic/stellar-to-halo-mass relationships at the high mass end for late-type galaxies.

I also found a number of in-tension galaxies, mainly at low mass, which were constrained to have little dark matter within their gas disc. I was able to carry out an analysis of the dark matter content of "dark-matter deficient" galaxies for a statistical sample, which had only been done for tiny samples previously (e.g. Mancera Piña et al., 2021). My method of quantifying consistency between kinematics and abundance matching using the two-dimensional posterior on halo-mass and concentration offers an informative view of possible tensions, and should be widely adopted. It is especially useful as the abundance matched-simulated halos properly capture our prior expectations of the full distribution of dark matter halo properties, including the non-Gaussian low concentration tails (Kong et al., 2022), which is not adequately captured by simply applying mass-concentration relationships such as Dutton & Macciò (2014) as priors on kinematic fits.

In Chapter 5 I paired our HI line profile model with MaNGA data, the first time halo properties have been constrained by jointly modelling stellar kinematics and HI for a population of galaxies. I found the method produced interesting constraints in the mass–concentration plane, and I was able to confirm the power-law high mass end of the SHMR found in our ALFALFA analysis. I also studied the inner slope, finding the profiles were slightly shallower than NFW on average. Studying inner slopes with multiple tracers and modelling methods is important, as potential biases in halo profile inferences with gas RCs have previously been highlighted in literature (Roper et al., 2023).

The galaxies that survived both IFU and HI quality cuts were unfortunately limited to high mass galaxies. Future HI surveys such as MIGHTEE, ASKAP, Apertif, and eventually the SKA will deliver resolved rotation curves for statistical samples of galaxies, as well as integrated flux profiles for many more. Both the Apertif and MIGHTEE surveys are planning to follow up their HI observations with WEAVE, which will allow many of the

analysis methods developed in this thesis to be applied to joint IFU and HI RC analyses of large samples of galaxies. However in the age of large interferometric HI surveys, my method of forward modelling the integrated flux profile will continue to be useful for pushing into regimes inaccessible to resolved RCs.

Firstly it can used to study low mass systems that are too small to be observed in cosmological volumes with resolved studies. In fact the only previous joint inference using stellar kinematics and HI was done for the WLM dwarf galaxy (Leung et al., 2021). High quality linewidths have recently been obtained for other low mass dwarfs (Sardone et al., 2023). However at the lowest masses inclination and asymmetric drift corrections are a significant uncertainty. An empirical model for asymmetric drift corrections could be constructed and marginalised over in a similar manner to the HI surface density. Future IFU surveys such as MaNDala (Cano-Díaz et al., 2022) are also targeting more massive dwarfs.

My integrated HI model will be of most use in extending the redshift range in which halo properties can be constrained using HI. Many studies are underway using IFU data to constrain dynamics at around redshift 1 (e.g. Stott et al., 2016), using tracers that are limited to only the inner regions of galaxies. Cosmological simulations predict significant evolution of the BTFR only above $z \sim 0.5$ (although they are calibrated on $z = 0$ data), a regime that will be barely accessible to resolved studies even with the SKA. In Fig. 7 I show some HI profiles from MIGHTEE Early Science data overlaid with ALFALFA observations of the same galaxy, which highlights the improved sensitivity and better control of systematic noise these new surveys will bring. Our method can also be adapted to model the integrated flux profiles of emission lines from other tracers of rotation such as molecular gas, that can be observed at very high-redshift using instruments such as ALMA.

The flood of higher redshift data from photometric surveys such as COSMOS and Rubin will enable the galaxy-halo connection to be constrained at increasing redshift with empirical models. An empirically derived galaxy-halo connection in the range $z = 0.5 - 2$ can also be used to generate predictions for the evolution of dynamical scaling relationships

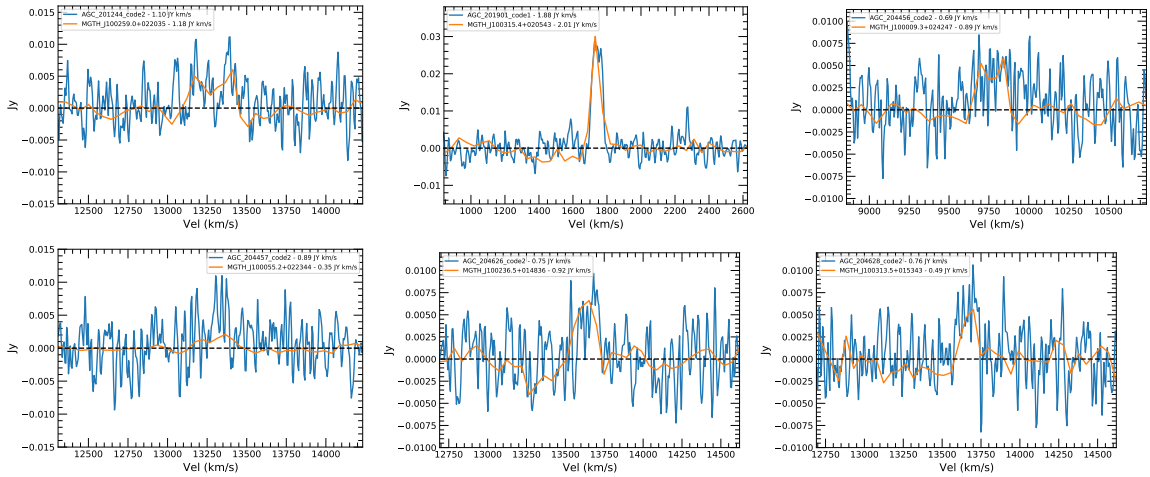

Figure 7.1: HI line profiles from the early-science data of the MIGHTEE survey (orange) plotted over the same galaxies from the ALFALFA survey (blue). The increased sensitivity and improved instrumental noise properties produces cleaner line profiles that are more amenable to detailed modelling. *Credit: Anastasia Ponomareva*

with redshift ahead of the kinematic data arriving.

In Chapter 6 I began investigating the potential of weak lensing to constrain the galaxy-halo connection. Unfortunately I found a central assumption of our method of choice was flawed. As previously discussed, the power of weak lensing is its homogeneous analysis between early and late-type galaxies and its ability to probe out to higher redshift (Chaurasiya et al., 2023). The power of weak lensing was also recently highlighted by (Brouwer et al., 2021), who extended the radial acceleration relationship to much lower acceleration using the KiDS data. EUCLID will allow the galaxy-halo connection to be well constrained out to $z \sim 2$, but only if methods such as those this thesis develops can be applied. Lensing is also being pushed into the regime of dwarf galaxies by the Merian survey (Luo et al., 2023), where it will help resolve issues such as cusp-core when combined with kinematic data (Leauthaud et al., 2020). Again I re-emphasise that the Bayesian formulation seems an optimal way to do this combination.

We attempted to select a sample of high mass spiral galaxies in KiDS to test and combine our results on the high-mass end of the SHMR in ALFALFA and MaNGA, but found the rarity of this type of object and the difficulty of morphological selection meant that current

sample sizes/image quality were not sufficient to obtain a large enough sample. EUCLID, along with developments in morphological classification should remedy this. A major limitation in the study on SHMR bimodality of Posti & Fall (2021) was the completely different analysis methods applied to ellipticals and spirals, as well as the small size of the effect relative to typical uncertainties on halo mass, both of which a lensing study would help overcome.

Whilst I have focused on late-type galaxies due to the availability of HI, my philosophy of combining different probes is readily applicable to early-type galaxies where high signal-to-noise data is more readily available, and tracers include including stellar and satellite kinematics, weak and strong lensing, and X-rays. A joint weak lensing analysis with MaNGA was recently carried out (Wang et al., 2023), but using the stacking method to compress both kinematics and weak lensing to a single halo profile for thousands of galaxies. A joint analysis of MaNGA IFU kinematics with weak lensing data using the Bayesian formalism would be highly informative on the galaxy-halo connection given the rich auxiliary data available. Overall, all of the science highlighted above presents a strong case for attempting to advance the Bayesian weak lensing program, in spite of the challenge.

In Chapter 4 I used machine-learning methods to examine the precision of constraints on halo properties as a function of galaxy and measurement properties for spectroscopic observations of late-type galaxies. I identified the most important variables for which either observation or modelling needs to be improved. This in line with other "information content" studies in literature that aim to optimally extract information from future surveys by informing their design. The method of course can be applied to other types of kinematic data, or applied to simulated data. The method could also be developed further to answer higher level questions, such as what are the optimal set of observations to constrain the galaxy-halo connection well enough to achieve a specific purpose such as constraining a screened modified gravity theory that requires knowledge of the gravitational potential around galaxies (Desmond et al., 2018a).

I bring this thesis to a close with musings on open questions and challenges in the wider field.

ΛCDM all the way down?

ΛCDM, in part due to the flexibility imbued by uncertainties in baryonic physics, can plausibly explain the majority of galaxy scale observations (e.g. Sales et al., 2022) (whilst making allowances for data that one suspects might not yet be watertight). Most alternate dark matter theories such as SIDM or warm dark matter are studied because they might be able to reproduce a specific observation (such as being able to generate a core) or because they are the simplest extensions to dark matter. Other particle candidates such as WIMP have a strong historical basis, even if the originally motivating theory may have since lost its shine. In the absence of a strongly motivated directly competing theory, the dominant question becomes whether data can be explained to a satisfactory level by ΛCDM.

The main limiting factor on tests of ΛCDM with the galaxy-halo connection are the impact of baryons on the dark matter distribution. Whilst there is evidence for the impact of feedback on the gas in dwarfs, and some evidence for it modifying the dark matter profile (reviewed in Collins & Read, 2022), other lines of evidence are mixed and simulations disagree on the theoretical prediction due to differing subgrid implementations. Many papers have argued for the dependence of the dark matter halo inner slope on ($M_*/M_{\rm vir}$) (e.g. Di Cintio et al., 2014; Lazar et al., 2020) with a U-shape from uncored to cored to uncored again, but this is not forthcoming observationally. This may reflect the difficult of measuring the inner profile both at low mass due to complex dynamics, and at high mass due to the small amount of dark matter in the inner region. Rey et al. (2023) find some low mass dwarfs with pristine NFW cusps and rotationally supported gas (enabling a kinematic analysis) in simulations. These should just about be observable with current technology, if we are able to find them.

Other authors have challenged whether evidence for strong supernova-driven outflows is

visible in the data (e.g. Marasco et al., 2023), although the fact they could be in multiple gas phases makes this challenging to answer. Efforts to build bridging models for the impact of supernova on gas that compress the complexity of whole of galaxy formation into simpler prescriptions (Freundlich et al., 2020; Hashim et al., 2022), and that may be implementable in semi-analytic models, seem like a promising path forwards.

Key confirmation of cold dark matter would be the detection of low mass dark subhalos through strong lensing or perturbations to stellar streams (e.g. Banik et al., 2021). Dynamical friction, of which there has been recent claimed detections with both the stellar bar (Chiba et al., 2021b) and stellar streams (Koposov et al., 2022) (with strength consistent with expectations) is another key observational prediction. These are challenging areas observationally and theoretically, with strong astrophysical degeneracies. On larger scales, the Hubble Tension (Riess & Breuval, 2023), planes of satellites and the up and coming "cosmic anisotropy" (e.g. Secrest et al., 2022) offer hope that ΛCDM may not be the end of the story.

SAMs versus hydrodynamical simulations?

Given the large unknowns in galaxy-formation, such as the strength of feedback, and the fact hydrodynamical simulations can only quantitatively match a limited amount of the available data (and are too expensive to vary parameters), an obvious path forwards seems to be to constrain SAMs against growing bodies of observational data simultaneously. However the galaxy formation models are complex and understanding the interactions of various model parameters and constraints will likely be very challenging. A solution to this might be to break the analysis down into smaller systems. As previously discussed, isolated galaxies, both at low mass and high mass seem important systems to study to isolate the impact of supernova feedback from environmental effects. Interestingly Brouwer et al. (2021), in studying the weak lensing RAR, found that only a ΛCDM model with a SHMR independent of galaxy isolation was able to match observations, in disagreement with hydrodynamical simulations such as BAHAMAS.

Recently the CAMELs project (Villaescusa-Navarro et al., 2021) has run suites of cosmological simulations whilst varying parameters controlling the strength of supernova and AGN feedback. In principle these can be constrained against observations like SAMs, whilst avoiding their limitations on physical accuracy. However the simulation volumes (25 Mpc) are too small to calculate mass/luminosity functions, and the parameter numbers limited. Perhaps machine learning-based "baryon-pasting" techniques will help (Osato & Nagai, 2023; Stiskalek et al., 2021), although the differing physics at play in different types of cosmic environment may make the extrapolation problematic.

Developments in dynamical inference

Machine learning methods enable a reduction in a priori model and data assumptions. Symbolic regression (e.g. La Cava et al., 2021; Bartlett et al., 2023) is a method that searches for the optimal functional form to describe a set of data based on both accuracy and simplicity. It is well-suited for studies of halo profiles as the complexity of the baryonic physics or the myriad dark matter models results in a lack of clear theoretical expectation (or there is simply the desire to be model agnostic for curiosity's sake). It is readily applicable to simple analyses such as rotation curves, where the enclosed mass is more directly accessibly. Embedding it in more complex inferences such as those developed in this thesis is challenging due to the computational cost of optimising parameters for large numbers of functions. One could imagine a day when it becomes possible to simply combine all available probes of the galaxy-halo connection into a giant inference and recover a general halo profile that would shed insight on the nature of dark matter.

In the past few years numerical machine learning methods have increasingly been applied to the dynamical modelling of nearby stellar systems. Tools such as neural networks and Gaussian processes are used to enable flexible model parameterisations (Naik et al., 2021; Diakogiannis et al., 2019; Ibata et al., 2021). Techniques including Generative Adversarial Networks (Diakogiannis et al., 2019) or Gaussian Process Emulation (Gration & Wilkinson, 2019) reduce cost by speeding up model evaluations or reducing the number required.

Likelihood-free inference enables models of non-equilibrium processes such as stream formation to be constrained through direct simulation (Alvey et al., 2023). How similar methods, or others, can be applied to enhance the dynamical inferences used in this thesis is an open question.

Summary

In summary, this thesis has provided an extensive analysis of dark matter halo properties by applying both new and established methodologies to diverse data sets, including constraining halo properties on a galaxy-by-galaxy basis for cosmological volumes of galaxies for the first time. Looking ahead, the influx of data from future instruments provides a promising landscape for enhancing our knowledge of dark matter's role in galaxy formation, and possibly its nature. This thesis has provided a framework for combining constraints on dark matter halos and maximising the information extracted from forthcoming large scale surveys, which, together with detailed studies of fewer objects, will be instrumental in forging a comprehensive understanding of the galaxy-halo connection over the coming decades.

Bibliography

Abdurro'uf et al., 2022, The Astrophysical Journal Supplement Series, 259, 35

Adhikari S., et al., 2022, Astrophysical Tests of Dark Matter Self-Interactions

Aguirre A., Schaye J., Quataert E., 2001, The Astrophysical Journal, 561, 550

Alam S., et al., 2017, Monthly Notices of the Royal Astronomical Society, 470, 2617

Albareti F. D., et al., 2017, The Astrophysical Journal Supplement Series, 233, 25

Almeida J. S., Filho M., 2019, Research Notes of the AAS, 3, 191

Alpher R. A., Bethe H., Gamow G., 1948, Physical Review, 73, 803

Alvey J., Gerdes M., Weniger C., 2023, Monthly Notices of the Royal Astronomical Society

Andrae R., Schulze-Hartung T., Melchior P., 2010, Dos and Don'ts of Reduced Chi-Squared (arxiv:1012.3754)

Arbey A., Battaglia M., Covi L., Hasenkamp J., Mahmoudi F., 2015, , 92, 115008

Arcadi G., Dutra M., Ghosh P., Lindner M., Mambrini Y., Pierre M., Profumo S., Queiroz F. S., 2018, The European Physical Journal C, 78, 203

Asgari M., et al., 2021, Astronomy & Astrophysics, 645, A104

Baldry I. K., Balogh M. L., Bower R. G., Glazebrook K., Nichol R. C., Bamford S. P., Budavari T., 2006, Monthly Notices of the Royal Astronomical Society, 373, 469

Baldry I. K., et al., 2012, Monthly Notices of the Royal Astronomical Society, pp no–no

Ball C. J., Haynes M. P., Jones M. G., Peng B., Durbala A., Koopmann R. A., Ribaudo J., O'Donoghue A., 2022 (arxiv:2212.08728)

Banik N., Bovy J., Bertone G., Erkal D., de Boer T. J. L., 2021, Journal of Cosmology and Astroparticle Physics, 2021, 043

Barnes J., Hut P., 1986, Nature, 324, 446

Bartlett D. J., Desmond H., Ferreira P. G., 2023, IEEE Transactions on Evolutionary Computation, pp 1–1

Bassett B. A., Hlozek R., 2009, Baryon Acoustic Oscillations (arxiv:0910.5224), doi:10.48550/arXiv.0910.5224

Bastian N., Covey K. R., Meyer M. R., 2010, Annual Review of Astronomy and Astrophysics, 48, 339

Baxter E. J., et al., 2018, Monthly Notices of the Royal Astronomical Society, 476, 2674

Begeman K. G., 1989, Astronomy and Astrophysics, 223, 47

Behroozi P. S., Conroy C., Wechsler R. H., 2010, The Astrophysical Journal, 717, 379

Behroozi P. S., Wechsler R. H., Wu H.-Y., 2013a, The Astrophysical Journal, 762, 109

Behroozi P. S., Wechsler R. H., Wu H.-Y., Busha M. T., Klypin A. A., Primack J. R., 2013b, The Astrophysical Journal, 763, 18

Behroozi P., Wechsler R., Hearin A., Conroy C., 2019, Monthly Notices of the Royal Astronomical Society, 488, 3143

Behroozi P., Hearin A., Moster B. P., 2022, Monthly Notices of the Royal Astronomical Society, 509, 2800

Bernacchia A., Pigolotti S., 2011, Journal of the Royal Statistical Society: Series B (Statistical Methodology), 73, 407

Bhattacharyya A., 1946, Sankhyā: The Indian Journal of Statistics (1933-1960), 7, 401

Bigiel F., Blitz L., 2012, The Astrophysical Journal, 756, 183

Binney J., 2010, Monthly Notices of the Royal Astronomical Society, 401, 2318

Binney J., Tremaine S., 2008, Galactic Dynamics: Second Edition

Blanchet L., Tiec A. L., 2009, Physical Review D, 80, 023524

Blanton M. R., Roweis S., 2007, The Astronomical Journal, 133, 734

Blanton M. R., Kazin E., Muna D., Weaver B. A., Price-Whelan A., 2011, The Astronomical Journal, 142, 31

Blumenthal G. R., Pagels H., Primack J. R., 1982, Nature, 299, 37

Bode P., Ostriker J. P., Turok N., 2001, The Astrophysical Journal, 556, 93

Bok J., Blyth S.-L., Gilbank D. G., Elson E. C., 2019, Monthly Notices of the Royal Astronomical Society, 484, 582

Bonaca A., Hogg D. W., 2018, The Astrophysical Journal, 867, 101

Boyarsky A., Drewes M., Lasserre T., Mertens S., Ruchayskiy O., 2019, Progress in Particle and Nuclear Physics, 104, 1

Boylan-Kolchin M., 2021, Nature Astronomy, 5, 1188

Boylan-Kolchin M., Bullock J. S., Kaplinghat M., 2011, Monthly Notices of the Royal Astronomical Society: Letters, 415, L40

Briggs D. S., 1995, PhD thesis

Brook C. B., Shankar F., 2016, , 455, 3841

Brouwer M. M., et al., 2021, Astronomy & Astrophysics, 650, A113

Bruzual G., Charlot S., 2003, Monthly Notices of the Royal Astronomical Society, 344, 1000

Bryan G. L., Norman M. L., 1998, The Astrophysical Journal, 495, 80

Bryant J. J., et al., 2015, Monthly Notices of the Royal Astronomical Society, 447, 2857

Buchner J., 2022, Research Notes of the American Astronomical Society, 6, 89

Bullock J. S., 2002, Shapes of Dark Matter Halos. eprint: arXiv:astro-ph/0106380, doi:10.1142/97898127780l7˙0018

Bullock J. S., Boylan-Kolchin M., 2017a, Ann. Rev. Astron. Astrophys., 55, 343

Bullock J. S., Boylan-Kolchin M., 2017b, Annual Review of Astronomy and Astrophysics, 55, 343

Bundy K., et al., 2014, The Astrophysical Journal, 798, 7

Bureau M., Carignan C., 2002, The Astronomical Journal, 123, 1316

Burkert A., 1995, The Astrophysical Journal, 447, L25

Burrage C., Copeland E. J., Millington P., 2017, Physical Review D, 95, 064050

Cadiou C., Pontzen A., Peiris H. V., 2022, Monthly Notices of the Royal Astronomical Society, 517, 3459

Calzetti D., Armus L., Bohlin R. C., Kinney A. L., Koornneef J., Storchi-Bergmann T., 2000, The Astrophysical Journal, 533, 682

Cano-Díaz M., et al., 2022, The Astronomical Journal, 164, 127

Cappellari M., 2002, Monthly Notices of the Royal Astronomical Society, 333, 400

Cappellari M., 2008, Monthly Notices of the Royal Astronomical Society, 390, 71

Cappellari M., 2016, Annual Review of Astronomy and Astrophysics, 54, 597

Cappellari M., 2020a, Monthly Notices of the Royal Astronomical Society, 494, 4819

Cappellari M., 2020b, Monthly Notices of the Royal Astronomical Society, 494, 4819

Cappellari M., Copin Y., 2003, Monthly Notices of the Royal Astronomical Society, 342, 345

Cappellari M., Emsellem E., 2004, Publications of the Astronomical Society of the Pacific, 116, 138

Cappellari M., et al., 2011, Monthly Notices of the Royal Astronomical Society, 416, 1680

Caserano SPR., Shostak GS., 1980, Astronomy & astrophysics, 81, 371

Chae K.-H., Desmond H., Lelli F., McGaugh S. S., Schombert J. M., 2021, arXiv:2109.04745 [astro-ph, physics:gr-qc, physics:hep-th]

Chauhan G., Lagos C. d. P., Obreschkow D., Power C., Oman K., Elahi P. J., 2019, Monthly Notices of the Royal Astronomical Society, 488, 5898

Chaurasiya N., More S., Ishikawa S., Masaki S., Kashino D., Okumura T., 2023, Galaxy-Dark Matter Connection of Photometric Galaxies from the HSC-SSP Survey: Galaxy-galaxy Lensing and the Halo Model, doi:10.48550/arXiv.2307.03915

Chaves-Montero J., Angulo R. E., Schaye J., Schaller M., Crain R. A., Furlong M., Theuns T., 2016, Monthly Notices of the Royal Astronomical Society, 460, 3100

Chiba R., Friske J. K. S., Schönrich R., 2021a, Monthly Notices of the Royal Astronomical Society, 500, 4710

Chiba R., Friske J. K. S., Schönrich R., 2021b, Monthly Notices of the Royal Astronomical Society, 500, 4710

Clowe D., Bradač M., Gonzalez A. H., Markevitch M., Randall S. W., Jones C., Zaritsky D., 2006, The Astrophysical Journal, 648, L109

Collaboration P., et al., 2016, Astronomy & Astrophysics, 594, A1

Collaboration D., et al., 2022, Physical Review D, 105, 023520

Collett T. E., et al., 2017, The Astrophysical Journal, 843, 148

Collins M. L. M., Read J. I., 2022, Nature Astronomy, 6, 647

Conroy C., Wechsler R. H., 2009, The Astrophysical Journal, 696, 620

Conroy C., Wechsler R. H., Kravtsov A. V., 2006, The Astrophysical Journal, 647, 201

Conselice C., Bundy K., Ellis R., Brinchmann J., Vogt N., 2004, Symposium - International Astronomical Union, 220

Contreras S., Chaves-Montero J., Angulo R. E., 2023, Consistent Clustering and Lensing of SDSS-III BOSS Galaxies with an Extended Abundance Matching Formalism (arxiv:2305.09637), doi:10.48550/arXiv.2305.09637

Couchman H. M. P., Thacker R. J., 2003, 208, 227

Courteau S., 1997a, The Astronomical Journal, 114, 2402

Courteau S., 1997b, The Astronomical Journal, 114, 2402

Croom S. M., et al., 2021, Monthly Notices of the Royal Astronomical Society, 505, 991

Dalal N., White M., Bond J. R., Shirokov A., 2008, The Astrophysical Journal, 687, 12

Dayal P., Giri S. K., 2023, Warm Dark Matter Constraints from the JWST (arxiv:2303.14239), doi:10.48550/arXiv.2303.14239

Deg N., et al., 2022, Publications of the Astronomical Society of Australia, 39, e059

Del Popolo A., Le Delliou M., 2021, Galaxies, 9, 123

Desmond H., 2017a, Monthly Notices of the Royal Astronomical Society, 464, 4160

Desmond H., 2017b, Monthly Notices of the Royal Astronomical Society, 472, L35

Desmond H., 2023, The Underlying Radial Acceleration Relation, doi:10.48550/arXiv.2303.11314

Desmond H., Wechsler R. H., 2015, Monthly Notices of the Royal Astronomical Society, 454, 322

Desmond H., Ferreira P. G., Lavaux G., Jasche J., 2018a, Physical Review D, 98, 064015

Desmond H., Ferreira P. G., Lavaux G., Jasche J., 2018b, Monthly Notices of the Royal Astronomical Society, 474, 3152

Desmond H., Katz H., Lelli F., McGaugh S., 2019, Monthly Notices of the Royal Astronomical Society

Di Cintio A., Brook C. B., Macciò A. V., Stinson G. S., Knebe A., Dutton A. A., Wadsley J., 2014, Monthly Notices of the Royal Astronomical Society, 437, 415

Di Teodoro E. M., Fraternali F., Miller S. H., 2016, Astronomy and Astrophysics, 594, A77

Diakogiannis F. I., Lewis G. F., Ibata R. A., Guglielmo M., Wilkinson M. I., Power C., 2019, Monthly Notices of the Royal Astronomical Society, 482, 3356

Diemer B., More S., Kravtsov A. V., 2013, The Astrophysical Journal, 766, 25

Djorgovski S., Davis M., 1987, The Astrophysical Journal, 313, 59

Dodelson S., 2011, International Journal of Modern Physics D, 20, 2749

Dubois Y., et al., 2021, Astronomy and Astrophysics, 651, A109

Durbala A., Finn R. A., Odekon M. C., Haynes M. P., Koopmann R. A., O'Donoghue A. A., 2020, The Astronomical Journal, 160, 271

Dutta S., Khandai N., Rana S., 2022, Monthly Notices of the Royal Astronomical Society, 511, 2585

Dutton A. A., Macciò A. V., 2014, Monthly Notices of the Royal Astronomical Society, 441, 3359

Dutton A. A., van den Bosch F. C., Dekel A., Courteau S., 2007, The Astrophysical Journal, 654, 27

Dutton A. A., et al., 2011, Monthly Notices of the Royal Astronomical Society, pp no–no

Dutton A. A., Obreja A., Macciò A. V., 2018, Monthly Notices of the Royal Astronomical Society

Dyson F. W., Eddington A. S., Davidson C., 1920, Philosophical Transactions of the Royal Society of London Series A, 220, 291

Einstein A., 1916, Annalen der Physik, 354, 769

Eisenstein D. J., Hut P., 1998, The Astrophysical Journal, 498, 137

El-Badry K., et al., 2018, Monthly Notices of the Royal Astronomical Society, 477, 1536

El-Zant A., Shlosman I., Hoffman Y., 2001, The Astrophysical Journal, 560, 636

Falcón-Barroso J., Sánchez-Blázquez P., Vazdekis A., Ricciardelli E., Cardiel N., Cenarro A. J., Gorgas J., Peletier R. F., 2011, Astronomy & Astrophysics, 532, A95

Ferrero I., Abadi M. G., Navarro J. F., Sales L. V., Gurovich S., 2012, Monthly Notices of the Royal Astronomical Society, 425, 2817

Foreman-Mackey D., Hogg D. W., Lang D., Goodman J., 2013, Publications of the Astronomical Society of the Pacific, 125, 306

Fowlie A., Handley W., Su L., 2020, Monthly Notices of the Royal Astronomical Society, 497, 5256

Fowlie A., Handley W., Su L., 2021, Monthly Notices of the Royal Astronomical Society, 503, 1199

Fraser-McKelvie A., Cortese L., 2022, The Astrophysical Journal, 937, 117

Freundlich J., et al., 2020, Monthly Notices of the Royal Astronomical Society, 499, 2912

Freundlich J., Famaey B., Oria P.-A., Bílek M., Müller O., Ibata R., 2022, Astronomy & Astrophysics, 658, A26

Friedmann A., 1922, Zeitschrift fur Physik, 10, 377

Fukugita M., Hogan C. J., Peebles P. J. E., 1998, The Astrophysical Journal, 503, 518

Geiger B., Schneider P., 1998, Monthly Notices of the Royal Astronomical Society, 295, 497

Gherghinescu P., Das P., Grand R. J. J., Orkney M. D. A., 2023, Action-Based Dynamical Models of M31-like Galaxies (arxiv:2307.09963)

Giblin B., et al., 2021, Astronomy and Astrophysics, 645, A105

Gilman D., Birrer S., Nierenberg A., Treu T., Du X., Benson A., 2020, Monthly Notices of the Royal Astronomical Society, 491, 6077

Glowacki M., Elson E., Davé R., 2021, Monthly Notices of the Royal Astronomical Society, 507, 3267

Goodman J., Weare J., 2010, Communications in Applied Mathematics and Computational Science, 5, 65

Gration A., Wilkinson M. I., 2019, Monthly Notices of the Royal Astronomical Society, 485, 4878

Gunn J. E., Gott III J. R., 1972, The Astrophysical Journal, 176, 1

Guo Q., White S., Li C., Boylan-Kolchin M., 2010, Monthly Notices of the Royal Astronomical Society

Guo H., Li C., Zheng Z., Mo H. J., Jing Y. P., Zu Y., Lim S. H., Xu H., 2017, The Astrophysical Journal, 846, 61

Guo Q., et al., 2020, Nature Astronomy, 4, 246

Hadzhiyska B., Bose S., Eisenstein D., Hernquist L., Spergel D. N., 2020, Monthly Notices of the Royal Astronomical Society, 493, 5506

Hafen Z., et al., 2019, Monthly Notices of the Royal Astronomical Society, 488, 1248

Hashim M., El-Zant A., Freundlich J., Read J., Combes F., 2022, Halo Heating from Fluctuating Gas in a Model Dwarf (arxiv:2209.08631), doi:10.48550/arXiv.2209.08631

Haynes M. P., et al., 2011, The Astronomical Journal, 142, 170

Haynes M. P., et al., 2018, The Astrophysical Journal, 861, 49

Hess K. M., Pisano D. J., Wilcots E. M., Chengalur J. N., 2009, The Astrophysical Journal, 699, 76

Hoaglin D. C., F. M., Tukey, J. W. 1983, Understanding Robust and Exploratory Data Anlysis.. Wiley Series in Probability and Mathematical Statistics, Wiley, New York

Hobson A., 1969, Journal of Statistical Physics, 1, 383

Hockney R. W., Eastwood J. W., 1981, Computer Simulation Using Particles

Hubble Edwin., 1926, Contributions from the Mount Wilson Observatory / Carnegie Institution of Washington, 324, 1

Hubble E., 1929, Proceedings of the National Academy of Science, 15, 168

Ibata R., Diakogiannis F. I., Famaey B., Monari G., 2021, The Astrophysical Journal, 915, 5

Iorio G., Fraternali F., Nipoti C., Di Teodoro E., Read J. I., Battaglia G., 2016, Monthly Notices of the Royal Astronomical Society, p. stw3285

Ishiyama T., Fukushige T., Makino J., 2009, Publications of the Astronomical Society of Japan, 61, 1319

Ishiyama T., Nitadori K., Makino J., 2015 (arxiv:1211.4406)

Ishiyama T., et al., 2021, Monthly Notices of the Royal Astronomical Society, 506, 4210

Jackson R. A., et al., 2021, Monthly Notices of the Royal Astronomical Society, 502, 1785

Jethwa P., Erkal D., Belokurov V., 2018, Monthly Notices of the Royal Astronomical Society, 473, 2060

Jiang F., et al., 2019, Monthly Notices of the Royal Astronomical Society, 488, 4801

Johnston K. V., Spergel D. N., Hernquist L., 1995, The Astrophysical Journal, 451, 598

Jones M. G., Haynes M. P., Giovanelli R., Papastergis E., 2016, Monthly Notices of the Royal Astronomical Society, 455, 1574

Jones M. G., Haynes M. P., Giovanelli R., Moorman C., 2018, Monthly Notices of the Royal Astronomical Society, 477, 2

Jones G. C., et al., 2021, Monthly Notices of the Royal Astronomical Society, 507, 3540

Jungman G., Kamionkowski M., Griest K., 1996, Physics Reports, 267, 195

Kamdar H. M., Turk M. J., Brunner R. J., 2016, Monthly Notices of the Royal Astronomical Society, 455, 642

Kaplinghat M., Turner M., 2002, , 569, L19

Karmakar T., Genel S., Somerville R. S., 2023, Monthly Notices of the Royal Astronomical Society, 520, 1630

Kashfi T., Roshan M., Famaey B., 2023, Monthly Notices of the Royal Astronomical Society, 519, L21

Katz H., Lelli F., McGaugh S. S., Di Cintio A., Brook C. B., Schombert J. M., 2017, Monthly Notices of the Royal Astronomical Society, 466, 1648

Kelso C., Savage C., Valluri M., Freese K., Stinson G. S., Bailin J., 2016, Journal of Cosmology and Astroparticle Physics, 2016, 071

Khelashvili M., Rudakovskyi A., Hossenfelder S., 2022, Dark Matter Profiles of SPARC Galaxies: A Challenge to Fuzzy Dark Matter (arxiv:2207.14165)

Knebe A., et al., 2011, Monthly Notices of the Royal Astronomical Society, 415, 2293

Knollmann S. R., Knebe A., 2009, The Astrophysical Journal Supplement Series, 182, 608

Kohavi R., 1995. Proceedings of the Fourteenth International. Joint Conference on Artificial Intelligence.

Komatsu E., et al., 2009, The Astrophysical Journal Supplement Series, 180, 330

Kong D., Kaplinghat M., Yu H.-B., Fraternali F., Mancera Piña P. E., 2022, The Astrophysical Journal, 936, 166

Koposov S. E., et al., 2022, $S\hat{5}$: Probing the Milky Way and Magellanic Clouds Potentials with the 6-D Map of the Orphan-Chenab Stream (arxiv:2211.04495), doi:10.48550/arXiv.2211.04495

Koribalski B. S., et al., 2020, Astrophysics and Space Science, 365, 118

Kostić A., Jasche J., Ramanah D. K., Lavaux G., 2022, Astronomy and Astrophysics, 657, L17

Kourkchi E., Tully B., Courtois H., 2022, Bulletin of the AAS, 54

Kravtsov A. V., Berlind A. A., Wechsler R. H., Klypin A. A., Gottlöber S., Allgood B., Primack J. R., 2004, The Astrophysical Journal, 609, 35

Kullback S., Leibler R. A., 1951, The Annals of Mathematical Statistics, 22, 79

La Cava W., Orzechowski P., Burlacu B., Olivetti de França F., Virgolin M., Jin Y., Kommenda M., Moore J. H., 2021, Contemporary Symbolic Regression Methods and Their Relative Performance

Landy S. D., Szalay A. S., 1993, The Astrophysical Journal, 412, 64

Lang R. H., et al., 2003, Monthly Notices of the Royal Astronomical Society, 342, 738

Lang P., et al., 2020, The Astrophysical Journal, 897, 122

Law D. R., et al., 2015, The Astronomical Journal, 150, 19

Lazar A., et al., 2020, Monthly Notices of the Royal Astronomical Society, 497, 2393

Leauthaud A., Singh S., Luo Y., Ardila F., Greco J. P., Capak P., Greene J. E., Mayer L., 2020, Physics of the Dark Universe, 30, 100719

Lehmann B. V., Mao Y.-Y., Becker M. R., Skillman S. W., Wechsler R. H., 2016, The Astrophysical Journal, 834, 37

Leisman L., et al., 2017, The Astrophysical Journal, 842, 133

Lelli F., 2023, Mass Models of Disk Galaxies from Gas Dynamics (arxiv:2305.18224)

Lelli F., McGaugh S. S., Schombert J. M., 2015, The Astrophysical Journal, 816, L14

Lelli F., McGaugh S. S., Schombert J. M., 2016a, The Astronomical Journal, 152, 157

Lelli F., McGaugh S. S., Schombert J. M., 2016b, The Astrophysical Journal Letters, 816, L14

Lelli F., McGaugh S. S., Schombert J. M., Pawlowski M. S., 2017, The Astrophysical Journal, 836, 152

Lelli F., McGaugh S. S., Schombert J. M., Desmond H., Katz H., 2019, Monthly Notices of the Royal Astronomical Society, 484, 3267

Lelli F., Di Teodoro E. M., Fraternali F., Man A. W. S., Zhang Z.-Y., De Breuck C., Davis T. A., Maiolino R., 2021, Science, 371, 713

Lelli F., et al., 2023, Astronomy and Astrophysics, 672, A106

Leroy A. K., Walter F., Brinks E., Bigiel F., de Blok W. J. G., Madore B., Thornley M. D., 2008, The Astronomical Journal, 136, 2782

Leung G. Y. C., et al., 2018, Monthly Notices of the Royal Astronomical Society, 477, 254

Leung G. Y. C., Leaman R., Battaglia G., van de Ven G., Brooks A. M., Peñarrubia J., Venn K. A., 2021, Monthly Notices of the Royal Astronomical Society, 500, 410

Li C., Kauffmann G., Fu J., Wang J., Catinella B., Fabello S., Schiminovich D., Zhang W., 2012, Monthly Notices of the Royal Astronomical Society, 424, 1471

Li H., Li R., Mao S., Xu D., Long R. J., Emsellem E., 2016, Monthly Notices of the Royal Astronomical Society, 455, 3680

Li P., Lelli F., McGaugh S. S., Starkman N., Schombert J. M., 2019, Monthly Notices of the Royal Astronomical Society, 482, 5106

Li P., Lelli F., McGaugh S., Schombert J., 2020, The Astrophysical Journal Supplement Series, 247, 31

Li P., McGaugh S. S., Lelli F., Schombert J. M., Pawlowski M. S., 2022a, Incorporating Baryon-Driven Contraction of Dark Matter Halos in Rotation Curve Fits

Li P., McGaugh S. S., Lelli F., Schombert J. M., Pawlowski M. S., 2022b, Astronomy and Astrophysics, 665, A143

Li P., et al., 2023, Measuring Galaxy Cluster Mass Profiles into the Low Acceleration Regime with Galaxy Kinematics, doi:10.48550/arXiv.2303.10175

Lieu M., Farr W. M., Betancourt M., Smith G. P., Sereno M., McCarthy I. G., 2017, Monthly Notices of the Royal Astronomical Society, 468, 4872

Lovell C. C., et al., 2023, A Hierarchy of Normalizing Flows for Modelling the Galaxy-Halo Relationship (arxiv:2307.06967), doi:10.48550/arXiv.2307.06967

Lu S., Zhu K., Cappellari M., Li R., Mao S., Xu D., 2023a, MaNGA DynPop – II. Global Stellar Population, Gradients, and Star-Formation Histories from Integral-Field Spectroscopy of 10K Galaxies: Link with Galaxy Rotation, Shape, and Total-Density Gradients, doi:10.48550/arXiv.2304.11712

Lu T., Haiman Z., Li X., 2023b, Monthly Notices of the Royal Astronomical Society, 521, 2050

Luo Y., et al., 2023, The Merian Survey: Design, Construction, and Characterization of a Filter Set Optimized to Find Dwarf Galaxies and Measure Their Dark Matter Halo Properties with Weak Lensing, doi:10.48550/arXiv.2305.19310

Maddox N., et al., 2021, Astronomy & Astrophysics, 646, A35

Mancera Piña P. E., et al., 2019, The Astrophysical Journal, 883, L33

Mancera Piña P. E., Fraternali F., Oosterloo T., Adams E. A. K., Oman K. A., Leisman L., 2021, Monthly Notices of the Royal Astronomical Society

Mancera Piña P. E., Fraternali F., Oosterloo T., Adams E. A. K., di Teodoro E., Bacchini C., Iorio G., 2022, Monthly Notices of the Royal Astronomical Society, 514, 3329

Mandelbaum R., Wang W., Zu Y., White S., Henriques B., More S., 2016, Monthly Notices of the Royal Astronomical Society, 457, 3200

Marasco A., et al., 2023, Astronomy and Astrophysics, 670, A92

Margon B., 1999, Philosophical Transactions of the Royal Society of London Series A, 357, 93

Martin D. C., et al., 2005, The Astrophysical Journal, 619, L1

Martin A. M., Giovanelli R., Haynes M. P., Guzzo L., 2012, The Astrophysical Journal, 750, 38

Martinez G. D., Minor Q. E., Bullock J., Kaplinghat M., Simon J. D., Geha M., 2011, The Astrophysical Journal, 738, 55

Martinsson T. P. K., Verheijen M. A. W., Westfall K. B., Bershady M. A., Schechtman-Rook A., Andersen D. R., Swaters R. A., 2013, Astronomy and Astrophysics, 557, A130

Massey F. J., 1951, Journal of the American Statistical Association, 46, 68

Masters K. L., 2005. eprint: arXiv:astro-ph/0503271

Masters K. L., et al., 2019, Monthly Notices of the Royal Astronomical Society, 488, 3396

McGaugh S. S., 2005, The Astrophysical Journal, 632, 859

McGaugh S. S., van Dokkum P., 2021, Research Notes of the AAS, 5, 23

McGaugh S. S., Schombert J. M., Bothun G. D., de Blok W. J. G., 2000, The Astrophysical Journal, 533, L99

McGaugh S. S., Lelli F., Schombert J. M., 2016, Physical Review Letters, 117, 201101

McGaugh S., Lelli F., Li P., Schombert J., 2019, Proceedings of the International Astronomical Union, 14, 144

McGaugh S. S., Lelli F., Schombert J. M., 2020, Research Notes of the AAS, 4, 45

Méndez-Abreu J., Sánchez-Janssen R., Aguerri J. A. L., 2010, The Astrophysical Journal, 711, L61

Milgrom M., 1983, The Astrophysical Journal, 270, 365

Miller L., Kitching T. D., Heymans C., Heavens A. F., van Waerbeke L., 2007, Monthly Notices of the Royal Astronomical Society, 382, 315

Miller L., et al., 2013, Monthly Notices of the Royal Astronomical Society, 429, 2858

Mitzkus M., Cappellari M., Walcher C. J., 2017, Monthly Notices of the Royal Astronomical Society, 464, 4789

Mo H. J., Mao S., White S. D. M., 1998, Monthly Notices of the Royal Astronomical Society, 295, 319

Mo H., van den Bosch F. C., White S., 2010, Galaxy Formation and Evolution

Mogotsi K. M., de Blok W. J. G., Caldu-Primo A., Walter F., Ianjamasimanana R., Leroy A. K., 2016, The Astronomical Journal, 151, 15

More S., Diemer B., Kravtsov A. V., 2015, The Astrophysical Journal, 810, 36

Moreno J., et al., 2022, Nature Astronomy, 6, 496

Moster B. P., Somerville R. S., Maulbetsch C., van den Bosch F. C., Macciò A. V., Naab T., Oser L., 2010, The Astrophysical Journal, 710, 903

Munshi F., Brooks A. M., Applebaum E., Christensen C. R., Quinn T., Sligh S., 2021, , 923, 35

Naab T., Ostriker J. P., 2017, Annual Review of Astronomy and Astrophysics, 55, 59

Nadler E. O., et al., 2020, The Astrophysical Journal, 893, 48

Nadler E. O., Birrer S., Gilman D., Wechsler R. H., Du X., Benson A., Nierenberg A. M., Treu T., 2021, The Astrophysical Journal, 917, 7

Naik A. P., Puchwein E., Davis A.-C., Sijacki D., Desmond H., 2019, Monthly Notices of the Royal Astronomical Society, 489, 771

Naik A. P., An J., Burrage C., Evans N. W., 2021,] 10.1093/mnras/stac153

Navarro J. F., Frenk C. S., White S. D. M., 1997, The Astrophysical Journal, 490, 493

Navarro J. F., Benítez-Llambay A., Fattahi A., Frenk C. S., Ludlow A. D., Oman K. A., Schaller M., Theuns T., 2017, , 471, 1841

Nipoti C., Binney J., 2015, Monthly Notices of the Royal Astronomical Society, 446, 1820

Nitschai M. S., Cappellari M., Neumayer N., 2020, Monthly Notices of the Royal Astronomical Society, 494, 6001

O'Brien T. A., Collins W. D., Rauscher S. A., Ringler T. D., 2014, Computational Statistics & Data Analysis, 79, 222

O'Brien T. A., Kashinath K., Cavanaugh N. R., Collins W. D., O'Brien J. P., 2016, Computational Statistics & Data Analysis, 101, 148

Obreschkow D., Croton D., De Lucia G., Khochfar S., Rawlings S., 2009, The Astrophysical Journal, 698, 1467

Oh S.-H., et al., 2015, The Astronomical Journal, 149, 180

Oman K. A., 2019, Astrophysics Source Code Library, p. ascl:1911.005

Oman K. A., et al., 2015, Monthly Notices of the Royal Astronomical Society, 452, 3650

Oman K. A., Brouwer M. M., Ludlow A. D., Navarro J. F., 2020, Observational Constraints on the Slope of the Radial Acceleration Relation at Low Accelerations (arxiv:2006.06700)

Oort J. H., 1932, Bulletin of the Astronomical Institutes of the Netherlands, 6, 249

Oosterloo T., Verheijen M., van Cappellen W., 2010 (arxiv:1007.5141)

Orkney M. D. A., et al., 2021, Monthly Notices of the Royal Astronomical Society, 504, 3509

Osato K., Nagai D., 2023, Monthly Notices of the Royal Astronomical Society, 519, 2069

Ostriker J. P., Peebles P. J. E., 1973, The Astrophysical Journal, 186, 467

Papastergis E., Shankar F., 2016, Astronomy & Astrophysics, 591, A58

Papastergis E., Giovanelli R., Haynes M. P., Rodríguez-Puebla A., Jones M. G., 2013, The Astrophysical Journal, 776, 43

Papastergis E., Giovanelli R., Haynes M. P., Shankar F., 2015, Astronomy & Astrophysics, 574, A113

Papastergis E., Adams E. A. K., van der Hulst J. M., 2016, Astronomy & Astrophysics, 593, A39

Paranjape A., Sheth R. K., 2021, Monthly Notices of the Royal Astronomical Society, 507, 632

Paranjape A., Srianand R., Choudhury T. R., Sheth R. K., 2021, arXiv:2105.04570 [astro-ph]

Pardo K., Spergel D. N., 2020, , 125, 211101

Pawlowski M. S., 2018, Modern Physics Letters A, 33, 1830004

Pearson S., Price-Whelan A. M., Hogg D. W., Seth A. C., Sand D. J., Hunt J. A. S., Crnojević D., 2022, The Astrophysical Journal, 941, 19

Pedregosa F., et al., 2011, Journal of Machine Learning Research, 12, 2825

Peebles P. J. E., 1980, The Large-Scale Structure of the Universe

Peebles P. J. E., 2020

Peñarrubia J., Pontzen A., Walker M. G., Koposov S. E., 2012, The Astrophysical Journal, 759, L42

Penzias A. A., Wilson R. W., 1965, The Astrophysical Journal, 142, 419

Planck Collaboration et al., 2020, Astronomy and Astrophysics, 641, A6

Ponomareva A. A., Verheijen M. A. W., Bosma A., 2016, Monthly Notices of the Royal Astronomical Society, 463, 4052

Ponomareva A. A., Verheijen M. A. W., Papastergis E., Bosma A., Peletier R. F., 2018, Monthly Notices of the Royal Astronomical Society, 474, 4366

Ponomareva A. A., et al., 2021, Monthly Notices of the Royal Astronomical Society, 508, 1195

Pontzen A., Governato F., 2014, Nature, 506, 171

Posti L., Fall S. M., 2021, Astronomy & Astrophysics, 649, A119

Posti L., Helmi A., 2019, Astronomy & Astrophysics, 621, A56

Posti L., Fraternali F., Marasco A., 2019, Astronomy and Astrophysics, 626, A56

Pound R. V., Rebka G. A., 1960, Physical Review Letters, 4, 337

Press W. H., Schechter P., 1974, The Astrophysical Journal, 187, 425

Putko J., Almeida J. S., Munoz-Tunon C., Ramos A. A., Elmegreen B. G., Elmegreen D. M., 2019, The Astrophysical Journal, 883, 10

Rampf C., 2021, Cosmological Vlasov-Poisson Equations for Dark Matter: Recent Developments and Connections to Selected Plasma Problems, doi:10.48550/arXiv.2110.06265

Read J. I., Erkal D., 2019, Monthly Notices of the Royal Astronomical Society, 487, 5799

Read J. I., Gilmore G., 2005, Monthly Notices of the Royal Astronomical Society, 356, 107

Read J. I., Agertz O., Collins M. L. M., 2016, Monthly Notices of the Royal Astronomical Society, 459, 2573

Read J. I., Iorio G., Agertz O., Fraternali F., 2017, , 467, 2019

Read J. I., Walker M. G., Steger P., 2019, Monthly Notices of the Royal Astronomical Society, 484, 1401

Reddick R. M., Wechsler R. H., Tinker J. L., Behroozi P. S., 2013, The Astrophysical Journal, 771, 30

Ren T., Kwa A., Kaplinghat M., Yu H.-B., 2019, Physical Review X, 9, 031020

Rey M. P., et al., 2023, EDGE – Dark Matter or Astrophysics? Clear Prospects to Break Dark Matter Heating Degeneracies with HI Rotation in Faint Dwarf Galaxies, doi:10.48550/arXiv.2309.00041

Reynolds T. N., Westmeier T., Staveley-Smith L., Chauhan G., Lagos C. D. P., 2020, Monthly Notices of the Royal Astronomical Society, 493, 5089

Riess A. G., Breuval L., 2023, The Local Value of H$_0$, doi:10.48550/arXiv.2308.10954

Riess A. G., et al., 2022, The Astrophysical Journal Letters, 934, L7

Rizzo F., Vegetti S., Fraternali F., Stacey H. R., Powell D., 2021, Monthly Notices of the Royal Astronomical Society, 507, 3952

Robertson A., Massey R., Eke V., 2017, Monthly Notices of the Royal Astronomical Society, 465, 569

Rogstad D. H., Lockhart I. A., Wright M. C. H., 1974, The Astrophysical Journal, 193, 309

Roper F. A., Oman K. A., Frenk C. S., Benítez-Llambay A., Navarro J. F., Santos-Santos I. M. E., 2022, The Diversity of Rotation Curves of Simulated Galaxies with Cusps and Cores

Roper F. A., Oman K. A., Frenk C. S., Benítez-Llambay A., Navarro J. F., Santos-Santos I. M. E., 2023, Monthly Notices of the Royal Astronomical Society, 521, 1316

Roshan M., Ghafourian N., Kashfi T., Banik I., Haslbauer M., Cuomo V., Famaey B., Kroupa P., 2021, Monthly Notices of the Royal Astronomical Society, 508, 926

Rubin V. C., Ford Jr. W. K., Thonnard N., 1980, The Astrophysical Journal, 238, 471

Saburova A. S., Kasparova A. V., Katkov I. Y., 2016, Monthly Notices of the Royal Astronomical Society, 463, 2523

Safarzadeh M., Loeb A., 2021, The Astrophysical Journal, 914, L37

Saha 2003, The Observatory, 123, 398

Saifollahi T., Trujillo I., Beasley M. A., Peletier R. F., Knapen J. H., 2021, Monthly Notices of the Royal Astronomical Society, 502, 5921

Sales L. V., Wetzel A., Fattahi A., 2022, Nature Astronomy, 6, 897

Salim S., Boquien M., Lee J. C., 2018, The Astrophysical Journal, 859, 11

Sánchez S. F., et al., 2012, Astronomy & Astrophysics, 538, A8

Sánchez S. F., et al., 2016, Astronomy and Astrophysics, 594, A36

Santos-Santos I. M., Brook C. B., Stinson G., Di Cintio A., Wadsley J., Domínguez-Tenreiro R., Gottlöber S., Yepes G., 2016, Monthly Notices of the Royal Astronomical Society, 455, 476

Sardone A., Peter A. H. G., Brooks A. M., Kaczmarek J., 2023, Closing the Gap between Observed Low-Mass Galaxy HI Kinematics and CDM Predictions (arxiv:2306.07417)

Schawinski K., et al., 2014, Monthly Notices of the Royal Astronomical Society, 440, 889

Schechter P., 1976, The Astrophysical Journal, 203, 297

Schittenhelm D., Wacker P., 2021, Preprint (arxiv:2005.08602)

Schmidt M., 1968, The Astrophysical Journal, 151, 393

Schneider M. D., Hogg D. W., Marshall P. J., Dawson W. A., Meyers J., Bard D. J., Lang D., 2015, The Astrophysical Journal, 807, 87

Schombert J., McGaugh S., Lelli F., 2022, The Astronomical Journal, 163, 154

Schrabback T., et al., 2021, Astronomy & Astrophysics, 646, A73

Schulman E., Bregman J. N., Roberts M. S., 1994, The Astrophysical Journal, 423, 180

Schulz A. E., Mandelbaum R., Padmanabhan N., 2010, Monthly Notices of the Royal Astronomical Society, 408, 1463

Schwarzschild M., 1979, The Astrophysical Journal, 232, 236

Secrest N. J., von Hausegger S., Rameez M., Mohayaee R., Sarkar S., 2022, The Astrophysical Journal, 937, L31

Seljak U., Makarov A., McDonald P., Trac H., 2006, Physical Review Letters, 97, 191303

Sellwood J. A., Sanders R. H., 2022, arXiv:2202.08678 [astro-ph]

Shajib A. J., Strides 2020, 235, 266.06

Shajib A. J., Treu T., Birrer S., Sonnenfeld A., 2021, Monthly Notices of the Royal Astronomical Society, 503, 2380

Shannon C. E., Weaver W., 1949, The mathematical theory of communication

Simard L., et al., 2002, The Astrophysical Journal Supplement Series, 142, 1

Skordis C., Z łośnik T., 2021, , 127, 161302

Smee S. A., et al., 2013, The Astronomical Journal, 146, 32

Somerville R. S., Primack J. R., 1999, Monthly Notices of the Royal Astronomical Society, 310, 1087

Sonnenfeld A., Leauthaud A., 2018, Monthly Notices of the Royal Astronomical Society, 477, 5460

Sonnenfeld A., et al., 2022, Astronomy and Astrophysics, 662, A55

Springob C. M., Haynes M. P., Giovanelli R., Kent B. R., 2005, The Astrophysical Journal Supplement Series, 160, 149

Stark D. V., et al., 2021, Monthly Notices of the Royal Astronomical Society, 503, 1345

Staveley-Smith L., Oosterloo T., 2015, HI Science with the Square Kilometre Array. eprint: arXiv:1506.04473, doi:10.22323/1.215.0167

Stevens A. R. H., Diemer B., Lagos C. d. P., Nelson D., Obreschkow D., Wang J., Marinacci F., 2019, Monthly Notices of the Royal Astronomical Society, 490, 96

Stiskalek R., Desmond H., 2023, On the Fundamentality of the Radial Acceleration Relation for Late-Type Galaxy Dynamics, doi:10.48550/arXiv.2305.19978

Stiskalek R., Desmond H., Holvey T., Jones M. G., 2021, Monthly Notices of the Royal Astronomical Society, 506, 3205

Stiskalek R., Bartlett D. J., Desmond H., Anbajagane D., 2022, Monthly Notices of the Royal Astronomical Society, p. stac1609

Stott J. P., et al., 2016, Monthly Notices of the Royal Astronomical Society, 457, 1888

Syer D., Tremaine S., 1996, Monthly Notices of the Royal Astronomical Society, 282, 223

Taranu D. S., et al., 2017, The Astrophysical Journal, 850, 70

Tim de Zeeuw P., et al., 2002, Monthly Notices of the Royal Astronomical Society, 329, 513

Tinsley B. M., 1980, Fundamentals of Cosmic Physics, 5, 287

Tomita K., 1969, Progress of Theoretical Physics, 42, 9

Trotta R., 2008, Contemporary Physics, 49, 71

Trujillo-Gomez S., Kruijssen J. M. D., Reina-Campos M., 2022, Monthly Notices of the Royal Astronomical Society, 510, 3356

Tully R. B., Fisher J. R., 1977, Astronomy and Astrophysics, 500, 105

Umetsu K., Broadhurst T., Zitrin A., Medezinski E., Coe D., Postman M., 2011, The Astrophysical Journal, 738, 41

Unterborn C. T., Ryden B. S., 2008, The Astrophysical Journal, 687, 976

Velmani P., Paranjape A., 2022, Preprint (arxiv:2206.07733)

Verbeke R., Papastergis E., Ponomareva A. A., Rathi S., Rijcke S. D., 2017, Astronomy & Astrophysics, 607, A13

Villaescusa-Navarro F., et al., 2021, The Astrophysical Journal, 915, 71

Villasenor B., Robertson B., Madau P., Schneider E., 2023, , 108, 023502

Vogelsberger M., Marinacci F., Torrey P., Puchwein E., 2020, Nature Reviews Physics, 2, 42

Walter F., Brinks E., de Blok W. J. G., Bigiel F., Kennicutt J., Thornley M. D., Leroy A. K., 2008, The Astronomical Journal, 136, 2563

Wambsganss J., Schmidt R., 1998, New Astronomy Reviews, 42, 101

Wang J., et al., 2014, Monthly Notices of the Royal Astronomical Society, 441, 2159

Wang J., Koribalski B. S., Serra P., van der Hulst T., Roychowdhury S., Kamphuis P., Chengalur J. N., 2016, Monthly Notices of the Royal Astronomical Society, 460, 2143

Wang B., Cappellari M., Peng Y., 2020a, Monthly Notices of the Royal Astronomical Society: Letters, 500, L27

Wang J., Bose S., Frenk C. S., Gao L., Jenkins A., Springel V., White S. D. M., 2020b, Nature, 585, 39

Wang W., et al., 2022, , 941, 108

Wang C., et al., 2023, MaNGA DynPop – IV. Stacked Total Density Profile of Galaxy Groups and Clusters from Combining Dynamical Models of Integral-Field Stellar Kinematics and Galaxy-Galaxy Lensing, doi:10.48550/arXiv.2304.11715

Watts A. B., Power C., Catinella B., Cortese L., Stevens A. R. H., 2020, Monthly Notices of the Royal Astronomical Society, 499, 5205

Wechsler R. H., Tinker J. L., 2018, Annual Review of Astronomy and Astrophysics, 56, 435

Weinberg S., 1972, Gravitation and Cosmology: Principles and Applications of the General Theory of Relativity

Westfall K. B., et al., 2019, The Astronomical Journal, 158, 231

White S. D. M., Rees M. J., 1978, Monthly Notices of the Royal Astronomical Society, 183, 341

XENON Collaboration 7 et al., 2018, Physical Review Letters, 121, 111302

Yahya S., Bull P., Santos M. G., Silva M., Maartens R., Okouma P., Bassett B., 2015, Monthly Notices of the Royal Astronomical Society, 450, 2251

Yang T., Cai Y.-C., Cui W., Davé R., Peacock J. A., Sorini D., 2022, Monthly Notices of the Royal Astronomical Society, 516, 4084

Yasin T., Desmond H., Devriendt J., Slyz A., 2022, Inferring Dark Matter Halo Properties for HI-selected Galaxies (arxiv:2206.15443), doi:10.48550/arXiv.2206.15443

Yasin T., Desmond H., Devriendt J., Slyz A., 2023a, Monthly Notices of the Royal Astronomical Society

Yasin T., Desmond H., Devriendt J., Slyz A., 2023b, Monthly Notices of the Royal Astronomical Society, p. stad2406

Yu N., Ho L. C., Wang J., 2020, The Astrophysical Journal, 898, 102

Yu N., Ho L. C., Wang J., Li H., 2022, arXiv:2203.13404 [astro-ph]

Zel'dovich Ya. B., 1970, Astronomy and Astrophysics, 5, 84

Zentner A., Dandavate S., Slone O., Lisanti M., 2022, Journal of Cosmology and Astroparticle Physics, 2022, 031

Zhang K., et al., 2020, Monthly Notices of the Royal Astronomical Society, 500, 1741

Zheng Z., et al., 2005, The Astrophysical Journal, 633, 791

Zhu K., Lu S., Cappellari M., Li R., Mao S., Gao L., 2023a, MaNGA DynPop – III. Accurate Stellar Dynamics vs. Stellar Population Relations in 6000 Early-Type and Spiral Galaxies: Fundamental Plane, Mass-to-Light Ratios, Total Density Slopes, and Dark Matter Fractions, doi:10.48550/arXiv.2304.11714

Zhu K., Lu S., Cappellari M., Li R., Mao S., Gao L., 2023b, Monthly Notices of the Royal Astronomical Society, 522, 6326

Zwaan M. A., Meyer M. J., Staveley-Smith L., 2010, Monthly Notices of the Royal Astronomical Society, 403, 1969

Zwicky F., 1933, Helvetica Physica Acta, 6, 110

van Dokkum P., et al., 2018, Nature, 555, 629

van Dokkum P., Danieli S., Abraham R., Conroy C., Romanowsky A. J., 2019, The Astrophysical Journal, 874, L5

van Dokkum P., et al., 2022, Nature, 605, 435

van den Bosch R. C. E., van de Ven G., 2009, Monthly Notices of the Royal Astronomical Society, 398, 1117